The Synthesis of CdTe-Based Quantum Dots

Taniguchi, Shohei

Awarding institution:
King's College London

Title: The Synthesis of CdTe-Based Quantum Dots

Author: Shohei Taniguchi

King's College London

University of London

The Synthesis of CdTe-Based Quantum Dots

by

Shohei Taniguchi

Doctor of Philosophy

School of Natural and Mathematical Sciences

Department of Physics

2012

Declaration of Authorship

I, Shohei Taniguchi, declare that this thesis titled 'The Synthesis of CdTe-Based Quantum Dots' is the result of the work undertaken between August 2009 and March 2012 under the supervision of Dr Mark Green. I confirm that:

- This work was done wholly or mainly while in candidature for a research degree at this University.
- Where any part of this thesis has previously been submitted for a degree or any other qualification at this university or any other institution, this has been clearly stated.
- Where I have consulted the published work of others, this is always clearly attributed.
- Where I have quoted from the work of others, the source is always given. With the exception of such quotations, this thesis is entirely my own work.
- I have acknowledged all main sources of help.
- Where the thesis is based on work done by myself jointly with others, I have made clear exactly what was done by others and what I have contributed myself.

Signed: 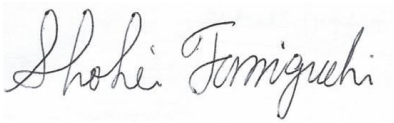

Date: 2012/05/18

Abstract

As a multipotent tool for scientific exploration, semiconductor nanoparticles, or quantum dots (QDs), have gained enormous interest in nanoscience in the past two decades. The research presented here focused on cadmium telluride (CdTe) QDs: novel synthetic methodologies were used to prepare previously inaccessible nanomaterials based on CdTe QDs.

CdTe/CdSe/ZnSe core/shell/shell QDs were prepared by a one-pot synthesis. The resulting QDs exhibited near infrared emission, were readily dispersed in aqueous media and applied to deep tissue imaging where emission through the skin indicated the gradual transition of the QDs *via* the lymphatic tract.

Using a different synthetic approach, CdTe QDs, which were dispersed in organic media, were exposed to mercury cations in a toluene/methanol solution, resulting in CdHgTe nanoalloy formation. The optical characteristics of the resulting materials were substantially red-shifted from those of the original CdTe QDs. Structural changes were also examined and the influence of the addition of metal cations to other colloidal QDs.

The organometallic compound $Cd(TeC_6H_5)_2$ was synthesised and used as a single-source precursor for CdTe QDs. Products isolated after thermal decomposition of the single-source precursors showed strong emission of various wavelengths depending on the reaction time. The underlying chemistry on QDs formation was investigated, and CdTe/ZnS QDs were prepared using only single-source precursors.

To make the QDs useful in biology, the surface of organically synthesised CdTe/ZnS QDs was modified with an amphiphilic protein (hydrophobin) to phase transfer the particles into aqueous solution. The QDs exhibited bright emission after phase transfer, and were applied to cell imaging in order to examine the validity as a fluorophore and the influence on a cell.

Acknowledgements

First of all, I would like to thank my family, Mitsunori, Kiyo, Haruka and Eiji for giving me an invaluable opportunity to pursue the PhD abroad. This thesis would not be possible without their helps and patience. Also, I would like to show my gratitude to Shinobu Tamura and Reiko Tamura for their support while staying in Japan.

I am very thankful to my supervisor, Mark Green. His knowledge and experience have been extremely helpful for the work. He has kindly regarded me as an independent researcher and provided me with precious opportunities and responsibilities for proceeding the projects, which would certainly be an important experience for my career.

Also, I thank my colleagues, Arun Panneerselvam, Melanie Bottrill, Phil Howes, Zeina Hashim, Wijittra Wichiansee and Hassan Mirzai. I am also grateful to learn many things from you through scientific discussions and daily conversations. I would like to thank to Bill Luckhurst and Nigel Arnot for technical assistance. Andy Cakebread, Roger Tye, Alice Warley, Gema Vizcay-Barrena, Tony Brain, Teck Lim, Sarwat Rizvi, Dave Lincoln, Raha Ahmad Khanbeigi, Lea Ann Dailey and Karen Shaw had considerable contributions to this thesis.

My personal thanks also go to Anuphon Laohavisit, Neil Dalchau, Katy Coxon, Emi&Ioannis Fostiropoulos, Pei-Hua Chung, James Levitt, Gianmarco Zanda, Giovanni Peralta, Jean-Sebastien Bouillard, Daniel O'Connor, Julia Kilpatrick, Taro Uematsu and Kazuki Yoshii for scientific discussions, transcripts, foods, wines and pints of ales. I will certainly buy you drinks next time.

Finally, I acknowledge the Japan Student Services Organization (JASSO), the British Council Japan Association (BCJA) and King’s College London (King’s Overseas Research Studentship) for financial supports.

Table of Contents

Declaration of Authorship ..... **II**

Abstract ..... **III**

Acknowledgements ..... **IV**

Table of Contents ..... **V**

List of Figures ..... **IX**

List of Tables ..... **XVI**

List of Equations ..... **XVII**

Glossary ..... **XVIII**

Chapter 1 General Background **1**

1.1 Current progress in Nanoscience 1

1.1.1 Carbon-based Nanomaterials 1

1.1.2 Inorganic Nanomaterials 2

1.1.3 Other Type of Nanomaterials 4

1.2 Theory of Quantum Dots 6

1.2.1 Wannier Exciton 6

1.2.2 Free Electron Model 8

1.2.3 Energy States in Semiconductor Quantum Dots 12

1.3 Synthetic Techniques for Quantum Dots 14

1.4 Application of QDs 21

1.5 CdTe QDs 25

1.6 The Objective of the Thesis 29

Chapter 2 Synthesis of CdTe/CdSe/ZnSe Quantum Dots for in vivo Deep Tissue Imaging **30**

2.1 Introduction 30

2.2 One-pot Synthesis of CdTe/CdSe/ZnSe QDs in Aqueous Media 33
2.3 Characterisation of the QDs 35
2.3.1 Optical Spectroscopy 35
2.3.2 Transmission Electron Microscopy (TEM) 39
2.4 QDs Formation Mechanism 41
2.5 Tuning the Emission Wavelength 45
2.6 Synthesis of Glutathione-Capped CdTe/CdSe/ZnSe QDs 47
2.7 Application to Deep Tissue Imaging 49
2.8 Conclusion 50
Chapter 3 The Room-Temperature Chemical Transformation of CdTe QDs by Reactive Cations 51
3.1 Introduction 51
3.2 Molecular Welding Effect on CdHgTe Synthesis 53
3.3 Optical Characterisation 60
3.4 Influences on Redox Potential of Metal Cations 62
3.5 Application to Other Nanomaterials 67
3.5.1 CdSe QDs 67
3.5.2 CdSe Nanorods 71
3.5.3 CdTe Tetrapods 73
3.6 Conclusion 75
Chapter 4 Colloidal CdTe/ZnS QDs Synthesis Using Molecular Single-Source Precursors 76
4.1 Introduction 76
4.2 CdTe SSPs Preparation 78
4.3 Synthesis of CdTe QDs from SSP 80
4.4 Formation of CdTe/ZnS Core/Shell QDs 85
4.5 Examination of Reaction Parameters 91
4.6 Conclusion 93
Chapter 5 Phase Transfer of QDs Using Hydrophobins for Cell Imaging 95

5.1 Introduction 95
5.2 Characteristics of Hydrophobins 98
5.3 Preparation of Water-soluble Hydrophobin-CdTe/ZnS QDs 99
5.4 Other Methods for Phase Transfer 103
5.5 Purification of Hydrophobin-CdTe/ZnS QDs 104
5.6 Phase Transfer Using Other QDs 109
5.7 Biological Experiments 111
5.8 Conclusion 114
Chapter 6 Experimental Methods 115
6.1 General Materials and Methods 115
6.1.1 Chemicals 115
6.1.2 General Analysis Techniques 116
6.2 CdTe/CdSe/ZnSe QDs 119
6.2.1 $(NH_4)_2Te$ Stock Solution 119
6.2.2 Na_2SeSO_3 Stock Solution 119
6.2.3 Water-soluble CdTe QDs 120
6.2.4 CdTe/CdSe/ZnSe QDs Synthesis 120
6.2.5 GSH-capped QDs 121
6.2.6 CdTe/CdSe/ZnSe QDs in Different Reaction Conditions 121
6.2.7 Tissue Imaging 121
6.3 QDs for Room-Temperature Chemical Transformation 122
6.3.1 CdTe QDs by Organometallic Route 122
6.3.2 CdSe QDs 122
6.3.3 CdSe Nanorods 123
6.3.4 CdTe Tetrapods 123
6.3.5 Purification of Nanocrystals 123
6.3.6 CdHgTe Nanoalloys 124
6.4 QDs Using SSPs 124

6.4.1 $Cd(TePh)_2$ Synthesis 124
6.4.2 Purification of $Cd(TePh)_2$ 125
6.4.3 CdTe QDs Synthesis from $Cd(TePh)_2$ 125
6.4.4 CdTe/ZnS Synthesis 126
6.5 Phase Transfer of QDs 126
6.5.1 CdTe/ZnS QDs for Phase Transfer Reaction 126
6.5.2 Phase Transfer with Hydrophobins 127
6.5.3 Cell Imaging 128
Chapter 7 Conclusion 130
7.1 Summary of Work 130
7.2 Future Work 133
Bibliography 135
Appendix A Concentration of QDs 154
Appendix B Calculation of the Amount of Shell Sources for One Monolayer 156

List of Figures

Figure 1.1. Schematics of Wannier exciton and a hydrogen atom. 6

Figure 1.2. Influences of structure on the movement of the corresponding exciton. An exciton in bulk semiconductors moves freely within its exciton Bohr radius, whilst nanomaterials which have dimensions smaller than the exciton Bohr radius in at least one dimension will result in limited movement on the exciton depending on the degree of physical confinement. 7

Figure 1.3. Energy diagram of a single atom, quantum dots and a bulk semiconductor. The band gap energy (E_g) of quantum dots changes depending on particle sizes as indicated above. A small quantum dot has a larger E_g, whilst a big quantum dot has a smaller E_g. 8

Figure 1.4. Energy-vector relationship in the solid material in each three direction (x, y, z). The difference between each vector (Δk) is very small so that a series of dots can be regarded as quasi-continuous. 9

Figure 1.5. Schematics of the particle-in-a-box model. Blue curves the indicate electron wave. Waves with n = 4, 5,… are omitted. 10

Figure 1.6. Energy-vector relationship in two-dimensional system. Whereas the graph in x- and y-direction is the same shape as Figure 1.4, the graph in z-direction is different, showing discrete wave vectors and energy states. Δk is relatively large hence energy states are quantised in the z-direction. 11

Figure 1.7. Free electron energy-vector relationship in quantum dots. Energy states in all direction have discrete level in contrast to Figure 1.6. 12

Figure 1.8. Schematics of the exciton energy-wave vector relationship. Energy states of excited electrons are on the upper side, whilst those of holes are on the lower side of the k-axis. The contribution of Coulombic interactions was omitted. 14

Figure 1.9. Schematic diagram of colloidal quantum dots synthesis. 15

Figure 1.10. Energy relationship in type II QDs (CdTe/CdSe). (CB and VB = conduction band and valence band, respectively.) 18

Figure 1.11. Schematic diagram of a cation exchange reaction. (a) List of hard/soft acids/bases and their relationship. (b) Visualisation of cation exchange in colloidal QD. Soft acids (light

blue) in the solution will replace hard acids (thick blue) in the QD because of strong binding affinity between soft acids and soft bases. 21

Figure 1.12. Absorption (black) and fluorescence (coloured) spectra of (a) a typical QDs sample in toluene (tetradecylphosphonic acid-capped CdTe QDs) and (b) rhodamine 6G ethanolic solution. The QDs were excited at 550 nm, and the rhodamine 6G at 460 nm. 23

Figure 1.13. Band gap energy of CdTe QDs as a function of diameter. Bulk band gap energy $E_g(bulk)$ is 1.45 eV at 300 K, the Planck constant h is $6.626 \cdot 10^{-34}$ Js. The effective masses of electron and hole for CdTe are $m_e = 0.11m_0$, $m_h = 0.35m_0$, where m_0 is the mass of free electron ($m_0 = 9.1095 \cdot 10^{-31}$ kg). Thus, $m^* = 0.0837m_0$. $\varepsilon_0 = 8.854 \cdot 10^{-12}$ $C^2N^{-1}m^{-2}$ and $\varepsilon_{CdTe} =$ 10.3. 26

Figure 2.1. Suggested structure of mercaptoundecanoic acid (MUA)-capped CdTe/CdSe/ZnSe QDs. 32

Figure 2.2. Energy band offsets for semiconductors comprised of the core/shell/shell QDs. The energy states in conduction band (CB) and valence band (VB) were obtained from literature.. 32

Figure 2.3. Prepared QDs under (a) room light and (b) UV lamp (λ = 365 nm). The left vial is MUA-CdTe QDs, whereas the right is MUA-CdTe/CdSe/ZnSe QDs. 34

Figure 2.4. Reaction schematics for the synthesis of CdTe/CdSe/ZnSe QDs using the SIPOP method. Extra cadmium and selenium ions are left in the solution for subsequent deposition of a CdSe inner shell and a ZnSe outer shell. 35

Figure 2.5. Normalised emission and absorption spectra for CdTe QDs (orange curves) and CdTe/CdSe/ZnSe QDs (brown curves). Solid lines show absorption spectra, whilst dashed lines indicate emission spectra. Excitation wavelength = 450 nm. 36

Figure 2.6. (a) Normalised spectral transition of QD during the shell formation. From the left to right, 1) crude CdTe, 2) first Se addition (0.025 mmol), 3) first Zn addition (0.10 mmol), 4) second Se addition (0.025 mmol), 5) second Zn addition (0.10 mmol), 6) third Se addition (0.025 mmol), and 7) the sample after 16 hours reaction from the final precursor addition. (b) Emission intensity as a function of reaction time. CdTe QDs formation was set as 0 hour. 38

Figure 2.7. Relationship between integrated emission intensity and absorbance of rhodamine 6G (black), CdTe QDs (orange), and CdTe/CdSe/ZnSe QDs (brown). The gradients of the slopes are indicated inside the graph. 38

Figure 2.8. TEM images of purified (a) CdTe, (b) CdTe/CdSe, and (c) CdTe/CdSe/ZnSe QDs. (d) high resolution TEM image of CdTe/CdSe/ZnSe QDs. 40

Figure 2.9. Size distribution of the QDs measured from TEM images. CdTe (blue), CdTe/CdSe (orange), and CdTe/CdSe/ZnSe QDs (red), respectively. 41

Figure 2.10. Photograph showing the colour change in the course of CdTe/CdSe/ZnSe QDs formation. (upper) Under room light and (lower) under 365 nm excitation. From left to right, a) CdTe, b) the first Se source addition, c) the first Zn source addition, d) the second Zn/S sources addition, and e) 16 hours after the final precursor addition. No samples were purified. 42

Figure 2.11. TEM image of CdTe QDs 1 hour after selenium source addition. 44

Figure 2.12. Suggested mechanism of nanorod formation after Na_2SeSO_3 addition on MUA-CdTe QDs. 44

Figure 2.13. Absorption (grey lines) and emission spectra (black lines) of CdTe/CdSe/ZnSe QDs with lower MUA concentration (solid lines) and the emission of original CdTe/CdSe/ZnSe QDs (dashed lines). In the QDs with lower amounts of MUA, 21 mg (0.098 mmol) of MUA was used in the CdTe QDs synthesis, resulting in a CdTe solution where the molecular ratio of Cd and MUA was 1:1.2, instead of 1:1.5. The remaining synthetic procedure was kept the same. 46

Figure 2.14. Molecular structure of glutathione (reduced form). 48

Figure 2.15. (a) Emission spectra of GSH-CdTe (green line) and the product after selenium and zinc source addition (red line). Excitation wavelength = 450 nm. (b) Emission wavelength at each reaction stage. (c) Intensity as a function of reaction time. For (b) and (c), each dot indicates 1) GSH-CdTe, 2) 1 minute after first selenium addition, 3) 20 minutes after first selenium addition, 4) 1 hour after the first selenium addition, 5) 10 minutes after zinc addition, and 6) 1 hour after the zinc addition. 48

Figure 2.16. (a) The image of the MUA-capped CdTe/CdSe/ZnSe QDs solution under excitation (630 nm) as viewed through a 680 nm long pass emission filter using a charged coupled device. (b) Subcutaneous injection of the CdTe/CdSe/ZnSe QDs into the hind leg of a rat. (c) The QDs migrating to lymphatic tracts. 49

Figure 3.1. Schematic diagram of post-synthetic chemical transformations of nanomaterials. The chemical transformations can be successfully controlled by the careful choice of starting materials, additives and reaction conditions. 52

Figure 3.2. Illustrated reaction scheme for the synthesis of CdHgTe nanoalloys. 54

Figure 3.3. TEM image of (a) CdTe QDs (diameter 4.5 ± 0.9 nm). (b) CdHgTe nanoparticles after the reaction with mercury bromide. (c,d) High resolution TEM images of CdHgTe nanorods. 55

Figure 3.4.XRD patterns for CdTe QDs (grey line) and CdHgTe nanoalloys (black line). Millar indices for zinc blende CdTe and zinc blende HgTe referred from other papers are shown below. 56

Figure 3.5. Schematic diagram of the molecular welding effect of CdTe QDs with Hg^{2+}. It is suggested that the mercury cations reacted with the CdTe in two ways: (1) cation exchange reactions and (2) reduction of the Hg^{2+} by surfactant molecules. 60

Figure 3.6. (a) Absorption spectra of CdTe QDs (grey) and CdHgTe nanoparticles (black). (b) Normalized emission spectra of CdTe QDs and CdHgTe nanoparticles (excitation wavelength = 450 nm for CdTe, 500 nm for CdHgTe). 62

Figure 3.7. Pictures of CdTe QDs and CdHgTe nanoparticles in toluene. 62

Figure 3.8. (a) Standard electrode potential and (b) acid hardness of metal cations. Values of acid hardness in each metal cation were obtained from previously reported literature. 63

Figure 3.9. Absorption and emission spectra of CdTe QDs reacted with some metal cations in the same manner as CdTe QDs with Hg^{2+} (a). Solid curves represent absorption spectra, whilst dashed curves represent emission spectra (emission was not observed for the products of the reaction with Ag^{+} and Au^{3+}). Excitation wavelength = 450 nm..... 64

Figure 3.10. (a) TEM images of the products from the reaction of CdTe QDs and silver(I) cations. (b) X-ray diffraction pattern of the resulting nanoparticles. Miller indices for monoclinic Ag_2Te were shown below. 65

Figure 3.11. (a) TEM images of the products from the reaction of CdTe QDs and gold (III) cations. (b) XRD pattern of the resulting nanostructures. Miller indices for elemental gold (fcc) were shown below..... 65

Figure 3.12. Change in absorption spectra of CdTe QDs with stepwise addition of mercury stock solution followed by purification. 66

Figure 3.13. TEM image of (a) CdSe QDs. (b) CdHgSe nanoalloys after the reaction with mercury bromide. (c) High resolution TEM image of CdHgSe nano alloys. 69

Figure 3.14. Optical properties of CdSe (grey curves) and CdHgSe (black curves), where solid lines show absorption whilst dashed lines indicate emission profiles. Excitation wavelength was 450 nm (CdSe) and 500 nm (CdHgSe). 70

Figure 3.15. X-ray diffraction pattern of CdSe QDs (grey line) and CdHgSe nanoalloys (black line). Miller indices for wurtzite CdSe were shown below and Miller indices for zinc blende HgSe were indicated on the upper end of the graph. 70

Figure 3.16. TEM image of (a, b) CdSe nanorods. (c, d) Resulted nanomaterials after the reaction with mercury bromide. 72

Figure 3.17. Optical changes in CdSe nanorods (grey curves) and CdHgSe nanorods (black curves), where solid lines show absorption whilst dashed lines indicate emission profiles. Excitation wavelength was 450 nm (CdSe) and 500 nm (CdHgSe). (Inset) Magnified absorption spectra of CdSe/CdHgSe nanorods, showing a red-shift in absorption threshold. 73

Figure 3.18. TEM images of CdTe tetrapods (a) before and (b) after mercury cation addition. 74

Figure 3.19. Absorption spectra of CdTe tetrapods (grey line) and the adduct with mercury cation (black line). 75

Figure 4.1. Pictures of (a) $Cd(TePh)_2$ powder after washing with anhydrous ether and toluene, (b) $Cd(TePh)_2$ dissolved in TOP, after sonication and centrifugation. 80

Figure 4.2. Absorption transition observed during CdTe QDs growth. 82

Figure 4.3. (a) Changes in emission spectra during CdTe growth, (b) evolution of quantum yield and (c) FWHM of the emission profile. Each plot represents the sample 1) 10 minutes, 2) 11 minutes, 3) 12 minutes, 4) 13 minutes, 5) 15 minutes, 6) 20 minutes, 7) 30 minutes and 8) 55 minutes after heating. Excitation wavelength = 500 nm. 83

Figure 4.4. Images of CdTe QDs prepared from SSPs (a) under room light and (b) excitation at 365 nm. Each vial represents the sample prepared 1) 12 minutes, 2) 13 minutes, 3) 15 minutes, 4) 20 minutes, 5) 30 minutes and 6) 55 minutes after heating. 84

Figure 4.5. Chemical structure of $ZnDDTC_2$. 85

Figure 4.6. Absorption spectra during the ZnS shell deposition on a CdTe surface. 87

Figure 4.7. (a) Changes in emission spectra of CdTe QDs at each ZnS shell deposition (excitation wavelength = 500 nm). (b) Relationship between emission intensity and reaction stage. 88

Figure 4.8. Emission spectrum of CdTe/ZnS QDs (6th ZnS shell addition) after purification. The excitation wavelength was 350 nm. 89

Figure 4.9. TEM images of (a) CdTe QDs prepared from SSPs and (b) CdTe/ZnS QDs after the 4th addition of $ZnDDTC_2$. (c) Size distribution of CdTe QDs and CdTe/ZnS QDs based on the TEM images. 90

Figure 4.10. XRD patterns of CdTe QDs (grey curve) and CdTe/ZnS (4th shell deposition) QDs (black curve) prepared from SSPs. Millar indices for zinc blende CdTe (bottom) and wurtzite ZnS (top) are included as references. 91

Figure 5.1. Schematic diagram of two phase transfer reactions of hydrophobic QDs. 97

Figure 5.2. Number distribution of 150 µL H*Protein B solution diluted with 3mL deionised water, measured initially (blue), 10 minutes (green), 20 minutes (orange) and 30 minutes (red) after the dilution. 99

Figure 5.3. As-prepared hydrophobin-CdTe/ZnS QDs solution under room light (left) and UV lamp excitation (365 nm, right). 100

Figure 5.4. (a) Absorption and emission spectra for hydrophobin-CdTe/ZnS QDs (excitation wavelength = 550 nm). Grey lines show absorption spectra (scale on the left side), whilst black lines indicate emission spectra (scale on the right). (b) Optical spectra of CdTe/ZnS QDs before phase transfer. 101

Figure 5.5. TEM images of hydrophobin-CdTe/ZnS QDs. (a) high resolution and (b) low resolution micrographs, respectively. 102

Figure 5.6. Number distribution of hydrophobin-CdTe/ZnS QDs after filtration (11 µm cut-off) and centrifugation. A peak at 1.5 ± 0.3 nm was detected by DLS. 103

Figure 5.7. (a) Absorption (grey line) and emission (black line) spectra for hydrophobin-CdTe/ZnS QDs after ultra-centrifuge. Excitation wavelength was 550 nm. (b) Number distribution of the hydrophobin-CdTe/ZnS QDs. A peak at 26.5 ± 9.5 nm was observed. (c) Low resolution and (d) high resolution TEM images of the hydrophobin-QDs. 105

Figure 5.8. Absorption (grey line) and emission (black line) spectra for hydrophobin-CdTe/ZnS QDs after centrifugal concentrator treatment. Excitation wavelength = 500 nm. 107

Figure 5.9. Hydrophobin-CdTe/ZnS QDs after the centrifugal concentrator treatment under room light (left) and under UV excitation at 365 nm (right). 107

Figure 5.10. (a,b) TEM images of hydrophobin-CdTe/ZnS QDs after centrifugal concentration treatment. (c) Number distribution of the hydrophobin-QDs conjugates. Two peaks (14.2 ± 2.0 nm, 49.9 ± 15.5 nm) were observed. 108

Figure 5.11. Possible mechanism of hydrophobin-QDs conjugation. Hydrophobic moieties are coloured light blue, whilst hydrophilic moieties are coloured red. 108

Figure 5.12. Absorption and emission spectra of (a) hydrophobin-CdSe/ZnS QDs in water and (b) CdSe/ZnS QDs in toluene before the phase transfer. Grey curves and black curves indicate absorption and emission spectra, respectively. Excitation wavelength was 500 nm. 109

Figure 5.13. Hydrophobin-CdSe/ZnS QDs after the centrifugal concentrator treatment in room light (left) and under UV excitation at 365 nm (right). 110

Figure 5.14. (a, b) TEM images of hydrophobin-CdSe/ZnS QDs. (c) Number distribution of the hydrophobin-CdSe/ZnS QDs conjugates. 111

Figure 5.15. Cell viability of macrophages after 2 hours incubation with hydrophobin-CdTe/ZnS QDs. Left bar represents the sample after the centrifugal concentrator treatment, whilst right bar represents before the treatment. The viability was quantified by crystal violet staining, followed by the measurement of absorption. 113

Figure 5.16. Macrophages cells incubated with hydrophobin-CdTe/ZnS QDs. (a): The blue stain represents depicts the cell nuclei. (b): The light-green stain represents the fluorescence channel used to attempt to determine QD fluorescence (excitation wavelength = 514 nm, detection wavelength = 500-550 nm). (c): An overlap with image (a) and (b). The image plane is set at approximately 50% of the total cell height. 113

List of Tables

Table 2.1. Changes in reaction parameters and their results. (Detailed descriptions of reaction conditions are outlined in Chapter 6.2.6). 46

Table 4.1. List of reaction conditions used to synthesise CdTe QDs from CdTe SSPs and the optical properties of the resulting products with additional comments. (RT = room-temperature, PL = photoluminescence) 92

Table 4.2. CdTe/ZnS QDs synthesis in different shell growth conditions (solvents, precursors and temperatures) and resulting emission changes with some additional comments. The last method was referred from the previous report of CdSe/ZnS QDs. 93

Table 5.1. Phase transfer methods known commonly in colloidal QDs, the obtained results when used with H*Protein B and comments. 104

Table 6.1. Setting parameters used in DLS measurements. 118

Table 6.2. List of the reaction conditions for CdTe/ZnS QDs. Shell thickness (ML = monolayer), reaction temperature, and reaction time. 127

List of Equations

Equation 2.1 Production of the selenium anion in alkaline solution..... 34

Equation 3.1. Proposed reaction mechanism of HgTe formation on the surface of CdTe. (R = $C_{14}H_{29}$, R' = C_8H_{17}.)..... 58

Equation 3.2. Reduction of Hg^{2+} by phosphonic acids and TOP and reaction of [Hg^0] with surface Te. (R = $C_{14}H_{29}$, R' = C_8H_{17})..... 59

Equation 3.3. Reduction of Hg^{2+} using methanol and phosphonic acid as reducing agents. R = $C_{14}H_{29}$..... 59

Equation 4.1. Synthetic pathway of the CdTe SSP proposed by the previous literature. 78

Equation 4.2. Synthesis of the cadmium precursor..... 79

Equation 4.3. Synthesis of CdTe SSP provided in this work..... 79

Equation 4.4. Pyrolysis of $Cd(TePh)_2$. 81

Equation 4.5. Pyrolysis of $ZnDDTC_2$ under vacuum condition to form ZnS. 86

Equation 4.6. ZnS formation by the thermal decomposition of $ZnDDTC_2$ in the presence of primary amines..... 86

Glossary

AFM	-	atomic force microscopy
a.u.	-	arbitrary unit
CNT	-	carbon nanotube
DLS	-	dynamic light scattering
DMF	-	N,N-dimethylformamide
DMSO	-	dimethyl sulfoxide
DNA	-	deoxyribonucleic acid
EDX	-	energy-dispersive X-ray spectroscopy
EMA	-	effective mass approximation
FWHM	-	full width at half maximum
GSH	-	glutathione
HDA	-	hexadecylamine
^{1}H NMR	-	proton nuclear magnetic resonance
HSAB	-	hard soft acid base
HWHM	-	half width at half maximum
ICP-MS	-	inductively coupled plasma-mass spectrometry
MEG	-	multiple exciton generation
MeOH	-	methanol
ML	-	monolayer
MPA	-	mercaptopropionic acid
MRI	-	magnetic resonance imaging
MUA	-	mercaptoundecanoic acid
NIR	-	near infrared
NP	-	nanoparticle
OAm	-	oleylamine
ODA	-	octadecylamine

ODE	-	1-octadecene
OLED	-	organic light-emitting diode
PEG	-	polyethylene glycol
PEI	-	polyethyleneimine
PET	-	positron emission tomography
PL QY	-	photoluminescence quantum yield
QD	-	quantum dot
RNA	-	ribonucleic acid
ROS	-	reactive oxygen species
rpm	-	revolutions per minute
SIPOP	-	successive injection precursors in one-pot
SPR	-	surface plasmon resonance
SSP	-	single-source precursor
STM	-	scanning tunnelling microscopy
TDPA	-	tetradecylphosphonic acid
TEM	-	transmission electron microscopy
TGA	-	thioglycolic acid
TOP	-	trioctylphosphine
TOPO	-	trioctylphosphine oxide
TOPS	-	trioctylphosphine sulfide
TOPSe	-	trioctylphosphine selenide
TOPTe	-	trioctylphosphine telluride
UV	-	ultraviolet
XRD	-	X-ray diffraction
$ZnDDTC_2$	-	zinc diethyldithiocarbamate

Chapter 1

General Background

1.1 Current progress in Nanoscience

One can argue that the emergence of nanoscience coincides with the realisation of the intermediate regime between molecules and bulk solids. In this size regime, non-catalysts exhibit catalytic activity, insulating materials show electrical/thermal conductivity, and colour changes occur in some materials when prepared in this size range.[1] Understanding how materials behave in the nanosize regime is a crucial aspect for material scientists.

Specifically, one nanometer is a billionth (10^{-9}) of a meter. The calculated diameter of a carbon atom is 0.067 nm and an iron atom is 0.156 nm, which implies that hundreds of atoms will be required to build up nanoscale materials, whilst the diameter of hemoglobin (*Lumbricus terrestris*) is 5.5 nm and the size of human blood cell is 7.6 μm. [2-4] It is assumed, therefore, that nanoscience routinely deals with the sub-cellular level.

The development of scientific instruments such as atomic force microscopes (AFM), scanning tunnelling microscopes (STM), and transmission electron microscopes (TEM) has contributed substantially to nanoscience. [5] Unlike conventional optical microscopes, which are limited to submicron objects due to the wavelength of visible light, the instruments listed above enable us to analyse materials in the nanoscale. Furthermore, AFM has been used as a nanoscale tool for moving and organising molecules.[6-8]

1.1.1 Carbon-based Nanomaterials

The exploitation of carbon nano tubes (CNTs) is arguably the most successful area of research in nanoscience.[9] There have been more than 100,000 relevant scientific papers on CNTs since their emergence (1992–2010)[10] and their applications have been

disseminated to broad academic fields, such as electronics, [11] biology,[12-16] material science[17-21] and engineering[22, 23] to name a few. Investigations into CNTs (which are also categorised by single-walled and multi-walled varieties) include enhanced electro/thermo conductivity, robust mechanical resistance, architecture design from a few nanometers to micrometers, and sophisticated growth methodologies. For example, single-walled CNTs can be used for transporting a single water molecule under an appropriate electric field, a novel nano-component inaccessible with conventional technology. [21] It is arguable that this research can be used in, for instance, desalination, medicine, and sensing devices.

Graphene, a single sheet of graphite, is also a promising material for nanoscience due to its intrinsic semiconducting behaviour.[24] Suggested applications include molecular electronics; graphene has the potential to replace conventional silicon based electronics and to be scaled down even smaller. Although concerns about scalability and synthetic methodology exist (it costed \$10,000,000/cm^2 in 2005),[25] research has now progressed enough to produce industrial scale (30 inch) graphene films for transparent electrodes using some fundamental techniques.[26]

1.1.2 Inorganic Nanomaterials

Inorganic nanomaterials have also been studied extensively. Many metal particles have been examined in order to obtain interesting nano-structured materials. For example, palladium, gold, silver, platinum and copper are the most commonly studied metals, whilst research on nano-sized cobalt, iron, nickel, ruthenium, rhodium and iridium is also increasing. [27, 28]

Gold nanoparticles (Au NPs) are one of the best known inorganic nanomaterials and show the surface plasmon resonance (SPR) effect, where electromagnetic waves adjacent to the particle surface interact with a collection of electrons (plasmon) in the metal, resulting in an electromagnetic wave. Researchers have applied this phenomenon to biosensing: for example, Stehr *et al.* have fabricated Au NP-based deoxyribonucleic acid (DNA) melting assays, where Au NPs were used as a heater as well as a colour indicator.[29] Because the SPR is very sensitive to the surrounding environment of Au NPs, the array is also highly sensitive. Also, the stability and biocompatibility of gold makes the material extremely suitable for biological applications.[30] DNA-Au NPs conjugation is an attractive candidate for the advanced functional materials; particularly,

Mirkin and co-workers have synthesised a variety of nanoparticles superlattices by careful choices of nanoparticles morphology and the type of DNA ligands.[31, 32] The complementary base pairing between DNAs on the different Au NPs leads the formation of the nanoparticles superstructures in an organised manner, which made it possible to prepare complex superstructures other than face-centred cubic and body-centred cubic structures.[33] Other examples include catalysis, where Au NPs absorb UV/visible light due to the SPR effect and convert the energy into catalytic activity on organic molecules.[34]

Metal oxide nanomaterials such as zinc oxide, manganese oxide and iron oxide are also common nanomaterials. A major advantage of using nano-sized inorganic materials instead of bulk solids is the increased surface-to-volume ratio. The reactive surface area is dramatically increased in nanomaterials compared to bulk counterparts, which is preferable in catalysis and sensing.

Other noteworthy nanomaterials are zinc oxide (ZnO) nanorods, or nanowires. The development in the organised growth of ZnO nanowires and their semiconducting behaviour has attracted attention with the hope of realising future nano devices. Fully transparent, flexible transistors using ZnO nanowires as active channels have been fabricated,[35] whilst Zhu *et al.* developed ZnO nanowires arrays and applied them to toxic vapour sensing, which showed enhanced sensitivity.[36] Furthermore, ZnO nanorods exhibit the piezoelectric effect, where physical strain in materials produces electrical energy. Structural deformations of ZnO nanorod crystals were found to produce the accumulation of electric charges on the rod surface. Using this phenomenon, nano-sized generators were reported.[37, 38]

Inorganic magnetic nanomaterials have also been synthesised, with iron oxide the most studied material, usually for medical applications. For example, an aerosol of iron oxide NPs was successfully delivered toward the lung *via* a magnetic field.[39] Also humic acid-coated iron oxide NPs were applied to water purification, resulting in 99 % removal of mercury and lead ions with a simple procedure using a magnetic field.[40]

Additionally, recent advances in synthesis such as the formation of hollow nanoparticles are noteworthy. An important paper describing the nanoscale Kirkendall effect – the phenomenon which occurs when two components have different diffusion rate in a core/shell system, causing empty voids – was published in 2004.[41] Whereas the first paper showed hollow cobalt oxides, sulfide and selenide, other metals (e.g. zinc,

cadmium and silver) have also shown similar behaviour.[42-44] Potential applications of such hollow nanocrystals include catalysis, which is required to have large surface areas.

1.1.3 Other Type of Nanomaterials

Apart from these nanomaterials, there has been substantial progress in the synthesis of other nanomaterials, which include organic based materials (polymers, dendrimers and fullerenes), biological components (small organisms, enzymes, viruses and DNA), and inorganic-organic composites.[5] Although characteristics of these materials listed differ, smart nano device fabrication is envisaged in all cases.

One of the main advantages of the use of polymer NPs is biocompatibility. Because of this, many studies have been reported on biological/medical applications of polymer nanomaterials. Polyethyleneimine (PEI) for example, was found to encapsulate DNA molecules and form nanoparticles. The DNA-containing PEI NPs were then functionalised with short peptides and successfully delivered to human neuron cells *in vitro*.[45] Another example is the use of conjugated polymer NPs, where single and double bonds are alternatively repeated on the polymer chain, giving semiconducting behaviour. Although the underlying photochemistry is different, the conjugated polymers are expected to overcome some difficulties in current inorganic semiconductors. One potential application is organic light-emitting diodes (OLEDs). Together with developments in synthetic chemistry, OLEDs have become smaller than the conventional bulk flat screen.[46]

Biological components such as cells and viruses are often regarded as "ready-made" nanomaterials. Researchers have used such materials as scaffolds to exploit their stability.[47, 48] Viruses, for example, were utilised as a stable scaffold for fluorescent probes, resulting in a virus-fluorophore complex. The complexes were shown to enter eukaryotic cells and were observed with optical microscopy.[49] Additionally, reports exist describing nanoscale artificial complexes, which contain integrated functionalities such as entering, releasing, sensing and reacting. Fernandes *et al.* prepared an assembly of antibodies and fusion proteins that can target, sense and destroy bacteria and showed successful antimicrobial treatment,[50] whilst Akin *et al.* fabricated gene-containing NP/bacteria complexes, which were injected into mice, where the internalised complexes released NPs followed by the genes showing the expression *in vivo*.[51]

Another emerging discipline is nanomedicine, which includes diagnostics (contrast and imaging agents), therapy (drug delivery and photodynamic therapy) and nanotoxicology.[5] Although the term appeared in the late 1990s, it has gained increasing attention as a consequence of the recent development of nanotechnology and its medical applications, as well as an involvement of governmental agencies since 2005.[52, 53] Also, researchers in molecular sciences have been working on "dual-modality imaging probes", which utilise two different diagnostic functionalities such as optical imaging, positron emission tomography (PET) and magnetic resonance imaging (MRI).[54-56] The probes have two independent reporters (luminescence, magnetism and radioactivity) in one nanomaterial. Additionally, from the therapeutic viewpoint, nanomaterials are commonly used for tumour treatment and drug delivery. Inorganic nanoparticles such as gold and iron oxide are used for thermal ablation to destroy tumour cells, whilst liposomes and polymer-carrying drug molecules can be accumulated inside tumour cells where upon the drugs are released by degradation of a surrounding nanomaterial entity.[57] Some of the nanomaterials for medical use are currently in clinical trials.

Despite the recent development and dissemination of these nanoscale medicines, substantial debate on the toxicological effect of artificially-made nanomaterials on humans and the environment still exists. As can be seen previously in industrialisation and nuclear physics, new technology always leads to unprecedented concerns in society: as does nanoscience. The prime issue is the risk to biological systems including humans. Some regulatory bodies, such as the US Food and Drug Administration and European Commission's Health and Consumer Protection Directorate, for instance, have started taking into account the risk of nanotechnology.[5] Unlike previous potential pollutants, however, conventional risk assessment cannot be applicable to nanomaterials because nanomaterials can change their behaviour with small changes in size. Therefore, an organised protocol of nanomaterials characterisation is desirable. Given this situation, there have been an increasing number of relevant reports. Baroli *et al.*, for example, have examined the permeability of iron-based nanoparticles with diameters less than 10 nm, on human skin tissues, showing that nanoparticles can penetrate skin to some extent *via* the stratum corneum.[58] The biocompatibility of artificial nanomaterials has been studied as well; recently, single-walled CNTs were found to bio-degrade *in vitro* by the human neutrophil enzyme. The enzyme generated reactive intermediates, which attacked the carboxylic moiety of CNTs and decomposed the nanomaterial.[59]

1.2 Theory of Quantum Dots

1.2.1 Wannier Exciton

When semiconductor materials are prepared in the nanosize regime, they often exhibit intrinsic behaviour associated from quantisation of their energy states: the quantum size effect. When a semiconductor material absorbs sufficient external energy (photo or electrical energy), an electron is excited from the valence band to the conduction band, leaving an electron vacancy (a hole) inside the valence band. The electron and the hole can travel freely in the material *via* the conduction band or the valence band; however, the movement of the electron is limited by coulombic interactions with the hole because the negatively charged electron and the positively charged hole attract each other, resulting in an energetically stable state. As a result, the electron-hole pair in a semiconductor exhibits particle-like behaviour called a Wannier exciton; it can be thought of as analogous to a hydrogen atom; an electron travels within a certain distance around a centred proton with coulombic attraction (Figure 1.1).

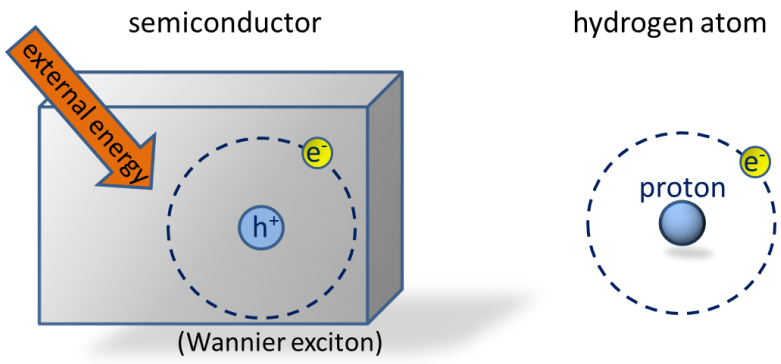

Figure 1.1. Schematics of Wannier exciton and a hydrogen atom.

The distance between hole (proton) and electron is determined by several factors (e.g. dielectric constant and effective mass) so that each semiconductor has a specific exciton radius (exciton Bohr radius); in ZnS (hexagonal), the exciton Bohr radius, a_B, is 2.2 nm, whilst the a_B of CdTe (cubic) is 7.5 nm, and the a_B of GaAs is 12.4 nm.[60] These exciton Bohr radii are significantly larger than the diameter of hydrogen atom (0.053 nm) and define the degree of quantum confinement. [2]

Quantum size effects occur when the size of semiconductor materials decreases below the diameter of exciton Bohr radius in at least one dimension. In this regime, the movement of an electron and hole is physically confined rather than by electrostatic attraction. The semiconductor displays unusual characteristics unlike either molecules or bulk semiconductor materials, depending on its size and shape. In a sheet-like nanostructure, the exciton movement will be limited in two dimensions. A "quantum wire" refers to the semiconductor material whose exciton is spatially confined in two dimensions, whereas a "quantum dot (QD)" has a three dimensionally confined exciton (Figure 1.2).

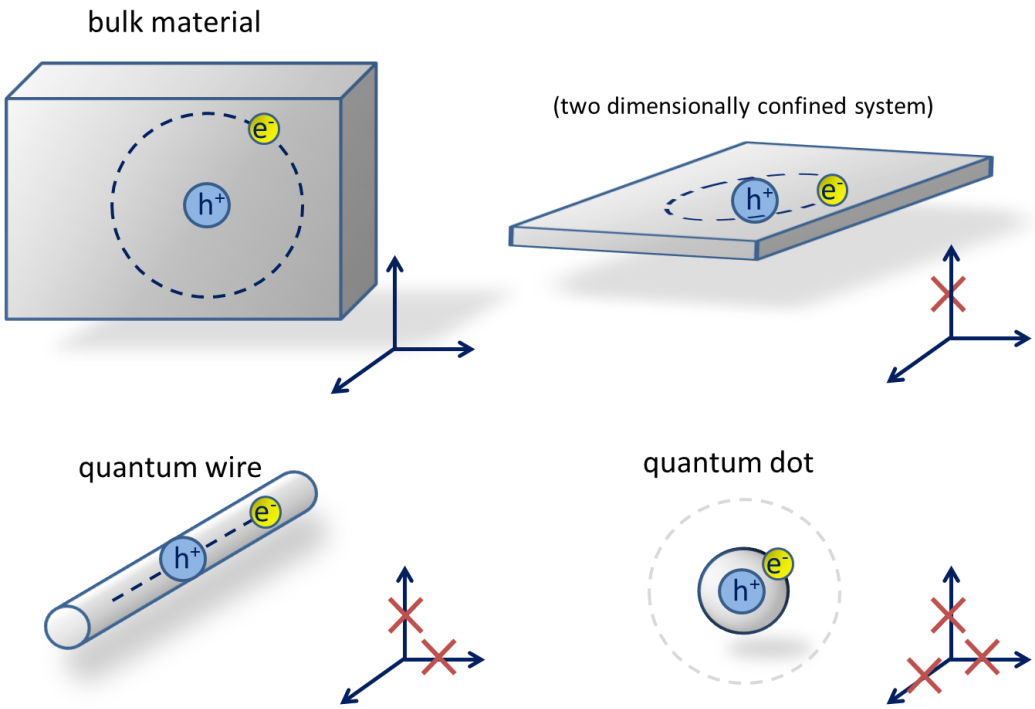

Figure 1.2. Influences of structure on the movement of the corresponding exciton. An exciton in bulk semiconductors moves freely within its exciton Bohr radius, whilst nanomaterials which have dimensions smaller than the exciton Bohr radius in at least one dimension will result in limited movement on the exciton depending on the degree of physical confinement.

As a result of quantum size effects, nano-sized semiconductors display optical properties between molecules and bulk materials. In QDs, the band gap energy is widened corresponding to particle diameter (Figure 1.3), which means the same semiconductor material with different size shows different band gaps. For example, the

band gap energy of bulk CdSe is 1.74 eV whilst that of QDs ranges from 1.94–2.53 eV,[61] which allows them to have various fluorescent wavelengths because the band gap energies of CdSe QDs correspond to visible light (480-620 nm wavelength).

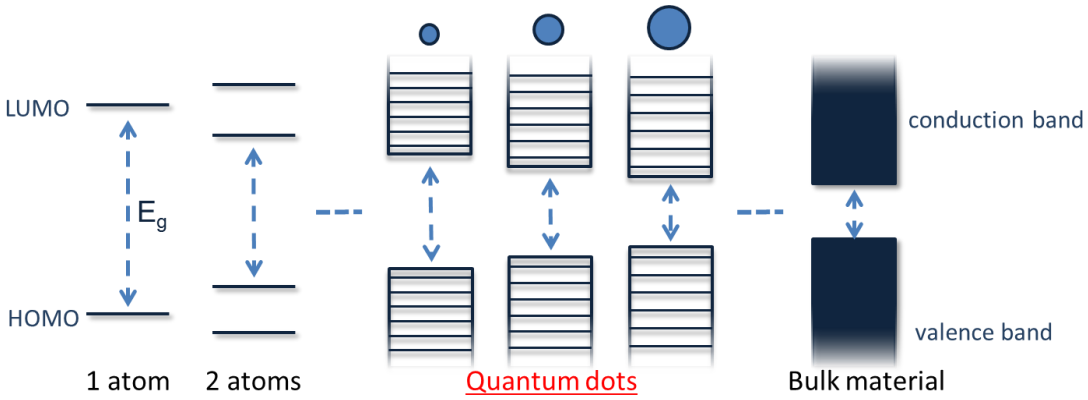

Figure 1.3. Energy diagram of a single atom, quantum dots and a bulk semiconductor. The band gap energy (E_g) of quantum dots changes depending on particle sizes as indicated above. A small quantum dot has a larger E_g, whilst a big quantum dot has a smaller E_g.

1.2.2 Free Electron Model

Apart from the intuitive way to understand the quantum size effect concept, a theoretical explanation using simple physics and quantum mechanics exists. Initially, a three dimensional system (bulk material) will be examined. Subsequently, the explanation will address the spatially confined systems of sheets, wires and dots. For simplicity, the free electron rather than exciton is examined.

In a bulk solid, the energy, E, of a free electron can be described as follows:

$$\mathrm{E} = \frac{1}{2} m\vec{v}^2 \qquad (1)$$

where m is the mass of an electron, v is the velocity and $\vec{v}^2 = (v_x^2 + v_y^2 + v_z^2)$. The v_x, v_y and v_z are the velocity of the electron in each direction. The wave momentum $\vec{p}$ is linear to the wave vector $\vec{k}$, which is explained as $\vec{p} = m\vec{v} = h\vec{k}/2\pi$, where h is the Planck constant. Therefore, using these two equations, equation (1) is modified so that E(k) is proportional to k^2.

$$\mathrm{E}(k) = \frac{1}{8} \cdot \frac{h^2 k^2}{m\,\pi^2} \tag{2}$$

The wave vector of the free electron is denoted as $\vec{k} = (k_x, k_y, k_z)$ and $|k|$ is the wave number. From the De Broglie relation, the wave number can be related to wavelength λ.

$$\pm k = |k| = \pm \frac{2\pi}{\lambda} \tag{3}$$

The wavelength, λ, is typically between 10 nm to 1 μm in semiconductors. In the bulk material, it is assumed that the size of the material, *d*, is infinite ($d \to \infty$) (periodic boundary condition). Next, we examine a wave along the x-direction. The Schrödinger equation under this condition yields the wave function:

$$\psi(x) = A \cdot \exp(ik_x x) = A \cdot \exp\big(ik_x(x+d)\big),$$

$$\text{with } k_x = \pm n \frac{2\pi}{d} \quad (n = 0, \pm 1, \pm 2, \ldots) \text{ as a solution} \tag{4}$$

where *A* is a constant, *n* is an integer. Also, the y and z-direction can be explained in the same manner. In the one dimensional free electron system, each vector k_x has two electrons ($m_s = \pm 1/2$), and k_x can have 0, $\pm\Delta k$, $\pm 2\Delta k$, $\pm 3\Delta k$ ⋯. Because $\Delta k = 2\pi/d$ from the equation (4) and $d \to \infty$, the wave vector can be assumed to be very small: $\Delta k = 2\pi/d \to 0$. Thus, using equation (2), the relationship between free electron energy and wave vector along x, y, z-directions can be depicted as Figure 1.4.

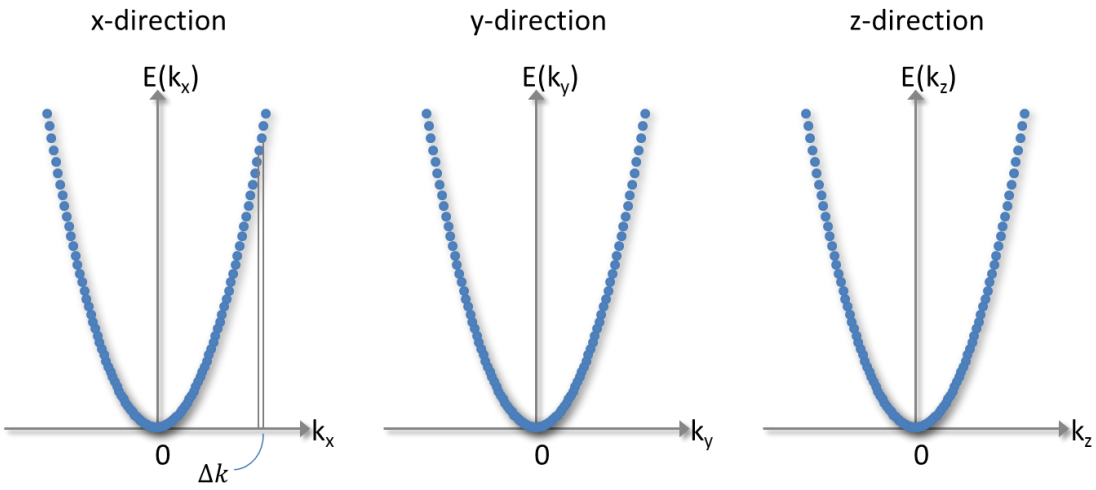

Figure 1.4. Energy-vector relationship in the solid material in each three direction (x, y, z). The difference between each vector (Δk) is very small so that a series of dots can be regarded as quasi-continuous.

Because Δk is small, the dots on the graph can be assumed as quasi-continuous, which indicates the wave vectors in each direction have continuous values from 0 to k_F (Fermi vector). Electron states are continuously occupied from zero energy to E_F (Fermi level) at 0 K.

Two dimensional systems, where a solid is considered bulk along the x- and y-axis, but only a few nm in the z-direction (a sheet-like structure in Figure 1.2), is then examined. It is necessary to consider additional contributions in energy in the z-direction unlike the x- and y-directions. The particle-in-a-box model (Figure 1.5) can be applied to the electron in the z-direction; the electron cannot leave the box, because the potential energy is considered infinite outside the barrier and zero within. In this condition, the wave function $\psi(z)$ must be zero in borders at z = ± d/2. Therefore, the Schrödinger equation can be written as follows:

$$\psi(z) = A \cdot \exp(ikz) + B \cdot \exp(-ikz), \qquad \psi\left(z = \pm\frac{d}{2}\right) = 0,$$

$$\text{with } k = n\frac{\pi}{d} \ (n = 1, 2, \dots) \text{ as a solution} \tag{5}$$

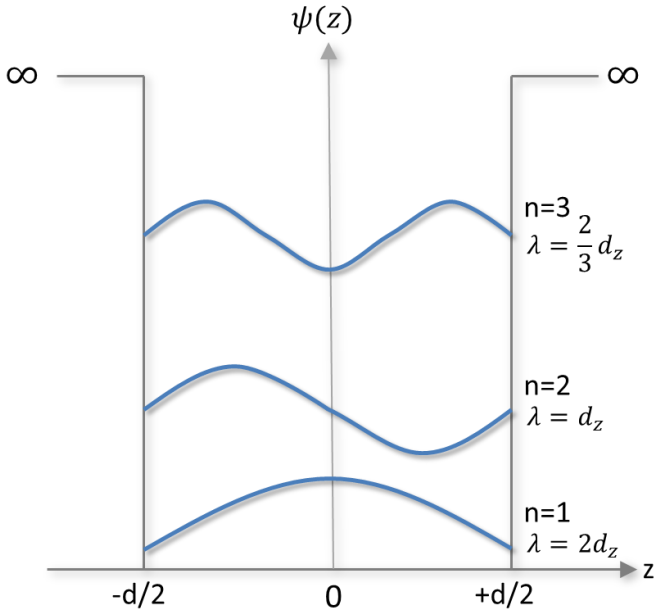

Figure 1.5. Schematics of the particle-in-a-box model. Blue curves the indicate electron wave. Waves with n = 4, 5,… are omitted.

In the lowest energy state (n = 1), the wave vector in the z-direction is $k = \pi/d$ from equation (5). The electron energy for equation (2) gives:

$$\mathrm{E}(k = \pi/d) = \frac{h^2}{8m\,d^2} \quad (n = +1) \tag{6}$$

This means that the extra energy ($h^2/8m\,d^2$) is added to the electron energy in the z-direction in the case of the two-dimensional system. Also, $\Delta k = \pi/d$ from equation (5) is no longer zero in the z-direction because d_z is the same order as the De Broglie wavelength. Therefore, Δk has a large value and energy states in the z-direction cannot have continuous, but discrete values. The relationship between free electron energy and wave vector along x, y, z-directions in two-dimensional system is shown in Figure 1.6.

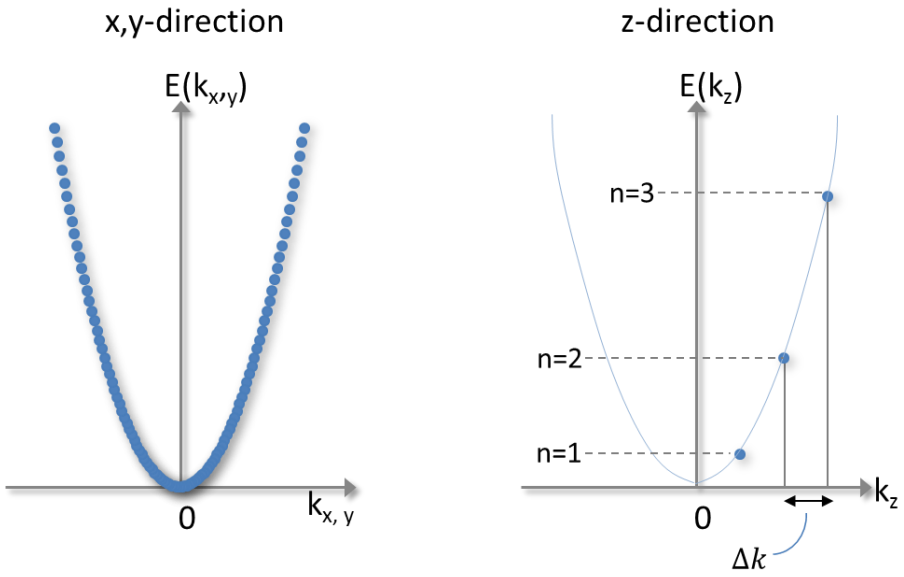

Figure 1.6. Energy-vector relationship in two-dimensional system. Whereas the graph in x- and y-direction is the same shape as Figure 1.4, the graph in z-direction is different, showing discrete wave vectors and energy states. Δk is relatively large hence energy states are quantised in the z-direction.

The same strategy as two-dimensional systems can be applied to both one- and zero-dimensional system. In a zero-dimensional system (quantum dot) where all three dimensions (x, y, z) have a length comparable to the De Broglie wavelength, the energy-vector relationship in quantum dot can be explained (Figure 1.7).

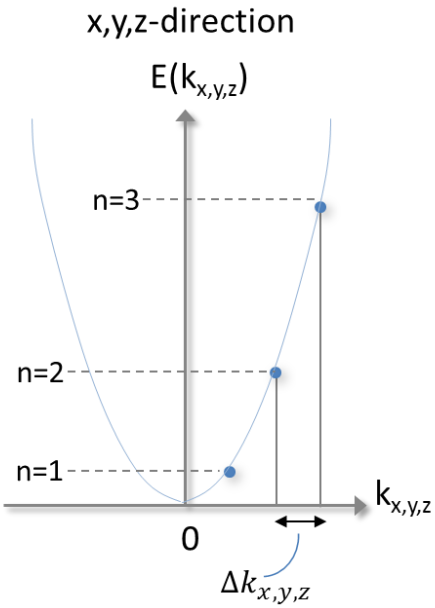

Figure 1.7. Free electron energy-vector relationship in quantum dots. Energy states in all direction have discrete level in contrast to Figure 1.6.

Because electron states in all directions are discrete, free electrons in the quantum dot are regarded as "quantised". The overall lowest energy of a cubic quantum dot is simply the sum of each dimension. Thus, from equation (6), $E_{QD,cube} = 3/8\ (h^2/m\ d^2)$ where d is the width of the cube. In the case of spherical quantum dots, the Schrödinger equation should be solved by spherical coordinate systems. It is known for the lowest energy:

$$E_{QD,sphere} = \frac{h^2}{2m\ d^2} \tag{7}$$

1.2.3 Energy States in Semiconductor Quantum Dots

So far, free electrons in a solid have been examined; however, as explained earlier, electrons in semiconductors are not unbound and an excited electron forms an exciton *via* Coulombic forces with the hole. Therefore, it is essential that a few modifications are made in order to explain the energy state of the semiconductor quantum dot. First, energy states of the hole need to be addressed. The lowest energy of the hole of a

quantum dot can be written in the same manner as equation (7) using the hole mass. In addition, because $E_{QD,sphere}(e^- + h^+) = E_{QD,sphere}(e^-) + E_{QD,sphere}(h^+)$, the lowest energy of electron-hole pair is:

$$E_{QD,sphere}(e^- + h^+) = \frac{h^2}{2m^* d^2} \tag{8}$$

where $1/m^* = 1/m_e + 1/m_h$. The m_e and m_h are the effective masses of an electron and a hole, respectively. The band gap energy of semiconductor quantum dots is a combination of (i) band gap energy of bulk semiconductor ($E_g(bulk)$), (ii) the lowest energy of quantised electron-hole pair ($E_{QD,sphere}(e^- + h^+)$) and (iii) Coulomb interaction (E_{coul}). Therefore,

$$E_g(QD) = E_g(bulk) + E_{QD,sphere}(e^- + h^+) + E_{coul}$$

$$= E_g(bulk) + \frac{h^2}{2m^* d^2} - \frac{1.8e^2}{2\pi\varepsilon\varepsilon_0 d} \tag{9}$$

where e is the charge of an electron, ε is the dielectric constant of semiconductor, $\varepsilon_0$is the dielectric constant of vacuum, and d is the diameter of the particle. Equation (9) is called the effective mass approximation (EMA) and used to estimate the behaviour of the band gap in semiconductors of varying size. The exciton-wave vector relationship in semiconductor quantum dots is shown in Figure 1.8. The energy curve of the hole is opposite to that of the excited electron. Because of the quantisation effect, the band gap energy of the quantum dot, $E_g(QD)$, is larger than the bulk band gap energy. Also, as can be assumed from equation (9), $E_g(QD)$ would become larger when the particle diameter (d) decreases, which is shown in Figure 1.3.

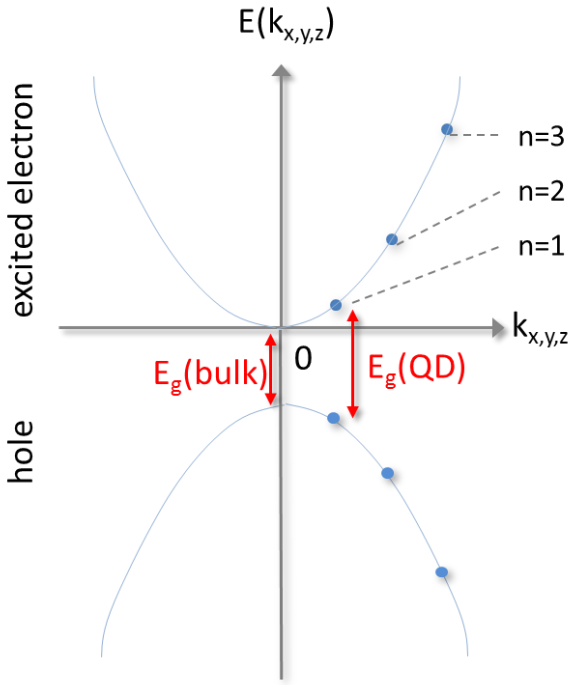

Figure 1.8. Schematics of the exciton energy-wave vector relationship. Energy states of excited electrons are on the upper side, whilst those of holes are on the lower side of the k-axis. The contribution of Coulombic interactions was omitted.

1.3 Synthetic Techniques for Quantum Dots

Although a number of synthetic procedures have been reported in the past decades, one can generally categorise the synthesis into two methods: top-down and bottom-up. In the top-down procedure, bulk materials are depleted by cutting, milling, or corrosion to obtain smaller sizes. Laser-related technique can also be included in this approach. For example, AlGaAs/GaAs quantum wells are processed using lithographic techniques, which are analogous to chip manufacturing.[1] Although the morphology can be modified almost arbitrarily, shape control with nanometer precision is still a challenge. In the bottom-up approach, atoms or molecules are used as building blocks to create larger complex structures. Self-assembly is a common technique often used in the bottom-up synthesis. It is known that chemical vapour deposition or molecular beam epitaxy can produce nano-sized islands of semiconductor when depositing the semiconductor on the substrate with a large lattice mismatch. The nano islands are often pyramidal in shape with dimensions in the order of nanometers, and therefore behave as quantum dots. Because the samples are already deposited on the substrate in an organised manner,

applications in optics and electronics are envisaged. Another common bottom-up technique, in contrast, is the formation of colloidal nanoparticles. The overall reaction can be achieved by chemical reactions in a flask. Typically, precursors of the semiconductor and surfactant molecules are put into a flask and the nanoparticle formation is driven by thermal decomposition. Because surfactant molecules have a bimodal functionality - to allow particle growth and to prevent particle aggregation - the synthesised quantum dots are stably dispersed in the solvent (Figure 1.9). Synthetic methodologies of colloidal quantum dots will be discussed hereafter, due to the relevance to this thesis.

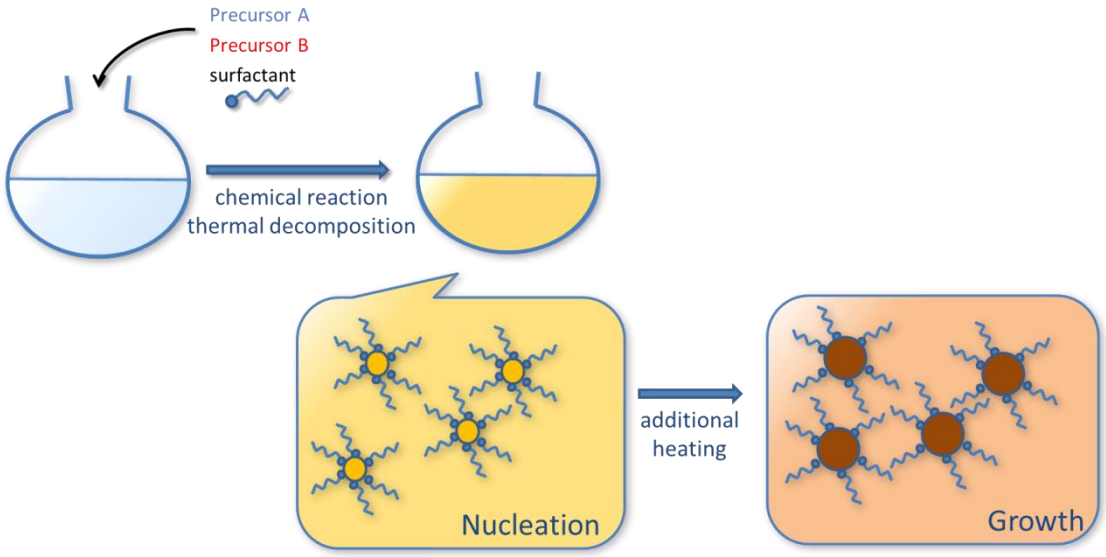

Figure 1.9. Schematic diagram of colloidal quantum dots synthesis.

As can be seen in Figure 1.9, colloidal QD formation involves two steps: nucleation and growth. In the nucleation process, precursors decompose/react to form nuclei of QDs; for example, when high amounts of precursors are injected into the solvent, the concentration of these precursors exceeds their solubility (supersaturation), resulting in nucleation until the precursor concentration lowers sufficiently. In the subsequent growth process, the nuclei absorb the remaining precursors in the solution (diffusion-limited growth), resulting in bigger particles with a relatively narrow size distribution.[62] Another phenomenon in the growth process is "Ostwald Ripening", where smaller particles dissolve in solution and grow on larger particles, resulting in larger particles with a broader size distribution. In order to achieve high quality QDs, high temperatures

are often used in the reaction because the constituent atoms in the QDs can be rearranged to produce higher crystalline QDs as a result of the large thermodynamic energy (annealing).[28, 62]

Another important factor to determine the property of the resulting QDs is surfactant. The surfactants routinely used in the synthesis of QDs were (i) trioctylphosphine oxide (TOPO), (ii) trioctylphosphine, (iii) phosphonic acid, (iv) thiol, (v) amine and (vi) carboxylic acid.[63] In a colloidal system, the surfactant molecules (also referred to as capping agent or ligand in some reports) have a key functionality as a stabilising agent, preventing undesired particle growth and agglomeration. Additionally, the surfactants control the rate of growth, reaction pathways and the particle size distribution as they are closely linked to the nucleation process, and in some case, the surfactants form metal-surfactant complexes in solution prior to the particle formation.[63, 64] Electronic and optical properties of the colloidal QDs can be controlled by the choice of surfactants; for example, thiols can effectively passivate the surface of CdTe QDs as their energy level inhibits a hole trapping and enhance radiative recombination of the excited electron/hole pair in CdTe QDs, while CdSe/thiol system causes the quenching of the emission and a reduced stability in solution.[63, 65] The choice of surfactants also affects the morphology of the nanocrystals. This originates from the fact that different surfactants exhibit different binding characteristics to the QD's surface. Theoretical modelling showed that TOPO preferentially binds to the cadmium terminated face but significantly less tightly to the selenium terminated face, whilst TOP binds strongly to the selenium terminated face on CdSe QDs.[66, 67] Combining with the control of the monomer concentration, Manna *et al.* synthesised CdSe nanocrystals in a variety of shapes by changing the ratio of hexylphosphonic acid and TOPO as surfactants.[68] Binding affinities to the cadmium surface also vary depending on the type of surfactants; typically, phosphonic acid and carboxylic acid can bind strongly to the surface cadmium *via* dative bonding which affects the particle growth mode. Amines, for example, are known to weakly coordinate.[63, 69]

To achieve the desired properties, several requirements should be fulfilled. As high reaction temperatures are routinely adopted in the QDs synthesis, surfactant molecules are required to be stable at such temperature. Also, surfactants should not quench the photoluminescence of the QDs, although some reports used surfactants which caused emission quenching for charge separation in photovoltaics.[63, 70, 71] The outer layer of the micelle is also a critical factor when considering the behaviour of the QDs in solution.

Usually, a long alkyl chain is used to dissolve QDs in organic solvents whilst hydrophilic functional groups (e.g. deprotonated carboxylic acid) would bestow solubility in aqueous solution. Furthermore, extra functionalities would be required on the outer surface of the colloidal QDs for applications such as biological imaging.[72]

Apart from some sporadic studies of colloidal formation of metals and semiconductors in the early 20th century,[73] the modern synthetic methodology of colloidal QDs emerged in the late 1980s in a series of papers regarding colloidal nanocrystals from inorganic compounds.[74-76] Although these reports provided early evidence for the quantised behaviour of colloidal semiconductors, the quality of material was poor due to poly-dispersity and the lack of suitable solvents. In 1993, Murray *et al*. published a paper regarding the synthesis of monodispersed CdS, CdSe, CdTe QDs (called "semiconductor nanocrystallites" at that time) using organometallic precursors in trioctylphosphine/trioctylphosphine oxide (TOP/TOPO).[77] The paper is arguably the seminal study for synthetic methodology of semiconductor QDs due to its versatility and simplicity. Therefore, the pyrolysis of organometallic precursors in TOP/TOPO (or simply the "TOP/TOPO method") has become a standard of nanocrystals synthesis particularly in II-VI semiconductors. The next breakthrough was the preparation of strongly luminescent semiconductor QDs by combining the TOP/TOPO method and shell deposition.[77-79] Hines *et al*. synthesised CdSe/ZnS QDs with 50% quantum yields in 1996, again using organometallic precursors.[80] The CdSe/ZnS QDs were subsequently examined carefully by Dabbousi *et al*.[61] These pioneering studies significantly contributed in two ways: (i) nearly monodispersed QDs enabled the detailed comparison between theoretical and experimental results, (ii) simple synthetic procedures for high quality QDs formation made it possible to carry out further work.

Also, synthetic techniques based on an organometallic route have evolved to produce a variety of semiconductor nanomaterials. One example is the synthesis of anisotropic nanocrystals using a modification of the TOP/TOPO method, where shape-controlled CdSe nanorods were reported.[81, 82] Although several papers describing nanorods from other II-VI and III-V semiconductors already existed at that time, this study gave reproducible controllability in shape and the resulting nanorods exhibited quantum size effects. The same group also reported CdE (E = S, Se, Te) nanocrystals synthesis using relatively benign cadmium oxide as a precursor, which made a substantial contribution to QDs synthesis as the previously-used dimethyl cadmium is highly toxic and

pyrophoric, a barrier for further development.[64] Subsequently, other morphologies, such as tetrapods have been investigated in CdSe and other II-VI semiconductors.[68, 83-85]

Another notable advance is quantum dots heterostructures with staggered band gap configurations, where a different semiconductor material is deposited on the surface of the original QD, causing a different pathway for the exciton recombination (type II core/shell QDs). Type I core/shell QDs, in contrast, have a shell semiconductor material with higher conduction band and lower valence band than the core semiconductor. In 2003, Kim *et al.* developed type II heterostructures, based on existing technology such as GaSb/GaAs and Ge/Si. Core/shell structures such as CdTe/CdSe, CdSe/ZnTe were prepared *via* a modified TOP/TOPO procedure.[86] The CdTe core was first prepared and a CdSe shell was then deposited, giving CdTe/CdSe. Because the CdTe and CdSe have staggered energy states as shown in Figure 1.10, the excited electron moved to the conduction band of CdSe followed by recombination of the electron and the hole. The resulting band gap energy is smaller than that of original CdTe, therefore the emission of CdTe/CdSe QDs was red-shifted from the original CdTe core. Despite a limited emission quantum yield, the CdTe/CdSe and CdSe/ZnTe showed a new strategy for the design of functional QDs.

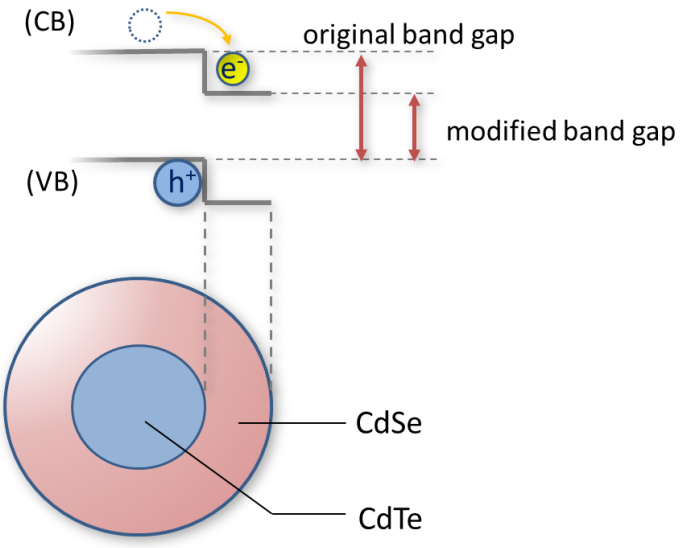

Figure 1.10. Energy relationship in type II QDs (CdTe/CdSe). (CB and VB = conduction band and valence band, respectively.)

Another notable synthetic technique is oriented attachment. Although the first example of oriented attachment was achieved with titanium dioxide nanocrystals,[62, 87] a key paper described CdTe QDs self-assembly which gave wire-like structures has gained much attention.[88] More sophisticated shape control by the oriented attachment of PbSe nanocrystals was subsequently developed.[89-91] These reports showed that careful choices of surfactant molecules in the solution (oleic acid, diphenyl ether, hexadecyl amine *etc*.) made it possible to control the morphologies of nanostructures, resulting in nanowires, zigzag, helical, branched and tapered nanowires.[90]

These emerging synthetic techniques such as heterostructure formation and oriented attachment of colloidal QDs, have created previously inaccessible nanomaterials as a result of the hybrid synthetic methodologies. For example, gold tips grown on CdSe nanorods (dumbbell-like structures), multi-branched CdE (E = S, Se, Te) heterostructures, Y-shape and tetrapod CdTe/CdSe, and PbSe tips on CdSe and CdS nanorods *etc.* have also been reported.[92-97]

In colloidal QDs, structural changes are required when one hopes to change the optical/electronic properties; for example, the particle size needs to be altered in order to change their emission wavelength in CdSe QDs: one potential solution of this is the formation of an alloy. Bailey *et al.* have made CdSeTe alloyed QDs by the modified TOP/TOPO method at high temperature, showing different band gaps of QDs keeping the nanoparticle sizes the same. While this was not the first report on alloyed nanostructures, it was the first careful examination of the relationship between composition and particle size, which was achieved due to the high quality QDs obtained by organometallic pyrolysis.[98, 99] Unusually, the CdSeTe QDs exhibited a non-linear composition-particle size relationship, showing red-shifted emission from normal CdSe and CdTe QDs. Other variants of alloyed QDs have also been reported.[100-102]

A similar technique to alloying is doping. Incorporating impurities into semiconductors is not a new idea, as doping technology was developed 50 years ago for bulk semiconductors.[103] The most studied dopants are manganese and cobalt, with CdSe QDs commonly used as a model semiconductor.[104, 105] This is simply because CdSe QDs prepared by the TOP/TOPO method exhibit excellent crystallinity and optical properties. Nevertheless, elucidating the internal physics/chemistry of doped QDs is not easy when compared to bulk solid doping due to the characteristics on the nanoscale. Supplemental

studies relevant to doping QDs have been therefore conducted in order for deeper understanding of nanoscale doping.

Advances in synthetic techniques have pushed the boundaries further. One breakthrough reported recently is cation exchange, where metal cations inside the nanocrystals are replaced with another type of metal cation in solution, resulting in compositional change of the nanocrystals while keeping the morphology. In 2004, Son *et al.* reported the rapid (<1 second), room-temperature conversion of CdSe QDs to Ag_2Se nanoparticles.[106] The resulting Ag_2Se NPs exhibited good crystallinity and interestingly, the Ag_2Se NPs could be converted back to CdSe QDs by the addition of appropriate reagents. According to the authors, the reaction was favourably driven by thermodynamics of the Ag_2Se formation and Cd^{2+} solvation. In following work reported by the same group, it was suggested that the hard soft acid base (HSAB) theory explained the cation exchange reaction in colloidal QDs (Figure 1.11).[107] The theory proposed that both acids and bases can be roughly divided into "hard" and "soft" depending on their ionic radii and polarizability, and binding affinity is generally higher in the case of hard acids and hard bases, or soft acids and soft bases. In the preparation of Ag_2Se from CdSe, for example, CdSe QDs consist of a hard acid (cadmium cation, Cd^{2+}) and a soft base (selenium anion, Se^{2-}). Because the silver cation (Ag^{+}) is a soft acid, the Ag^{+} is easily replaced with Cd^{2+} in the presence of a hard acid (methanol (MeOH), in this case), resulting in the energetically more favoured combination, Ag_2Se (soft acid + soft base) and Cd^{2+}/MeOH (hard acid + hard base) (Figure 1.11(b)). The versatility of this method towards other colloidal nanomaterials has been reported by many groups[107-109] and notably, metal/semiconductor core/shell structures which used to be extremely difficult to prepare with conventional synthetic techniques have been achieved by the cation exchange reaction.[110]

Apart from the methodologies in colloidal semiconductor QDs reported so far, many unique reports on synthetic techniques also exist. For example, QDs made in ionic liquids,[111] phosphine-free synthesis,[112] and microwave synthesis,[113] to name a few.

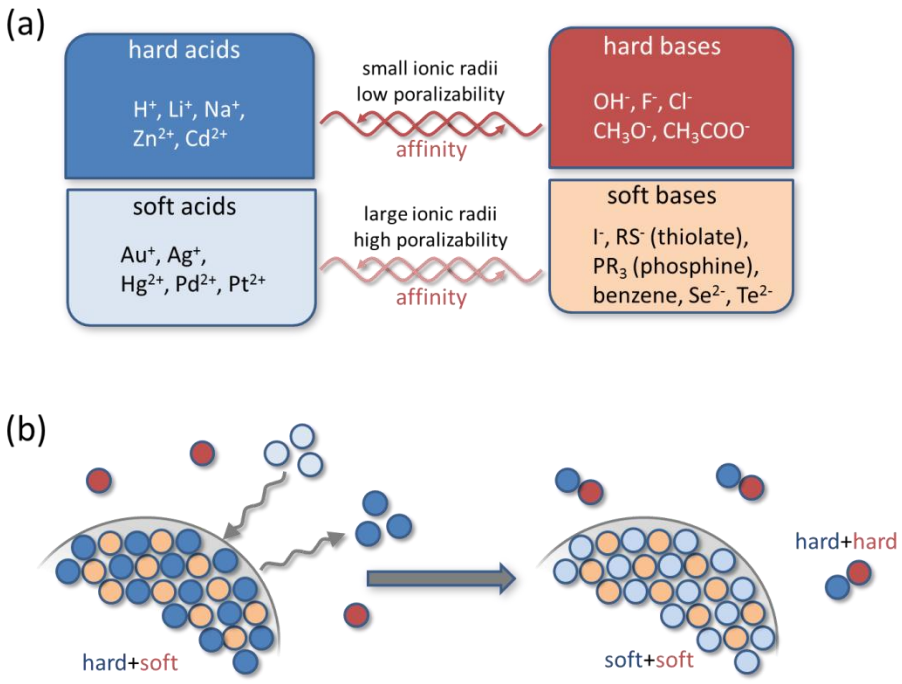

Figure 1.11. Schematic diagram of a cation exchange reaction. (a) List of hard/soft acids/bases and their relationship. (b) Visualisation of cation exchange in colloidal QD. Soft acids (light blue) in the solution will replace hard acids (thick blue) in the QD because of strong binding affinity between soft acids and soft bases.

1.4 Application of QDs

Compared to other nano-sized counterparts, the applications of semiconductor QDs might be somewhat limited. The intrinsic toxicity of heavy metals is regarded as a major drawback. Nonetheless, advances in the synthesis of colloidal QDs have created some specific applications that are impossible with other nanomaterials.

Firstly, the production of high quality QDs (particularly the II-VI family) allows the incorporation of device-quality materials for the first time. These materials represent an intermediate between molecular and solid-state entities. (Additionally, quantum size effect can be seen in semiconductors more significantly than metals.) The size-dependent band gap energy of QDs has been examined using several models such as pseudopotential, tight binding model and effective mass approximations.[1] The early transition from organometallic molecular precursors to nanoparticles was investigated in

several II-VI QDs using optical microscopy and size determination by transmission electron microscopy (TEM).[114, 115]

The radiative recombination process of the electron-hole pair (fluorescence) of a semiconductor QD has been also studied extensively. Since the discovery of the "dark exciton", the lowest state of exciton energy that is optically forbidden in a QD,[116] many studies regarding the internal energy states in QDs have been carried out. One of the reasons that colloidal QDs are the best candidate for such studies is because QDs exhibit quantum size effects, causing the difference of energy states inside the semiconductor to become more significant compared to bulk semiconductor solids. With advances in fluorescence lifetime decay measurement, it is now possible to examine in more detail the energy states and establish a sophisticated model.[117]

The most common use of semiconductor QDs, particularly II-VI QDs, is as light-emitting fluorophores. Semiconductor QDs can exhibit multiple colours covering almost the entire visible region by changing their particle sizes. In colloidal synthesis, the prepared QDs are already dispersed in various solvents, which potentially makes the colloidal QDs excellent candidates for biological imaging studies. Biological imaging using colloidal QDs has received increasing attention since the publication of a series of reports in *Science* in 1998, both of which used CdSe/ZnS QDs with surface modifications to internalise them into animal and human cells.[118, 119] The colloidal QDs mostly used in imaging application are CdSe/ZnS, whilst the use of other II-VI QDs (e.g. CdTe, CdTe/CdSe) and III-V (e.g. InP/ZnS) families have also been reported.[120-126] Because of the intrinsic incompatibility of semiconductor QDs toward biological entities, the importance of the surface modification of colloidal QDs has also been realised. A brief review of this surface modification of colloidal QDs will be presented in Chapter 5.

The optical properties of QDs exhibit distinctive differences from conventional organic dyes. Figure 1.12 shows absorption and emission spectra of colloidal QDs synthesised *via* organometallic route (tetradecylphosphonic acid-capped CdTe QDs in toluene) and an organic dye (rhodamine 6G in ethanol). Whilst the narrow absorption/excitation range of the conventional organic dye molecules makes simultaneous excitation difficult, QDs that can be excited efficiently at any wavelength shorter than the band gap energy show almost similar emission spectra regardless of the excitation wavelength. Therefore, many sizes of QDs (with different emission wavelength) may be excited with a single

wavelength of light, resulting in numerous emission colours that may be detected simultaneously.[72, 118] Other optical properties of QDs that can be ideal for biological application include: high quantum yield, high molar extinction coefficients (10 to 100 times those of small fluorophores and fluorescence proteins),[127] narrow and symmetric emission spectra (usually, full width at high maximum (FWHM) is 25–40 nm), high resistance to photo-bleaching and resistance to chemical degradation.[72] Therefore, colloidal QDs are regarded as a supplemental toolbox for biological imaging, together with fluorescent proteins, fluorescent genetic tags and small organic dyes. However, some intrinsic drawbacks still exist when using colloidal semiconductor QDs for biological application. A water-soluble QD conjugated to biomolecules usually exhibits a larger hydrodynamic diameter (typically, 10-30 nm) than other conventional fluorophores for biological applications, which prevents efficient traversal of intact membranes. Also, a large particle size restricts their use to permeabilised cells or extracellular proteins.[127]

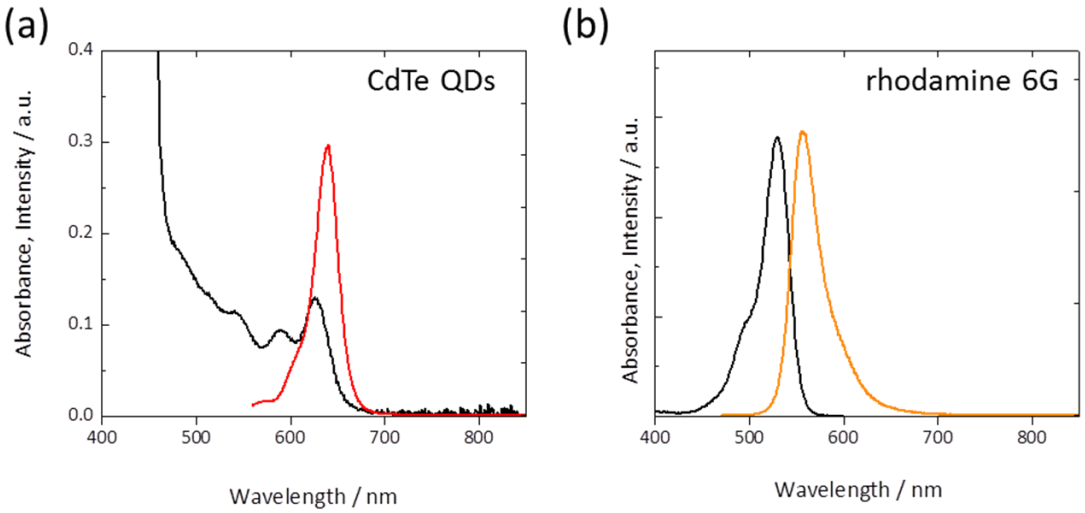

Figure 1.12. Absorption (black) and fluorescence (coloured) spectra of (a) a typical QDs sample in toluene (tetradecylphosphonic acid-capped CdTe QDs) and (b) rhodamine 6G ethanolic solution. The QDs were excited at 550 nm, and the rhodamine 6G at 460 nm.

One of the issues often stated in biological imaging is that fluorescent probes are expected to fluctuate between "on" and "off" states in terms of fluorescence, called fluorescence blinking. Although some studies actively exploit this behaviour,[128] the fluorescence blinking is generally an undesired characteristic in single molecule imaging.[129] Wang *et al.* have reported that colloidal CdZnSe/ZnSe core/shell QDs with a gradual core/shell composition showed non-blinking characteristics.[130] In the paper the authors reported that the QDs continued to photoluminesce despite being ionized, which is usually associated with Auger recombination and subsequent blinking of the QDs. Thus, the possibilities of using colloidal QDs as effective probes in single molecular imaging are promising.

Another application related to QDs' emission is quenching. The phenomenon is observed when an excited electron (or a hole) is trapped by the surface or outer energy states of the QDs, resulting in the disappearance of fluorescence. Inherently, inorganic nanocrystals have structures which may result in quenching: for example, dangling bonds on the surface, insufficient ligands coordination and stacking faults inside the crystal. Therefore, investigations into the quenching behaviour have been reported since the earliest synthetic reports.[65, 71, 131-133] The work regarding quenching behaviour generally addresses two features: (i) the underlying photochemistry in order to achieve more efficient fluorophores, (ii) to actively apply the phenomenon to devices such as sensors[134, 135] and photovoltaics.[71, 136-138] For example, Uematsu *et al.* fabricated a glucose sensor that uses luminescent NPs as an indicator.[135]

Quenching phenomena in semiconductor QDs can also be applied to photovoltaics applications. This is because quenching, which can be due to charge entrapment in another energy state, gives the possibility of electron-hole charge separation – a crucial step in photovoltaics. One can intuitively associate semiconductor QDs with photovoltaics due to the fact that bulk semiconductor materials (silicon, CdTe-CdS, $CuInS_2$) are often used as the core component in solar cells. Although still at the "proof of concept" stage, the use of QDs for photovoltaics has several advantages: tuneable band gap energy depending on the particle sizes, large cross-section of absorption, availability of various QDs to cover the solar radiation spectrum and scalability. Since the first studies of charge separation and photo conduction of QDs,[71] much work has been done using various strategies in order to achieve high efficient photovoltaics.[92, 136-139] Kongkanand *et al.* used CdSe QDs of differing diameters and assembled QDs-TiO_2 solar cells.[137] The influence of particle size and morphology were investigated and

"rainbow solar cells" which used multi-coloured CdSe QDs for sensitizers was suggested. Recently, tandem type photovoltaics using PbS QDs with two different diameters have been fabricated. The device, consisting of PbS QDs with different band gaps (1 eV and 1.6 eV), covers most of solar radiation spectrum and achieved a solar power conversion efficiency of up to 4.2 %.[140]

A relevant, intriguing but controversial theory is multiple exciton generation (MEG). The MEG occurs when the excess photon energy associated with one carrier (typically the electron) is instead used to generate additional carriers, which results in one or more additional excitons. The theory was first indicated by Nozik[141] and experimentally assessed by Schaller and Klimov using PbSe nanocrystals which are, so far, the most studied MEG-active semiconductor.[142] However, despite an expectation of the improvement in solar cells, experimental observations of the MEG and measuring the efficiency have been extremely challenging, which leads to scepticism of the theory.[143]

Other applications include quantum dot lasers,[144, 145] photodetector,[146] and reagents for photodynamic therapy.[147]

1.5 CdTe QDs

Cadmium telluride (CdTe) QDs are a member of the same semiconductor family as CdS and CdSe QDs and exhibit similar chemical/physical properties. However, CdTe QDs are different from other QDs in II-VI families for several reasons; the band gap is different, covering the near infrared region to visible region in nanosize regime (1.65–2.21 eV for CdTe QDs, while 1.94–2.53 eV for CdSe QDs and 2.53–4.13 eV for CdS QDs).[61, 148, 149] The favoured crystal structure is zinc blende (cubic) in contrast to wurtzite (hexagonal) in CdSe, which can make a difference in crystal growth. Notably, water-soluble CdTe QDs have generally stronger emission than CdSe QDs in water due to the difference in energy states and the subsequent photochemical interaction with ligands.[65]

Figure 1.13 shows band gap energy (E_g) of CdTe QDs as a function of diameter calculated from effective mass approximation (EMA) using equation (9). The E_g(QD) gradually increases from the original E_g(bulk) of CdTe (1.45 eV at 300 K) as the particle size decreases. The EMA can give a good picture of how particle size on the nanoscale affects the band gap energy of QDs. Nevertheless, it is now found that the

experimentally determined E_g/diameter relationships do not precisely follow the estimated curve determined by the EMA. The E_g(QD) from the EMA shows a reasonable agreement with the particle above 5 nm, whilst the difference between theoretical and experimental E_g(QD) becomes significant in smaller sizes. The possible explanation of such a mismatch in the EMA and experimental values is that the crystal anisotropy and spin orbit coupling can affect the QDs energy states, whilst the influence of surfactants and solvents should also be considered in a colloidal system.[1]

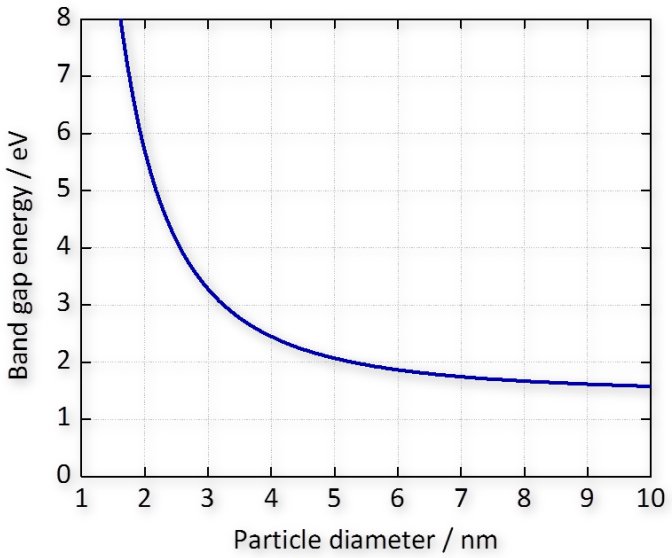

Figure 1.13. Band gap energy of CdTe QDs as a function of diameter. Bulk band gap energy $E_g(bulk)$ is 1.45 eV at 300 K,[60] the Planck constant h is $6.626 \cdot 10^{-34}$ Js.[150] The effective masses of electron and hole for CdTe are $m_e = 0.11m_0$, $m_h = 0.35m_0$, where m_0 is the mass of free electron ($m_0 = 9.1095 \cdot 10^{-31}$ kg).[151] Thus, $m^* = 0.0837m_0$. $\varepsilon_0 = 8.854 \cdot 10^{-12}$ $C^2N^{-1}m^{-2}$ and $\varepsilon_{CdTe} = 10.3$.[60]

Historically, the synthesis of colloidal CdTe QDs has developed both in aqueous and organic media. Brennan *et al*. synthesised an organometallic molecular precursor for CdTe, ($Cd(TePh)_2$), and showed an electron micrograph of the pyrolysis products, indicating the presence of CdTe QDs.[76] CdSe and HgTe nanocrystals were also prepared in the same manner.[75, 76] Studies using this synthetic procedure have been superceded by the highly effective TOP/TOPO method.[77] Developments of CdTe QD synthesis by the organometallic route are as described in Chapter 1.3 with some important improvements noted.[64, 84, 149, 152, 153] The organometallic synthesis of colloidal CdTe QDs can be described thus; typically, the cadmium precursor (cadmium oxide) is

heated with a long alkyl carboxylic acid, and reacted with trioctylphosphine telluride (TOPTe). TOPTe is still considered the best candidate as a tellurium precursor, and various solvents (such as long alkyl amines and acids, TOPO) are available to yield high quality CdTe QDs grown at high temperature (e.g. 270 $^{\circ}$C).

Unusually, CdTe can also be prepared as a high-quality material in water; usually the aqueous synthesis of QDs yields substandard particles. Predominantly, thiols, which are known to bind strongly to cadmium on the surface, are used as surface stabilizers. The successful aqueous synthesises of CdTe QDs using short alkyl thiols such as mercaptopropionic acid (MPA) and thioglycolic acid (TGA) with quantum yield up to 60 % have been reported.[154-156] Strong photoluminescence in the visible region, in water, is a critical difference from other semiconductor QDs, particularly CdSe QDs. Therefore, thiol-capped CdTe QDs are expected to have potential applications in biological imaging and biosensing.[156] In addition to strong fluorescence, thiol-caped CdTe QDs can be easily synthesised relative to the organometallic counterpart. The synthesis is easy and simple because the nucleation and growth of the QDs proceed at relatively lower temperature (<100 $^{\circ}$C), although the Te precursor, H_2Te gas, is regarded as toxic and harmful, alternative tellurium precursor such as NaHTe and $(NH_4)_2Te$ have been developed.[120] Last but not least, thiol-capped CdTe QDs generally have small hydrodynamic diameter in contrast to organically synthesised QDs which need to be covered with a thick shell (e.g. silica and polymer) to keep their functionality in water. However, aqueous synthesised QDs are generally not as monodispersed as organically synthesised QDs due to different particle growth kinetics from the TOP/TOPO route.

A number of papers describing cell imaging using thiol-capped CdTe QDs have been reported to date. In order to obtain high quality images, the surface of CdTe QDs is often modified with proteins[157, 158], small peptides, oligonucleotides[159, 160], polymers[160], or commercially available transfection regents.[120] It is commonly known that QDs with unmodified surface would experience unspecific binding to the surface of cells and therefore cause a decrease in image quality.[161] The CdTe QDs bioconjugates are thought to be small enough for facile internalisation into cells. For example, glutathione-capped CdTe QDs with hydrodynamic diameters of 4 nm and 5 nm were incubated with Hep G2 cells, staining two regions in a cell depending on the particle size and their mobility; smaller QDs accessed the nucleus within 1 hour, whilst larger QDs could not reach the nucleus and stayed in the cytoplasm 24 hours after the incubation.[157]

Although many reports concluded that imaging applications using CdTe QDs were successful, little work regarding the influence of the CdTe QD on cells' biological activity and mortality has been done. This viewpoint is crucial for both understanding and developing semiconductor QDs as fluorescent probes. The study and reviews based on the toxicity of QDs (predominantly II-VI semiconductors such as CdSe/ZnS, CdSe and CdTe) state that the main causes of CdTe QDs toxicity are cadmium leakage and reactive oxygen species (ROS) produced by photochemical reaction of fluorescent QDs. Cadmium causes acute injury in the liver, whilst at a subcellular level, cadmium binds strongly to thiol group of some critical mitochondrial proteins, resulting in dysfunction of the liver, in addition to several reports on cell internalisation of Cd^{2+} and damages to DNA and ribonucleic acid (RNA).[162, 163] The ROS is a collective term of singlet oxygens, super peroxide anions, hydrogen peroxides and free radicals. The ROS readily reacts with peripheral biological molecules such as proteins and DNA, causing irreversible damage to an entire cell. There have been a number of studies focusing on free radical production and/or cadmium leakage in order to systematically investigate the influence of semiconductor QDs on single cells, animals and bacteria.[158, 163-166] Although there are some controversies on QDs toxicity (for example, whether CdSe/ZnS QDs produce free radicals or not [164, 165]), it seems that some consensus have been gradually formed thanks to an accumulation of the knowledge in the field; (i) Cd^{2+} is likely to be released from the surface of QDs if the surfactants are short (e.g. MPA-capped CdTe QDs).[166] (ii) Thiol-capped CdTe (or CdSe) QDs are known to produce free radicals upon irradiation. (iii) Particle size and surface charge can have significant influence on the toxicity because these two factors dominate the physical property (mobility, permeability and non-specific adsorption) of the QDs.[163]

It is somewhat unfortunate that there is no clear answer to the toxicity of QDs. This is in part due to the wide variation in quantum dot size and structure, which in turn leads to a lack of standard protocols for determining the cause of toxicity. For example, CdSe/ZnS QDs vary depending on core size, shell thickness, mono-dispersity, surfactants and solvent to be used, storage conditions *etc*. However, most of the parameters are often overlooked and the material is used simply as "CdSe/ZnS QDs". Also, it is impossible to adopt one global standard of QDs synthesis. Therefore it is advisable that QDs synthesis should provide as much of information and parameters as possible so that other researchers can evaluate the characteristics more precisely.

Other applications using CdTe based materials include sensors,[167-169] self-assembled structure for optoelectronics,[88, 170-172] and photovoltaics.[86, 136] For example, Tang *et al*. modified the surface of thiol-capped CdTe QDs and fabricated light emitting one-dimensional superstructures, whilst antigen/antibody-QDs bioconjugates were fabricated using different coloured CdTe QDs, showing Förster resonance energy transfer between different QDs when forming antigen-antibody immunocomplexes. Both examples took advantage of thiol-capped CdTe QDs, where strong emission was obtained and surface chemistry could be controlled by simple treatment.

1.6 The Objective of the Thesis

This thesis concerns the synthesis of functional nanomaterials based on CdTe QDs. As discussed in Chapter 1.5, there are several potential applications for CdTe QDs-based nanomaterials. However, because of their inherent toxicity, it is unlikely that CdTe QDs can overtake all the competing candidates in these applications (e.g. silicon in photovoltaics, or fluorescent proteins in imaging). The thesis describes a variety of synthetic techniques for colloidal QD preparation including both aqueous and organometallic synthesis. The thesis will present detailed synthetic procedures and experimental observations of the resulting nanomaterials so that one can investigate and repeat the work reproducibly in future. The thesis will also show previously inaccessible CdTe-based nanomaterials which will be useful in some specific applications.

In Chapter 2, the synthesis of core/shell/shell type QDs in a one-pot reaction for biological imaging is described. In Chapter 3, CdTe QDs from the TOP/TOPO route are chemically transformed into other materials using reactive metal cations. In Chapter 4, the use of single-source precursors, which contains both cadmium and tellurium sources, is described and their use in the synthesis of CdTe and CdTe/ZnS QDs are reported. In Chapter 5, phase transfer techniques from organic solvent to water using amphiphilic proteins are presented.

Chapter 2

Synthesis of CdTe/CdSe/ZnSe Quantum Dots for *in vivo* Deep Tissue Imaging

2.1 Introduction

There have been many studies regarding biological imaging with colloidal semiconductor QDs, as mentioned in the last chapter, since the pioneering reports using CdSe/ZnS bioconjugates.[118, 119] Because CdSe-based fluorophores cover most of the visible wavelength (e.g. 480-620 nm),[61] they are expected to offer intriguing opportunities for imaging science and, therefore, research has evolved rapidly from the early stages. However, CdSe/ZnS QDs have an intrinsic limitation when it comes to biological imaging. CdSe-based QDs do not exhibit optical characteristics past the visible region, which indicates that the material itself needs to be altered when one hopes to prepare fluorophores with wavelength outside the visible region, such as near infrared (NIR) region. Certain imaging applications, specifically deep tissue imaging, take advantage of the optical transparency of biological materials at the NIR wavelength. Emission in this region can penetrate through skin with less interference when compared to visible emission. Pushing the optical characteristics towards the NIR region has, therefore, gained increasing attention in colloidal QDs synthesis.

Applications using NIR-emitting colloidal QDs for biological imaging have been realised since the report of alloyed CdSeTe QDs which can emit at 850 nm.[98, 173] Also, type II core/shell QDs offered new alternative NIR emitting materials.[86] The same group showed successful imaging of lymph nodes using CdTe/CdSe QDs.[174] Because of the variety of choices for core and shell materials, in addition to the band gap tuning for the core particle, type II QDs are expected to achieve various wavelengths which were previously inaccessible, typically toward the NIR region. Another advantage is that both alloyed and type II QDs can effectively avoid the drastic change in size required in bare

QDs alone. For example, the synthesis of CdTe QDs which emit in the NIR region will involve substantial particle sizes along with a decrease in emission efficiency.[149, 156]

Several studies regarding the synthesis of other type II QDs have been reported.[175-179] It is also worth mentioning that III-V semiconductors based on InAs and InP can be exploited in tissue imaging, although these have yet to be used routinely in the NIR region.[180, 181] The synthesis of QDs in organic solvents, however, has an inherent drawback in biological applications; extra synthetic steps are required to transfer organically soluble QDs into water, by changing surfactants or by adding extra hydrophilic shells on the QDs (phase transfer). The phase transfer process generally results in adverse effects, such as an increase in hydrodynamic diameter and a decrease in fluorescence efficiency.

A potential solution for such a problem is the aqueous synthesis of colloidal QDs. There are, however, few studies based on the aqueous synthesis of QDs for NIR imaging reported so far. HgTe and CdHgTe QDs which have IR to NIR emission were reported *via* an aqueous route, but these QDs are unlikely to be useful in biological imaging without further processing. [99, 182] Recently, however, alloyed CdHgTe-based nanomaterials synthesised in aqueous solution were used in biological studies.[183, 184] Thiol-capped CdHgTe/CdS alloys emitting at 780 nm with an approximate 20 % quantum yield were injected in living mice for fluorescence imaging. Type II CdTe/CdSe QDs have also been prepared directly in water. Zhang *et al.* reported the synthesis of QDs *via* an aqueous route which utilised a cadmium-cysteine complex, NaHTe and KaHSe as precursors,[122] whilst similar work on CdTe/CdSe QDs used a thioglycolic acid (TGA)-cadmium complex and Na_2TeO_3 and Na_2SeO_3.[185] The resulting QDs from both reports were injected to HeLa cells for imaging studies.[122, 167, 185] CdTe/CdS QDs are also known to have type II behaviour and several reports on the aqueous synthesis of CdTe/CdS based materials and their biological uses have been published.[121, 186, 187] For example, ultra small (magic-sized) CdTe/CdS QDs with emission wavelengths up to 820 nm were synthesised in water for tissue imaging studies.[187, 188]

In the work reported in this thesis, a simple aqueous synthesis for core/shell/shell QDs (CdTe/CdSe/ZnSe) capped by long alkyl thiol ligands is presented as shown in Figure 2.1. The band gap configuration between CdTe and CdSe is type II, whilst the band gap between CdSe and ZnSe is type I (Figure 2.2). When the CdTe core is excited, the

excited electron moves to the conduction band of the inner shell (CdSe) and recombines with the hole in CdTe, whereas the outer shell (ZnSe) presents an energy barrier, which prevents the exciton from escaping to surface traps. The ZnSe shell also works to stop cadmium leakage – a major toxicity issue associated with II-VI quantum dots. Furthermore, an established synthetic technology, successive injection precursors in one-pot (SIPOP), was adopted for the synthesis. Previous reports showed the production of core/shell/shell (CdSe/ZnSe/ZnS, CdTe/CdS/ZnS) QDs with greater scalability and less by-products when using this technique.[121, 189] The CdTe/CdSe/ZnSe QDs reported in this work exhibited emission in NIR region and were the first report (to the best of knowledge) showing *in vivo* deep tissue imaging with CdTe-based QDs synthesised in water.

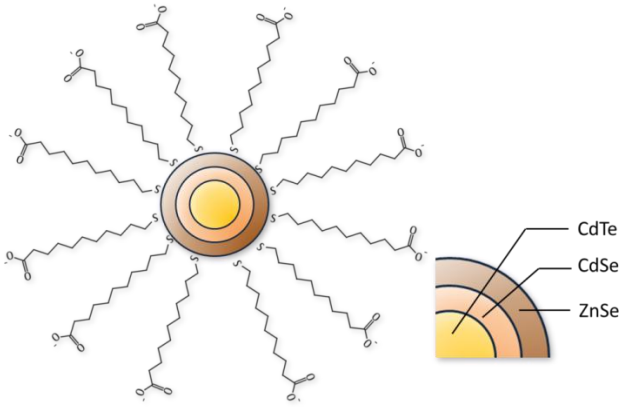

Figure 2.1. Suggested structure of mercaptoundecanoic acid (MUA)-capped CdTe/CdSe/ZnSe QDs.

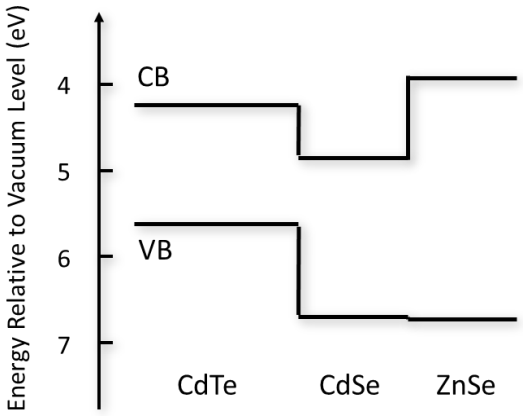

Figure 2.2. Energy band offsets for semiconductors comprised of the core/shell/shell QDs. The energy states in conduction band (CB) and valence band (VB) were obtained from literature.[190]

2.2 One-pot Synthesis of CdTe/CdSe/ZnSe QDs in Aqueous Media

The basic procedure for CdTe QDs synthesis was referred from the work published from our group with some minor modifications (detailed procedure can be found in Chapter 6.2.3).[120, 121] Mercaptoundecanoic acid (MUA), which has a relatively long alkyl chain (estimated length is ~1.9 nm)[191], was used as a surfactant molecule in contrast to commonly known shorter thiols such as TGA. The use of MUA in biological applications is assumed to be ideal whilst referring to the work of Mikulec, who reported the chain length of MUA is optimum for labelling application of colloidal QDs (CdSe/ZnS).[192] The molecular ratio of precursors used was a major factor which determined the characteristics of the resulting QDs. The molar ratio of cadmium to MUA was changed to 1:1.5, from the original ratio of 1:2.0-2.3.[120, 121, 193] This is due to several reports arguing that the optimised ratio of cadmium and thiol surfactant is 1:1.3-1.5 in aqueous CdTe system.[156, 194] The CdTe QDs synthesised under such conditions should contain the minimum amount of surfactants, allowing the addition of selenium to readily proceed on the CdTe surface. Furthermore, the concentration of overall precursors was reduced to prevent undesired precipitation. Indeed, our experimental observations indicated difficulties when preparing core/shell/shell QDs when precursors addition of all the monomers exceed as >0.1 mmol. Therefore, initial monomer concentrations for core CdTe QDs synthesis were: cadmium acetate ($Cd(OAc)_2$) 0.079 mmol, $Te(NH_4)_2$ 0.04 mmol, and MUA 0.126 mmol in 60 mL deionised water. Extra cadmium precursor was left in the solution to allow shell formation following selenium precursor addition. This concept is the key principle of the SIPOP method.[189] The resulting MUA-capped CdTe QDs showed bright green emission (Figure 2.3).

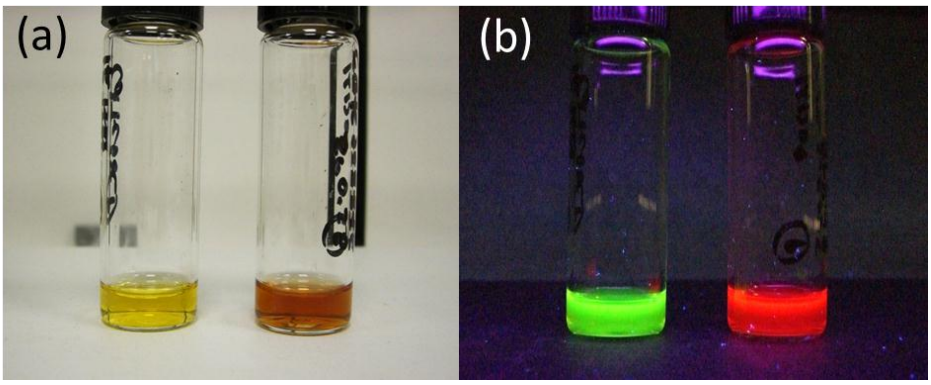

Figure 2.3. Prepared QDs under (a) room light and (b) UV lamp (λ = 365 nm). The left vial is MUA-CdTe QDs, whereas the right is MUA-CdTe/CdSe/ZnSe QDs.

For the CdSe shell formation, Na_2SeSO_3 was chosen as a selenium source due to the previous report by Hankare *et al.* on HgSe thin film synthesis using this precursor.[195] The reason for using Na_2SeSO_3 is the stability in ambient condition, in contrast to conventional water-soluble selenium precursors such as NaHSe and H_2Se, which are highly reactive and immediately oxidised when exposed to an ambient atmosphere. It was observed that the Na_2SeSO_3 precursor solution was stable for a day, although the interface between liquid and air yielded small amounts of red solid (thought to be polymerised selenium due to oxidation). Therefore, Na_2SeSO_3 could be readily used and it was not necessary for the CdTe QDs solution to be degassed and purified before shell deposition, allowing the synthesis on a large scale.

The CdSe shell was deposited on the CdTe surface by the decomposition of selenium precursor in alkaline condition.[195]

$$Na_2SeSO_3 + OH^- \rightarrow Na_2SO_4 + HSe^-$$

$$HSe^- + OH^- \rightarrow Se^{2-} + H_2O$$

Equation 2.1 Production of the selenium anion in alkaline solution.

The resulting Se^{2-} reacted with the excess cadmium monomer left in the solution to form a CdSe Shell. There is still a possibility, however, of cadmium leakage from CdTe/CdSe to cells. Therefore, an additional ZnSe shell was added on the CdSe shell by injecting a Zn-MUA complex which was prepared from zinc nitrate and MUA. Addition

of the zinc precursor caused a reaction with excess selenium ions left in the solution, depositing a ZnSe shell (Figure 2.4). After 16 hours of reflux at 90 °C, the solution was found to be slightly cloudy and had red emission when excited at 365 nm (as shown in Figure 2.3).

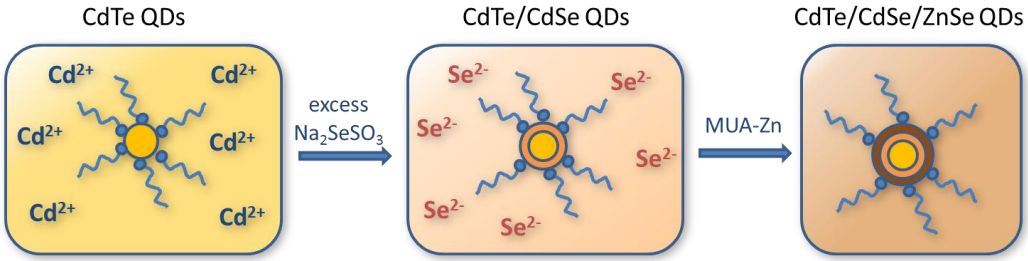

Figure 2.4. Reaction schematics for the synthesis of CdTe/CdSe/ZnSe QDs using the SIPOP method. Extra cadmium and selenium ions are left in the solution for subsequent deposition of a CdSe inner shell and a ZnSe outer shell.

2.3 Characterisation of the QDs

2.3.1 Optical Spectroscopy

Absorption and emission spectra of the prepared CdTe/CdS/ZnSe QDs are shown in Figure 2.5. The emission peak of CdTe/CdSe/ZnSe QDs was largely red-shifted after shell deposition. Absorption spectra were also slightly red-shifted, whilst the disappearance of excitonic peak of CdTe QDs at 450 nm was observed after shell formation. The full width at half maximum (FWHM) of the emission changed from original 51 nm to 101 nm. All the spectral changes mentioned can be explained as a consequence of CdSe shell formation on CdTe surface as previously reported.[86, 122, 177, 185]

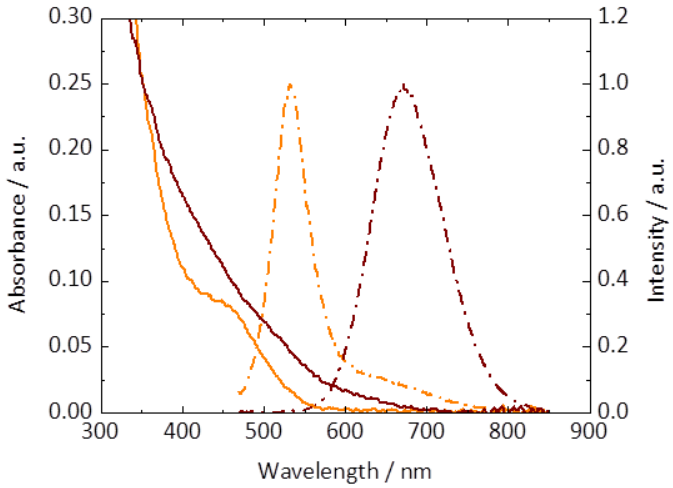

Figure 2.5. Normalised emission and absorption spectra for CdTe QDs (orange curves) and CdTe/CdSe/ZnSe QDs (brown curves). Solid lines show absorption spectra, whilst dashed lines indicate emission spectra. Excitation wavelength = 450 nm.

Figure 2.6 shows the emission spectrum at each reaction stage, and the emission intensity as a function of reaction time. The steady red-shift was observed from emission peak (Figure 2.6 (a)), whereas an unusual change of emission intensity regardless of reaction time was shown (Figure 2.6 (b)). These non-linear intensity changes can be separated into three stages: (i) rapid increase in intensity (0-4 hours), (ii) rapid drop in intensity (4-6 hours), and (iii) slow recovery to higher intensity (6-22 hours). The change in emission intensity (or quantum yield) such as stage (i) and (ii) was also observed in conventional core/shell QDs such as CdTe/CdSe and ZnSe/ZnS QDs in both organic and aqueous solution, where emission is improved at the first stage of thin shell formation on a core, whilst the emission quenched as the shell becomes thicker.[122, 153, 177, 185, 196] Therefore, it is assumed that stage (i) and (ii) in our QDs are associated with the formation of CdTe/CdSe QDs. Interestingly, the emission intensity again increased by prolonged reaction after the final precursor addition, which suggested that additional ZnSe outer shell was formed on the CdSe inner shell. ZnSe shell formation indicated internalisation of the exciton within the QDs, as well as the removal of surface trapping site, resulting in the enhancement of the emission.

It should be mentioned that the first zinc source was added in the stage (i) in order to avoid the precipitation of the particles (Figure 2.6 (b) plot 3); we observed that after the first selenium source addition, the particles aggregated after 1.5 hours without zinc-

MUA addition, which indicated that the selenium-rich surface tended to aggregate due to the lack of surfactants. Also, given the thermodynamic driving forces such as standard redox potential, E^0 (E^0 for $Cd^{2+} + 2e^- \rightarrow Cd$ = -0.40 eV, whilst $Zn^{2+} + 2e^- \rightarrow Zn$ = -0.76 eV) and acid softness (the cadmium cation is softer than the zinc cation, hence the cadmium cation preferably binds to the selenium anion, a soft base, over the zinc cation),[197, 198] it is reasonable that the CdSe formation is favoured over ZnSe formation in our reaction system. Under these conditions, zinc-MUA addition did not cause immediate ZnSe formation and allowed CdSe shell deposition prior to ZnSe whilst preventing the particle aggregation. Therefore, we suggest that CdTe/CdSe formation occurred in stage (i) and (ii) although the zinc precursor already existed in the solution. The zinc source gradually formed a ZnSe shell after the complete deposition of the inner CdSe shell at the stage (iii).

Photoluminescence quantum yields (PL QY) were calculated (detailed procedure is described in Chapter 6.1.2.2) from the comparison of a fluorescence standard using:

$$\Phi_x = \Phi_{st} \cdot \frac{G_x}{G_{st}} \cdot \left(\frac{\eta_x}{\eta_{st}}\right)^2 \qquad (10)$$

where Φ_x is the quantum yield of QDs, $\Phi_{st}$is the known quantum yield of a standard fluorophore, G is the gradient from the plot of integrated emission intensity versus absorbance, and η is the refractive index of the solvent. The gradient was calculated from Figure 2.7, $(\eta_x/\eta_{st})^2$ is 0.96 in a water/methanol system, and Φ_{st} is known to be 0.95 for an ethanolic solution of rhodamine 6G excited at 450 nm.[199] Thus, the PL QY of CdTe/CdSe/ZnSe QDs was 4.8 %, whereas CdTe was 1.4 %. The obtained quantum yield is comparable to the quantum yield reported from Kim *et al.* of 4 %.[86] The final materials were found to be stable in ambient conditions for months.

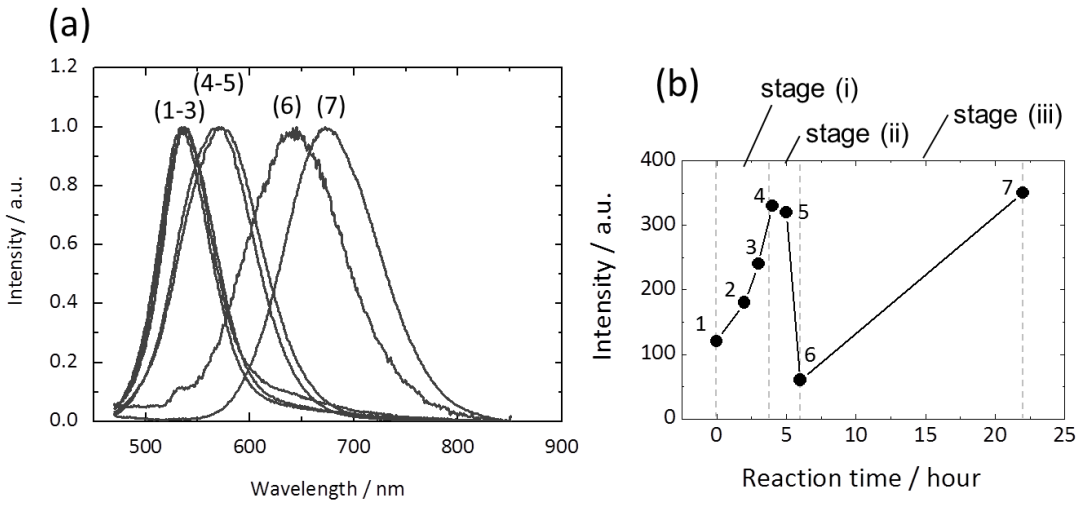

Figure 2.6. (a) Normalised spectral transition of QD during the shell formation. From the left to right, 1) crude CdTe, 2) first Se addition (0.025 mmol), 3) first Zn addition (0.10 mmol), 4) second Se addition (0.025 mmol), 5) second Zn addition (0.10 mmol), 6) third Se addition (0.025 mmol), and 7) the sample after 16 hours reaction from the final precursor addition. (b) Emission intensity as a function of reaction time. CdTe QDs formation was set as 0 hour.

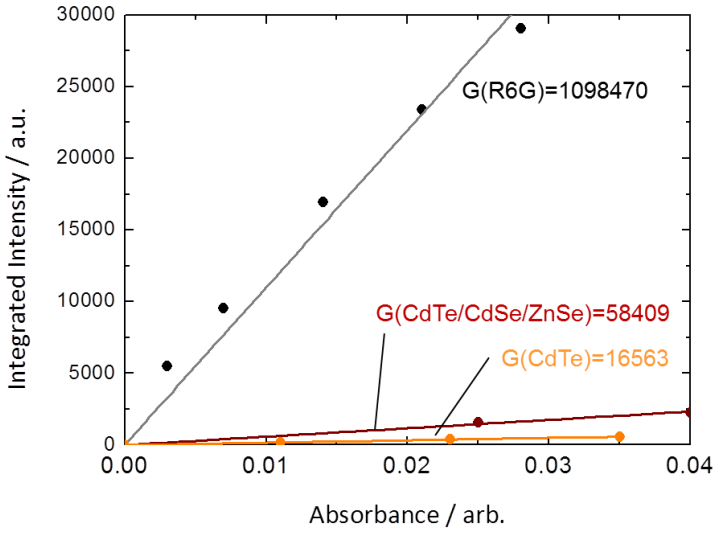

Figure 2.7. Relationship between integrated emission intensity and absorbance of rhodamine 6G (black), CdTe QDs (orange), and CdTe/CdSe/ZnSe QDs (brown). The gradients of the slopes are indicated inside the graph.

2.3.2 Transmission Electron Microscopy (TEM)

Transmission electron micrographs of CdTe, CdTe/CdSe (CdTe/CdSe QDs were prepared by the same procedure as CdTe/CdSe/ZnSe but excluded additional zinc and selenium additions), and CdTe/CdSe/ZnSe QDs are shown in Figure 2.8. Whilst CdTe QDs are predominantly spherical, a slight anisotropy was observed in the sample of CdTe/CdSe/ZnSe QDs (Figure 2.8 (c) and (d)). Anisotropic particle growth is a commonly observed phenomenon in colloidal nanostructures and was in good agreement with other reports of core/shell QDs. For example, CdSe/CdS nanorod growth was examined, where the c-axis of the material was elongated at lower temperature synthesis (120-130 $^{\circ}$C in an organometallic route) due to the kinetic factor of wurtzite CdSe and CdS.[94] It is possible for the CdSe component in our samples to induce crystal growth along the c-axis. Other QDs previously reported in our group (CdTe/CdS/ZnS) also exhibited anisotropic crystal growth with an aspect ratio of 1.8.[121] From high resolution TEM image (Figure 2.8 (d)), the lattice fringe can be seen, indicating the good crystallinity of the prepared QDs.

The particle diameter was investigated by measuring approximately 200 particles on each sample. Figure 2.9 shows the size distribution of CdTe, CdTe/CdSe, and CdTe/CdSe/ZnSe QDs. The average diameters were 2.2 ± 0.4 nm for CdTe QDs, 2.9 ± 0.6 nm for CdTe/CdSe and 4.0 ± 0.8 nm for CdTe/CdSe/ZnSe QDs, respectively. Given zinc blende lattice constant for CdSe (6.050 Å) and ZnSe (5.668 Å), the CdSe shell is assumed to be one monolayer (ML) on the CdTe core and 2 MLs of ZnSe on the CdSe shell. The resulting shell thicknesses were comparable to the previously reported core/shell/shell QDs. CdTe/CdS/ZnS QDs synthesised in aqueous solution using the SIPOP method showed *ca.* 1.4 ML of CdS inner shell formation, while ZnS outer shell formation showed pronounced anisotropic growth (0.57 ML and 5.8 ML along short and long axes, respectively).[121] Other core/shell QDs, however, exhibited different behaviours in shell formation. For example, CdTe/CdSe QDs synthesised in water using stepwise addition of the shell precursors achieved thicker shell formation up to 4.2 ML,[185] whilst organically synthesised CdTe/CdSe showed up to 4 ML of the CdSe shell.[177] Although it is reasonable that different precursors, solvents and reaction procedure should lead different shell growth mode, we suggest that relatively stable nature of the selenium precursor and reaction temperature (90 $^{\circ}$C) affected the rate of the shell growth, both in CdSe and ZnSe, which leads to relatively thinner shell growth in this work. Also, it was difficult to prove from only the TEM study that exactly one

ML of the CdSe shell and two ML of the ZnSe shell formed on the CdTe core. For example, some CdTe particles formed CdSe and ZnSe shells effectively, whereas other CdTe particles stayed as bare particles, which could cause poly-dispersity in the size distribution. Nonetheless, the broaden size distribution, as can be seen in Figure 2.9, was a common phenomenon in the core/shell QDs synthesis. The emission wavelength of the CdTe/CdSe/ZnSe QDs was similar to the reported emission wavelength of CdTe/CdSe (1 ML of CdSe shell) at 650 nm.[61, 177] Therefore, our estimation that CdTe/CdSe/ZnSe QDs had 1 ML of the CdSe and 2 ML of the ZnSe shells is to some extent reasonable.

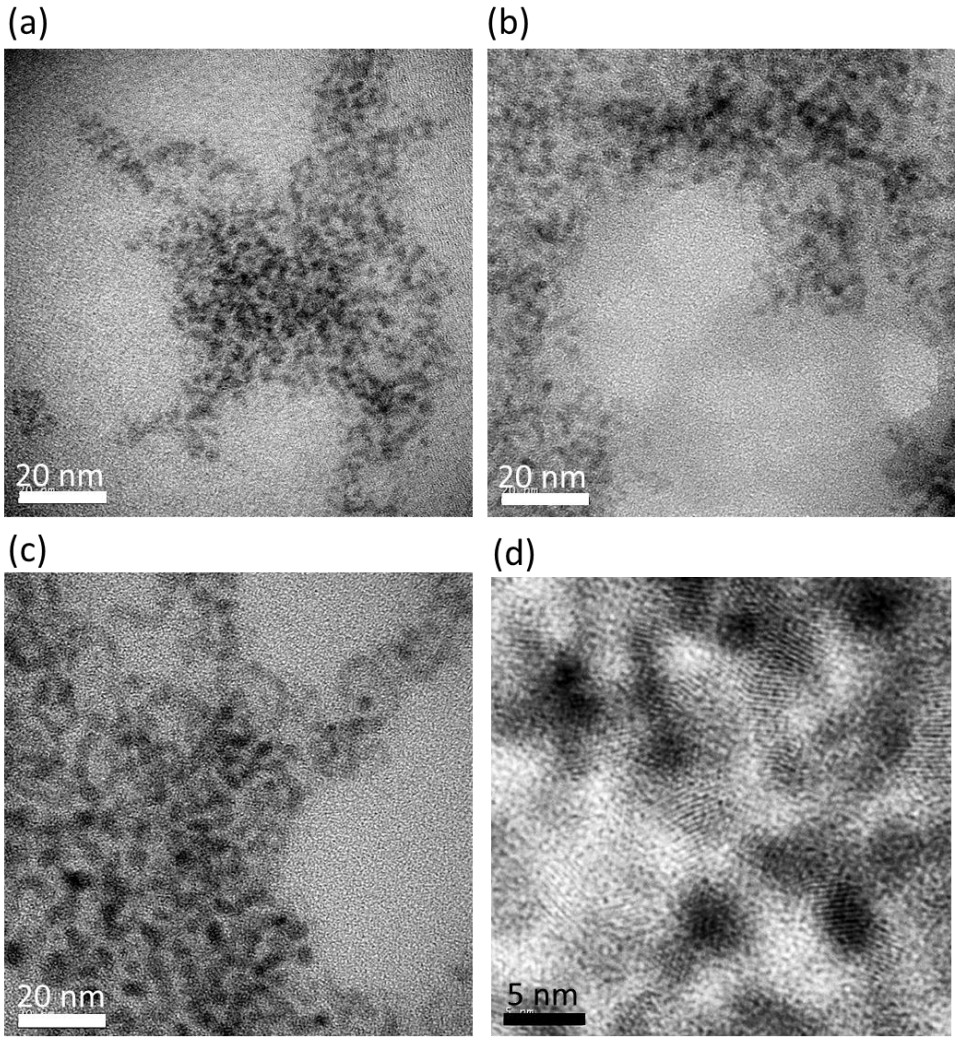

Figure 2.8. TEM images of purified (a) CdTe, (b) CdTe/CdSe, and (c) CdTe/CdSe/ZnSe QDs. (d) high resolution TEM image of CdTe/CdSe/ZnSe QDs.

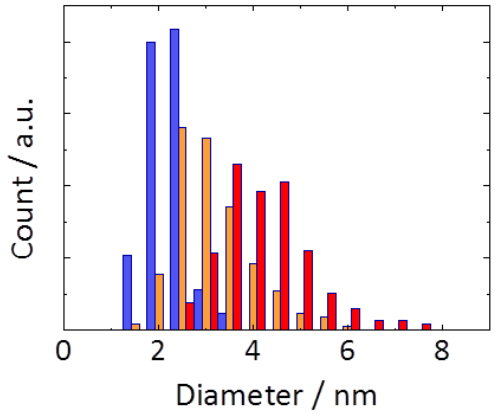

Figure 2.9. Size distribution of the QDs measured from TEM images. CdTe (blue), CdTe/CdSe (orange), and CdTe/CdSe/ZnSe QDs (red), respectively.

2.4 QDs Formation Mechanism

The main advantage of CdTe/CdSe/ZnSe QDs described in this work is the simplicity and scalability bestowed by the SIPOP method. In order to use the SIPOP method, several unconventional precursors for the synthesis, such as $(NH_4)_2Te$ and Na_2SeSO_3 in contrast to commonly used chemicals (e.g. NaHTe, H_2Te, Na_2TeO_3, NaHSe and H_2Se) have been chosen. It is essential, therefore, to analyse the reaction observed in this system and to suggest a plausible mechanism for the formation of CdTe/CdSe/ZnSe QDs. CdTe QDs capped with short alkyl thiols such as mercaptopropionic acid (MPA) and TGA show Ostwald ripening, a thermodynamically favoured particle growth mode, resulting in the formation of bigger QDs *via* the dissolution of smaller particles. For example, when CdTe QDs capped with TGA were heated to reflux, a red-shift in optical properties could be observed after a few hours reaction; the particle size reached around 5 nm after 40 hours reflux with an emission wavelength at 620 nm.[194] MUA-capped CdTe QDs, however, did not show any growth consistent with Ostwald ripening. A comparison of CdTe QDs heated for the usual 16 hours during synthesis and a sample heated for a prolonged duration (68 hours) displayed no change in emission wavelength. Instead, the emission intensity was notably increased after the prolonged reflux time, which could be explained as annealing.[62, 100] Therefore, the observed optical red-shift in the MUA-capped CdTe/CdSe/ZnSe (Figure 2.5) was consistent with type II core/shell formation, rather than Ostwald ripening of the CdTe core. Another intriguing

phenomenon specific to this reaction system is the transition of solution colour during the shell addition. Figure 2.10 shows the colour change during CdTe/CdSe/ZnSe QDs synthesis. The yellow CdTe QDs solution turned darker after Na_2SeSO_3 addition (in <10 minutes), whilst the dark colouration faded as the reaction proceeded, resulting in a light orange solution. The lower picture of Figure 2.10 shows the same samples excited at 365 nm. The emission colour shifted gradually towards the red end of the spectrum with changes in emission intensity, which was comparable to the results presented in Figure 2.6. Interestingly, it seemed that the black colouration in the sample (b) and (c) in Figure 2.10 did not affect the emission, showing strong fluorescence under excitation. From these experimental observations, the dark colouration obtained after the first selenium precursor addition is assumed not to influence the exciton and energy states of QDs, but to be a result of macroscopic changes in environment surrounding the CdTe QDs.

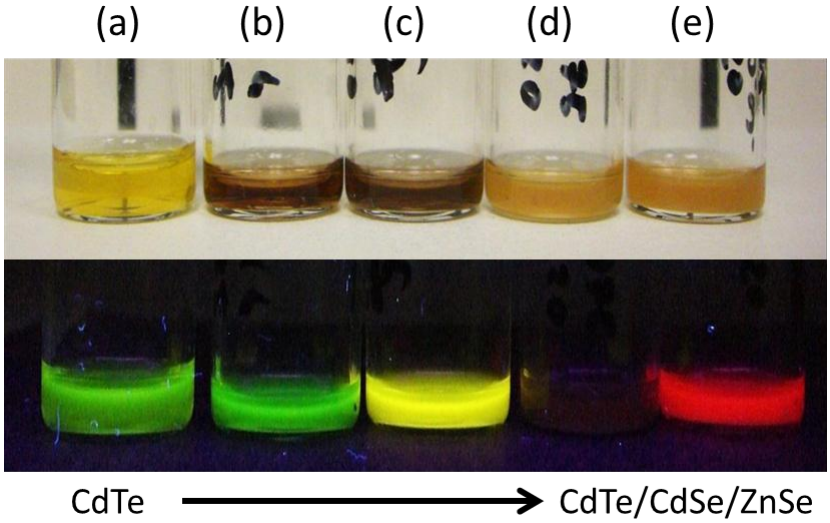

Figure 2.10. Photograph showing the colour change in the course of CdTe/CdSe/ZnSe QDs formation. (upper) Under room light and (lower) under 365 nm excitation. From left to right, a) CdTe, b) the first Se source addition, c) the first Zn source addition, d) the second Zn/S sources addition, and e) 16 hours after the final precursor addition. No samples were purified.

To investigate the reaction mechanism further, a TEM image was taken from the darker solution (Figure 2.10, sample (b)) and shown in Figure 2.11, displaying rod-shaped structures and individual particles present in the same image. The smaller CdTe

particles appeared to be clustered together, indicating the rod structure formation possibly through oriented attachment. It is suggested that the addition of the selenium precursor induced a network consisting of CdTe QDs and other compounds such as Cd-MUA and Na_2SeSO_3. There are several papers which reported the formation of 1-D structures in thiol-capped CdTe QDs solution.[88, 171, 200, 201] In these reports, it is suggested that thiol-Cd complexes in solution were polymerised to form rod-like structures,[202] which subsequently worked as a "glue" and internalised CdTe QDs inside (Figure 2.12). Chen *et al*. described crude TGA-capped CdTe QDs, which inherently contained excess TGA-Cd in the solution, when mixed with ethanol and sodium acetate at 70 $^{\circ}$C for 8 minutes, caused the formation of rod-like structures (several micrometres in length and 25 ± 8 nm in width). The rod-like structures included CdTe QDs (as determined by high resolution TEM) and the sample was still emissive without any significant red-shift,[171] all of which were in good agreement with the observations in this study. Also, other groups observed black colouration upon nanorod formation using TGA and CdTe QDs, where the dark colouration was thought to be concentration dependant. The precursor concentrations needed to be lower than 2.4 mM in order to obtain the darker solution.[201] The CdTe/CdSe/ZnSe QDs reported here were prepared with a comparable concentration. It is possible that the black colouration and rod-like structures obtained in the TEM after selenium source addition were a result of MUA-Cd polymerisation followed by CdTe QDs inclusion.

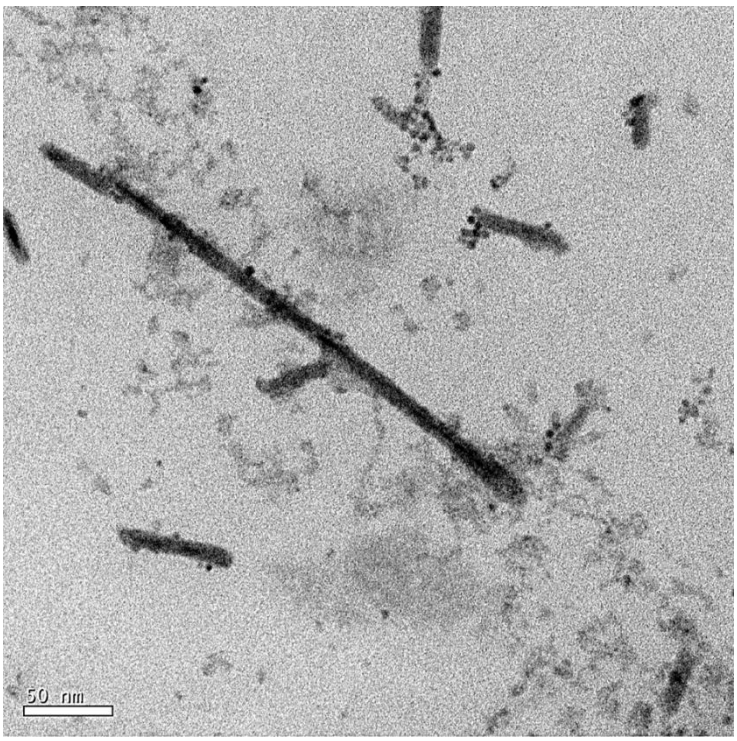

Figure 2.11. TEM image of CdTe QDs 1 hour after selenium source addition.

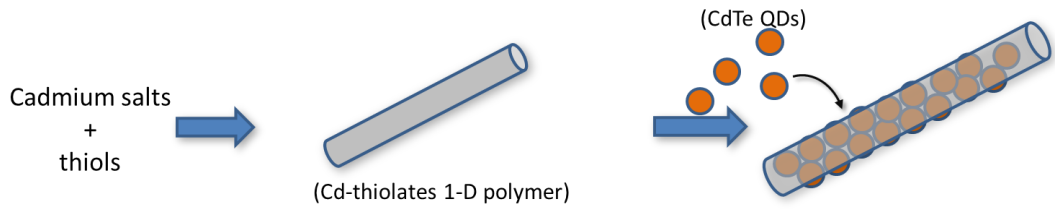

Figure 2.12. Suggested mechanism of nanorod formation after Na_2SeSO_3 addition on MUA-CdTe QDs.

Another unusual aspect was the fading from dark brown to light orange of the QDs solution after prolonged reaction. A possible explanation is "digestive ripening." Digestive ripening is one of the less common growth modes where bigger structures break into smaller fragments or are "digested." There are a limited number of reports on the digestive ripening of inorganic nanomaterials such as gold nanoparticles, PbS QDs, Co nanoparticles and CdTe QDs from our group. [120, 203-205] Additionally, Zhang *et al.* reported that a light-black solution of CdTe nanotubes turned to a light-red solution after prolonged storage. The authors checked both samples by TEM and indicated the degradation of rod-like structure into individual particles of luminescent QDs.[201]

Since the rod formation could not be seen at lower temperature (below 70 °C) during shell precursor addition, the rod formation is assumed to be a temperature dependent process (as well as concentration dependant). Therefore, we assign two driving forces - kinetics and thermodynamics - to the reaction chemistry for CdTe/CdSe/ZnSe QD synthesis. The rod formation after the first Na_2SeSO_3 addition was attributed to a kinetically driven process, whilst subsequent digestive ripening into spherical QDs was thermodynamically favoured.

2.5 Tuning the Emission Wavelength

We have explored tuning the emission wavelength further towards the red region of the spectrum (Figure 2.13). The emission peak of CdTe/CdSe/ZnSe could be further red-shifted by 57 nm by reducing the amount of MUA in the CdTe synthesis. The decreased amount of MUA on the CdTe cores possibly caused an increase in the CdSe shell formation rate and hence subsequent thicker CdSe/ZnSe shell growth on CdTe. Other variables are listed in Table 2.1. For example, addition of twice the amount of selenium precursor caused precipitation of the QDs, whilst a temperature change in shell addition from 90 °C to 70 °C caused a blue-shift in emission peak of the products. Given these results, it is arguable that the emission wavelength of the CdTe/CdSe/ZnSe QDs is highly dependent on each reaction parameter and it may be possible to synthesise QDs with emission wavelengths further into the infrared region by appropriate combinations of reaction parameters.

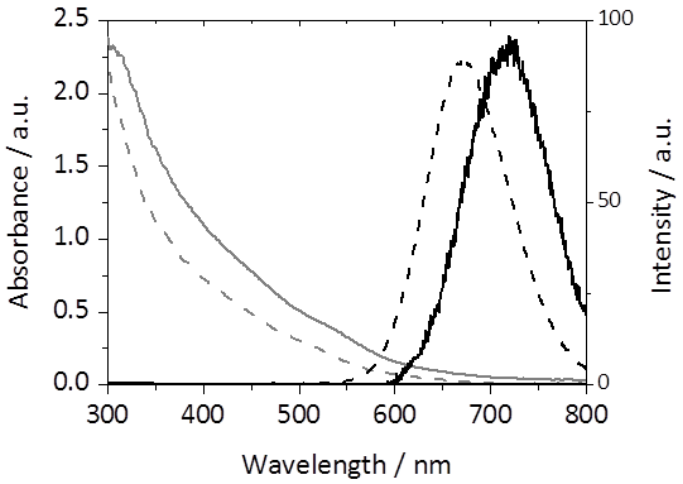

Figure 2.13. Absorption (grey lines) and emission spectra (black lines) of CdTe/CdSe/ZnSe QDs with lower MUA concentration (solid lines) and the emission of original CdTe/CdSe/ZnSe QDs (dashed lines). In the QDs with lower amounts of MUA, 21 mg (0.098 mmol) of MUA was used in the CdTe QDs synthesis, resulting in a CdTe solution where the molecular ratio of Cd and MUA was 1:1.2, instead of 1:1.5. The remaining synthetic procedure was kept the same.

Condition	Result
Increased selenium source amount	QDs precipitated
Reduced zinc source amount	QDs precipitated
High reaction temperature (90 °C → 100 °C)	QDs precipitated
Low reaction temperature (90 °C → 70 °C)	Emission blue shifted
Higher MUA amount	Emission blue shifted
Lower MUA amount	Emission red shifted

Table 2.1. Changes in reaction parameters and their results. (Detailed descriptions of reaction conditions are outlined in Chapter 6.2.6).

2.6 Synthesis of Glutathione-Capped CdTe/CdSe/ZnSe QDs

One of major factors determining the optical characteristics of QDs is the surface ligand. Although MUA has shown excellent ligand functionality for CdTe/CdSe/ZnSe QDs synthesis, a single functional group (carboxylic group) does not necessarily provide the best functionality for biological imaging applications. When one considers bioconjugation to biological molecules such as antibodies, it is preferable that a surface ligand has other functional groups. Glutathione (GSH), a short peptide comprised of three amino acids, can be used as an excellent ligand for QDs as it has a thiol moiety to bind to QD's surface and a carboxylic acid and amino group on the terminal end (Figure 2.14). The aqueous synthesis of glutathione-capped CdTe QDs (GSH-CdTe QDs) was first reported in 2007 with application in cell imaging experiments.[157] There is no report on direct aqueous synthesis of GSH capped core/shell type QDs. In the synthesis of GSH-CdTe/CdSe/ZnSe QDs, an analogous procedure was adopted by substituting MUA with GSH. The reaction temperature was maintained at 90 $^{\circ}$C and the overall reaction time was shortened to 3 hours in order to suppress Ostwald ripening.

The emission spectra are shown in Figure 2.15. The emission wavelength was clearly red-shifted, resulting in an emission peak at almost 700 nm after selenium and zinc precursor addition, as can be seen in Figure 2.15 (a) and (b). Figure 2.15 (c) shows the change in emission intensity at each reaction stage, showing the similar tendency to the MUA-capped CdTe/CdSe/ZnSe QDs in Figure 2.6 (b). It seems at first glance that the synthesis of GSH-CdTe/CdSe/ZnSe QDs was successful. However, there have been several critical issues which need to be mentioned. Firstly it was not possible to exclude the possibility of Ostwald ripening due to the higher reaction rate when using the GSH capping system. (The emission wavelength of GSH-CdTe QDs reached 630 nm after only 2.5 hours reflux.) Secondly, the resulting solution contained an insoluble grey metallic precipitate, presumably selenium or tellurium. Lastly, prepared GSH-CdTe-based materials were extremely unstable compared to MUA-capped QDs. Samples turned darker after 1 day storage under ambient condition, with emission quenching. Although further investigation would be preferable, the observed instability in GSH-capped QDs seems difficult to address, especially in our core/shell/shell system. It is, therefore, reasonable that other ligand molecules or ligand exchange should be explored to prepare functional CdTe/CdSe/ZnSe QD-bioconjugates.

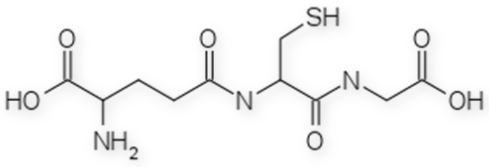

Figure 2.14. Molecular structure of glutathione (reduced form).

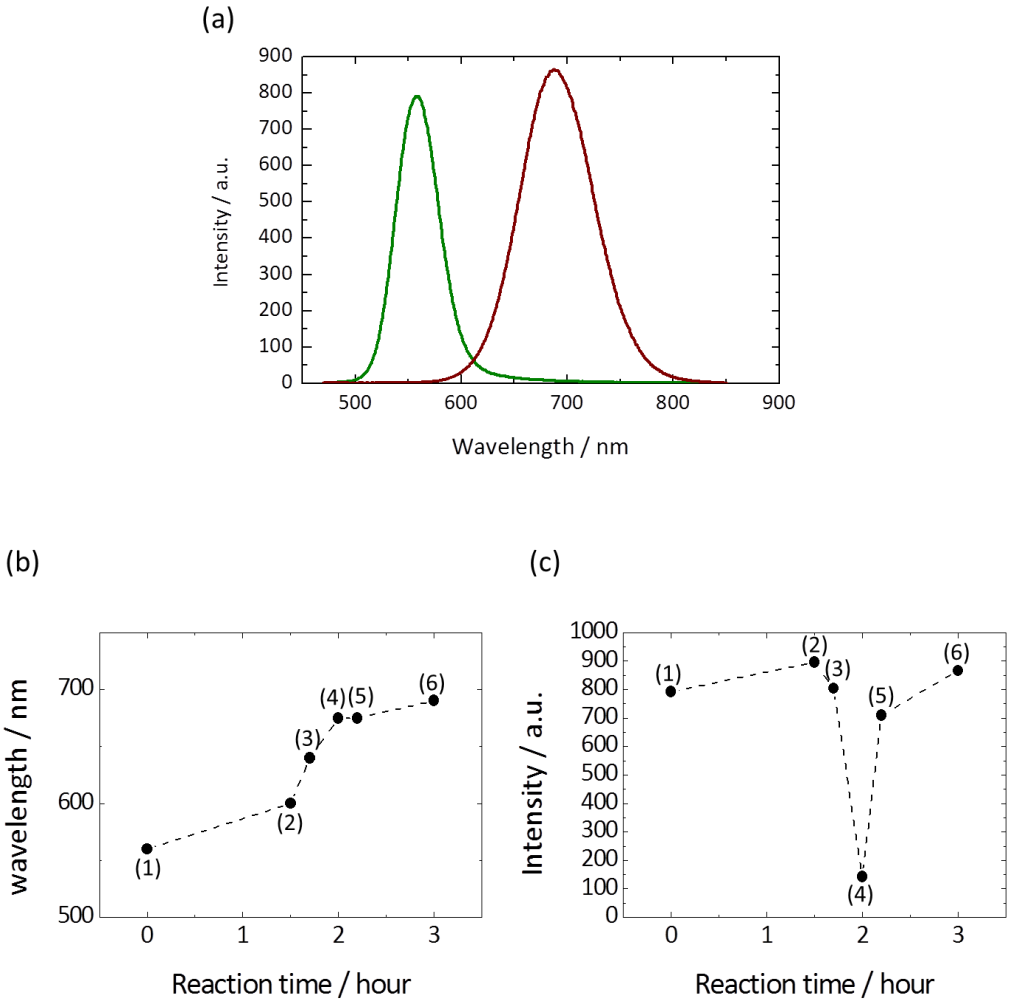

Figure 2.15. (a) Emission spectra of GSH-CdTe (green line) and the product after selenium and zinc source addition (red line). Excitation wavelength = 450 nm. (b) Emission wavelength at each reaction stage. (c) Intensity as a function of reaction time. For (b) and (c), each dot indicates 1) GSH-CdTe, 2) 1 minute after first selenium addition, 3) 20 minutes after first selenium addition, 4) 1 hour after the first selenium addition, 5) 10 minutes after zinc addition, and 6) 1 hour after the zinc addition.

2.7 Application to Deep Tissue Imaging

(This work was carried out by Dr Sarwat Rizvi at the Division of Surgery and Interventional Science, University College London.) As a "proof of concept" experiment, we injected 0.2 mL of purified QDs (Figure 2.16 (a)) subcutaneously into the hind leg of a 200 g male Wistar rat (detailed description is outlined in Chapter 6.2.7). The NIR fluorescence of the QDs was detected immediately after subcutaneous injection (Figure 2.16 (b)). Within 5 minutes, the QDs were seen migrating up lymphatic tracts (Figure 2.16 (c)) indicating that the QDs easily entered the lymphatic channels and could be imaged in deep tissue. Biological tissues are relatively transparent to light in the NIR range and as these QDs have an absorption threshold and emission in the NIR range, they can be excited and detected in deep tissues, allowing numerous possibilities for their application in biology and biomedicine. However, further investigation into their *in vitro* and *in vivo* toxicity profiles is required along with an optimisation of their optical properties prior to this application.

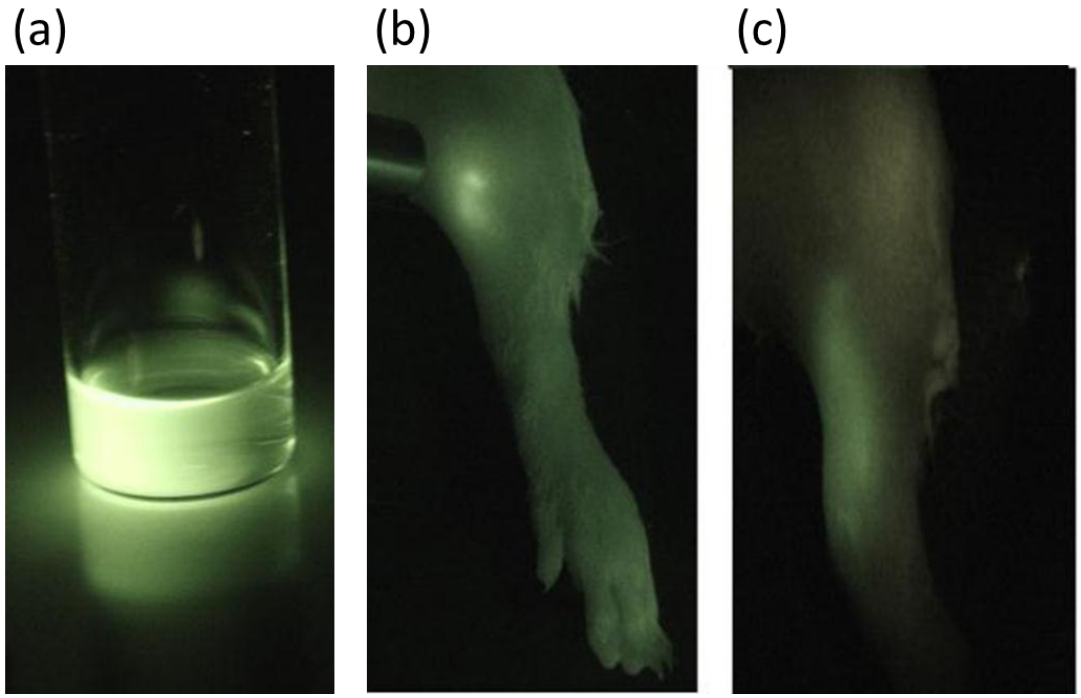

Figure 2.16. (a) The image of the MUA-capped CdTe/CdSe/ZnSe QDs solution under excitation (630 nm) as viewed through a 680 nm long pass emission filter using a charged coupled device. (b) Subcutaneous injection of the CdTe/CdSe/ZnSe QDs into the hind leg of a rat. (c) The QDs migrating to lymphatic tracts.

2.8 Conclusion

In conclusion, NIR emitting CdTe/CdSe/ZnSe QDs capped with MUA were prepared in aqueous solution using a SIPOP method. Optical measurements indicated that the shells were successfully deposited on a CdTe core, giving a substantial red-shift in the emission which was associated with type II core/shell formation. Improvement in the emission intensity was also observed after a prolonged reaction time, due to ZnSe shell formation. The resulting CdTe/CdSe/ZnSe QDs were approximately spherical crystals, consisting of 1 ML of CdSe and 2 ML of ZnSe shell. The PL QY of prepared QDs was 4.8 % for MUA-capped CdTe/CdSe/ZnSe QDs and 1.4 % for MUA-capped CdTe QDs. The reaction mechanism was studied, indicating rod formation through the polymerisation of Cd-thiolate complexes after selenium source addition, whilst the possibility of digestive ripening was suggested. Reaction conditions were modified to control optical characteristics of resulting CdTe/CdSe/ZnSe QDs. Glutathione-capped CdTe/CdSe/ZnSe QDs were explored and the difficulty associated with their use was described. The MUA-capped CdTe/CdSe/ZnSe QDs were successfully used for *in vivo* deep tissue imaging.

Chapter 3

The Room-Temperature Chemical Transformation of CdTe QDs by Reactive Cations

3.1 Introduction

A variety of synthetic techniques have emerged in the field of colloidal nanocrystals in the past decades as described in Chapter 1.3, which enabled nanomaterials to be manufactured with controlled morphologies, optical and electronic properties. In general, multiple synthetic steps are required in order to obtain materials which exhibit the desired property in the nanostructural regime. One emerging recent strategy is the post-synthetic chemical transformation, where nanocrystals, which are synthesised from established procedures such as the TOP/TOPO method or the aqueous method with thiol ligands, are defined as starting materials and are chemically transformed to designer complex nanocrystalline materials by addition of the relevant reagents or alteration of the reaction environment.[206, 207] Figure 3.1 shows several examples of the chemical transformations of nanomaterials, highlighting a variety of changes in conformation. An obvious advantage of using a nanomaterial over bulk materials in chemical transformations is the high surface-to-volume ratio. As most of the chemical reactions proceed on a surface or at an interface, the high surface-to-volume ratio in nanomaterials can make the transformation easier and quicker than in bulk alternatives. For example, the chemical conversion to Ag_2Se from 4.2 nm CdSe QDs was achieved rapidly ($\ll$1 second), whereas comparable reaction using ZnS wires of ~200 nm diameter took up to 17 hours.[106, 208] These observations clearly support the observation that the reaction rate can be substantially shortened in the nanosize regime and nanoscale chemical transformation is an effective strategy to design innovative materials.

Regardless of the techniques used in the nanoscale chemical transformation, the quality of starting nanomaterial is thought to be an essential factor deciding the successfulness of subsequent chemical transformation. Therefore, nanomaterials with an established synthetic methodology are routinely chosen for the starting materials. In all examples depicted in Figure 3.1, the complex chemistry was made possible by the accumulation of the synthetic knowledge of almost all families of metal/semiconducting systems specifically in a form of colloid;[27, 28, 62, 63] the synthesis and shape control of nanomaterials, such as gold, silver and cadmium selenide are advanced enough that one could reproducibly prepare them with ease, as precursors for further reactions. The nanomaterials synthesised in nanoscale chemical transformations have already been utilised in some areas such as electronics,[209] photonic devices,[210] sensors[211] and photovoltaics,[136, 138] whilst there is a wealth of underlying chemistry yet to be understood.

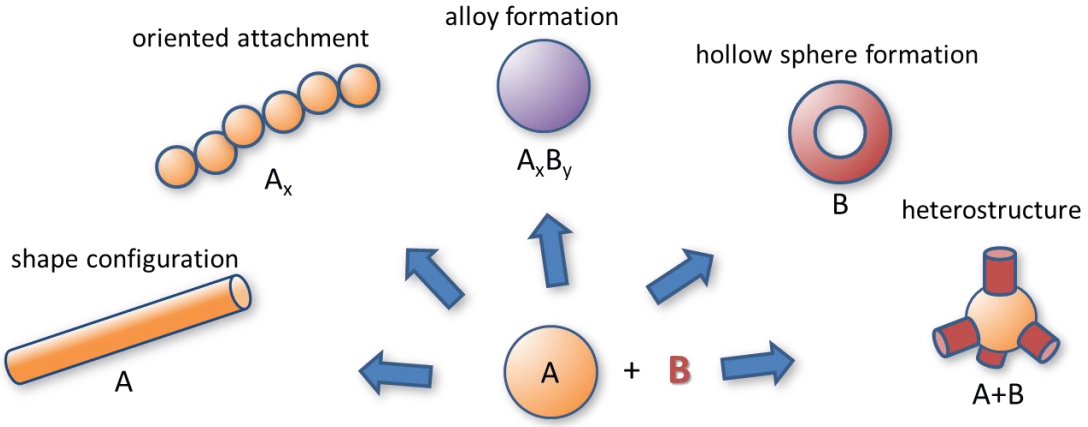

Figure 3.1. Schematic diagram of post-synthetic chemical transformations of nanomaterials. The chemical transformations can be successfully controlled by the careful choice of starting materials, additives and reaction conditions.

Despite the number of methodologies in nanoscale chemical transformations, studies exploring the role of redox potentials have not been reported. The colloidal solution system, particularly in metal/semiconductor nanocrystals, is thought to exhibit a highly complex electrochemical nature due to the quantised energy states depending on the crystal size, the high surface-to-volume ratio of the nanocrystals, and the contribution of surfactant molecules. Also, there is currently a lack of theoretical understanding in this

nanosize regime (e.g. many reports assume the nanocrystals are isotropic in shape, but in reality the nanocrystals exist as a form of polyhedron). The study presented in this chapter regards the chemical transformations in preformed nanoparticles as explained by redox potentials which can be explored further leading to new and innovative designer structures. Previous reports from our group have shown the reactive nature of mercury cations in HgE QDs (E = S, Se, Te) synthesis and suggested that room-temperature preparation of HgE QDs can be explained by redox potentials.[197, 212, 213] In this chapter, the knowledge obtained from these studies has been utilised for post-synthetic particle growth. In particular, CdTe QDs were reacted with mercury cations to result in distinctly anisotropic structures. Subsequently, several analogous nanocrystals and different metal cations were used as starting materials, and the influence of redox potential on nanocrystal was systematically examined.

Finally, it is noteworthy to mention the impact of research regarding cation exchange reactions, which is comparable to this work. Cation exchange reactions, as introduced in Chapter 1.3, is one of the emerging synthetic techniques in nanoscience and can potentially overcome the difficulty in preparing complex and monodispersed nanomaterials. As the cation exchange reaction retains the structure of starting parent material, several nanomaterials which were previously impossible to synthesise have been reported.[106, 108, 110, 214]

3.2 Molecular Welding Effect on CdHgTe Synthesis

For this study, CdTe QDs were chosen as a starting material. CdTe QDs are routinely prepared with a highly monodispersed size distribution and have a tuneable emission wavelength with high quantum efficiencies, in addition to solubility in various solvents. Furthermore, a number of studies have been reported on the shape-controlled synthesis of CdTe, from spherical particles to rods, wires and branched shapes.[83, 92, 149] Additionally, the small energy differences between polytypes are important to produce a variety of CdTe nanocrystals with different shapes.[83, 215] Therefore, CdTe is an ideal candidate for studies into the chemical transformations of nanomaterials.[149, 156, 216] There are several recent reports which describe the use of CdTe nanocrystals to create functional nanomaterials. Post-synthetic modification of TGA-capped CdTe QDs caused an aggregation of particles and produced wire-like structures keeping their emissive characteristics,[88, 171] whilst CdTe nanocrystals were used as seeds to deposit

CdSe or CdS, leading to branched topologies or elongated shapes for potential use in optoelectronic devices and photovoltaics.[92, 95, 97]

The basic synthetic procedure in this work stemmed from the report describing the cation exchange reactions of colloidal QDs (detailed procedure can be found in Chapter 6.3.1 and Chapter 6.3.6).[107] First, tetradecylphosphonic acid (TDPA)/hexadecylamine (HDA) capped CdTe QDs (4.5 ± 0.9 nm) in toluene were used as starting materials.[153] To a vigorously stirred $HgBr_2$ toluene/methanol solution, the CdTe solution was swiftly injected, causing an immediate precipitation with a change in colour from yellow to brown. The resulting precipitate was collected by centrifugation and readily re-dispersed in toluene (Figure 3.2).

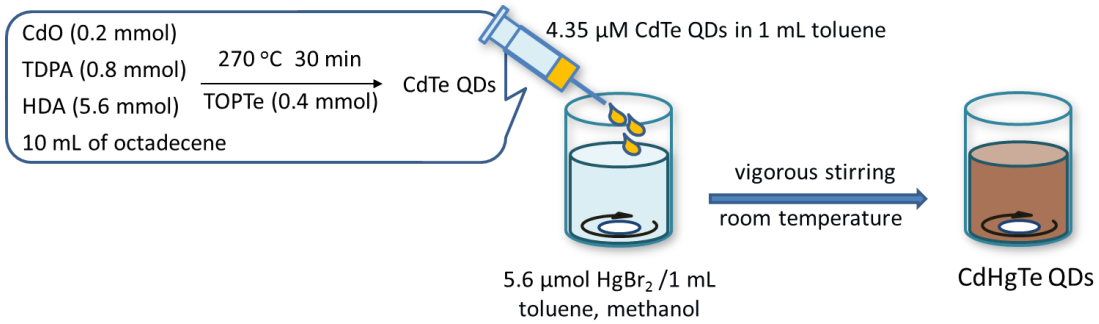

Figure 3.2. Illustrated reaction scheme for the synthesis of CdHgTe nanoalloys.

From TEM investigations, nearly monodispersed spherical CdTe QDs were found to form randomly directed, wire-like structures, as can be seen in Figure 3.3 (a) and (b). Most of the anisotropic particles were elongated or connected to a neighbouring structure to form a complex material, whilst few apparently original CdTe QDs (in terms of size and shape) were observed. High resolution TEM (Figure (c) and (d)) confirmed each crystalline entity was completely linked with another, whilst the overall anisotropic particles showed several crystalline orientations with different directions in lattice fringes, suggesting that several individual particles were attached regardless of their crystalline axis. The high resolution TEM measurement was carried out by Dr Teck Lim at the Department of Materials, University of Oxford.

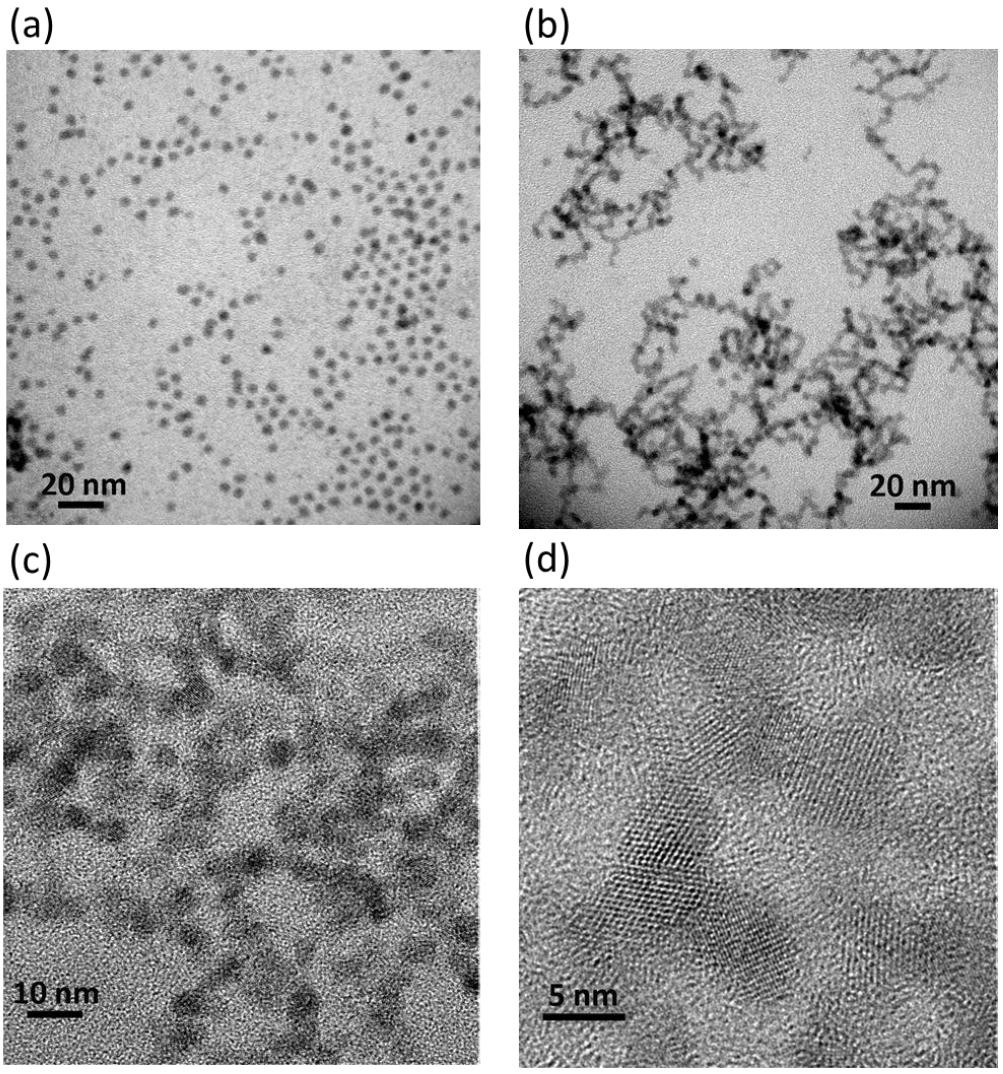

Figure 3.3. TEM image of (a) CdTe QDs (diameter 4.5 ± 0.9 nm). (b) CdHgTe nanoparticles after the reaction with mercury bromide. (c,d) High resolution TEM images of CdHgTe nanorods.

Figure 3.4 shows X-ray diffraction (XRD) analysis of the particles before and after the reaction. A previous report from Smith *et al.* suggested CdTe QDs prepared under similar reaction conditions to this work showed a zinc blende structure, and is in good agreement with the XRD pattern of CdTe QDs presented here, indicating the successful formation of zinc blende CdTe QDs. Despite the almost identical lattice parameter in CdTe and HgTe (0.648 nm in CdTe; 0.646 nm in HgTe (cubic)), the diffraction pattern after mercury bromide addition showed a shift in the reflection at ~25° (2θ) to a smaller angle, consistent with an increase in lattice parameter and in agreement with Vergard's law, which suggested the participation of the relatively larger mercury atoms into the

structure and thus an alloyed composition.[217] This demonstrated a change in the solid state material whilst maintaining the overall cubic crystal structure. Similar effects have been observed in ZnCdS alloyed nanoparticles.[100]

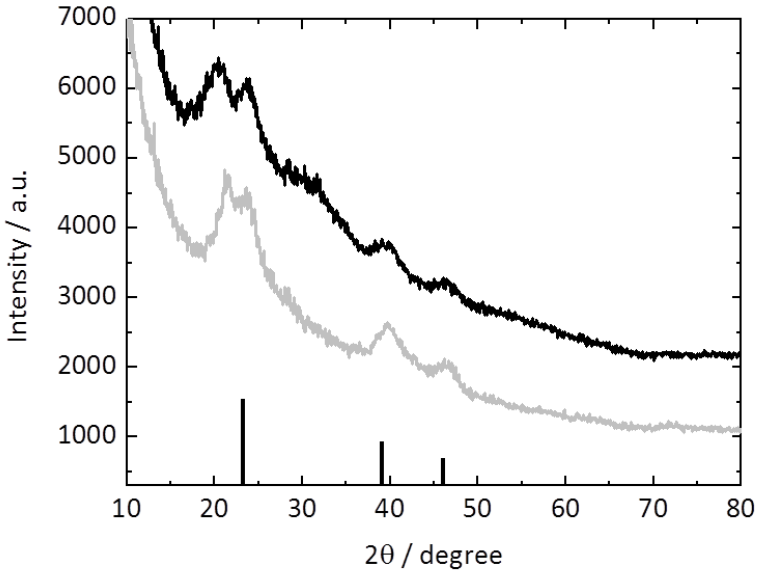

Figure 3.4.XRD patterns for CdTe QDs (grey line) and CdHgTe nanoalloys (black line). Millar indices for zinc blende CdTe and zinc blende HgTe referred from other papers are shown below.[152, 218]

Analysis using inductively coupled plasma-mass spectrometry (ICP-MS) showed significant mercury content after the reaction (Cd: 63.3 %, Hg: 19.8 %, Te: 16.9 %), equivalent to $Cd_{3.7}Hg_{1.2}Te_{1.0}$. (The ICP-MS work was conducted by Andrew Cakebread and Roger Tye in the Mass Spectrometry Facility, King's College London.)

The average width of the elongated structure in Figure 3.3 (b) was 3.9 ± 0.8 nm, which was consistent with the hypothesis that the resulting structures were predominantly based on CdTe QDs. To elucidate the mechanism of the heterostructure formation from CdTe QDs, the reactive nature of the mercury cation (a relatively soft acid and strong oxidising agent) has been focused on. In this work, it is suggested that a partial cation exchange reaction from CdTe to HgTe proceeded under the hard soft acid base (HSAB) theory. In the CdTe solution, Cd^{2+} is regarded as a relatively hard acid when compared to monovalent metal ions or ions with larger ionic radii (e.g. Ag^{+}, Hg^{2+} and Pb^{2+}).

Therefore, the Cd^{2+} would be preferably exchanged with Hg^{2+} using methanol (MeOH), a hard base, which binds strongly with Cd^{2+} instead of Hg^{2+}, leading the cation exchange from CdTe to HgTe. Indeed, as discussed earlier, some notable reports on the synthesis of Ag_2Se, Cu_2Se, Cu_2S and PbS nanocrystals using an analogous methodology were based on the same theory.[106-108, 110] It is, therefore, probable that in our case, displaced Cd^{2+} was dissolved into the MeOH, whilst Hg^{2+} was incorporated partially into the particle to form CdHgTe.

It is also necessary to explore the strong oxidising nature of the Hg^{2+} ion, which has a positive redox potential, and the effect such species could have on the surface chemistry of the CdTe QDs, unlike other metal species commonly used in QDs synthesis (cadmium, zinc and lead) which have negative redox potentials. Previous reports from our group into the remarkably rapid growth of HgSe QDs and the difficulty in shape control proposed that the difference was possibly explained by redox potential of Hg^{2+},[197, 213] where the standard electrode potential, E^0, for $Hg^{2+} + 2e^- \rightarrow Hg$ is +0.85 V, in contrast, E^0 for $Cd^{2+} + 2e^- \rightarrow Cd$ is -0.40 V. Another possibility is that a surfactant molecule reduced the mercury cation from Hg^{2+} to [Hg^0], a key step in the reaction mechanism which led to the rapid growth and difficult controllability. The positive redox potential means $Hg^{2+} + 2e^- \rightarrow Hg$ is favoured and rapid, unlike the reduction of other metal species.

Given the similarity in the reaction conditions and the environment surrounding the QDs, surfactant molecules (TDPA, HDA and TOP) could reduce Hg^{2+} to provide elemental Hg or provide Hg-Te bonds through a dangling bond on the CdTe surface. The possibility of a phosphine being a reducing agent was firstly indicated in the synthesis of PbSe nanocrystals and subsequently examined in other II-VI nanocrystals (e.g. CdSe, HgSe and HgS) by several groups.[197, 213, 219, 220] In the synthesis of CdHgTe nanoalloys presented in this work, however, there are several important differences from these reports; (i) phosphonic acid was used as a ligand instead of carboxylic acid, (ii) TOPTe would not exist as a monomer in the CdTe QDs solution after purification. Despite these differences, we assume that phosphonic acid exhibits an analogous reactivity to a carboxylic acid. Also, a certain amount of the TOPTe species should exist on the surface of CdTe *via* the coordination of TOP on the chalcogen site as suggested in several reports.[63, 66, 67] Whilst referring to reports on other II-VI QDs, as well as noting the positive redox potential of the mercury cation, a reaction mechanism for Hg-Te formation on the CdTe surface is proposed (Equation 3.1).[197, 219, 220] Negative

charged TDPA readily coordinates to the mercury cation, followed by formation of $(TDPA)_2$-Hg-Te-TOP intermediate. Subsequently, the phosphorus in TOP undergoes a nucleophilic attack by an anionic counterpart of phosphonic acid, yielding TOPO and an anhydride of TDPA. As a result, a Hg-Te bond is formed.

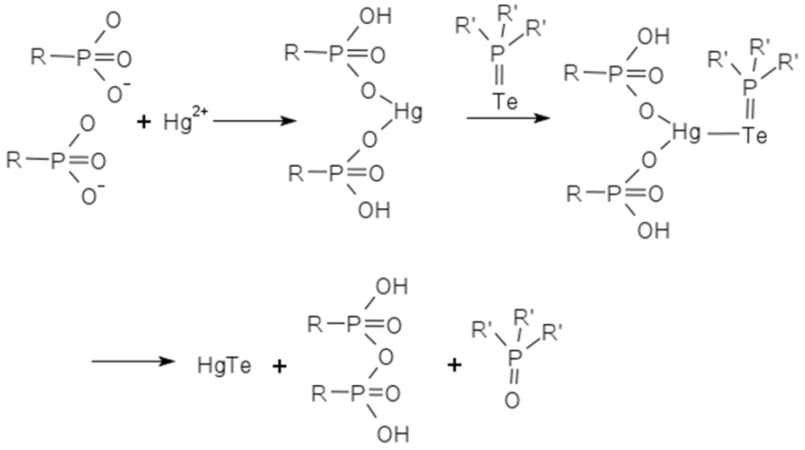

Equation 3.1. Proposed reaction mechanism of HgTe formation on the surface of CdTe. ($R = C_{14}H_{29}$, $R' = C_8H_{17}$.)

Another suggested mechanism involves the reduction of the Hg^{2+}, or the oxidation of surfactant molecules, which can yield [Hg^0]. The elemental mercury may then react with a Te species on the nanoparticle surface to give the alloy. It is envisaged that this could lead to the particles "welding" together, as the alloy forms while the deactivated surfactants would separate from the nanoparticle surface. Steckel *et al.* studied the reduction of the lead cation in PbSe QDs formation, whilst Howes *et al.* extended the theory in order to understand the high reactivity of a mercury salt in the synthesis of HgSe QDs.[197, 219] Both groups suggested that the oxidation of TOP and carboxylic acid to form the anhydride is a key reaction for the reduction of metal cations. Using phosphonic acid and TOP, the reduction of the mercury cation can be explained as follows (Equation 3.2):

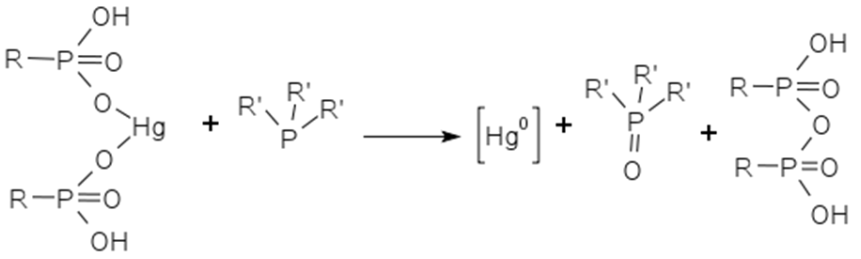

$[Hg^0]$ + Te·····Cd·····Te ⟶ Hg·····Te·····Cd·····Te

Equation 3.2. Reduction of Hg^{2+} by phosphonic acids and TOP and reaction of $[Hg^0]$ with surface Te. (R = $C_{14}H_{29}$, R' = C_8H_{17})

However, it is reasonable to assume that the reaction proceeded without TOP, which is excluded from the solution after the purification of CdTe QDs, although it is on the QD surface, and surfaces are known to be labile. Therefore, we suggest an alternative route of the Hg^{2+} reduction using methanol as a reducing agent instead of TOP (Equation 3.3).

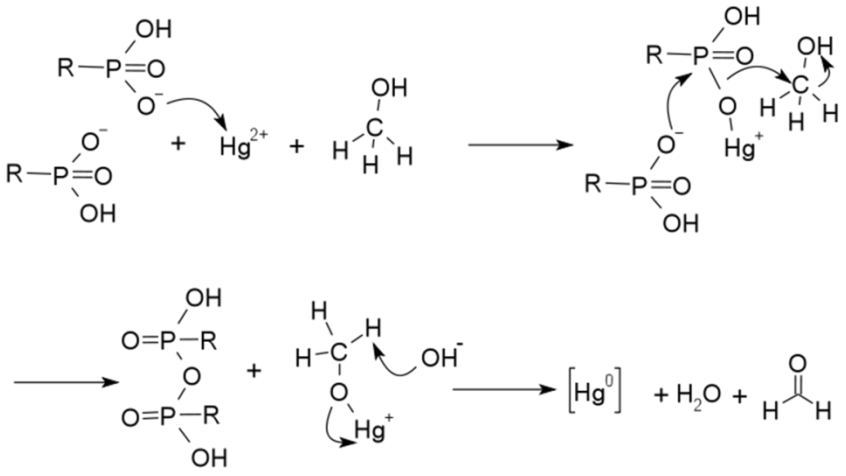

Equation 3.3. Reduction of Hg^{2+} using methanol and phosphonic acid as reducing agents. R = $C_{14}H_{29}$.

As there is clearly cadmium still present in the final anisotropic nanomaterial as confirmed by mass spectrometry, it is proposed that this is a surface phenomenon, which corresponded with the TEM observation that the final anisotropic CdHgTe structures were slightly narrower than the diameter of the parent CdTe particles; CdTe QDs acted as a donor material in the reaction with mercury, causing a partial digestion

of CdTe QDs and the formation of HgTe-like species on the surface. The resulting HgTe then acted to "weld" surrounding particles together, leading to a series of anisotropic CdHgTe alloy structures. Figure 3.5 shows the schematic diagram of the molecular welding reaction of CdTe QDs with mercury cations.

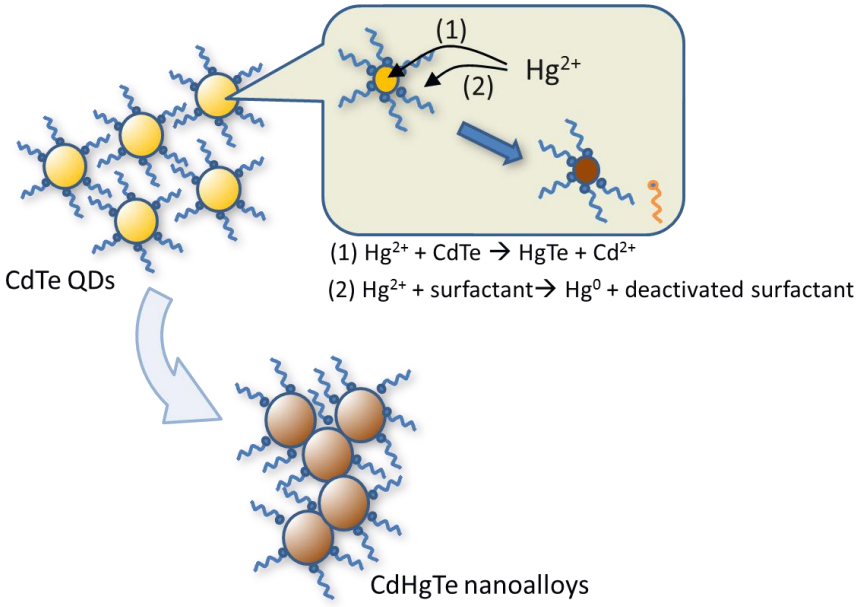

Figure 3.5. Schematic diagram of the molecular welding effect of CdTe QDs with Hg^{2+}. It is suggested that the mercury cations reacted with the CdTe in two ways: (1) cation exchange reactions and (2) reduction of the Hg^{2+} by surfactant molecules.

3.3 Optical Characterisation

Figure 3.6 (a) shows the absorption spectra of CdTe QDs and CdHgTe alloyed nanoparticles after $HgBr_2$ addition. An excitonic peak at 620 nm is clearly observed in the starting CdTe QDs, whilst the CdHgTe product exhibited a notable excitonic peak at 780 nm. Whilst referring to the red-shift in the absorption peak, one might take into account the effect of particles aggregation or rod formation. When considering the optical red-shift in QDs, Gaponik *et al.* and Chen *et al.* reported 3D nanostructures where water-soluble CdTe nanoparticles aggregated, exhibiting a solid-like material.[170, 171] According to the reports, the optical characteristics of the original CdTe and CdTe self-assembly showed similar optical features with a slight broadening of the excitonic

peak shape in the case of the assembly. An optical red-shift can also be observed when highly anisotropic CdTe nanocrystals are formed, although not as significant as the shift reported in this work. For example, CdTe nanorods (<10 nm width and 40 nm length) have an excitonic peak at 715 nm and CdTe tetrapods (<10 nm core and <50 nm arms) have the peak at 730 nm. It should be mentioned that the resulting heterostructures from our work had a profoundly small width (< 5nm).[83, 221] It is likely, therefore, that the large red-shift in the absorption peak in our heterostructure was caused by mercury incorporation and hence alloy formation rather than by simple aggregation of CdTe nanoparticles. Indeed, alloyed CdHgTe nanocrystals synthesised *via* aqueous routes were reported to have absorption peak around 800 nm,[172, 183] whereas Smith *et al.* showed CdHgTe QDs in chloroform with a significant excitonic peak from 550 nm to 900 nm, depending on reaction conditions, which were in good agreement with our CdHgTe particles.[222] The red-shift in absorption spectra could be visually observed as the solution colour changed from the original yellow to dark brown immediately after the mercury cation addition (Figure 3.7).

The emission spectra are shown in Figure 3.6 (b). The original CdTe solution exhibited strong narrow band edge emission, whereas the CdHgTe nanostructures displayed weak (<1% quantum yield) red-shifted band edge emission whose shape was slightly broadened. Additionally, it should be mentioned that the emission profile from this work would exclude the possibility of the trap emission of CdTe nanocrystals, which is typically much broader and generally located around 100 nm red-shifted from the original band edge emission.[223] Again, the emission profile was consistent with previously reported CdHgTe nanoparticles.[183, 222]

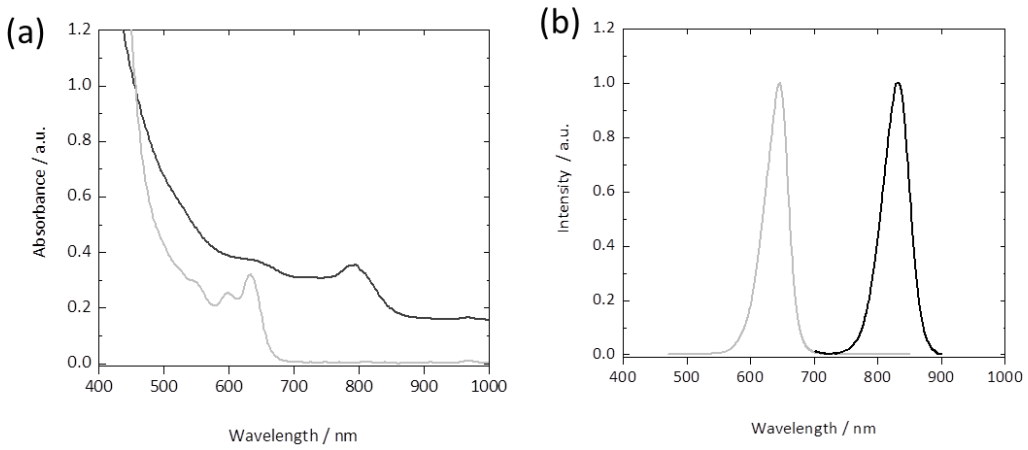

Figure 3.6. (a) Absorption spectra of CdTe QDs (grey) and CdHgTe nanoparticles (black). (b) Normalized emission spectra of CdTe QDs and CdHgTe nanoparticles (excitation wavelength = 450 nm for CdTe, 500 nm for CdHgTe).

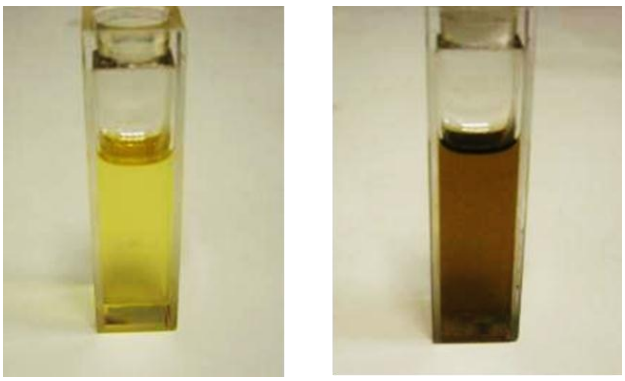

Figure 3.7. Pictures of CdTe QDs and CdHgTe nanoparticles in toluene.

3.4 Influences on Redox Potential of Metal Cations

Whilst observing the nanoscale chemical transformations, the reactive natures of mercury cation - the relative softness and positive redox potential - have been mentioned. Figure 3.8 (a) shows a list of standard redox potentials of metal cations commonly used for nanomaterials synthesis. Metal cations such as Cd^{2+}, Pb^{2+} and Zn^{2+} have a more negative redox potential than Hg^{2+}, and they can be regarded as less reactive oxidising agents. Hence, they are less likely to react with the surfactants at room-temperature, which was subsequently followed by the reaction with CdTe

nanoparticles. To investigate the possibility that these transformations were driven by the positive redox potential of the mercury cation, the addition of other metal cations to CdTe with analogous condition (Pb^{2+}, Cd^{2+}, Zn^{2+}, Ag^{+} and Au^{3+}) was explored in order to see the difference in the electronic and optical properties of the resulting materials (Figure 3.9). Addition of the Pb^{2+}, Cd^{2+} and Zn^{2+} cations enhanced the emission spectra but did not change the position of either the emission or absorption spectra, unlike the addition of Hg^{2+} as shown in Figure 3.6. The result suggested that a coordination of the Pb^{2+}, Cd^{2+} or Zn^{2+} to the particle surface occurred but no further change in internal electronic structure, whilst it is predictable that Cd^{2+} addition essentially does not cause any spectral shift – the cadmium cation was added simply to provide a baseline for a series of cation additions. Notably, if an alloyed CdZnTe, or pure ZnTe had formed, significant blue shift should be expected, which was not observed.

Also, it should be noted that mercury cation has other redox modes which involve Hg(II) → Hg(I) and Hg(I) → Hg(0) as indicated in Figure 3.8 (a). As all the redox potentials for the mercury cation have relatively positive redox potential (+0.8 to 0.85 V), we used the redox reaction of Hg(II) → Hg^{0} (described as "Hg^{2+}/Hg" in Figure 3.8) as a representative redox reaction for the mercury in this work, for the simplicity.

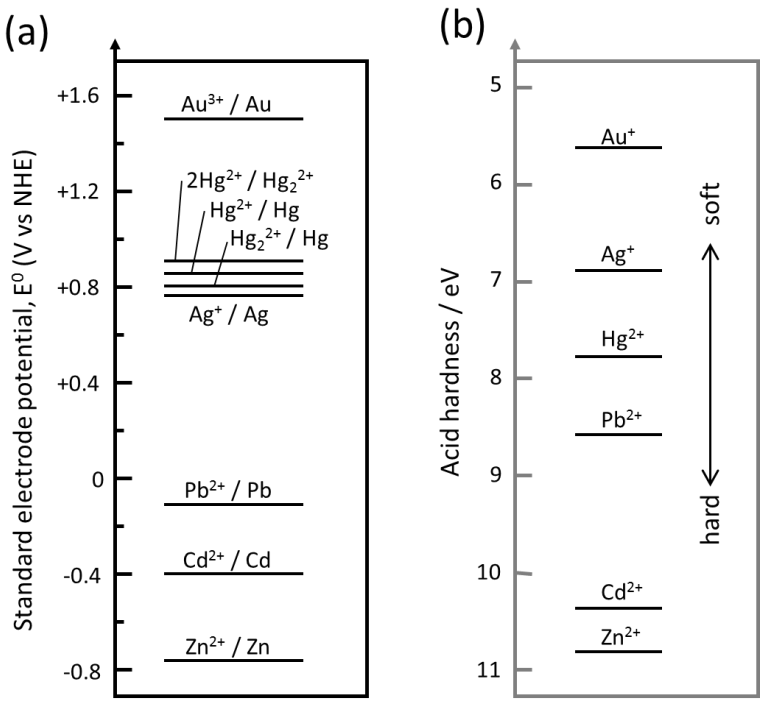

Figure 3.8. (a) Standard electrode potential and (b) acid hardness of metal cations. Values of acid hardness in each metal cation were obtained from previously reported literature.[198]

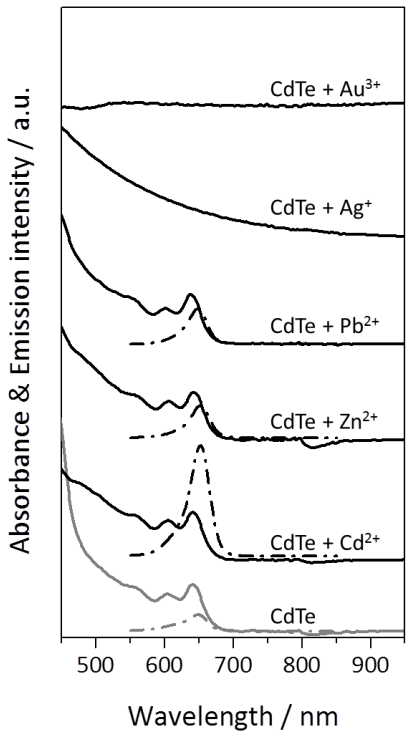

Figure 3.9. Absorption and emission spectra of CdTe QDs reacted with some metal cations in the same manner as CdTe QDs with Hg^{2+} (a). Solid curves represent absorption spectra, whilst dashed curves represent emission spectra (emission was not observed for the products of the reaction with Ag^{+} and Au^{3+}). Excitation wavelength = 450 nm.

Addition of the Ag^{+} and Au^{3+} which have positive redox potentials, however, resulted in a drastic change in the spectra, leaving no trace of the original excitonic peak of CdTe QDs, whilst all measurable emission was quenched from both materials. The structural configuration was then examined after the reaction CdTe QDs with either Ag^{+} or Au^{3+}. Figure 3.10 (a) shows CdTe after Ag^{+} addition, maintaining a spherical morphology (diameter of 6.0 ± 1.2 nm), which was a slight enlargement when compared to the original CdTe QDs. The product resulting from Ag^{+} addition was identified as Ag_2Te nanoparticles as confirmed by XRD (Figure 3.10 (b)). The absorption spectrum shown in Figure 3.9 was also similar to the previous report of cation exchange reactions using CdSe QDs and silver cation to produce Ag_2Se nanoparticles,[106] and was consistent with the absorption profile of Ag_2Te nanoparticles prepared from other routes.[224]

Au^{3+} addition to CdTe QDs resulted in an immediate formation of poorly soluble black material and this was reflected in the absorption profile, which was a featureless curve with absorbance throughout the measured spectrum range (Figure 3.9). The electron

micrograph showed a complex anisotropic nanostructure whose minimum dimension (<15 nm) was considerably larger than the original CdTe QDs (Figure 3.11 (a)). A similar morphology has been observed with gold nanowire capped with adenosine in aqueous solution.[225] Additionally, XRD studies identified the product primarily as elemental gold, as shown in Figure 3.11 (b). These results clearly indicated that the chemical, optical and structural properties of the reaction product from CdTe QDs and extraneous metal cations are dependent on the reactivity, in this case redox potential, of the different cation species added.

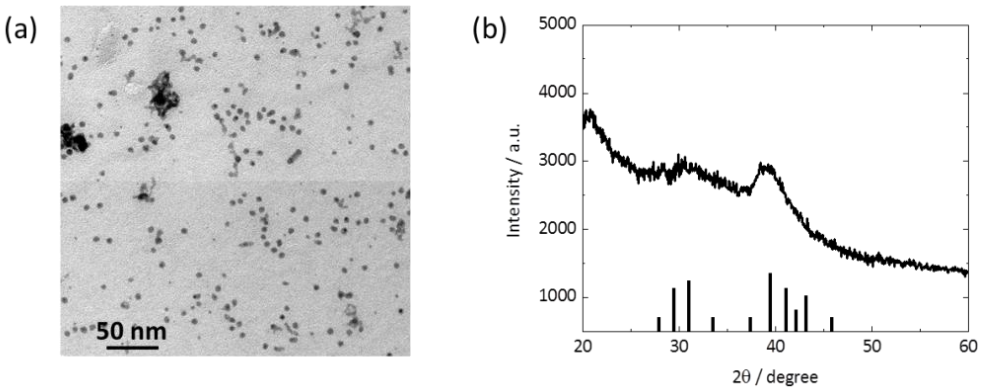

Figure 3.10. (a) TEM images of the products from the reaction of CdTe QDs and silver(I) cations. (b) X-ray diffraction pattern of the resulting nanoparticles. Miller indices for monoclinic Ag_2Te were shown below.

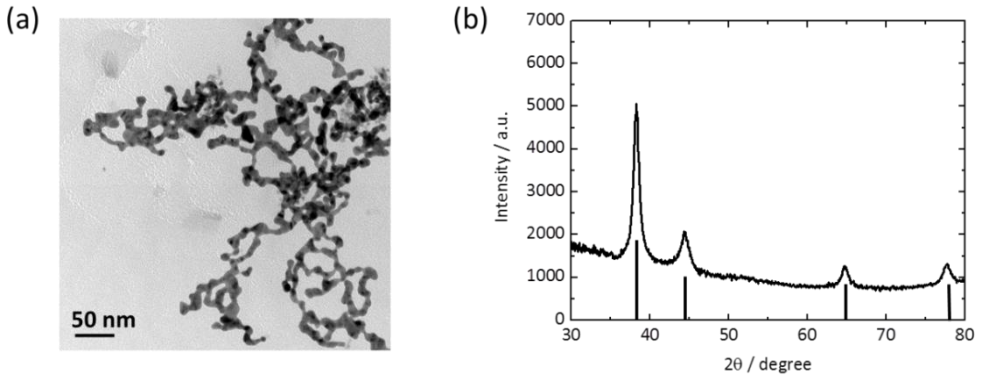

Figure 3.11. (a) TEM images of the products from the reaction of CdTe QDs and gold (III) cations. (b) XRD pattern of the resulting nanostructures. Miller indices for elemental gold (fcc) were shown below.

Interpretation from Redox Potential and HSAB theory

The redox potential theory is also supported by observations in other reports that gold tips could be grown on CdSe nanorods at room-temperature ($Au^{3+} + 3e^- \rightarrow Au$ is +1.52 V),[93] whilst the transformations of CdS to Cu_2S was also rapid at room-temperature ($Cu^{2+} + 2e^- \rightarrow Cu$ is +0.34 V).[107, 108] In contrast, depositing PbSe tips on CdSe rods required mild heating due to Pb^{2+} having a relatively negative redox potential as can be seen in Figure 3.8 (a).[96] In this work, the synthetic methodology of CdHgTe nanoalloys was inspired from the cation exchange reaction of CdS nanorods dispersed in toluene to Cu_2S nanorods (within a second) using a copper salt in methanol. Likewise, the reaction system in this study involved toluene/methanol solution as a parent solution but using mercury bromide as an additive. The cation exchange reaction required vigorous stirring and an excess of mercury species relative to the CdTe QDs. Indeed, alternative methods such as stepwise addition of a methanolic mercury bromide solution into a CdTe QDs/toluene solution caused precipitation without any optical red-shift (Figure 3.12). It is suggested that stepwise addition of Hg^{2+} introduced only a small amount of the reagent to the CdTe QDs, which reacted with only the surfactant molecules instead of the CdTe itself, resulting in the subsequent aggregation due to a lack of surfactants. The resulting solution did not show any spectral shifting as the mercury cations were not incorporated into the particle's solid state structure.

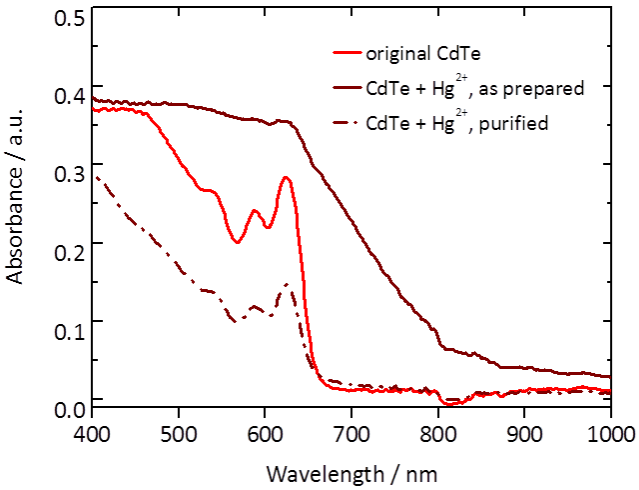

Figure 3.12. Change in absorption spectra of CdTe QDs with stepwise addition of mercury stock solution followed by purification.

One of the most useful theories in cation exchange reactions is the hard soft acid base (HSAB) theory, in which harder acids preferentially bind with harder bases and *vice versa*, as shown in Figure 1.11. Also, the acid hardness of some metal cations is listed in Figure 3.8 (b). CdHgTe formation in this work can also be explained by such a hypothesis; Cd^{2+} is a harder acid than Hg^{2+} and in the solution containing methanol, the Hg^{2+} preferably binds to the Te component of the QDs, whilst Cd^{2+} tends to replace the Hg^{2+} and binds to the harder base, methanol. One problem in this theory, however, is that Hg^{2+} and Pb^{2+} have an almost similar hardness from Figure 3.8 (b) and one should expect, therefore, that Pb^{2+} when reacted with CdTe QDs would yield either PbTe or CdPbTe alloy particles in a similar manner to Hg^{2+} addition. From a redox potential viewpoint, however, Hg^{2+} and Pb^{2+} are significantly different (Figure 3.8 (a)). Whilst the addition of Hg^{2+} had a distinct effect, the addition of Pb^{2+} did not appear to shift the absorption of emission spectra as one might expect. Apart from the redox potential, it is possible to explain that the low solubility of PbTe in CdTe may hinder alloy formation.

The change in conformation after Ag^{+} and Au^{3+} cation addition can also be explained through redox potentials. Also, the conversion products might be affected by redox potential; the Au^{3+} addition (which has a more positive redox potential than either Ag^{+} or Hg^{2+}) resulted in materials mostly consisting of elemental gold. Mercury or silver cation addition did not cause total conversion to elemental mercury or silver, and instead resulted in an alloyed or compound structure or partial substitution in the composition.

3.5 Application to Other Nanomaterials

3.5.1 CdSe QDs

The redox potential-driven nanoscale chemical transformations have been discussed so far with CdTe QDs and some metal cations. To further investigate whether the conformational evolution triggered by the metal cations addition was an intrinsic feature for CdTe QDs capped with TDPA and HDA, a similar quantum dot system (stearic acid/octadecylamine-capped CdSe QDs) was synthesised and reacted with mercury cations in the same manner (synthetic procedure is stated in Chapter 6.3.2). Figure 3.13 (a) shows electron micrographs of monodispersed CdSe QDs (4.0 ± 0.6 nm) showing a

similar morphology to CdTe QDs. The micrograph after mercury cation addition, however, showed less obvious inter-particle connectivity, although each particle appeared to be attached to some extent from TEM images (Figure 3.13 (b) and (c)). Although several factors such as different surfactants, crystal structure and chalcogen ions need to be taken into account, it is possible that the mercury cation had a distinctive influence on the morphology of CdSe QDs and the molecular welding effect appeared to be applicable to other colloidal QDs with similar surface environments.

Figure 3.14 shows absorption and emission spectra of the CdSe QDs before and after mercury salt addition, displaying the similar trend with CdTe QDs, in terms of absorption spectrum, where the excitonic peak and band edge in CdSe at 560 nm were broadened and red-shifted with a resulting excitonic peak at 660 nm. The emission peak which originated from CdSe QDs was almost completely quenched, and no significant emission was observed after mercury cation addition. Although little research has been done for the optical properties of CdHgSe nanoparticles to the best of our knowledge, $Cd_{1-x}Hg_xSe$ thin films (x = 0.3) were reported to show red-shifted absorption thresholds compared to pure CdSe thin films, which is consistent with the results in this work.[226] An additional systematic examination of the particle diameter and absorption peaks in the quantum dots provided by Yu *et al.* strongly suggested that the possibility of simple CdSe QDs having an absorption peak at 660 nm without any drastic size change was unlikely.[148] Anisotropic CdSe nanorods, however, were known to have an absorption peak around 660 nm depending on their dimension (e.g. 25.7 nm × 5.7 nm rods).[84] Given the result from the micrograph, spectra, and the similarity to the case of CdHgTe formation described above, it is reasonable that the resulting optical change was caused by mercury cation addition rather than by CdSe-only morphological transformation. Hence, it is possible to refer to the resulting materials as CdHgSe nanoalloys.

The XRD pattern for CdSe QDs are clearly assigned to wurtzite (hexagonal) CdSe and no distinct change can be observed after mercury cation addition (Figure 3.15). Importantly, most of the reflections for zinc blende HgSe are consistent with wurtzite CdSe, which presents a difficulty in analysing the crystal structure of the resulting CdHgSe nanoalloys. Also, the empirical formula of CdHgSe nanoalloys obtained by ICP-MS was $Cd_{1.00}Hg_{0.03}Se_{0.91}$. The result indicated that less than 3% of the original CdSe particles was doped with mercury and was consistent with the XRD results, where no drastic change in diffraction peaks were observed. In terms of optical spectra, however, a small amount of mercury can lead to substantial red-shifts in optical

characteristics as Qian *et al.* observed in CdHgTe alloys, in which a 5% inclusion of mercury in CdTe QDs caused more than a 100 nm red-shift in emission.[183]

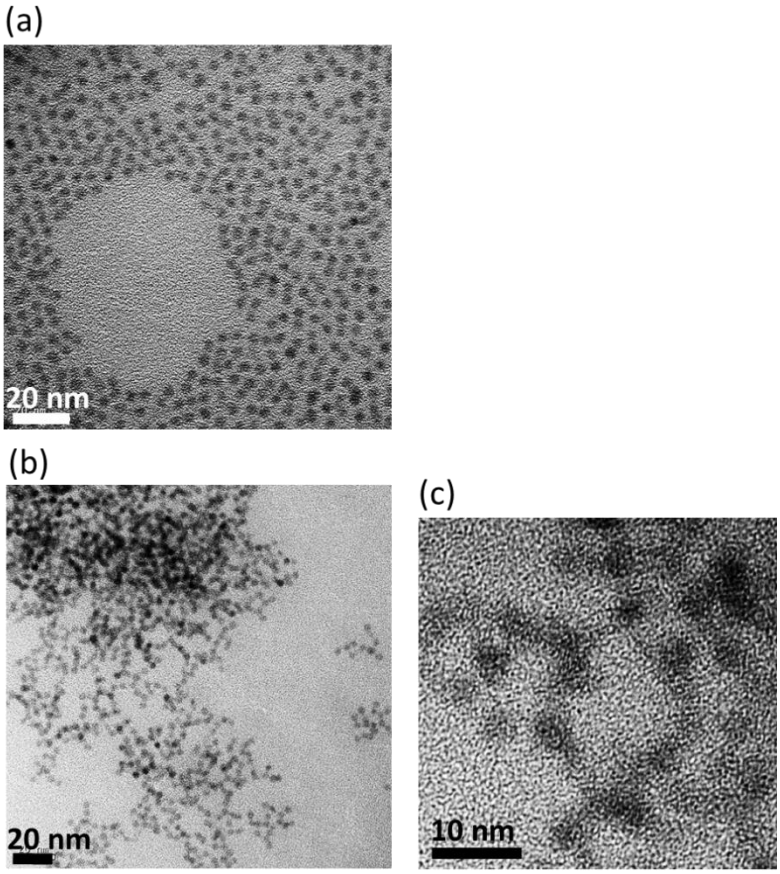

Figure 3.13. TEM image of (a) CdSe QDs. (b) CdHgSe nanoalloys after the reaction with mercury bromide. (c) High resolution TEM image of CdHgSe nano alloys.

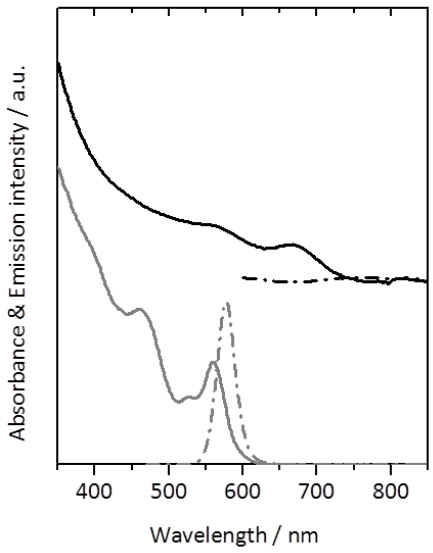

Figure 3.14. Optical properties of CdSe (grey curves) and CdHgSe (black curves), where solid lines show absorption whilst dashed lines indicate emission profiles. Excitation wavelength was 450 nm (CdSe) and 500 nm (CdHgSe).

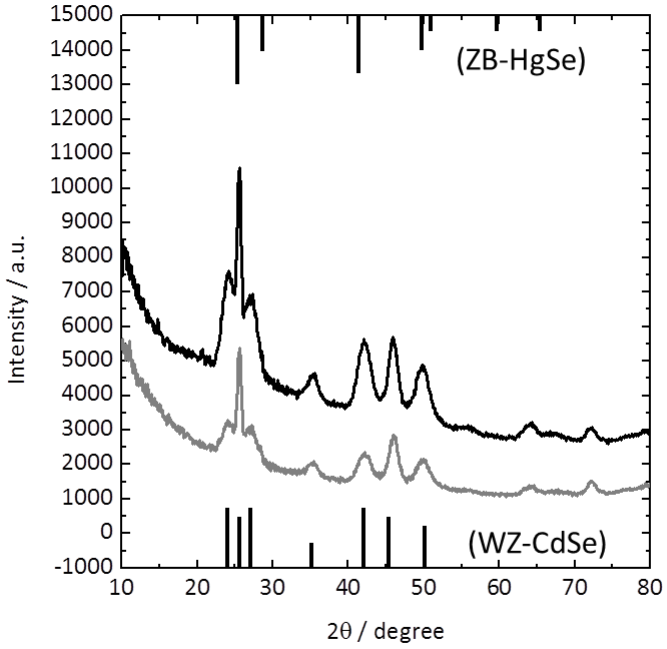

Figure 3.15. X-ray diffraction pattern of CdSe QDs (grey line) and CdHgSe nanoalloys (black line). Miller indices for wurtzite CdSe were shown below and Miller indices for zinc blende HgSe were indicated on the upper end of the graph.

3.5.2 CdSe Nanorods

The chemical transformation triggered by mercury cation addition which converted cadmium chalcogenide nanoparticles into cadmium mercury chalcogenide nanoalloys was further explored using anisotropic nanocrystals. CdSe nanorods have a different morphology yet have approximately the same elemental composition as spherical CdSe. It is known that the nanorod formation could be driven by the different growth kinetics from the nanoparticle formation.[82] Typically, the nanocrystal shape could be controlled by changing monomer concentrations and the type of stabilising agents. (e.g. phosphonic acid binds strongly to the CdSe surface than TOPO,[69] which causes anisotropic growth in wurtzite CdSe) The CdSe nanorods (5.3 ± 0.8 nm by 15.4 ± 1.8 nm, see Chapter 6.3.3 for detailed synthetic procedure), capped with TDPA and TOPO, are shown in Figure 3.16 (a) and (b). Although they were packed closely, CdSe nanorods appeared to be appropriately capped with surfactant molecules and hence separated with a specific distance (< 3 nm), which was consistent with the experimental observation in the previous report.[84] The effect of mercury cation addition is shown in Figure 3.16 (c) and (d). The observed width and length of the rods were measured after mercury addition at 5.4 ± 0.9 nm and 13.4 ± 1.7 nm, around 2 nm shorter whilst keeping the width from the original CdSe nanorods. Additionally, one could observe a different trend in nanorods alignment. CdSe nanorods which reacted with the mercury cation were attached with the next nanorod on, possibly, a certain aspect of the rod; the nanorods preferentially attached through c-axis of the crystal, forming a series of end-to-end structures. Figure 3.17 shows absorption and emission spectra of the CdSe nanorods before and after addition of the mercury cation. The absorption profile of the CdSe nanorods exhibited an absorption band edge at *ca.* 670 nm, which red-shifted by *ca.* 40 nm upon cation addition (Figure 3.17, inset), although the excitonic peak maintained the same position. The emission of CdSe nanorods was red-shifted after the mercury cation addition, resulting in a weak, broadened emission at 810 nm, suggesting incorporation of the mercury cation. From the absorption spectra, it is assumed that the resulting CdSe nanorods from mercury cation addition maintained their electronic states and did not obviously form alloyed particle, unlike the significant spectral change in absorption as can be seen in Figure 3.6. It is plausible that the mercury cations preferentially attached to the c-ends of the rods, possibly causing ligand detachment/etching of the material which leads to oriented attachment of each rod. This

is supported by the observation in other reports where CdSe nanorods/gold tip dumbbell structures retained the absorption peak of the CdSe nanorods at the same wavelength after addition of other metal cations.[93]

Due to the intrinsic morphology of nanorods, applications in biological labelling experiments and chromospheres in light-emitting diode are envisaged, in preference to spherical nanoparticles.[81]

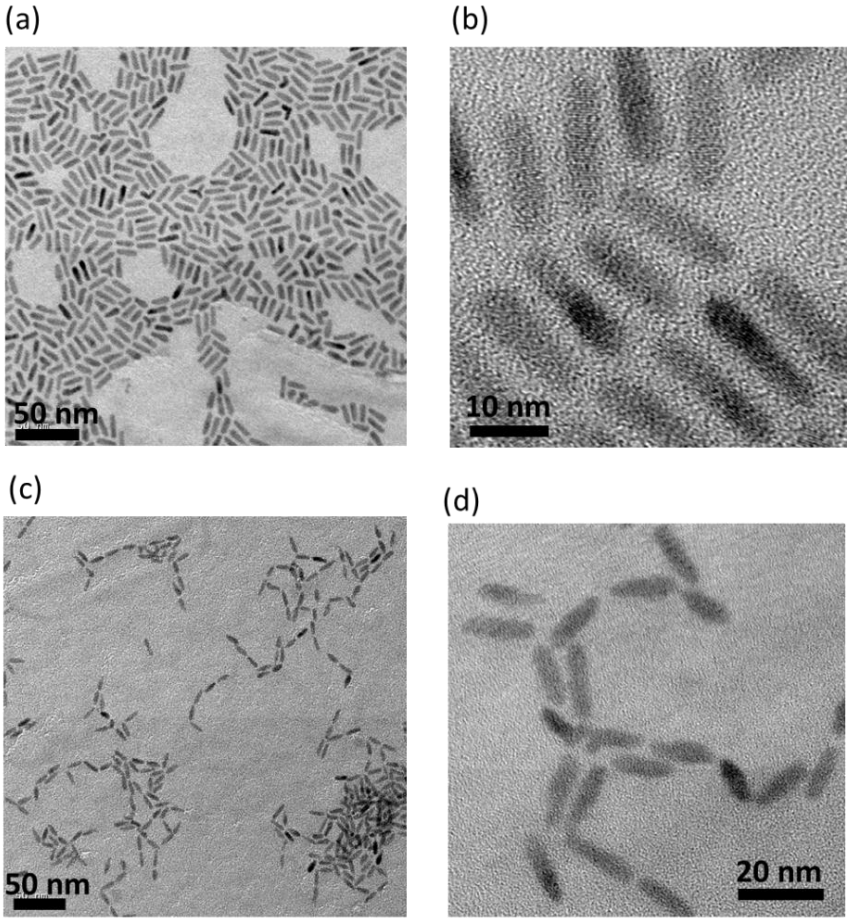

Figure 3.16. TEM image of (a, b) CdSe nanorods. (c, d) Resulted nanomaterials after the reaction with mercury bromide.

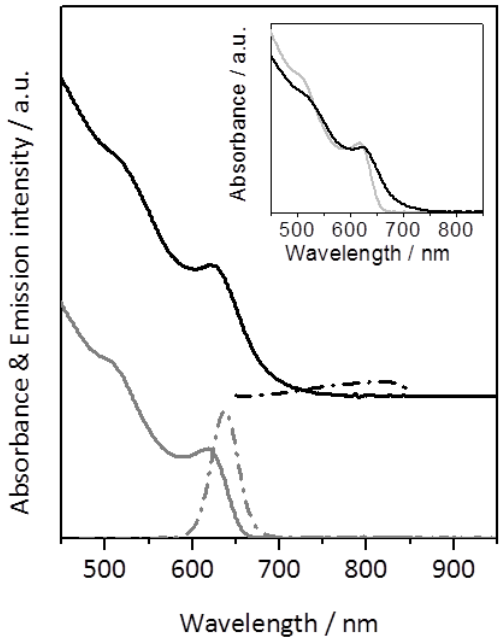

Figure 3.17. Optical changes in CdSe nanorods (grey curves) and CdHgSe nanorods (black curves), where solid lines show absorption whilst dashed lines indicate emission profiles. Excitation wavelength was 450 nm (CdSe) and 500 nm (CdHgSe). (Inset) Magnified absorption spectra of CdSe/CdHgSe nanorods, showing a red-shift in absorption threshold.

3.5.3 CdTe Tetrapods

The mercury cation addition technique was applied to CdTe tetrapods, which were synthesised *via* an analogous procedure using different surfactant molecules (oleic acid, oleylamine and TOP). CdTe, in contrast to CdS, CdSe and ZnS, is known to favour the tetrapod shape growth mode due to an appropriate energy difference between two crystal structures (cubic and hexagonal structures); selective nucleation in the zinc blende (cubic) structure occurs whilst subsequent wurtzite (hexagonal) arms growth is also allowed at the elevated temperature.[83] Tetrapods can potentially be applied to solar cells due to the inherent benefits such as the self-alignment on the surface and tuneable arm length/bandgap energy.[83, 85, 92]

TEM images of CdTe tetrapods capped with oleic acid/oleylamine/TOP are shown in Figure 3.18 (a) (detailed synthetic procedure can be found in Chapter 6.3.4). The calculated core diameter and arm length were 6.9 ± 0.9 nm and 6.7 ± 0.7 nm,

respectively. Figure 3.18 (b) shows the CdTe tetrapods after mercury cation addition. No distinct nanocrystals attachment was observed unlike in CdTe QDs, CdSe QDs and CdSe nanorods. Also, the core diameter and arm length appeared to be almost the same as the original CdTe tetrapods. Absorption profiles, in contrast, showed spectral red-shift after mercury cation addition. The excitonic peak of the original CdTe tetrapods was at 710 nm, whilst the peak shifted to 870 nm after the reaction, which suggested the modification of internal energy states by the addition of mercury. However, the lack of study on tetrapod-shaped CdHgTe nanocrystals hinders the mercury incorporation into CdTe. Therefore, further characterisation such as elemental analysis would be essential to confirm the possibility of the CdHgTe formation. Our experimental observation also indicated that the resulting nanostructures after mercury cation addition also had poor solubility in toluene, possibly due to the removal of surfactant molecules.

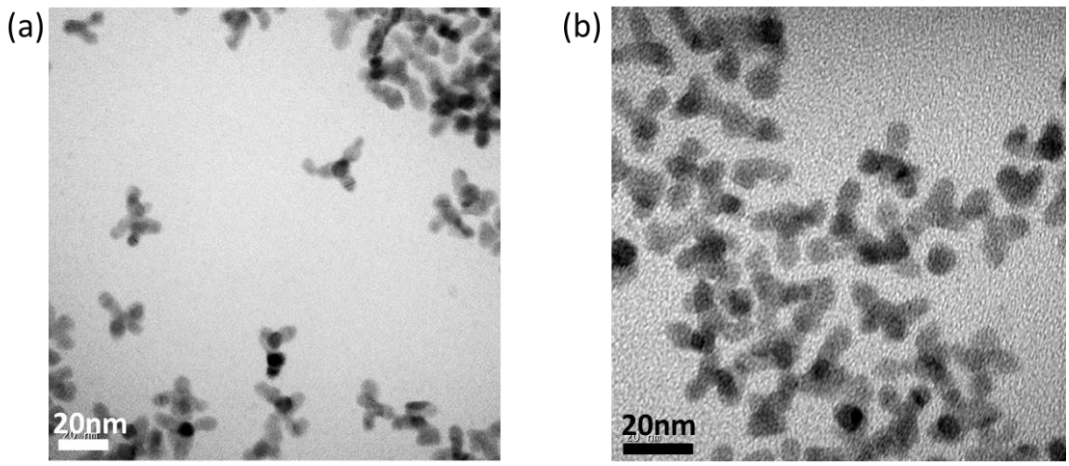

Figure 3.18. TEM images of CdTe tetrapods (a) before and (b) after mercury cation addition.

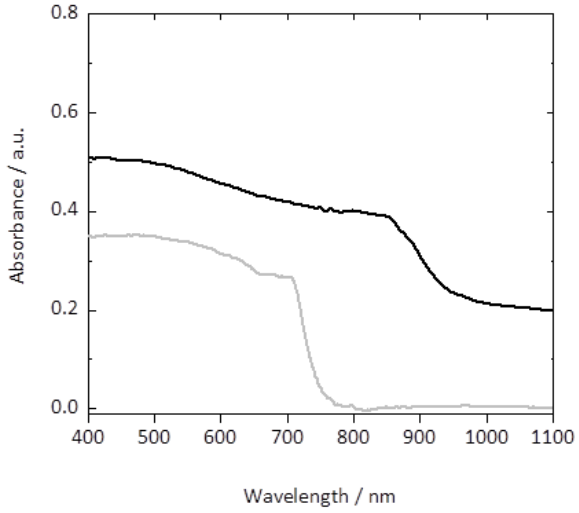

Figure 3.19. Absorption spectra of CdTe tetrapods (grey line) and the adduct with mercury cation (black line).

3.6 Conclusion

In conclusion, CdHgTe nanoalloys with complex morphologies have been synthesised at room-temperature. The redox potential of the metal cation has been used as an indicator of reactivity and a possible explanation for CdHgTe anisotropic structure formation ("molecular welding effect") was investigated. The addition of other cations such as Cd^{2+}, Zn^{2+} and Pb^{2+} did not show any spectral shift from original CdTe solution, whilst Ag^{+} and Au^{3+} addition to a CdTe solution resulted in Ag_2Te and Au formation. The redox potential and acid hardness were compared, which suggested that contribution of redox potential to the nano-conversion chemistry was extremely important.

The procedure has been applied to CdSe QDs to produce alloyed materials with similar optical and structural characteristics to CdHgTe. CdSe nanorods were reacted with mercury cations in the same manner and the oriented attachment of the rods was observed. The reaction between tetrapod-shaped CdTe nanocrystals and mercury cations was examined, showing spectral red-shift but without distinctive structural change.

Chapter 4

Colloidal CdTe/ZnS QDs Synthesis Using Molecular Single-Source Precursors

4.1 Introduction

As discussed in Chapter 1.3, a number of synthetic methodologies have been developed for colloidal QDs synthesis, which enable one to prepare monodispersed, high quality nanomaterials. Additionally, it is noteworthy that most of the synthetic methodologies for novel compound semiconductor QDs, particularly for II-VI semiconductors, have stemmed from the organometallic pyrolysis of molecular precursors in a hot organic solvent; typically, the procedure is described as the "TOP/TOPO method", where a chalcogen precursor dispersed in TOP is reacted with a metal precursor in hot TOPO (up to 350 $^{\circ}$C) as a coordinating solvent, leading to the formation of the QDs.[1, 28, 62, 64, 77] Despite being a sophisticated methodology, the TOP/TOPO method (or any other synthetic method using separate sources) has limitations because the nature of nanocrystal formation strongly depends on the reaction of two (or more) constituent precursors (monomers) with differing chemical properties and reactivities. The properties of each precursor (e.g. inherent purity, reactivity and stability) are critical factors, as subtle changes in reaction precursor conditions effect the morphology and optical properties of the nanomaterials; hence, difficulties in reproducibility.[227]

An organometallic single-source precursor (SSP) is a compound having both metal and chalcogen atoms within a molecular structure.[228] SSPs are regarded as benign precursors compared to separate precursors due to the nature of preformed ionic bonds between metal and chalcogen. Additionally, the use of SSPs can exclude unfavourable uncertainties arising from the dual-precursors system, where the quick injection of precursors at higher temperature and the subsequent diffusion-controlling nucleation are required.[227, 229, 230] The prime application of SSPs is in thin film fabrication using metal

organic chemical vapour deposition, where SSPs for a variety of compound semiconductors have been synthesised in order to obtain homogeneous high quality thin films.[228, 231, 232]

Molecular SSPs for colloidal nanomaterials have also been studied from the early stages of nanoparticle synthesis. SSPs with a $M(ER)_2$ structure (M = Zn, Cd, Hg, E = S, Se, Te and R = short alkyl or phenyl group) were synthesised in the mid-1980s by Osakada *et al.* and Steigerwald *et al.*[74, 233, 234] Steigerwald reported that $Cd(SePh)_2$ when heated to reflux in 4-ethylpyridine yielded particle-like CdSe clusters with a distinctive excitonic peak.[75] Subsequently, a systematic study using analogous SSPs based on $M(EPh)_2$ was carried out by the same group, showing early evidence of nano-crystalline CdSe, CdTe and HgTe particles.[76] Nevertheless, the synthesis of colloidal nanomaterials using these precursors appeared to be limited due to their polymeric nature and the difficulty in isolation of the resulting particles.[228, 235] O'Brien and co-workers have prepared a number of SSPs and applied the precursors to colloidal QDs synthesis using the TOP/TOPO method. The group reported the synthesis of CdS, CdSe and ZnSe nanocrystals using molecular SSPs of metal dithio/diselenocarbamate and metal imino-bis(diisopropylphosphine selenide) compounds, yielding colloidal II-VI nanocrystals with optical properties suggesting the quantum size effects.[236-241] Other example includes $Zn(TePh)_2$ and organometallic complexes such as $[M_{10}Se_4(SPh)_{16}]^{4-}$ (M = Cd, or Zn).[227, 242, 243]

Whilst a number of cadmium chalcogenide nanocrystals such as CdS and CdSe have been prepared using SSPs, little is reported regarding the synthesis of CdTe nanocrystals using such methods. Synthetic challenges in tellurium-containing SSP may hinder further progress in CdTe-based material fabrication, despite an apparent chemical analogy between tellurium, sulfur and selenium. Early reports showed that $Cd(TePh)_2$-1,2-bis(diethylphosphino)ethane (DEPE) complexes dissolved in 4-ethylpyridine, when heated at 168 $^{\circ}$C, resulted in nanoparticulate CdTe with an exciton peak at 600 nm.[76] Other CdTe-based SSPs such as $Cd[(TePiPr_2)_2N]_2$ have been used for thin films deposition.[231] In the work reported in this thesis, a CdTe SSP was synthesised whilst referring to the previous literature and applied to current QDs synthesis using established solvent and ligand systems. The prepared CdTe QDs were then overcoated with a ZnS shell in order to obtain photo-stable, bright nanoparticles. Although several issues regarding quality and reaction mechanism still exist and need to

be addressed, the provided synthetic methodology is clearly advantageous in potential scale-up and hence in practical applications thereafter.

4.2 CdTe SSPs Preparation

To maximise the advantages of using molecular SSPs (e.g. scalability, safety and controllability), it is important that the CdTe SSPs also are prepared in an accessible way. In this work, $Cd(TePh)_2$ was chosen as a single-source precursor for CdTe QDs (detailed synthesis is stated in Chapter 6.4.1). The synthetic procedure (as well as proton nuclear magnetic resonance (^{1}H NMR) spectra) for $Cd(TePh)_2$ was reported by Steigerwald *et al.*[234] The group successfully achieved colloidal particle formation *via* pyrolysis of the precursor in a coordinating solvent, yielding quantum dot-sized CdTe colloids.[75] The QDs prepared by this previous work were of poor quality. The particles had no reported emissive properties, possibly due to the solvent system used. The choice of correct ligands to passivate a QD surface is a key parameter, and we report here the utilisation of $Cd(TePh)_2$ with a suitable passivating agent, yielding high quality particles. The synthesis of the precursor as reported by Steigerwald involved harmful starting materials such as dimethyl cadmium ($CdMe_2$) (Equation 4.1).[234]

$$CdMe_2 + 2PhESiMe_3 \xrightarrow[-2\ SiMe_4]{} Cd(EPh)_2$$

(E = S, Se, Te)

Equation 4.1. Synthetic pathway of the CdTe SSP proposed by the previous literature.[234]

Therefore, an alternative synthetic procedure avoiding the use of dimethyl cadmium is desired. The use of bis[bis(trimethylsilyl)amido] cadmium, $Cd[N(SiMe_3)_2]_2$, towards the cadmium tellurolato complex, $Cd(TePh)_2$ was achieved from commercially available, benign precursors.[244] The $Cd[N(SiMe_3)_2]_2$ formation is shown in Equation 4.2, where cadmium iodide (CdI_2) and sodium bis(trimethylsilyl)amide, $NaN(SiMe_3)_2$, were reacted from -196 °C to room-temperature using liquid nitrogen, yielding a clear yellow liquid ($Cd[N(SiMe_3)_2]_2$) and a white residue (NaI).[244]

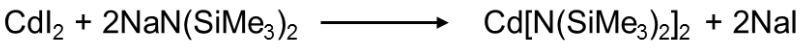

Equation 4.2. Synthesis of the cadmium precursor.

The resulting cadmium precursor was then reacted with phenyl tellurol (PhTeH) to give $Cd(TePh)_2$. Due to the instable nature of tellurol, diphenyl ditelluride, $(PhTe)_2$, was used instead and converted *in situ* to phenyl tellurol by an addition of $NaBH_4$ in the mixture of cadmium precursor.[245] The overall synthetic route can be described as in Equation 4.3. Each chemical addition proceeded at liquid nitrogen temperature (-196 °C) to prevent undesired reactions, and after adding all the necessary precursors, the temperature was gradually increased to room-temperature with stirring.

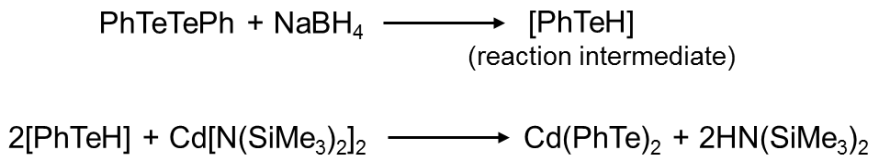

Equation 4.3. Synthesis of CdTe SSP provided in this work.

After 1 hour of the reaction, a yellow precipitate ($Cd(TePh)_2$) was observed in diethyl ether, in good agreement with experimental observations from previous reports.[74, 234, 244] Potential by-products such as diphenyl ditelluride and bis(trimethylsilyl)amine were removed *via* washing with warm toluene and diethyl ether. Analysis using inductively coupled plasma mass spectrometry (ICP-MS) of the purified SSPs gave an elemental ratio of Cd:Te = 1.22:2.00, which indicated the formation of $Cd(TePh)_2$. However, mass spectrometry also showed that strong signals arose from Na and B. These signals can be associated with the residue from $NaBH_4$. The resulting $Cd(TePh)_2$ was readily dissolved in coordinating solvents such as N,N-dimethylformamide (DMF), pyridine and dimethyl sulfoxide (DMSO). Re-crystallisation of $Cd(TePh)_2$ in DMF yielded yellow needle-like crystals, which were then characterised using ^1H NMR (detailed descriptions are outlined in Chapter 6.4.2).

4.3 Synthesis of CdTe QDs from SSP

CdTe QDs were then synthesised using the $Cd(TePh)_2$ as a precursor (detailed reaction procedure is outlined in Chapter 6.4.3). As a growing number of synthetic procedures towards QDs have been reported in the last decade, an extensive choice of solvents and surfactant molecules are now available to obtain the desirable characteristics of QDs. In this study, TOP was first used to coordinate and stabilise the CdTe SSP, as phosphines are often thought to be efficient ligands for organometallic compounds. Typically, an excess of TOP (>50 times more than $Cd(TePh)_2$ by molar ratio) was mixed with the CdTe SSP under an inert atmosphere and sonicated in an ultrasound bath until the yellow colour from $Cd(TePh)_2$ faded, giving a clear solution. A similar phenomenon was reported by Jun *et al.*, in which pale-yellow coloured $Zn(TePh)_2$ turned to colourless after formation of a $Zn(TePh)_2$-tetramethylethylenediamine complex.[243] After removal of insoluble precipitates by centrifugation, a transparent colourless solution of $Cd(TePh)_2$-TOP was obtained (Figure 4.1).

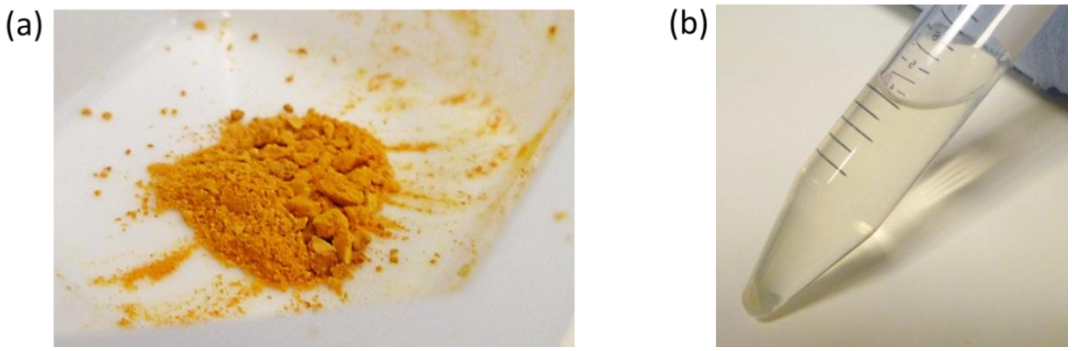

Figure 4.1. Pictures of (a) $Cd(TePh)_2$ powder after washing with anhydrous ether and toluene, (b) $Cd(TePh)_2$ dissolved in TOP, after sonication and centrifugation.

The prepared $Cd(TePh)_2$-TOP was then injected into degassed oleylamine (OAm) at room-temperature. The solution at room-temperature was gradually increased (*ca.* 10 $^{\circ}$C/min) up to 210 $^{\circ}$C, and the solution displayed a light-yellow colouration at 120 $^{\circ}$C, followed by a red-shift in solution colour. The observed colour change suggested the formation of nuclei of CdTe QDs, which is described by this reaction:

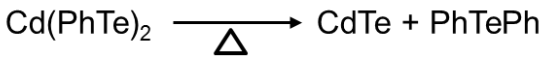

Equation 4.4. Pyrolysis of $Cd(TePh)_2$. [74]

The obtained absorption spectra are shown in Figure 4.2, showing a gradual red-shift in the absorption profiles. Quantum size effects can be seen from the spectra where the absorption onset was shifted from 530 nm to 680 nm as the band gap energy becomes smaller as the particle size increases. Additionally, the half width at half maximum (HWHM) of the excitonic peaks, which were determined from the centre of absorption peak to the half value of the absorbance in lower energy, were investigated, showing that the HWHM of the absorption profile of CdTe QDs after 10 minutes of the reaction was 18 nm, whilst that of the sample after 55 minutes of heating was 35 nm. (HWHM was used instead of the full width at half maximum (FWHM) as absorption peaks in Figure 4.2 were asymmetric and the FWHM could not be obtained from the given spectra.) The single observable excitonic peak present throughout the reaction and wide excitonic HWHM in larger particles can be comparable to thiol-stabilised CdTe QDs synthesised in aqueous solution, where the Ostwald ripening process is the major driving force in particle growth.[156, 246] It is reasonable that QDs formation using the SSPs has a similar growth dynamics to thiol-stabilised aqueous routes as Cd-Te clusters are thought to be formed already (or instantly) in the solution at lower temperature, where thermodynamics then dominate the particle growth, in contrast to diffusion-controlling growth dynamics achieved by slow decomposition of metal precursor such as TDPA-Cd in hot solvent.[62, 149]

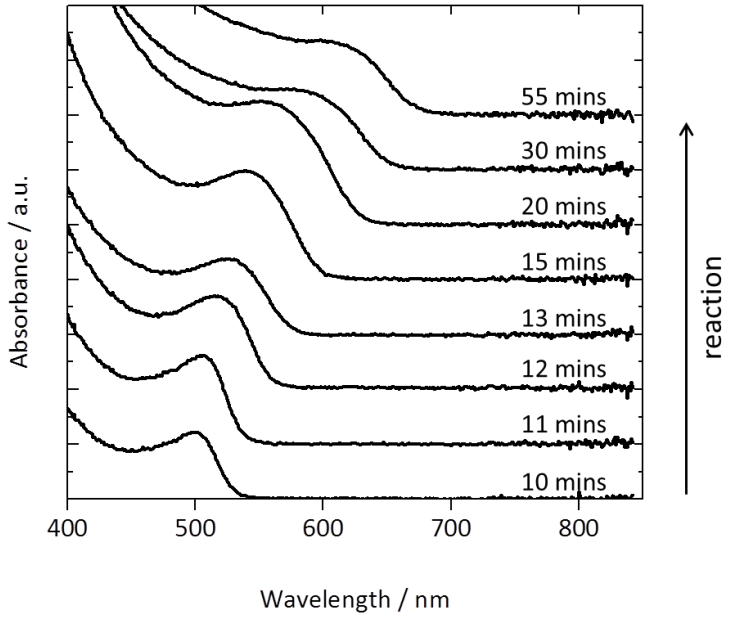

Figure 4.2. Absorption transition observed during CdTe QDs growth.

The resulting CdTe QDs showed a tuneable emission wavelength dependant on the particle size (Figure 4.3 (a)). It is possible to control the emission wavelength continuously from 528 nm to 664 nm. Figure 4.3 (b) and (c) show the temporal evolution of photoluminescence quantum yield (PL QY) and FWHM of emission profiles at each reaction stage. The PL QY of CdTe QDs prepared through the SSPs route changes depending on peak wavelength and the maximum PL QY (18 %) was recorded in the sample with an emission peak at 641 nm. The obtained PL QY was not as high as other CdTe QDs, with PL QY typically up to 70%.[149, 152, 156] The FWHM of the emission profile was in good agreement with the CdTe QDs prepared *via* the aqueous routes, where the values started from as low as 35 nm and increased above 50 nm as the particles grew, [156, 246] whilst CdTe QDs prepared by the organometallic route gave smaller FWHM below 30 nm.[149] Despite this, it is possible to improve the quality of the CdTe QDs through the SSPs route by the optimisation of reaction condition and post-synthetic treatment, such as size selective precipitation. Figure 4.4 shows pictures of purified CdTe QDs in toluene under ambient condition and excitation at 365 nm, confirming their notable fluorescence. Given the optical characteristics, $Cd(TePh)_2$ could be successfully used as an alternative to the conventional dual precursors system for the synthesis of colloidal CdTe QDs.

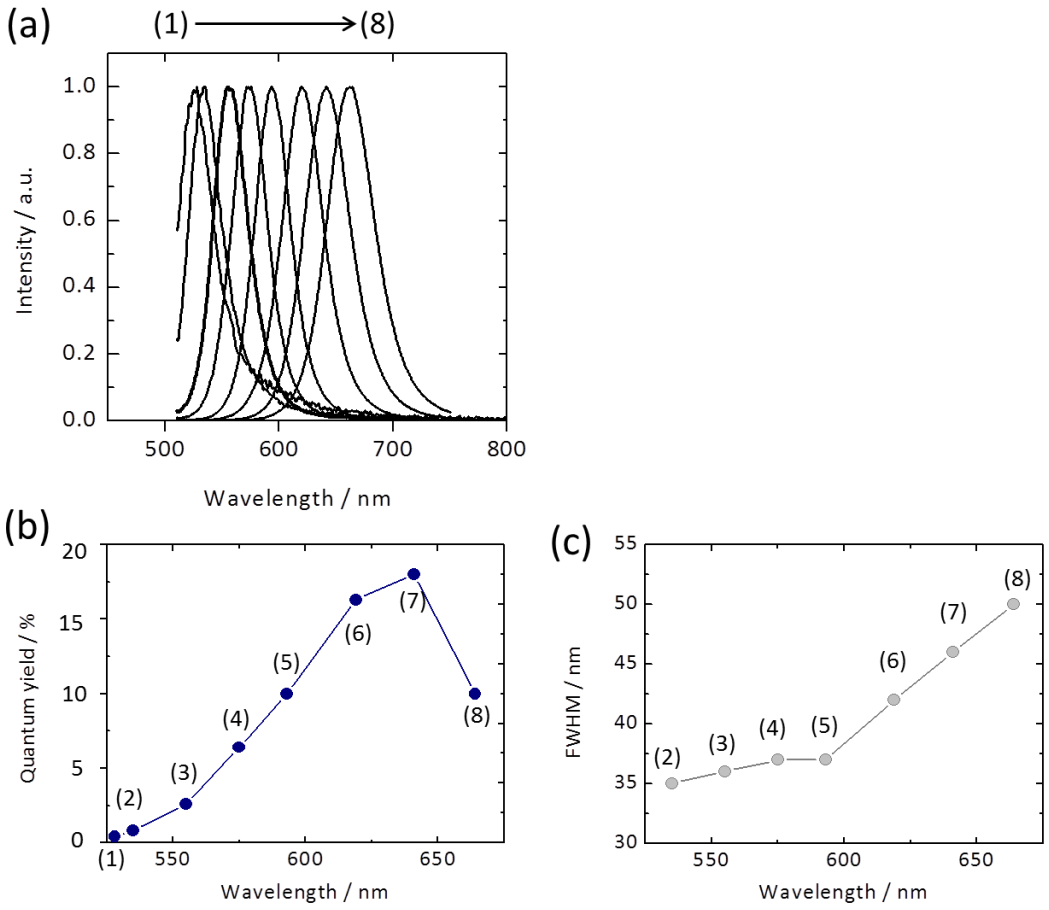

Figure 4.3. (a) Changes in emission spectra during CdTe growth, (b) evolution of quantum yield and (c) FWHM of the emission profile. Each plot represents the sample 1) 10 minutes, 2) 11 minutes, 3) 12 minutes, 4) 13 minutes, 5) 15 minutes, 6) 20 minutes, 7) 30 minutes and 8) 55 minutes after heating. Excitation wavelength = 500 nm.

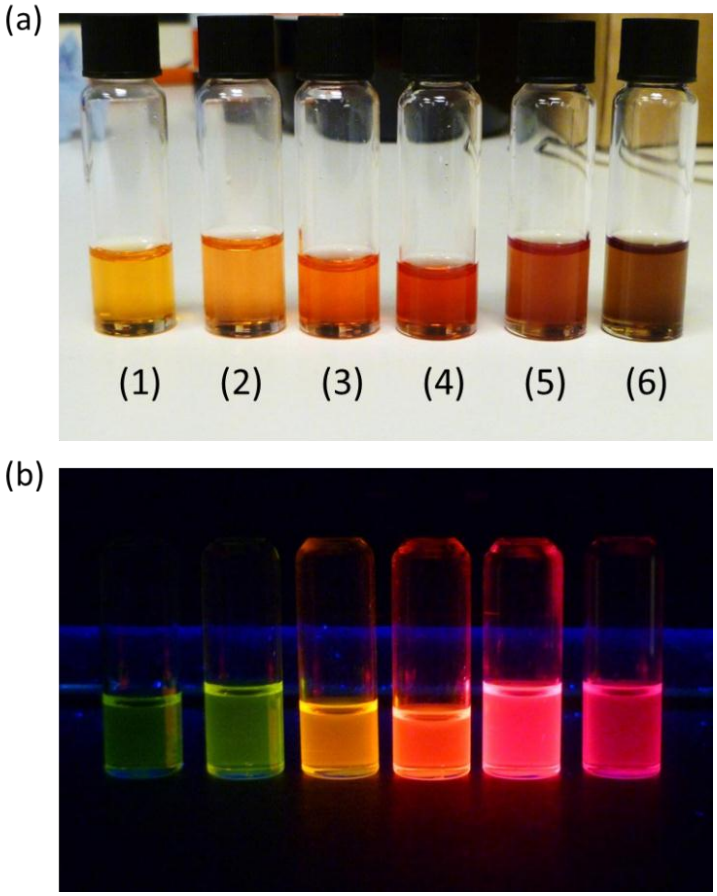

Figure 4.4. Images of CdTe QDs prepared from SSPs (a) under room light and (b) excitation at 365 nm. Each vial represents the sample prepared 1) 12 minutes, 2) 13 minutes, 3) 15 minutes, 4) 20 minutes, 5) 30 minutes and 6) 55 minutes after heating.

The elemental ratio of the resulting CdTe QDs has been investigated using ICP-MS, showing Cd:Te = 1.00:0.74. The Cadmium content exceeded the tellurium content in contrast to the elemental ratio in $Cd(TePh)_2$. The result was in good agreement with other reports, where elemental analysis by energy-dispersive X-ray spectroscopy (EDX) gave Cd:Te = 1.0:0.7-0.8.[247, 248] Furthermore, the resulting cadmium concentration calculated from ICP-MS showed close values to theoretical value given by the mass of $Cd(TePh)_2$ used in the reaction. The fact indicates that most of the $Cd(TePh)_2$ in solution was successfully consumed to form CdTe QDs with a preferable reaction yield. For example, 100 mg of $Cd(TePh)_2$ (0.19 mmol) resulted in 3.3 nm CdTe QDs solution containing 0.14 mmol of cadmium (73.7 % reaction yield), from the calculation explained in Appendix A.[148] In contrast, the organometallic dual-precursor procedure described in Chapter 3 gave a limited reaction yield; 0.2 mmol of CdO produced 3.9 nm

CdTe QDs solution containing only 0.034 mmol of cadmium contents (17% reaction yield).

4.4 Formation of CdTe/ZnS Core/Shell QDs

As interest in the application of colloidal QDs favours biological imaging, it is important to suppress unfavourable effects arising from the nature of cadmium-related materials. Therefore, a ZnS shell deposited on a core surface - one of the best known synthetic treatments of colloidal QDs systems – was investigated (detailed reaction procedure is stated in Chapter 6.4.4). To further simplify the reaction procedure, a SSP was used as a ZnS source. In this study, zinc diethyldithiocarbamate ($ZnDDTC_2$), whose chemical structure is depicted in Figure 4.5, was used as a SSP.

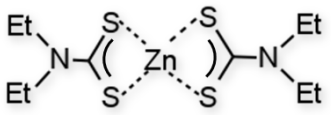

Figure 4.5. Chemical structure of $ZnDDTC_2$.

$ZnDDTC_2$ is a common dithiocarbamate and used extensively as a precursor for thin film deposition due to its stability.[228] The use of $ZnDDTC_2$ for the shell formation on colloidal nanoparticles was also reported by several groups. Particularly, CdSe/ZnS, CdTe/CdSe/ZnS and CdS/ZnS QDs have been achieved using $ZnDDTC_2$ and the resulting QDs showed enhanced/photo-stable fluorescent characteristics.[177, 249, 250] The rationale for the use of $ZnDDTC_2$ in this work is; (i) air stability and ease of handling, (ii) viability of shell deposition as proven by several researchers, and (iii) commercial availability and cost. The reaction mechanism of ZnS deposition is known to be as follows (Equation 4.5):[228]

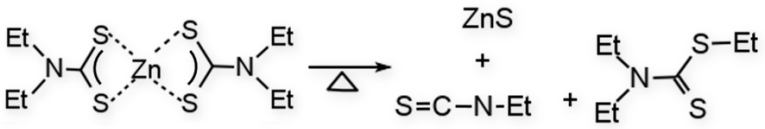

Equation 4.5. Pyrolysis of $ZnDDTC_2$ under vacuum condition to form ZnS.

whilst another reaction route is proposed in the presence of primary amines (Equation 4.6).[249, 251]

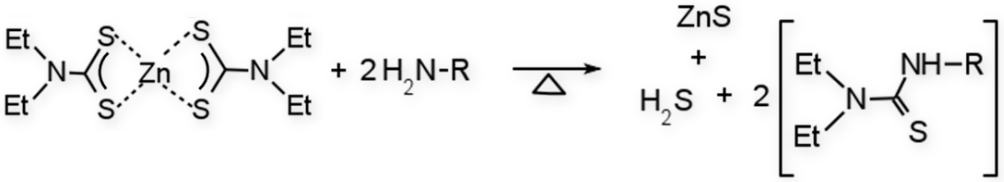

Equation 4.6. ZnS formation by the thermal decomposition of $ZnDDTC_2$ in the presence of primary amines.

In a typical synthesis of CdTe/ZnS QDs, CdTe QDs (emission peak at 610 nm, absorption exciton peak at 557 nm) were precipitated by methanol and re-dispersed in hexane, and then mixed with degassed oleylamine (OAm). To the QDs solution at 90 °C, the $ZnDDTC_2$ dissolved in TOP was added and the temperature was increased to deposit the ZnS shell. The amount of ZnS SSPs added was calculated so that only one layer of ZnS should deposit on the CdTe surface (see detailed calculation process in Appendix B). The original clear red colour turned slightly cloudy due to the addition of the less soluble $ZnDDTC_2$, then a distinct brown colouration was observed upon heating at 130 °C presumably due to the thermal decomposition of $ZnDDTC_2$ with amines (Equation 4.6). The solution was stirred at 180 °C for 20 minutes and cooled to 100 °C. The solution was ready for a second addition of $ZnDDTC_2$ and the same process was repeated six times to ensure sufficient ZnS was formed. The procedure mentioned above is described as "thermal-cycling using single-source precursors" inspired from the work of Chen *et al.* reporting the CdS/ZnS QDs formation using $ZnDDTC_2$.[250]

Figure 4.6 shows absorption spectra of the resulting CdTe/ZnS QDs solution after purification. Although the excitonic peak at 570 nm became less pronounced after each shell addition, there was no significant spectral red-shift observed, which is thought to be a common phenomenon in CdTe/ZnS synthesis.[153, 173] It should be mentioned that the absorption threshold also became unclear due to the difficulty in separating pure CdTe/ZnS QDs from reaction solution: purified QDs still showed a slight cloudiness in solution and this contributed to the shape of the resulting absorption spectra.

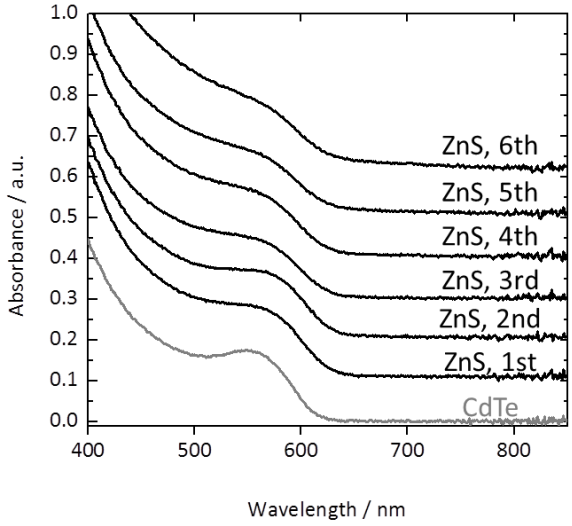

Figure 4.6. Absorption spectra during the ZnS shell deposition on a CdTe surface.

The emission spectra of the resulting CdTe/ZnS QDs were also studied (Figure 4.7 (a)). No observable change in fluorescence wavelength was seen, as can be expected from the absorption spectra. Figure 4.7 (b) shows the change in fluorescence intensity at each ZnS shell deposition stage, indicating a rapid decrease in fluorescence intensity after the first ZnS addition. The intensity then gradually increased and decreased at the point of 4th shell addition, which is well known behaviour in core-shell QDs synthesis where the quantum yield declines after several monolayers of shell formation. The decrease in emission intensity can partly be explained as a result of the unwanted nucleation of ZnS nanoparticles and by-products. Figure 4.8 shows the emission spectrum of CdTe/ZnS (6th shell addition) excited at shorter wavelength (350 nm). The spectrum showed emission peak at higher energy (*ca*. 420 nm), which indicated the presence of other

chemical species in the solution (e.g. ZnS nanoparticles), affecting the fluorescence quality of CdTe/ZnS QDs. Whilst it is necessary to investigate the underlying surface chemistry to obtain improved optical properties, it is also important to consider that the correct shell precursor needs to be chosen and that subtle difference in reaction conditions can result in insufficient shell deposition or a drop in emission.[153, 177] For example, Smith *et al.* reported emission quenching of CdTe QDs after an addition of Zn and S source equivalent to 1 monolayer (ML), whilst 0.5 ML shell addition achieved improved emission. Also, Zhang *et al.* observed successful shell deposition using $ZnDDTC_2$ but failed to deposit a ZnS shell using a dual precursors system with zinc carboxylate and elemental sulfur. Optimisation of the ZnS shell deposition is currently being investigated.

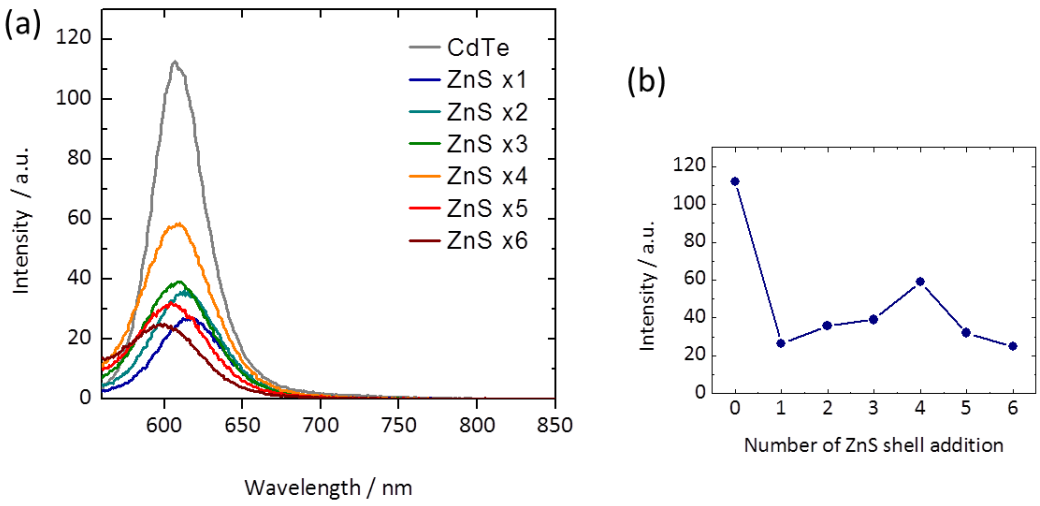

Figure 4.7. (a) Changes in emission spectra of CdTe QDs at each ZnS shell deposition (excitation wavelength = 500 nm). (b) Relationship between emission intensity and reaction stage.

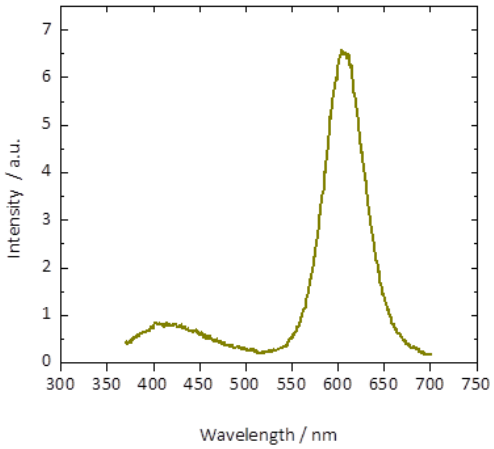

Figure 4.8. Emission spectrum of CdTe/ZnS QDs (6th ZnS shell addition) after purification. The excitation wavelength was 350 nm.

The structural characterisation of the resulting CdTe/ZnS QDs is shown in Figure 4.9. TEM images of CdTe QDs before and after ZnS addition are shown in Figure 4.9 (a, b). The CdTe QDs appeared to be spherical, although clearly aggregated on the grid making it difficult to identify individual nanoparticles. The observed aggregation could be explained by the lower coordinating capability of primary amines as ligands.[63, 252] Particularly, it has been reported that two to three purification steps by precipitation with non-solvents caused almost complete removal of hexadecylamine from the surface of CdSe QDs.[69] It is therefore reasonable to assume that the same effect occurred on our nanoparticles given the similarity in the system. Hence, the surface of the CdTe QDs when lacking sufficient ligands became highly susceptible to aggregation as can be seen in Figure 4.9 (a). The electron micrograph of CdTe/ZnS QDs can be seen in Figure 4.9 (b). Although individual particles could be observed, rod-like materials were also observed, adjacent to the spherical particles. Figure 4.9 (c) shows the size distribution of obtained CdTe and CdTe/ZnS QDs calculated by measuring approximately 150 particles for each sample. The average diameter of each sample is 3.1 ± 0.9 nm for CdTe and 3.7 ± 0.7 nm for CdTe/ZnS QDs. Given the amount of ZnS precursor added (4ML equivalent) and estimated thickness of monolayer of ZnS (0.31 nm), theoretical prediction of the diameter of CdTe/ZnS QDs would be 5.6 nm. There is a substantial difference between obtained and estimated diameter on CdTe/ZnS QDs and this is possibly due to an insufficient deposition of ZnS on the CdTe surface and unwanted nucleation of ZnS clusters.

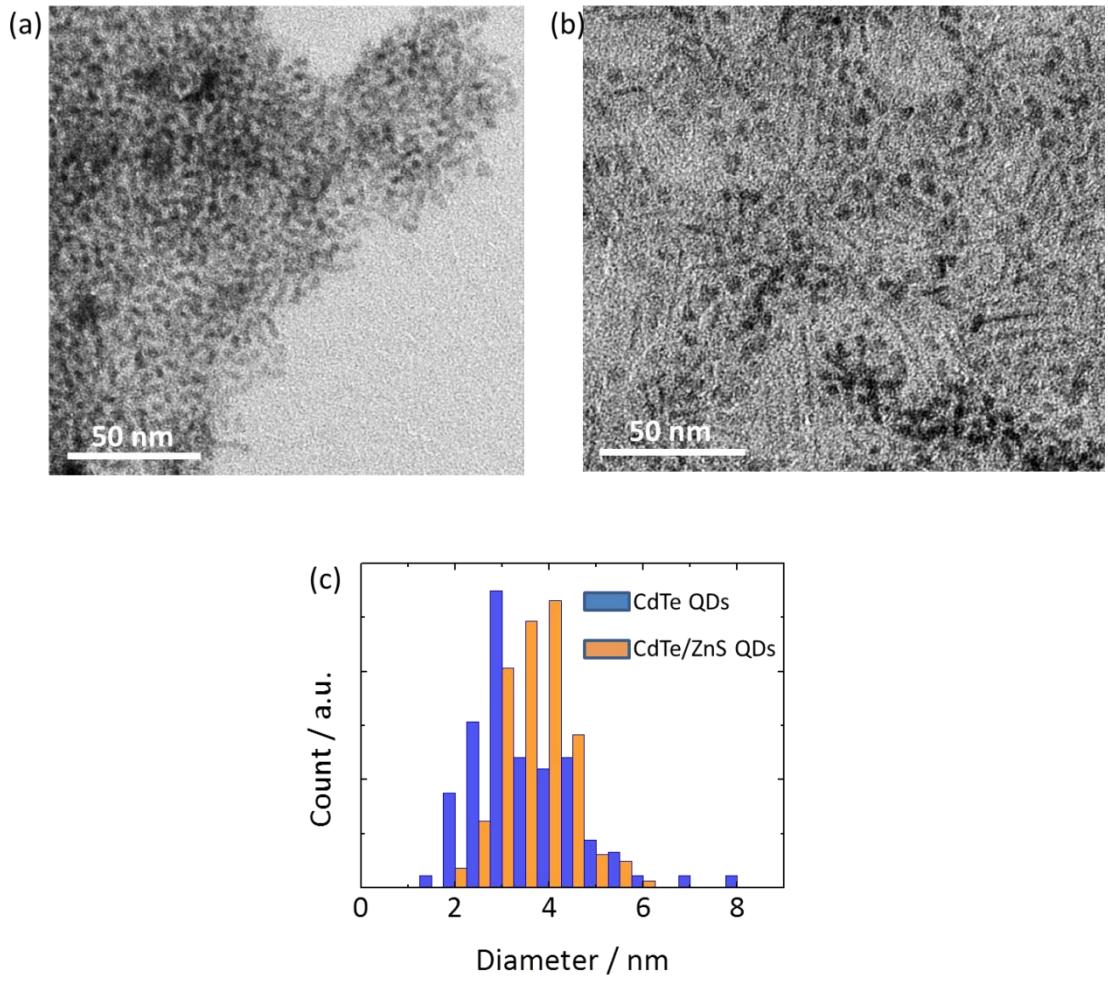

Figure 4.9. TEM images of (a) CdTe QDs prepared from SSPs and (b) CdTe/ZnS QDs after the 4th addition of $ZnDDTC_2$. (c) Size distribution of CdTe QDs and CdTe/ZnS QDs based on the TEM images.

The crystal phase of the resulting QDs was studied using X-ray diffraction (XRD) analysis. Figure 4.10 shows the XRD patterns of CdTe QDs and CdTe/ZnS QDs prepared from SSPs. The patterns showed a phase transition of the QDs after shell deposition; whilst CdTe QDs indicates a zinc blende (cubic) structure, CdTe/ZnS QDs clearly shows the characteristics of wurtzite (hexagonal) ZnS. From the fact that the peak at 24° (2θ) of the original CdTe QDs completely disappeared after the shell formation, we can conclude that the internal crystal structure of the CdTe core was affected by the ZnS shell formation, rather than maintaining the structure. It is somewhat unusual, as other reports using $ZnDDTC_2$ showed that XRD patterns after ZnS deposition were predominantly zinc blende structure;[177, 250] the formation of

wurtzite ZnS is less common compared to zinc blende ZnS. There are a limited number of papers showing the XRD patterns of wurtzite ZnS nanocrystals, where, for example, diethyl zinc/bis(trimethylsilyl)sulfide, or zinc ethylxanthate were decomposed in organic solvents.[100, 253, 254] It is possible that the crystal structure of a ZnS shell does not only depend on the type of precursors; other factor such as core crystals, reaction media, temperature and surfactants also affect the final crystal structure. It is also possible that the XRD pattern is from separate ZnS nanoparticles not on the CdTe core (i.e. individual particles). However, we would expect the pattern from the core particles to still be visible, which is not the case.

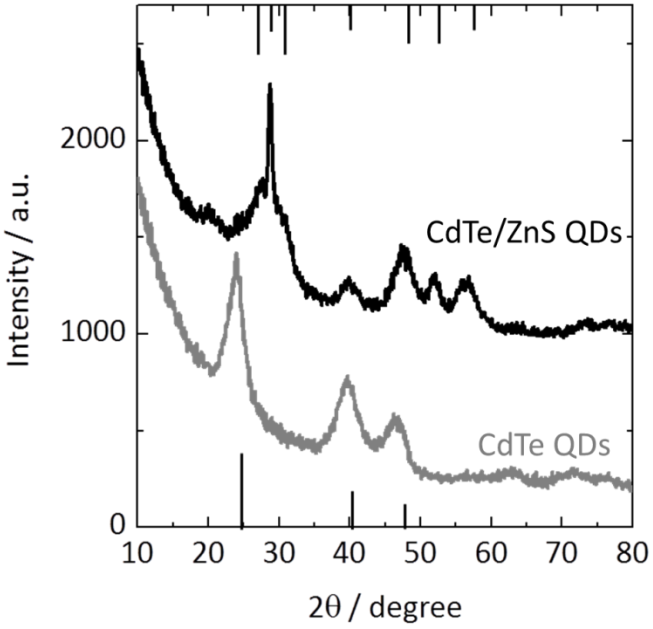

Figure 4.10. XRD patterns of CdTe QDs (grey curve) and CdTe/ZnS (4th shell deposition) QDs (black curve) prepared from SSPs. Millar indices for zinc blende CdTe (bottom) and wurtzite ZnS (top) are included as references.

4.5 Examination of Reaction Parameters

Table 4.1 shows a list of changes in reaction condition and their outcomes for the synthesis of CdTe QDs. Other reaction conditions were the same as those described in

Chapter 4.3 unless noted. As discussed in many previous studies, solvents and capping agents are major factors for particle growth. Whilst long alkyl amines such as hexadecylamine (HDA) had virtually the same effect as oleylamine (OAm), carboxylic acids and phosphonic acids caused negative effects on the optical properties of QDs. $Cd(TePh)_2$-TOP was injected in OAm at 230 °C (hot injection) to compare to the conventional TOP/TOPO method. The solution colour changed immediately after injection and the emission wavelength reached 650 nm within 10 seconds of the injection, which indicated the rapid particle growth at high temperature.

solvent	Injection temperature	optical properties [a)]	additional comment
HDA/ octadecene	RT	moderate PL	Compatible result to the synthesis in OAm.
octadecene	RT	weak PL, slightly precipitated	Insufficient coordinating capability.
oleic acid	RT	no PL, precipitated	Carboxylic acid can cause adverse reaction towards CdTe SSPs.
TDPA/ octadecene	RT	no PL, precipitated	Phosphonic acid have the same effect as carboxylic acid.
OAm	230 °C	weak PL	Solution colour changed rapidly, indicating rapid particle growth.

a) "Moderate" means the emission efficiency is comparable (up to 20%) to the CdTe QDs described in Chapter4.3. "Weak" emission means the emission efficiency of up to 5%.

Table 4.1. List of reaction conditions used to synthesise CdTe QDs from CdTe SSPs and the optical properties of the resulting products with additional comments. (RT = room-temperature, PL = photoluminescence)

The influence of reaction parameters on the synthesis of CdTe/ZnS was also investigated. Table 4.2 shows conditions for the synthesis of CdTe/ZnS QDs using different solvents, shell precursors and reaction temperatures. Several reports suggested that successful deposition of a ZnS shell on a CdTe core gave optical red-shifting with significant enhancement in emission efficiency.[153, 173] However, none of the reactions in this work gave similar result, causing either a decrease in the emission intensity or an optical blue-shift. Although further study is necessary, the decrease in emission efficiency suggested undesired Ostwald ripening of CdTe and/or an insufficient ZnS

shell formation, whereas an optical blue-shift strongly indicated etching of the CdTe surface.

solvent	shell precursors	reaction temperature	emission change	additional comment
OAm	$Zn(NO_3)_2$-TOP, TOPS	180–210 °C	red-shift (620 nm → 680 nm) PL decreased >60 % (3rd shell)	Growth behaviour was similar to the Ostwald ripening of core-only CdTe QDs.
OAm	$ZnEt_2$-TOP, TOPS	180– 10 °C	red-shift (620 nm → 645 nm) PL decreased >40 % (4th shell)	Similar result to CdTe/ZnS QDs prepared in Chapter 4.4.
octadecene	$ZnDDTC_2$-TOP	180–210 °C	slight red-shift PL decreased >90 % (3rd shell)	
OAm/TOP/ octadecene	$ZnDDTC_2$	120 °C	blue-shift (<10 nm) PL increased	Referred from previous report of CdSe/ZnS QDs (Dethlefsen *et al*., 2011).

Table 4.2. CdTe/ZnS QDs synthesis in different shell growth conditions (solvents, precursors and temperatures) and resulting emission changes with some additional comments. The last method was referred from the previous report of CdSe/ZnS QDs.[249]

4.6 Conclusion

A molecular single-source precursor, $Cd(TePh)_2$, was prepared using a modified procedure utilising relatively stable starting materials. Colloidal CdTe QDs were synthesised in oleylamine using $Cd(TePh)_2$ coordinated with TOP. The resulting QDs showed quantum size effects and their particle size could be controlled by changing reaction times to produce the QDs emitting from green to red. The QDs showed the highest quantum yield of 18% (emission peak of 647 nm). The mechanism of particle growth and the optical characteristics recorded in this study were comparable to thiol-capped CdTe QDs prepared in aqueous solution. The SSPs for ZnS, $ZnDDTC_2$, has been used to deposit a ZnS shell on a CdTe core. The overall fluorescence intensity decreased as the ZnS shell formed. TEM results showed spherical particles of both CdTe and CdTe/ZnS QDs having diameter of 3.1 ± 0.9 nm and 3.7 ± 0.7 nm, respectively. The structural study indicated a less effective ZnS shell formation on CdTe. An XRD study suggested that a phase transition occurred after ZnS shell deposition on a CdTe core, showing the characteristics of less-known wurtzite ZnS. The synthesised $Cd(TePh)_2$ showed excellent potential as an alternative precursor for CdTe QDs

synthesis, whilst the optimisation of optical characteristics and the stability of CdTe/ZnS QDs are currently underway.

Chapter 5

Phase Transfer of QDs Using Hydrophobins for Cell Imaging

5.1 Introduction

Fluorescent labelling (e.g. cell/tissue imaging, biodistribution mapping) is one of the primary interests in colloidal semiconductor QDs, and considerable progress in converting inorganic nanoparticles into biocompatible robust fluorophore for extensive biological work has been reported in the past decade and a half.[72, 255-257] The favourable optical characteristics of semiconductor QDs, such as tuneable emission, high photoluminescence quantum yield (PL QY) and photo-stability, could provide distinct advantages over conventional dyes for fluorescent imaging applications.[127, 258] However, the synthetic nature of commonly used monodispersed QDs dictates that most of as-prepared colloidal QDs have a hydrophobic surface, which would hinder further biological applications in aqueous environments. Two options are suggested in order to address the problem: altering the reaction medium to an aqueous solution ("aqueous synthesis") as discussed in Chapter 2, or modifying the hydrophobic surface to hydrophilic ("phase transfer"). Considering the former option, the synthesis of water-soluble (typically thiol-capped) QDs has been extensively studied because the method is simple and can provide particles which can be readily used in biological applications,[156, 160, 246] although poor morphology would still need to be addressed.[259] Whilst several synthetic steps are necessary, the latter option can circumvent the problems which arise from the aqueous synthesis by using robust, bright and high quality QDs (e.g. CdSe/ZnS QDs) as a starting material.

The significance of the surface modification of hydrophobic QDs was originally described by the work of two research groups in 1998,[118, 119] and important breakthroughs have been reported by other groups afterwards.[258, 260-262] In all studies,

researchers have overcome the sensitive nature of surface chemistry and succeeded in retaining the strong emission of the QDs, despite the fact that emission from colloidal QDs can be easily quenched. The surface modification of the colloidal QDs can be further subcategorised; ligand exchange and surface encapsulation (Figure 5.1). The ligand exchange is a post-synthetic treatment where hydrophobic surfactants are replaced with hydrophilic alternatives, whereas the surface encapsulation is a process to cover the hydrophobic surfactants with amphiphilic molecules. These processes have their own advantages, depending on their possible applications. For example, the ligand exchange generally requires only simple steps (typically mixing with an excess amount of hydrophilic surfactants and stirring for a couple of hours to a day), hence is reproducible and a number of reports described this method in imaging studies.[131, 164, 166, 176, 177, 189] However, the QDs covered with hydrophilic ligands, typically short alkyl thiols, which are less stable, are known to be cytotoxic in some studies, and the process is also known to quench emission.[163, 166] Therefore, additional surface treatment (e.g. silica coating, polymer coating) will be required for practical applications.[118, 134, 263] Recently, polyethyleneimine (PEI) was found to be a useful ligand exchange agent.[261, 264] The resulting QDs-PEI-polyethylene glycol (PEG) conjugates were biologically stable and showed endosomal disruption. Also, a novel ligand exchange strategy using metal chalcogen complexes has been reported, describing a versatile method for dissolving nanoparticles in various solvents whilst keeping their optical and structural properties,[262] although the usefulness in biological imaging is yet not fully realised.[265-267]

Alternatively, the surface encapsulation techniques using synthetic amphiphilic molecules have been developed to maintain the optical properties of QDs for biological applications. The amphiphilic molecules can be phospholipids,[173, 258, 268] poly(styrene *co*-maleic anhydride),[269] and multidentate molecules.[259, 270, 271] Also, electrostatic interaction is proven to form an additional surrounding layer.[272] In addition to converting the polarity of the QD's surface, additional functionalities can be added by attaching other molecules or functional groups on the outer layer of the amphiphilic molecules. For example, PEG is commonly known to prevent non-specific adsorption inside the biological entity.[258]

In this work, hydrophobins (amphiphilic proteins) were used as a phase transfer agent for colloidal QDs, from organic to aqueous solvent. Hydrophobins are small proteins consisting of approximately 100 amino acid residues, originated from filamentous fungi.

The prime function of the protein is lowering the surface tension of materials, allowing them to escape an aqueous environment and to enhance their dispersion capability in air.[273] Because of the amphiphilic nature of the protein, it is hypothesised that the hydrophobic moiety of the hydrophobins interacts with the surface of hydrophobic QDs to form hydrophobin-QDs bioconjugates. Furthermore, the biocompatibility of the protein could prevent non-specific binding, as well as providing stability against pH and ionic salts arising in biological media.[274] In this study, CdTe/ZnS QDs were synthesised in organic media and the phase transfer reaction using hydrophobins was examined. Because of their versatility, biocompatibility and simplicity, hydrophobins are an attractive phase transfer agent for inorganic nanomaterials in biological applications.

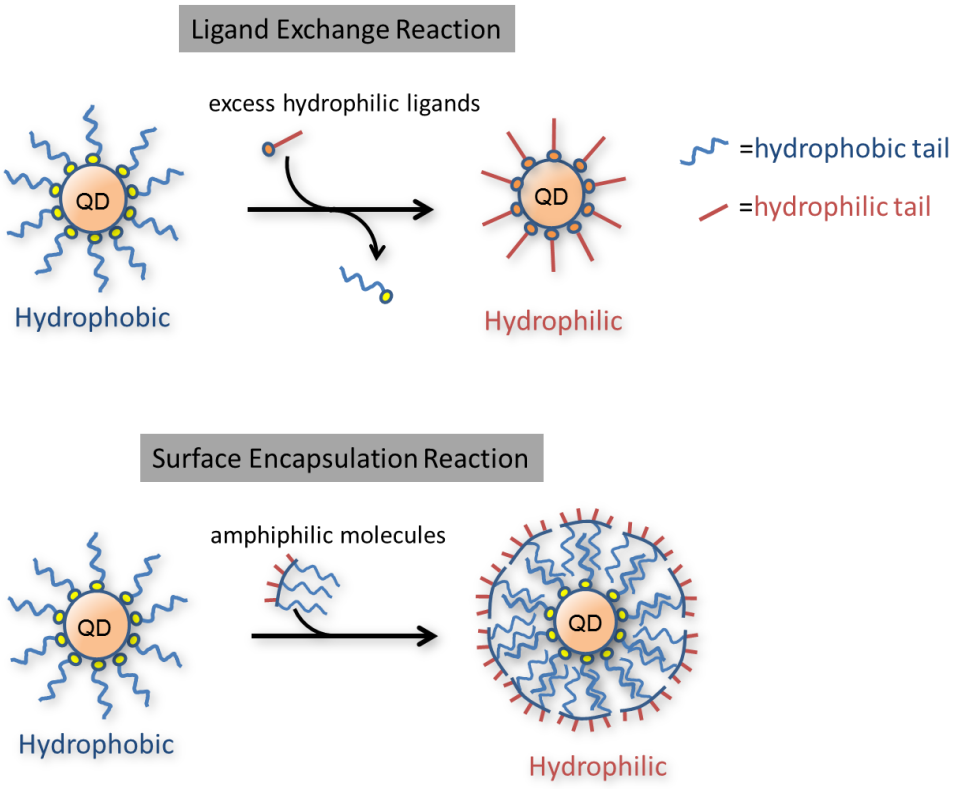

Figure 5.1. Schematic diagram of two phase transfer reactions of hydrophobic QDs.

5.2 Characteristics of Hydrophobins

Although the protein sequence differs between originating organisms, hydrophobins typically have eight cysteine residues in a specific pattern in its sequence, which contributes to the hydrophobin's specific characteristics and structural robustness.[275] Early studies showed that hydrophobins can be further divided into two classes depending on genetic patterns: class I and class II. The sequences could be classified based on the occurrence of hydrophilic and hydrophobic amino acid residues in the protein sequence *via* their hydropathy plots.[276, 277] These proteins have significant differences in solubility and polymeric structure, whilst maintaining their amphiphilic nature. Class I hydrophobins are stable proteins with relatively large molecular masses compared to class II hydrophobins and form highly insoluble aggregates in aqueous solution (typically rod-like aggregations).[275, 278] In addition, the proteins have a higher stability versus solvents and detergents.[273] Class II hydrophobins have lower molecular mass of less than 10 kDa and are easily dissolved at high concentration.[274]

The hydrophobin used in this work was obtained as a commercial product named H*Protein B from BASF. The H*Protein B is a recombinant protein consisting of hydrophobin DewA (*A. nidulans*) and the 40 N-terminal amino acids of yaaD with a molar mass of 18.8 kDa.[273] The protein is classified as a class I hydrophobin and showed reasonable similarity to other class I hydrophobins in oligomerisation and emulsification properties. (As the company does not provide the product based on class II hydrophobins, we used the class I hydrophobins as a phase transfer agent.) The H*Protein B showed characteristic protein self-assembly-type behaviour depending on concentration, ionic strength, surfactants and temperature. Figure 5.2 shows the number distribution versus hydrodynamic diameter taken by dynamic light scattering (DLS). The peak at 15 nm disappeared after dilution, whereas the peak at around 1.5 nm increased and became narrower. This behaviour can be explained as self-assembled hydrophobins exhibited agglomerated structures at the beginning of dilution, which gradually dis-assembled to lower sized structures, which is in good agreement with other experimental observations.[273] The final hydrodynamic diameter calculated from DLS result was 1.2 nm ± 0.2 nm, which is a close value to the hydrodynamic diameter of H*Protein B diluted 100 times and stored at 4 °C over a day (1.3 nm ± 0.3 nm).

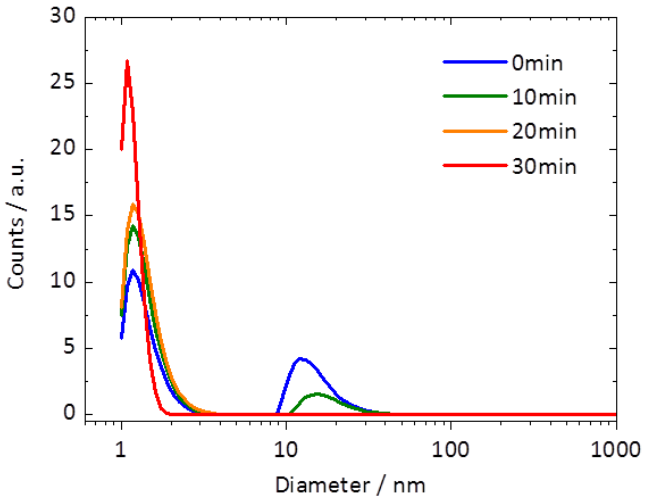

Figure 5.2. Number distribution of 150 µL H*Protein B solution diluted with 3mL deionised water, measured initially (blue), 10 minutes (green), 20 minutes (orange) and 30 minutes (red) after the dilution.

5.3 Preparation of Water-soluble Hydrophobin-CdTe/ZnS QDs

Many studies have focused on the hydrophobin's capability of altering the polarity of surfaces, converting hydrophobic surfaces to hydrophilic or *vice versa*. Potential envisaged applications by surface modification with hydrophobins are drug delivery,[274, 279] biosensing,[280] lithographic processing,[281] and surfactants.[273, 282, 283] Particularly, Linder and co-workers have published several studies, suggesting the application of hydrophobins as phase transfer agents in material sciences. For example, the hydrophobic surface of single-walled carbon nanotubes (SWCNTs) was covered with class II hydrophobins to induce dissolution in water, in addition to conjugation with gold nanoparticles (Au NPs) forming SWCNT-hydrophobin-Au NPs bioconjugations.[284] The group also applied the analogous procedure to solubilise graphene sheets in aqueous solution.[285] Therefore, it is reasonable to assume that surface modification using hydrophobins can be applied other nanomaterials such as QDs.

For the phase transfer experiments, oleylamine (OAm)-capped CdTe/ZnS QDs with a ZnS thickness of 6 monolayers (theoretical value) were synthesised and used as starting

nanomaterials, following a previously reported procedure with some amendments (detailed synthetic procedure can be found in Chapter 6.5.1).[153] The resulting CdTe/ZnS QDs had a narrow emission profile at 659 nm with a FWHM of 29 nm, indicating a good mono-dispersity. For the phase transfer, H*Protein B solution (50 mg/mL) was diluted 20 times in deionised water, sonicated with an ultrasonic bath for a minute to ensure protein dispersion. To 2 mL of protein solution, 50 μL of concentrated CdTe/ZnS QDs/hexane solution (concentration assumed to be up to 5 μM)[148] was added, followed by sonication again (5 minutes). The water/hexane mixture was subsequently emulsified to a stable cloudy solution, and the solution retained bright photoluminescence under UV excitation (365 nm) (Figure 5.3). See Chapter 6.5.2 for more detailed reaction procedures.

Hydrophobins are known to be robust and it is unlikely that sonication affected the structure. For example, it is suggested that the class II hydrophobin keeps its secondary and ternary structure after exposure to sodium dodecyl sulfate, a compound routinely used to denature proteins.[282] In addition, ultrasound treatment has been applied in some phase transfer reactions using both class I and class II hydrophobins, showing no evidence of protein unfolding.[280, 284, 285] Despite the H*Protein B having minor differences from these proteins in the amino acid sequence, it is possible that the H*Protein B kept its structure after ultrasound treatment in our study, given the functional similarity provided elsewhere.[273]

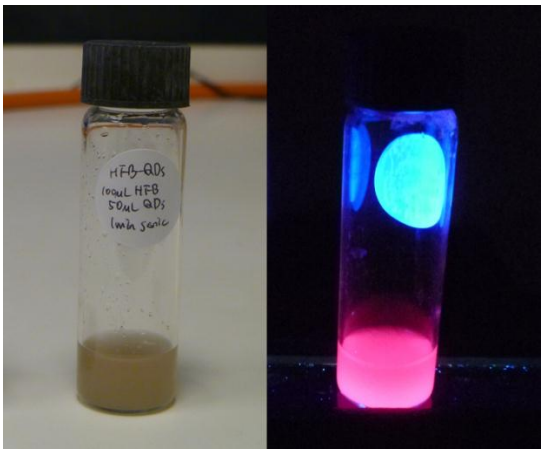

Figure 5.3. As-prepared hydrophobin-CdTe/ZnS QDs solution under room light (left) and UV lamp excitation (365 nm, right).

After the phase transfer reaction, it was observed that the initial cloudiness gradually cleared to over three hours storage, although the solution after standing overnight still retained turbidity to some extent. The gradual fading of the cloudiness can be explained as a result of the hydrophobins' slow dynamic transition and the reorganisation of micelles in solution. Figure 5.4 (a) shows absorption and emission spectra of hydrophobin-CdTe/ZnS QDs which were isolated *via* filtration (11 μm cut-off). The absorption profile clearly indicated characteristics associated with the original semiconductor QDs and there was no significant change from original hydrophobic CdTe/ZnS QDs (Figure 5.4 (b)) except a small back ground absorbance which arose after the phase transfer, presumably due to the turbidity of the solution. Additionally, emission profile after the phase transfer was almost unchanged with the emission peak at 662 nm with a FWHM of 30 nm. The emission efficiency was decreased (about a half), although direct comparison is difficult because of the cloudiness. The decline of emission efficiency is a phenomenon often observed in phase transfer in ligand exchange reaction, whilst not in surface encapsulation.[177, 261, 269, 270] This small quenching suggests that the exciton from the QDs is not completely isolated from the outer environment, even though the CdTe is coated with a ZnS shell and a hydrophobic layer.

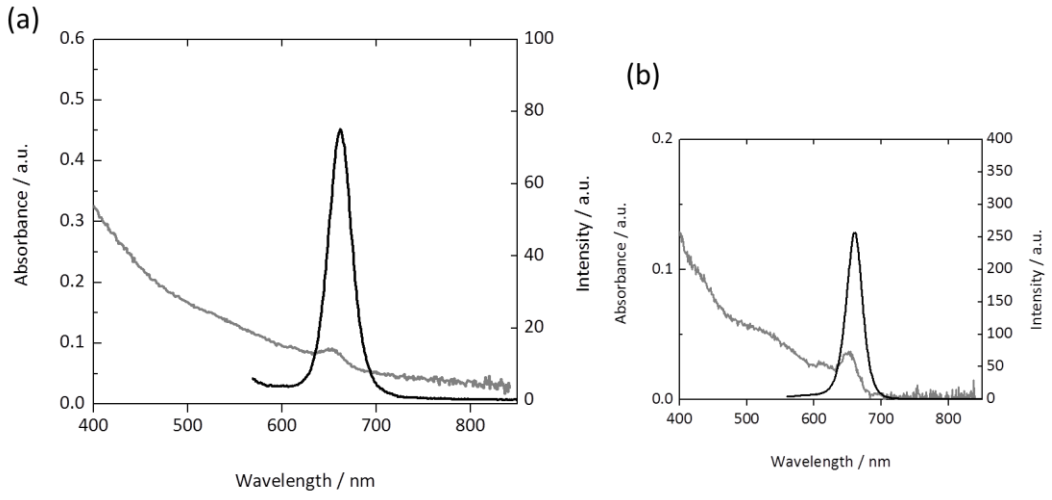

Figure 5.4. (a) Absorption and emission spectra for hydrophobin-CdTe/ZnS QDs (excitation wavelength = 550 nm). Grey lines show absorption spectra (scale on the left side), whilst black lines indicate emission spectra (scale on the right). (b) Optical spectra of CdTe/ZnS QDs before phase transfer.

Figure 5.5 (a, b) shows TEM images of hydrophobin-CdTe/ZnS QDs. The nanoparticles, which are assumed to be CdTe/ZnS QDs, can be observed in both micrographs. Also, as can be seen in Figure 5.5 (b), the electron micrograph shows a darker area located on the TEM grid. Given the reaction procedure, where the molar ratio of hydrophobins:QDs was approximately 1,000:1, with no further isolation other than centrifugation (4,000 revolutions per minute (rpm), 2 minutes) and filtration (11 µm cut-off, it is plausible that the dark contrast comes from the proteins. This was confirmed by DLS, showing no signal corresponding to individual hydrophobin-CdTe/ZnS QDs (which is thought to be around 10-20 nm) (Figure 5.6). The number distribution showed a predominant signal at 1.5 nm, due to excess hydrophobins. Further procedures for isolating hydrophobin-CdTe/ZnS QDs from unreacted hydrophobins were therefore necessary for any practical applications.

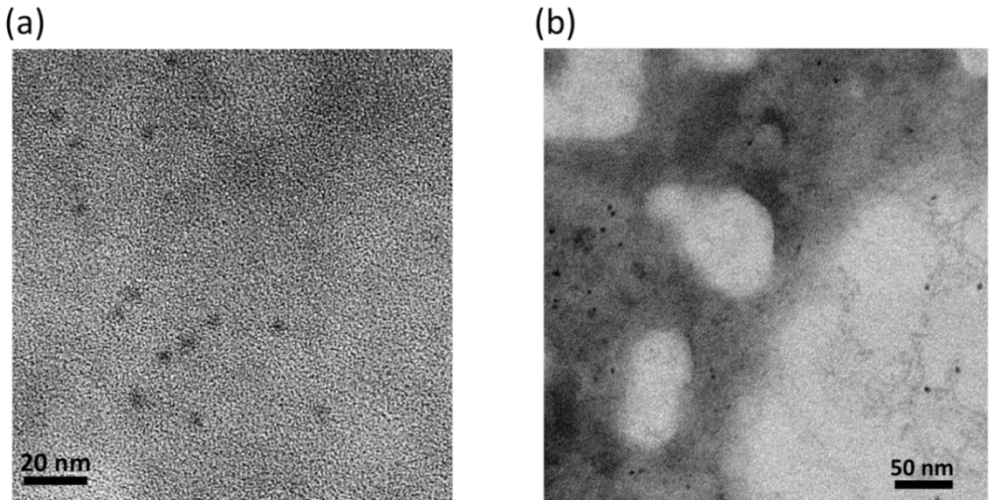

Figure 5.5. TEM images of hydrophobin-CdTe/ZnS QDs. (a) high resolution and (b) low resolution micrographs, respectively.

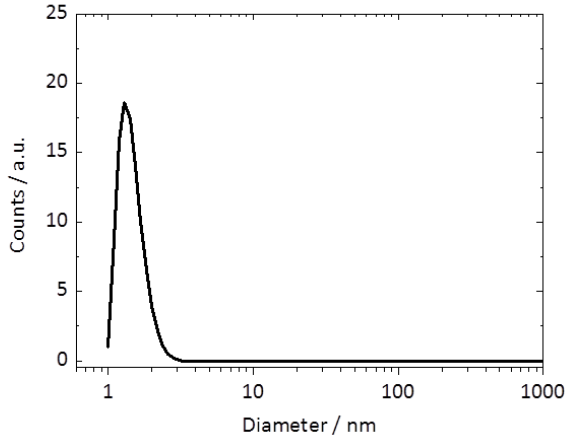

Figure 5.6. Number distribution of hydrophobin-CdTe/ZnS QDs after filtration (11 μm cut-off) and centrifugation. A peak at 1.5 ± 0.3 nm was detected by DLS.

5.4 Other Methods for Phase Transfer

Several other methods have been explored for a better understanding of the phase transfer using hydrophobins. Table 5.1 summarises the phase transfer reactions with hydrophobins in different conditions. These reactions were inspired from the literature, focusing on phase transfer reactions of colloidal QDs from organic solvent to water. Unfortunately, none of these methods gave water-soluble QDs with bright emission. For example, Method 1 in the Table 5.1 is a common proven strategy.[258, 261, 264, 270] However, this technique was not applicable to hydrophobins, as they crystallised after the evaporation of water and found to be insoluble in both organic solvents and water, which prevented further processing that is essential in this method. Method 2 is a simple shaking, in which Wohlleben *et al.* showed that oil/water emulsions were successfully formed by adding up to 5 ppm of H*Protein B.[273, 279] In our work with H*Protein B/water and CdTe/ZnS QDs/hexane, despite an initial formation of emulsion after several times of manual shaking, the solution appeared less stable and tended to separate into two original layers after overnight storage. Method 3, where precipitated QDs are stirred in protic solvents such as ethanol with excess phase transfer reagents, is referred from ligand exchange reactions using small organic molecules (Figure 5.1, top).[131, 164, 176, 177, 189] Although the QDs appeared to be dispersed in the hydrophobin-ethanol mixture, the emission of the QDs was completely quenched during the reaction. Also,

the resulting materials could not pass through an 11 μm cut-off filter, indicating the formation of large aggregates.

The phase transfer method described in Chapter 5.3 was therefore used, and all further discussion refers to this method.

	procedure	result	comment
Method 1	mixing amphiphilic molecules and QDs in chloroform → evaporation of solvents → re-dispersion in water	H*Protein B did not dissolve in chloroform.	Class I hydrophobins are known to form solids that are hardly soluble in water and organic solvents.
Method 2	mixing QDs/hexane and hydrophobin/water → manual shaking → leaving for 24 hours	The solution separated in water/hexane layers.	No emission was observed in aqueous layer, whilst the organic layer retained the emission from QDs.
Method 3	precipitation of QDs by ethanol → stirring the precipitants with excess hydrophobins in water/ethanol mixture	The QDs did not re-disperse in water.	Emission of QDs was quenched.

Table 5.1. Phase transfer methods known commonly in colloidal QDs, the obtained results when used with H*Protein B and comments.

5.5 Purification of Hydrophobin-CdTe/ZnS QDs

Two strategies have been examined for isolating the hydrophobin-CdTe/ZnS QDs from excess hydrophobins and other by-products in the solution: ultra-centrifugation and the use of centrifugal concentrator. It is expected that ultra-centrifugation could precipitate hydrophobin-CdTe/ZnS QDs selectively as the material should have a larger density than other dissolved constituents such as hydrophobins or other small molecules. In ultra-centrifugation, which was carried out with the support of Dave Lincoln at the School of Biomedical Sciences, King's College London, 5 mL of the hydrophobin-QDs solution (after 11 μm cut-off filtration) was applied at 300,000 g for 30 minutes, yielding a brown pellet. The pellet was re-dispersed in water and the optical properties were characterised. Figure 5.7 (a) shows absorption and emission spectra of hydrophobin-CdTe/ZnS QDs recovered in water from the pellet. The emission was quenched dramatically and no visible fluorescence was observed under excitation at 365 nm, whilst the absorption profile maintained its shape. DLS results showed a peak at 26.5 ± 9.5 nm (Figure 5.7 (b)). Interestingly, signals from the small size range that was

predominant in Figure 5.6 were not present due to the removal of free hydrophobins by ultra-centrifugation. In the TEM image (Figure 5.7 (c)), a number of clustered small particles up to 100 nm were observed. Figure 5.7 (d) is a high resolution TEM image, showing spherical particles (average 4.5 ± 0.6 nm) with high contrast from the background. The particles were clustered, and it is likely that the hydrophobins encapsulated numerous particles. For example, some particles seen in the Figure 5.7 (d) had an inter-dot distance as short as 2.0 nm. Given the weight of H*Protein B (18.8 kDa),[283] it is reasonable that the majority of particles were separated *via* the surfactant molecule (OAm), and hydrophobins did not participate in single particle encapsulation. Possibly, hydrophobins formed relatively larger micelles as indicated in DLS result and internalise CdTe/ZnS QDs.

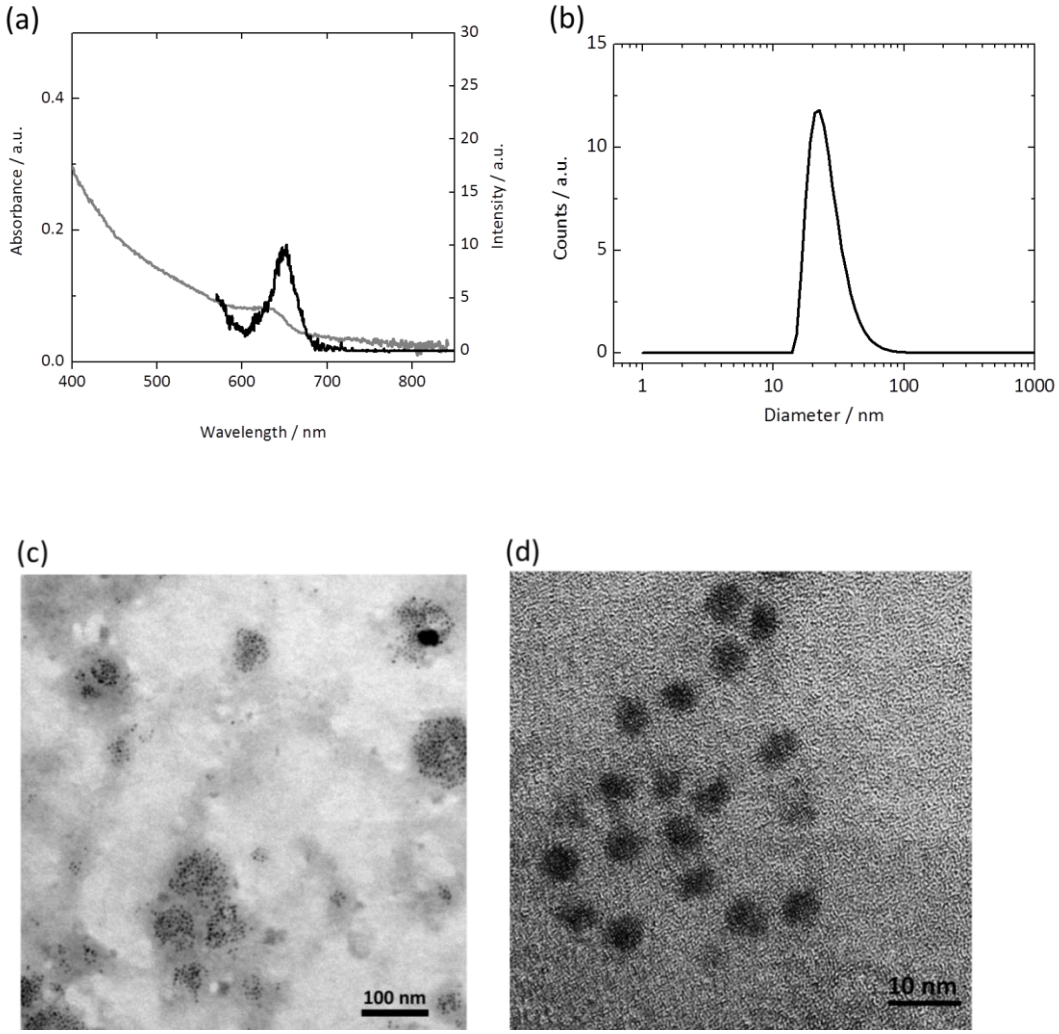

Figure 5.7. (a) Absorption (grey line) and emission (black line) spectra for hydrophobin-CdTe/ZnS QDs after ultra-centrifuge. Excitation wavelength was 550 nm. (b) Number distribution of the hydrophobin-CdTe/ZnS QDs. A peak at 26.5 ± 9.5 nm was observed. (c) Low resolution and (d) high resolution TEM images of the hydrophobin-QDs.

Purification using a centrifugal concentrator has also been examined. The centrifugal concentrator with an appropriate cut-off range (100 kDa in this work) should exclude the proteins and other small molecules whilst keeping relatively large hydrophobin-QDs conjugates in solution. In a typical reaction, 2 mL hydrophobin-CdTe/ZnS QDs (after brief filtration by a filter paper (11 μm cut-off) and following centrifugation at 4,000 rpm for 2 minutes) was put in a centrifugal concentrator and centrifugation was applied at 5,000 rpm for 5 minutes, giving a concentrated solution *via* removal of the solvent and the small molecules. The concentration process was repeated until the volume of the solution became 200 μL. The process was repeated twice and the concentrated product was diluted with pure water for further analysis. Figure 5.8 shows the emission and absorption spectra of the product after treatment by a centrifugal concentrator. The absorption excitonic peak at 640 nm became more prominent, compared to the sample before the centrifugal concentrator treatment (Figure 5.4, absorption profile), implying a removal of excess hydrophobins. The emission profile appears unchanged and the fluorescence of the solution was visible under UV excitation at 365 nm (Figure 5.9). The PL QY of the final product was 3.5 % from 15 % of the original CdTe/ZnS QDs in hexane.

Analysis of the hydrophobin-CdTe/ZnS QDs after centrifugal concentrator treatment was undertaken using TEM and DLS (Figure 5.10). Unlike samples purified by the ultra-centrifugation, the particles were completely separated from each other. Nonetheless, there were clusters consisting of several nanoparticles (mostly two to three particles) still present. These results suggest that the hydrophobin-CdTe/ZnS QDs formation is a competitive reaction between single particle encapsulation and multi-particles encapsulation. Additionally, DLS result supports the argument, showing two peaks at 14.2 ± 2.0 nm, and 49.9 ± 15.5 nm. The smaller peak could be assigned to single-particle encapsulation of hydrophobin-QD conjugates, whereas the larger peak was thought to be multiple-particle encapsulation. The suggested hydrophobin-QDs formation mechanism is illustrated in Figure 5.11.

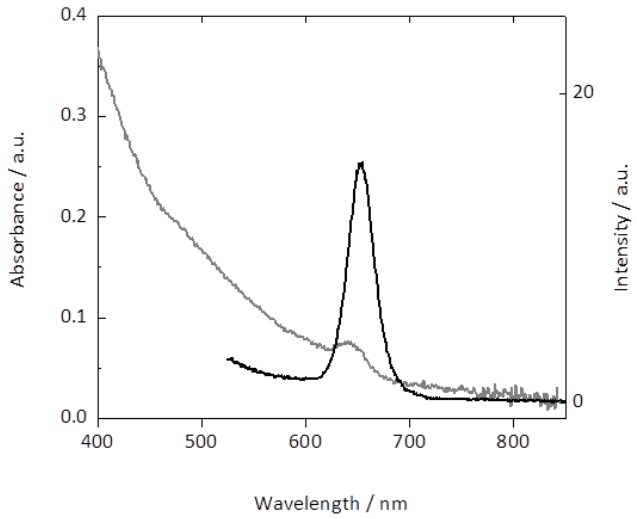

Figure 5.8. Absorption (grey line) and emission (black line) spectra for hydrophobin-CdTe/ZnS QDs after centrifugal concentrator treatment. Excitation wavelength = 500 nm.

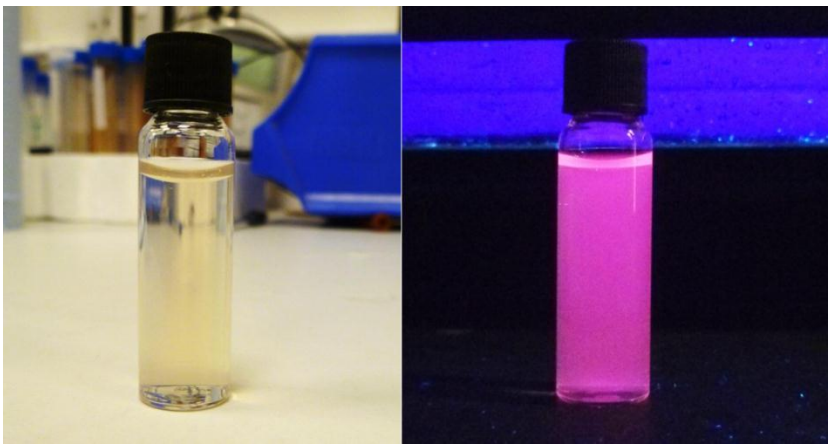

Figure 5.9. Hydrophobin-CdTe/ZnS QDs after the centrifugal concentrator treatment under room light (left) and under UV excitation at 365 nm (right).

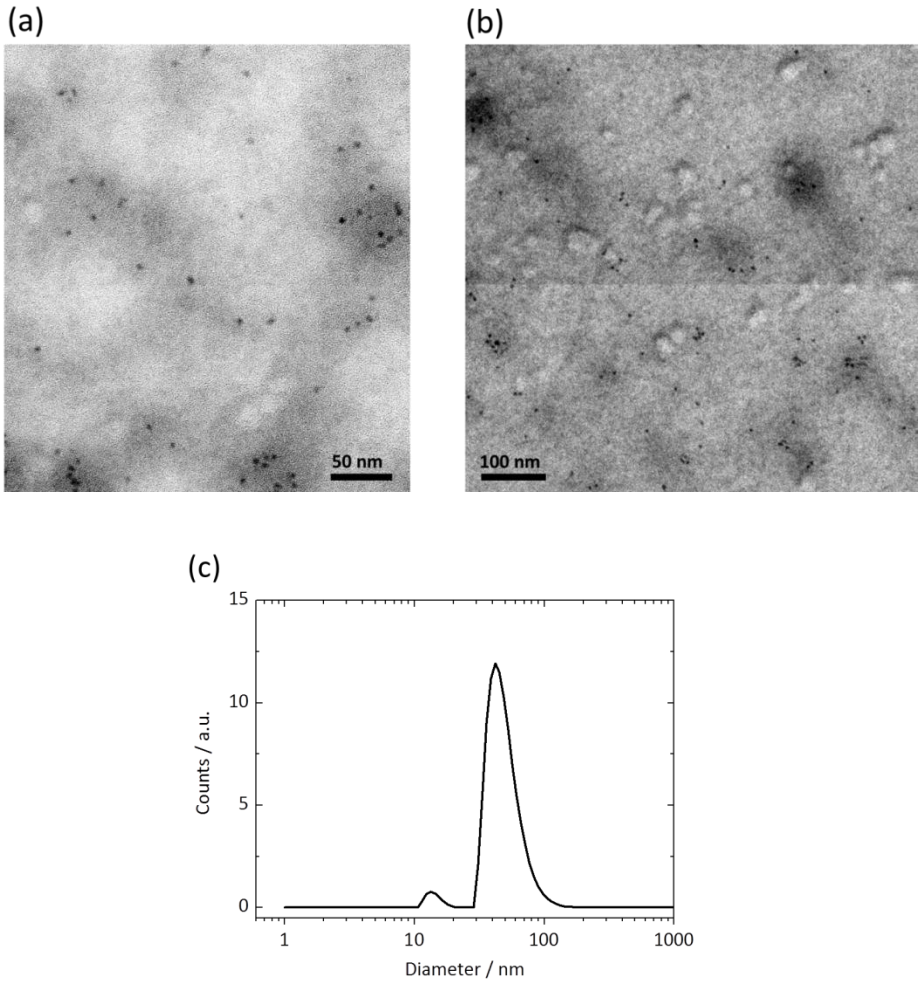

Figure 5.10. (a,b) TEM images of hydrophobin-CdTe/ZnS QDs after centrifugal concentration treatment. (c) Number distribution of the hydrophobin-QDs conjugates. Two peaks (14.2 ± 2.0 nm, 49.9 ± 15.5 nm) were observed.

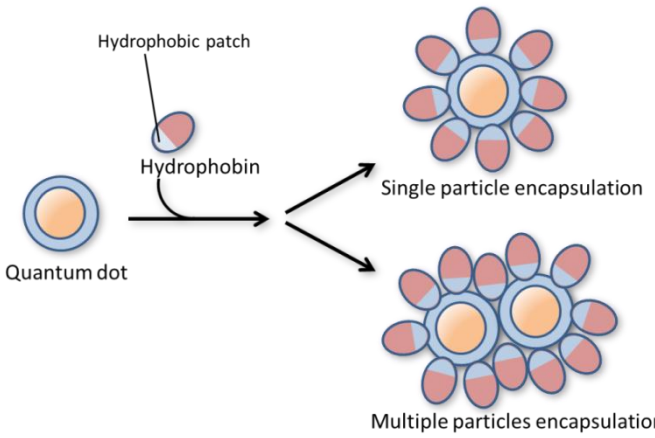

Figure 5.11. Possible mechanism of hydrophobin-QDs conjugation. Hydrophobic moieties are coloured light blue, whilst hydrophilic moieties are coloured red.

Considering these results, a centrifugal concentrator would be a more favourable way to purify the hydrophobin-CdTe/ZnS QDs. Thus, the samples treated with the centrifugal concentrator were used for further imaging work.

5.6 Phase Transfer Using Other QDs

The viability of the phase transfer reaction described above was tested using different type of colloidal QDs. As a standard nanomaterial, commercially available CdSe/ZnS core-shell QDs, dissolved in toluene, were reacted with H*Protein B followed by the analogous procedure described above and purified further by the centrifugal concentrator. Figure 5.12 shows absorption and emission spectra of purified hydrophobin-CdSe/ZnS QDs. The absorption and emission profiles were mostly unchanged after the phase transfer to water (Figure 5.12 (b)). The resulting solution shown in Figure 5.13 appeared to be relatively transparent and maintained fluorescence in aqueous solution. It should be also mentioned that emission efficiency was decreased after the phase transfer, which was a similar consequence to CdTe/ZnS QDs based products. The final PL QY of hydrophobin-CdSe/ZnS QDs was 3.0 % from 10 % of the original as-received CdSe/ZnS QDs in toluene.

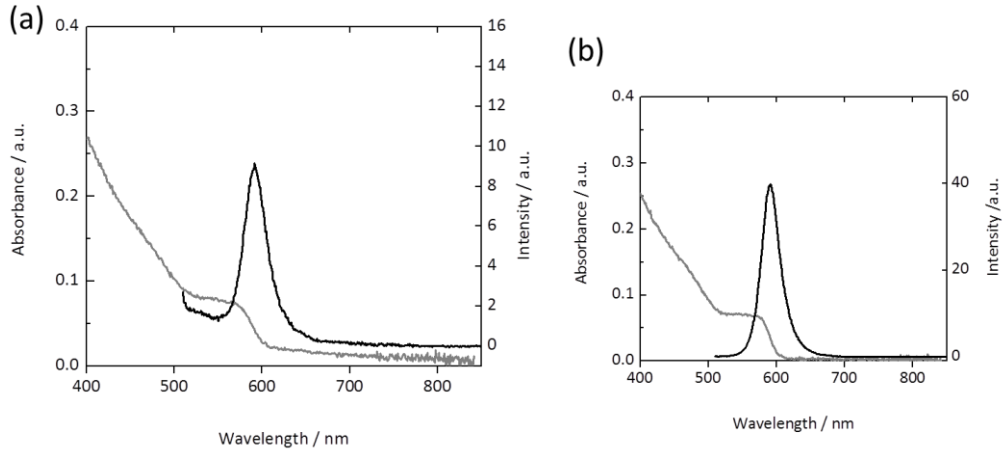

Figure 5.12. Absorption and emission spectra of (a) hydrophobin-CdSe/ZnS QDs in water and (b) CdSe/ZnS QDs in toluene before the phase transfer. Grey curves and black curves indicate absorption and emission spectra, respectively. Excitation wavelength was 500 nm.

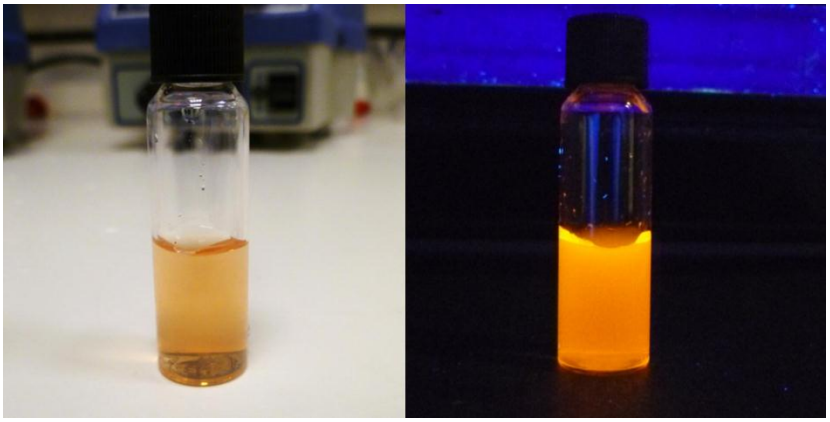

Figure 5.13. Hydrophobin-CdSe/ZnS QDs after the centrifugal concentrator treatment in room light (left) and under UV excitation at 365 nm (right).

Hydrophobin-CdSe/ZnS QDs were analysed by TEM and DLS. Electron micrographs in Figure 5.14 (a, b) shows clustered elongated particles. An anisotropic structure is commonly seen in CdSe/ZnS QDs,[61] and no structural change in CdSe/ZnS QDs after the reaction is assumed. However, hydrophobin-CdSe/ZnS QDs appear to form clusters more likely than the CdTe-based reaction, as shown in Figure 5.14 (b). This can be explained by the fact that CdSe/ZnS QDs have different surface environments when compared to the CdTe/ZnS QDs (different particle size, particle shape and surfactant molecules). It is necessary to systematically study how these differences have an effect on the optical/structural properties of the resulting products. Figure 5.14 (c) shows the number distribution based on DLS, giving consistent pattern with previous result from hydrophobin-CdTe/ZnS QDs (Figure 5.10 (c)). Two peaks were seen in the hydrophobin-CdSe/ZnS QDs as well, but peak diameters were slightly different to those observed with CdTe/ZnS QDs; the smaller peak was at 9.4 ± 2.1 nm, and the larger peak at 60.1 ± 19.5 nm. These differences can be explained by the fact that CdSe/ZnS QDs have a smaller diameter and that relatively large numbers of particles were clustered, as shown in the TEM image. However, it is difficult to quantitatively investigate the hydrodynamic diameter of hydrophobin-QDs by DLS as it is known that the signal/noise ratio of a number distribution significantly decreases at lower size ranges.[286, 287] Despite the small variances observed, CdSe/ZnS QDs were reproducibly phase transferred to aqueous solution with the analogous method described in Chapter

5.3 and Chapter 5.5. Therefore, it is expected that the phase transfer method provided in this work has a certain degree of compatibility for colloidal nanomaterials.

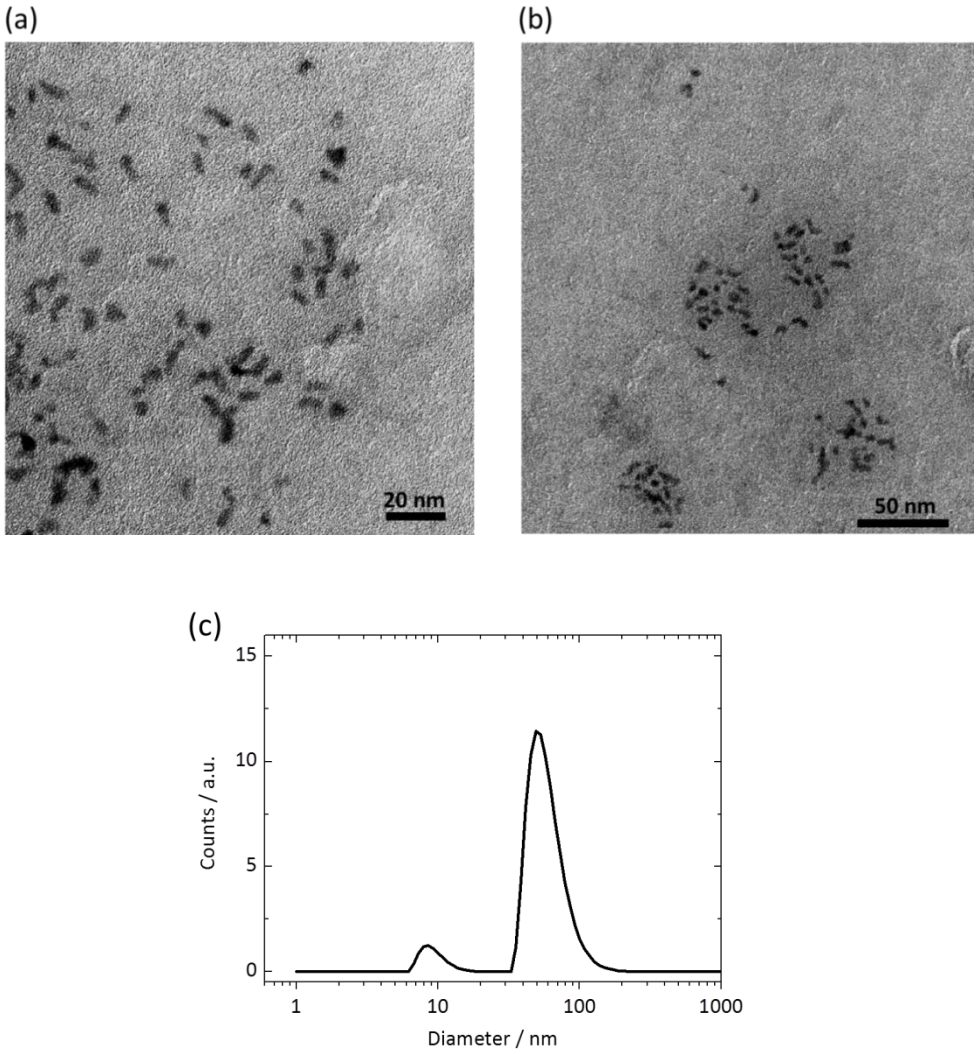

Figure 5.14. (a, b) TEM images of hydrophobin-CdSe/ZnS QDs. (c) Number distribution of the hydrophobin-CdSe/ZnS QDs conjugates.

5.7 Biological Experiments

(This work was carried out with the support of Raha Ahmad Khanbeigi and Lea Ann Dailey at the Institute of Pharmaceutical Sciences, King's College London.) Figure 5.15 shows cell viability of macrophages (J774A.1) after 2 hours exposure to hydrophobin-CdTe/ZnS QDs before and after the centrifugal concentrator treatment (detailed

procedure is described in Chapter 6.6.3). A significant improvement in cell viability was observed after the centrifugal concentrator treatment, whilst the sample before the treatment showed only 30 % cell viability. The possible explanation is the existence of excess hydrophobins, as well as potential impurities such as organic surfactants and organic solvent, which are likely to be acutely toxic to macrophages.

Using the same hydrophobin-CdTe/ZnS QDs after the centrifugal concentrator treatment, cell imaging experiment using the macrophages was explored (Figure 5.16). Figure 5.16 (a) indicates the typical staining of the nuclei by standard fluorescence dyes (4',6-diamidino-2-phenylindole (DAPI)), and the light-green signal seen in Figure 5.16 (b) is hydrophobin-CdTe/ZnS QDs. It showed that most of the light-green fluorescence was observed in the peripheral region of the nuclei, which is not consistent with a typical nanoparticles uptake *via* phagocytosis, in which the fluorescence could be observed as vesicles inside the cytosol.[288] Hence, we suggest that hydrophobin-CdTe/ZnS QDs were attached on the cell surface or trapped in the membrane of the macrophages (also, it is possible that the particles were fixed on the glass surface through the experimental setup). The observed fluorescence images strongly indicated a non-specific binding of the hydrophobin-QDs on the surfaces. Therefore, it is essential to control the surface environment of the hydrophobin-QDs as there are several factors to explore in order to optimise the cell uptake of nanoparticles. For example, the hydrophobicity of the surface of the hydrophobin-QDs is not fully investigated, whilst it is possible that free cysteine moieties in the hydrophobins interact with biological materials. Surface modification such as PEG coordination could mitigate the non-specific bindings, whereas bioconjugation with signalling proteins such as transferrin is known to mediate the endocytosis.[119, 258]

Further investigation for the improvement of the optical properties of the resulting hydrophobin-CdTe/ZnS QDs is currently underway, as well as an optimisation of the cell imaging experiment.

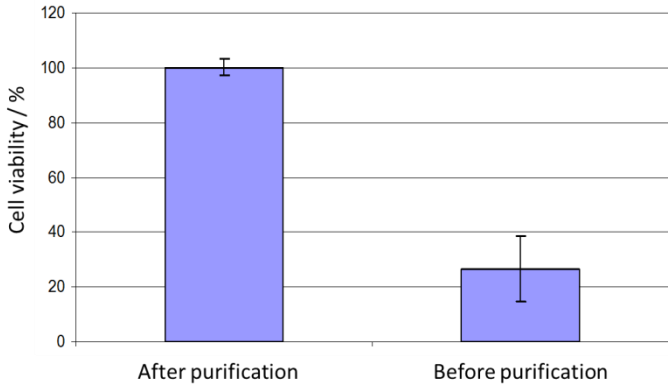

Figure 5.15. Cell viability of macrophages after 2 hours incubation with hydrophobin-CdTe/ZnS QDs. Left bar represents the sample after the centrifugal concentrator treatment, whilst right bar represents before the treatment. The viability was quantified by crystal violet staining, followed by the measurement of absorption.

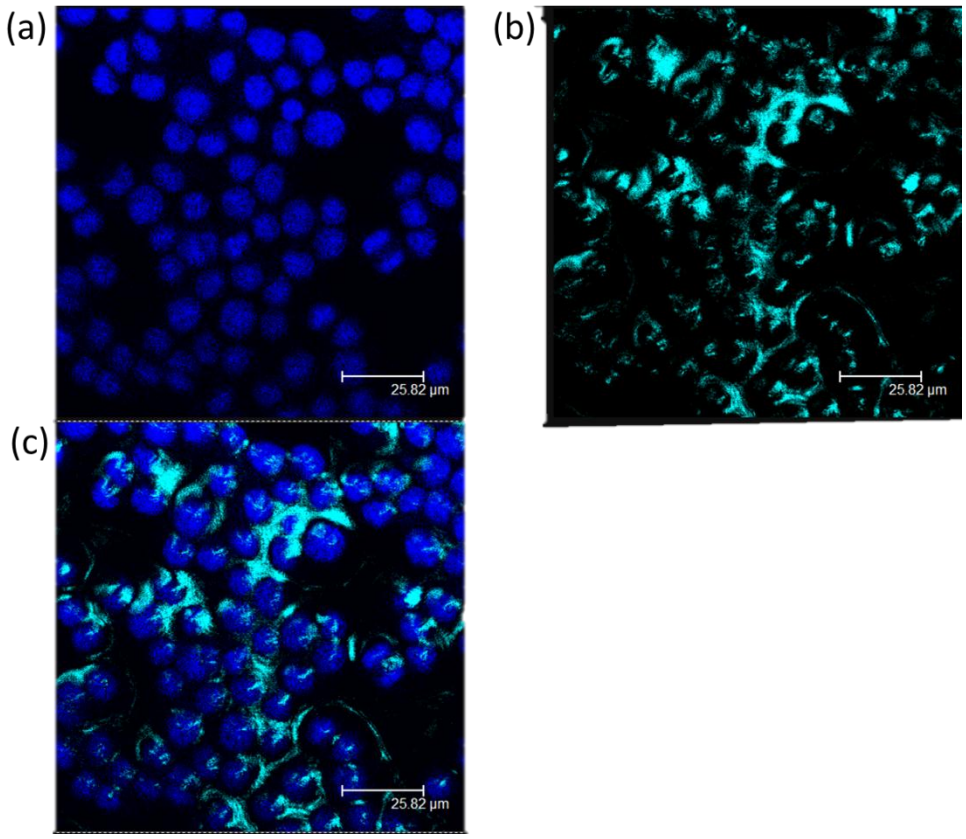

Figure 5.16. Macrophages cells incubated with hydrophobin-CdTe/ZnS QDs. (a): The blue stain represents depicts the cell nuclei. (b): The light-green stain represents the fluorescence channel used to attempt to determine QD fluorescence (excitation wavelength = 514 nm, detection wavelength = 500-550 nm). (c): An overlap with image (a) and (b). The image plane is set at approximately 50% of the total cell height.

5.8 Conclusion

As a phase transfer agent, a commercially available recombinant hydrophobin, H* Protein B, was applied to inorganic nanoparticles. CdTe/ZnS QDs were made water-soluble by co-sonication with the hydrophobins, resulting in a cloudy hydrophobin-CdTe/ZnS QDs solution. The solution maintained the same optical profiles and retained bright emission. Excess hydrophobins dissolved in the solution could be removed by using a centrifugal concentrator. TEM images of the purified hydrophobin-CdTe/ZnS QDs showed that the products were homogeneously dispersed, forming either single particle-proteins conjugation or multiple particles-proteins conjugations. The phase transfer method was successfully applied to commercially available CdSe/ZnS QDs. Cell viability could be improved by the centrifugal concentrator treatment. Cell imaging studies showed no observable uptake of hydrophobin-CdTe/ZnS QDs, possibly due to non-specific binding and insufficient surface modification of the hydrophobin-CdTe/ZnS QDs.

Chapter 6

Experimental Methods

6.1 General Materials and Methods

6.1.1 Chemicals

6.1.1.1 Quantum dots

Cadmium acetate dihydrate ($Cd(OAc)_2 \cdot 2H_2O$) (98.5 %), mercaptoundecanoic acid (MUA) (95 %), tellurium powder (99.8 %), aluminium powder (99 %), 5 M ammonium hydroxide solution, selenium powder (99.8 %), sodium sulfite (98 %), zinc nitrite hexahydrate ($Zn(NO_3)_2 \cdot 6H_2O$) (98 %), L-glutathione reduced (GSH, 98.0 %), cadmium oxide (CdO, 99.5 %), trioctylphosphine (TOP, 90 %), trioctylphosphine oxide (TOPO, 90 %), stearic acid (97.0 %), hexadecylamine (HDA, 90 %), octadecylamine (ODA, 97 %), diethylzinc ($ZnEt_2$, 15 wt. % in toluene), sulfur powder (99.5 %) were obtained from Sigma Aldrich. 1-tetradecylphosphonic acid (TDPA, 98 %) was obtained from Alfa Aesar. All the chemicals were used as received.

6.1.1.2 Cation Exchange Reagents

Mercury(II) bromide ($HgBr_2$, 99.998 %), lead(II) acetate trihydrate ($Pb(OAc)_2 \cdot 3H_2O$, 99.999 %), gold(III) chloride trihydrate ($HAuCl_4 \cdot 3H_2O$, 49.0 %), silver nitrate ($AgNO_3$, 99 %) were obtained from Sigma Aldrich. All the chemicals were used as received.

6.1.1.3 Single-Source Precursors

Cadmium iodide (CdI_2, 99.0 %), sodium bis(trimethylsilyl)amide solution ($NaN(SiMe_3)_2$, 1.0 M in tetrahydrofuran), diphenyl ditelluride (PhTeTePh, 98 %),

sodium borohydride ($NaBH_4$, 99 %), zinc diethyldithiocarbamate ($ZnDDTC_2$, 97 %), oleic acid (90 %), anhydrous N,N-dimethylformamide (DMF, 99.8%), dimethyl sulfoxide-d_6 (DMSO-d_6, 99.96 atom % D) were obtained from Sigma Aldrich. Technical grade oleylamine (OAm, 70 %) was obtained from Fluka. All the chemicals were used as received.

6.1.1.4 Phase Transfer Agents

CdSe/ZnS QDs (Lumidot™590, 5 mg/mL in toluene, emission peak at 590 nm, approximate particle size = 4.0 nm)[289] was purchased from Sigma Aldrich. Hydrophobins (H*Protein B, 50 mg/mL)[290] was obtained from BASF. All the chemicals were used as received.

6.1.1.5 Solvents

1-octadecene (ODE, 90 %) was obtained from Sigma Aldrich and was degassed by the freeze–pump–thaw method before use and stored under nitrogen. Reagent grade ethanol, 2-propanol, butanol, hexane, anhydrous diethyl ether, anhydrous toluene were purchased from Sigma Aldrich. Reagent grade toluene and methanol were purchased from Fisher Scientific. Ultra-pure water (Millipore, Direct-Q 3 UV Water Purification System, 18.2 MΩ cm^{-1}) was used at all stages.

6.1.2 General Analysis Techniques

6.1.2.1 Transmission Electron Microscopy (TEM)

TEM was carried out using a Tecnai 20 (acceleration voltage 200 kV) for normal resolution images. Samples were dropped on a copper grid with a carbon amorphous film (Agar Scientific) and dried in ambient conditions.

High resolution images were obtained using a JEOL JEM-4000EX HREM at 400 kV. This work was carried out at the Department of Materials, University of Oxford with the support of Dr Teck Lim (C. Hetherington group).

Particle size analysis was performed by measuring diameters from the TEM images using ImageJ.[291] A minimum of 100 measurements were made for each sample, from which the mean and standard deviation were calculated. Both longer and shorter axes were measured per particle if the particles were anisotropic.

6.1.2.2 Optical Characterisations

Absorption spectroscopy measurements were taken using a Hitachi U-4100 UV-Visible-NIR spectrophotometer in a 1 cm path length quartz cuvette. Emission spectra were obtained using a Perkin Elmer LS 50B spectrometer.

Photoluminescence quantum yields (PL QY) were calculated by comparison with fluorescent standards. Rhodamine 6G (99 %, Sigma Aldrich) was used for the samples excited at 450-500 nm, whilst Rhodamine 101 inner salt (Sigma Aldrich) was used for the excitation at 550 nm. The PL QYs of these standards were obtained from previous reports.[199, 292] In a typical procedure, the fluorescence standard was diluted until the absorbance at the excitation wavelength was below 0.1 in order to avoid potential scattering and inner filtering effects. The emission spectrum was then taken with the same solution, and the integrated emission intensity was calculated using the obtained emission spectrum. Then, a plot was produced using the obtained absorbance and the integrated emission intensity. Measuring the absorption and emission spectra were repeated at least four times with the fluorescence standard solution diluted at an arbitrary ratio from the original solution. The same procedure was followed using the samples using the same measurement settings. The obtained values were then plotted to get the integrated emission intensity – absorbance relationship (such as Figure 2.7), followed by the calculation of the PL QY using the equation (10) in Chapter 2.2.

6.1.2.3 Powder X-ray Diffraction (XRD)

Solid samples for XRD were prepared by precipitating QDs with non-solvents several times to ensure no extra surfactant remained. The precipitate was subsequently dried by vacuum pump and stored under nitrogen before use.

XRD measurements were taken using a Panalytical X'Pert Pro MPD diffractometer using nickel-filtered copper Kα radiation operating at a voltage of 40 kV and a beam

current of 30 mA. Diffraction data were collected using an X'Celerator multiple strip detector. The diffractometer was configured to operate in programmable divergence slit mode with an observed length of 10.0 mm. The specimens were placed onto the surface of a zero-background silicon crystal sample holder during the diffraction experiments. The experimental data were processed using Panalytical Highscore Plus. The program interpolated the data to rationalise the step size to multiples of 0.001°. The data were then transposed to represent a fixed divergence slit configuration with a slit size of 1.00° as this allowed comparison to existing crystallographic databases.

This analysis was performed in ITRI labs, United Kingdom.

6.1.2.4 Dynamic Light Scattering (DLS)

DLS measurements were performed using Delsa Nano C Particle Analyzer using 1 cm path length quartz cuvettes. The experimental data were processed using DelsaNano software. Number distributions of the samples were automatically converted from the original intensity distributions by the software. Some important parameters used in the DLS measurements were listed in Table 6.1.

Dust limit	10	Analysis method	CONTIN	Cell type	Size cell
Upper dust limit	100	Weight function	1	Accumulation time	70 sec
Lower dust limit	100	Fitting range	G2(T)		
Optimum intensity	40,000	G2(T)max	2		
Maximum intensity	60,000	G2(T)min	1.003		
Minimum intensity	5,000	Noise cut level	0%		
pinhole	50 µm	Data selection	256ch exponential		
Equilibration	0 sec				

Table 6.1. Setting parameters used in DLS measurements.

6.1.2.5 Mass Spectrometry

Elemental analysis was performed using a Perkin Elmer 'Elan DRC plus' inductively coupled plasma-mass spectrometer (ICP-MS), with a Perkin Elmer 'AS93' autosampler and a cross-flow nebuliser and a Scott double pass spray chamber, using 'Elan' software (Perkin Elmer). The measurements were performed in the Mass Spectrometry Facility, King's College London with the support of Andrew Cakebread and Roger Tye.

The samples for the mass spectrometry were prepared *via* nitric acid digestion, where precipitated QDs or SSPs (<50 mg) were mixed with 1 mL nitric acid (65 %) and sonicated for 2 hours, followed by a dilution in water to obtain appropriate concentrations.

6.2 CdTe/CdSe/ZnSe QDs

6.2.1 $(NH_4)_2Te$ Stock Solution

A stock solution of $(NH_4)_2Te$ (0.16 M) was prepared as described by Boudjouk *et al.*[293] In a typical reaction, tellurium powder (1.30 g, 0.01 mol) and aluminium powder (0.77 g, 0.028 mol) were added into a 100 mL one-neck flask. Then, 60 mL of deionized water (purged with nitrogen gas) was added to the flask and stirred under nitrogen for 1 hour. Ammonium hydroxide (14 mL of 5 M aqueous solution) was added and stirred for one day. After standing for an additional 2 days, the supernatant of the solution was used for further reactions mentioned below.

6.2.2 Na_2SeSO_3 Stock Solution

The synthesis procedure for 0.25 M Na_2SeSO_3 was an amendment of that reported by Hankare *et al.*[195] Selenium powder (0.5 g, 6.3 mmol) and anhydrous sodium sulfite (1.2 g, 9.5 mmol) were added into 100 mL one-neck flask followed by 20 mL of deionized water, which was allowed to reflux for 16 hours. One hour after cooling to room-temperature, the clear portion of the solution was used for further reactions.

6.2.3 Water-soluble CdTe QDs

MUA-stabilized CdTe QDs were synthesized using the procedure reported by our group with some modifications.[121] In a typical reaction, cadmium acetate dihydrate (2.0×10^{-2} g, 0.079 mmol) and MUA (2.7×10^{-2} g, 0.126 mmol) were dissolved in 60 mL deionized water in a 100 mL three neck flask. The pH was adjusted to 11.4 using sodium hydroxide solution, which caused a cloudy dispersion, and stirred for 1 hour. The flask was degassed with nitrogen then the solution was purged with a constant stream of nitrogen gas. To the reaction flask, 0.25 mL of $(NH_4)_2Te$ stock solution (0.4 mmol) was added, causing an immediate clear brown colouration. The solution was then allowed to stir for 1 hour, followed by exposure to ambient conditions. The aqueous solution was heated to reflux for 16 hours, the solution transformed to a light yellow solution at this time, exhibiting strong green emission under UV excitation (wavelength = 365 nm).

6.2.4 CdTe/CdSe/ZnSe QDs Synthesis

To the resulting 60 mL of CdTe solution at 90 $^{\circ}$C, 0.1 mL of Na_2SeSO_3 (0.025 mmol) was added and then allowed to stir for 1.5 hours, causing a change in the solution colour from yellow to dark brown. After the reaction, 5 mL of Zn–MUA solution (0.100 mmol, obtained by dissolving 6.0×10^{-2} g of zinc nitrate and 6.7×10^{-2} g of MUA in 10 mL of deionized water, pH 11.0) and 0.1 mL of Na_2SeSO_3 (0.025 mmol) were injected twice, respectively (injection order for the CdSe/ZnSe shell was Se, Zn, Se, Zn, Se). These precursors were injected at 1 hour intervals to the solution at 90 $^{\circ}$C. Although a change in solution colour could not be observed due to the dark colouration, the emission of each aliquot was red-shifted as additional precursors were injected. The solution was then allowed to stir for 16 hours at 90 $^{\circ}$C after all the precursors had been injected. After cooling to room-temperature, a clear light brown solution exhibiting red emission resulted. The resulting solution was cloudy due to solid waste products. At any stage of the reaction (CdTe, CdTe/CdSe, CdTe/CdSe/ZnSe), the resulting material could be isolated/purified by the addition of twice volume of 1:1 isopropanol/butanol mixture followed by centrifugation (Eppendorf centrifuges 5804 with fixed-angle rotor F-34-6-38, 3,000 rpm, 2 minutes) and re-dispersion in water.

6.2.5 GSH-capped QDs

CdTe/CdSe/ZnSe QDs capped by GSH were synthesised by the similar procedure to MUA-capped QDs in this work. 20 mg of $Cd(OAc)_2$ (0.08 mmol) and 40 mg GSH (0.12 mmol) were dissolved in 60 mL deionised water and the pH was adjusted to 11.3, followed by stirring the solution for 1 hour, causing a clear solution. The solution was bubbled with N_2 gas for 30 minutes and 0.25 mL of $(NH_4)_2Te$ stock (0.04 mmol) was injected in the Cd precursor solution, causing light orange colouration. The solution was then heated at 90 $^{\circ}C$ for 1.5 hours, followed by an addition of 0.15 mL Na_2SeSO_3 stock (0.025 mmol). After heating for 2 hours, 5 mL of zinc precursor (0.10 mmol, prepared by mixing 60 mg $Zn(NO_3)_2 \cdot 6H_2O$ and 90 mg GSH) was injected, and the solution was allowed to stir for further 1 hour to yield bright dark-red solution. The purification procedure was the same as for the MUA-CdTe/CdSe/ZnSe QDs.

6.2.6 CdTe/CdSe/ZnSe QDs in Different Reaction Conditions

For the increased selenium source, 0.2 mL of Na_2SeSO_3 (0.05 mmol) was injected instead of 0.1 mL. For the reduced zinc source, 2.5 mL of zinc precursor was injected instead of 5 mL at the stage of the shell deposition. For the changes in MUA amount, 50.0 mg or 21 mg of MUA (0.230 mmol and 0.098 mmol, respectively) was used in the CdTe QDs synthesis. Other reaction conditions were the same as those described in Chapter 6.2.4 unless noted.

6.2.7 Tissue Imaging

Animals were used in accordance with an approved institutional protocol. Briefly, 6–8 week old male Wistar rats (200 g) were obtained from Charles River Labs. Anesthesia was induced by the inhalation method using isoflurane and maintained using 1.5 % isoflurane/98.5 % O_2 at 5l min^{-1}. 0.2 mL of purified CdTe/CdSe/ZnSe QDs (dried weight was *ca.* 0.1 mg) was injected subcutaneously into the hind leg of a 200 g male Wistar rat. A fixed wavelength excitation light source at 630 nm and a 680 nm long pass emission filter were used to capture *in vivo* images using a charged coupled device camera. This work was carried out at the Division of Surgery and Interventional Science, University College London by Dr Sarwat Rizvi (A. Seifalian group).

6.3 QDs for Room-Temperature Chemical Transformation

6.3.1 CdTe QDs by Organometallic Route

The basic synthetic procedure of TDPA/HDA-capped CdTe QDs was taken from Smith *et al.* with some minor amendments.[153] For TOPTe, 0.127 g (1.0 mmol) of tellurium powder was charged to a round neck flask and flushed with nitrogen. To the flask, 2 mL TOP (4.5 mmol) and 18 mL ODE were injected, followed by heating the solution at 80 °C for 30 minutes. The solution was used after cooling to room-temperature.

Into another flask, 0.025 g of CdO (0.2 mmol) and 0.22 g of TDPA (0.8 mmol) were charged, then the atmosphere was repeatedly evacuated and replaced with nitrogen, followed by heating at 250 °C until the reagents turned clear. After cooling to room-temperature, 1.35 g of HDA (5.6 mmol) and 10 mL of ODE were added into the flask, which was then heated at 280 °C for 30 minutes. To the flask, 4 mL of prepared TOPTe (0.4 mmol of Te) was injected swiftly, causing a colour change in solution to light-yellow within a minute. The solution was then set at 270 °C and the heating maintained for 30 minutes. The solution colour after the heating was dark brown at 270 °C, which changed to a cloudy red solution at 70 °C.

6.3.2 CdSe QDs

CdSe nanoparticles were prepared according to a previous report.[189] Typically, 0.05 g (0.4 mmol) of CdO and 0.46 g (1.6 mmol) of stearic acid were charged to a round bottom flask under nitrogen. The mixture was then heated at 250 °C, yielding a clear liquid which was then cooled to room-temperature. In another flask, 10 mL of 1 M TOPSe solution was prepared by mixing 0.78 g (10 mmol) selenium powder and 10 mL TOP under a nitrogen atmosphere. To the cadmium precursor, 2.0 g (7.4 mmol) of ODA, 2.0 g (5.2 mmol) of TOPO, and 15 mL of ODE were added, then the solution was heated at 295 °C yielding a clear solution. 2 mL of TOPSe (2 mmol of Se) was swiftly injected into the cadmium precursor. The colour changed from yellow to deep red almost immediately. The solution was then maintained at 290 °C for 5 minutes, which resulted in a deep brown/red solution.

6.3.3 CdSe Nanorods

CdSe nanorods were prepared as described by Bunge *et al.*[84] For the TOPSe precursor, 0.15 g (1.8 mmol) selenium powder and 9 mL TOP were mixed at room-temperature, resulting in a clear solution. Separately, 0.11 g (0.4 mmol) of $Cd(OAc)_2$ and 0.22 g (0.8 mmol) of TDPA, and 3.77 g (9.0 mmol) of TOPO were charged to a flask followed by heating at 100 $^{\circ}$C to melt the solid TOPO. The solution was degassed and filled with nitrogen at this stage. Afterwards, the solution was heated at 320 $^{\circ}$C for 30 minutes. To the flask, 3 mL TOPSe solution (0.6 mmol Se) was injected and the solution was stirred for an additional 11 minutes, resulting in a dark brown solution.

6.3.4 CdTe Tetrapods

CdTe tetrapods were synthesised using the method described by Cho *et al.*[85] In a typical reaction, CdO (25 mg, 0.2 mmol) and oleic acid (0.3 mL, 1.0 mmol) were mixed with 10 mL ODE, followed by heating at 270 $^{\circ}$C for 30 minutes, causing a clear solution. In another flask, a Te stock solution was prepared by mixing 64 mg tellurium powder, 1.3 mL TOP and 2 mL oleic acid. The mixture was heated at 90 $^{\circ}$C for 30 minutes to ensure the solution was mixed. To the Cd precursor solution at 260 $^{\circ}$C, 0.33 mL of Te stock (0.05 mmol) was swiftly injected, causing immediate dark-black colouration. The solution was then allowed to stir for 10 minutes at 260 $^{\circ}$C.

6.3.5 Purification of Nanocrystals

The resulting CdTe QDs, CdSe QDs and CdTe tetrapods could be purified as follows: after cooling down to approximately 70 $^{\circ}$C, 3 mL of the reaction solution was mixed and extracted with 4 mL of 1:1 hexane/methanol mixture, followed by precipitation with 10 mL of ethanol (or 10 mL acetone). The precipitate was collected using centrifugation (3,000 rpm, 2 minutes) and re-dispersed in 1 mL toluene. The solution was centrifuged (4,500 rpm, 2 minutes) to remove any insoluble materials before further reactions with the quantum dots. For CdSe nanorods, 2 mL of the CdSe nanorods reaction solution was cooled down to 70 $^{\circ}$C. The solution was mixed with 2 mL toluene and 4 mL acetone, causing precipitation. The precipitate was collected by centrifugation (3,000 rpm, 2 minutes) and re-dispersed with 2 mL toluene.

6.3.6 CdHgTe Nanoalloys

The procedure was inspired from the cation exchange reaction method for Cu_2S nanocrystals with some amendments.[107, 108] A mercury cation stock solution was prepared by mixing 2 mg of $HgBr_2$ (5.6 mmol) with 10 mL methanol. Afterwards, 1 mL of the mercury stock and 1 mL of toluene were added to a glass vial with rigorous stirring. To the vial, 1 mL of the nanocrystals solution (4.35 μM, concentration of the QDs was calculated by the procedure in Appendix A) was injected swiftly, causing an immediate brown precipitation in all cases. After quenching the reaction by adding 10 mL methanol, the precipitate was collected by using centrifugation (3,000 rpm, 2 minutes), followed by decantation. The precipitate was then re-dispersed in 1 mL toluene and any insoluble material was removed by additional centrifugation (3,000 rpm, 2 minutes).

For reactions using other metal cations, typical preparations were as described above for the CdHgTe nanoparticles synthesis using an analogous number of moles of metal salt with 10 mL methanol, followed by the same purification procedure as CdHgTe.

6.4 QDs Using SSPs

6.4.1 $Cd(TePh)_2$ Synthesis

This method was inspired by the reports of the synthesis of $M(TeAr)_2$ (M = Zn, Cd, Hg; Ar = C_6H_5, 4-MeC_6H_4, 2,4,6-$Me_3C_6H_2$).[74, 234, 244] 0.436 g of CdI_2 (1.2 mmol) was put into a 100 mL two-neck flask and flushed by nitrogen three times, then the flask was cooled with liquid nitrogen. To the cooled flask, 2.4 mL of 1 M $NaN(SiMe_3)_2$ solution (2.4 mmol) was slowly injected. The reaction flask was taken from the liquid nitrogen and the mixture was gradually warmed to room-temperature with moderate stirring. After 1.5 hours, the mixture separated into yellow liquid ($Cd[N(SiMe_3)_2]_2$) with a white precipitate (NaI).

In another 100 mL two-neck flask, 480 mg of $(PhTe)_2$ (2.4 mmol) and 10 mL anhydrous diethyl ether were mixed under nitrogen, allowed to stir for 1 hour. Afterwards, the

solution was frozen with liquid nitrogen and 50 mg $NaBH_4$ (2.4 mmol) was added. The flask was kept frozen in liquid nitrogen until the Cd precursor addition. Then, the yellow Cd precursor solution was taken into a centrifuge tube filled with nitrogen, and was centrifuged at 4,000 rpm for 3 minutes, separating the clear yellow solution from the precipitates. The supernatant was taken and injected into the frozen $(TePh)_2$/diethyl ether mixture. The mixture was gradually warmed to room-temperature and stirred for 1 hour, yielding a yellow solid ($Cd(TePh)_2$) in a clear orange solution. ($Cd(TePh)_2$ precipitated out of solution.)

6.4.2 Purification of $Cd(TePh)_2$

The flask containing $Cd(TePh)_2$ in diethyl ether was sonicated to ensure no solid was attached to the flask wall. Then, all the reactants including the yellow solid were transferred to a centrifuge tube filled with nitrogen. The reagents were then centrifuged at 3,000 rpm for 2 minutes, separating the liquid/solid layers. The supernatant was then discarded and 2 mL anhydrous diethyl ether was added to wash the solid. This wash/centrifuge process was repeated twice using 2 mL anhydrous diethyl ether and 2 mL anhydrous toluene. The resulting yellow $Cd(TePh)_2$ solid in the tube was dried by vacuum to give yellow fine powder (*ca*. 200 mg). The resulting $Cd(TePh)_2$ (50 mg) was readily dissolved by 2 mL anhydrous DMF, yielding a clear yellow solution with a small amount of white insoluble material. Storage at 4 $^{\circ}$C or evaporation by vacuum gave yellow crystals. ^{1}H NMR (DMSO-d_6): δ 6.76 (t, 2H), δ 6.96 (t, 1H), δ 7.73 (d, 2H). Analysis of both $Cd(TePh)_2$ and $Cd(TePh)_2$–DMF using electrospray ionization mass spectrometry (ESI-MS) failed, possibly due to the poor solubility of the analyte in the solvent.

6.4.3 CdTe QDs Synthesis from $Cd(TePh)_2$

100 mg of $Cd(TePh)_2$ powder was charged to a centrifuge tube and filled with nitrogen. To the tube, 5 mL of TOP was injected and sonicated for 1 hour, causing a cloudy beige solution. The solution was then centrifuged at 4,000 rpm for 10 minutes, yielding a clear solution (TOP-$Cd(TePh)_2$) with a white precipitate on the bottom. 5 mL of the TOP-$Cd(TePh)_2$ was injected in 10 mL of degassed oleylamine (OAm) at room-temperature. The solution was quickly heated to 200 $^{\circ}$C to monitor the solution colour change. At the

stage of desired particle size, the reaction was quenched by cooling the reaction medium. The resulting QDs were precipitated by an addition of methanol.

6.4.4 CdTe/ZnS Synthesis

The basic synthetic procedure was taken from Chen *et al.* with some minor amendments.[250] ZnS SSPs stock solution was prepared by mixing 360 mg of zinc diethyldithiocarbamate ($ZnDDTC_2$, 1 mmol) and 5 mL TOP, followed by sonicating for 10 minutes. In another flask, 6 mL of purified CdTe QDs (50 µM in hexane) and 10 mL OAm were mixed and the hexane was evaporated at 100 °C for 30 minutes. Then, 0.25 mL of ZnS stock (0.05 mmol) was injected in the CdTe solution at 70 °C. The reaction temperature was then increased to 180 °C for 30 minutes, causing a change in solution colour to brown. Afterwards, the solution was cooled down to 100 °C for the next shell addition. After depositing the desired thickness of the ZnS shells, the crude CdTe/ZnS solution was cooled down to 70 °C and diluted with 3 mL of hexane. The QDs were then precipitated by adding acetone (half volume of the original solution was enough to precipitate the QDs). After centrifugation, the solid layer was re-dispersed in toluene, causing a brown cloudy solution. The remaining insoluble materials could be removed by repeating the purification process.

6.5 Phase Transfer of QDs

6.5.1 CdTe/ZnS QDs for Phase Transfer Reaction

Mono-dispersed, high quality CdTe/ZnS QDs were synthesised using the procedure reported by Smith *et al.* with some amendments.[153] TDPA-capped CdTe core particles (diameter = *ca.* 4.0 nm) were prepared and purified as described in Chapter 6.3.1 and Chapter 6.3.5. The resulting CdTe solid were re-dispersed in 6 mL hexane (6.3 µM), showing bright emission at 630 nm. Afterwards, the CdTe QDs/hexane solution and 10 mL OAm were charged in a flask, and hexane was removed by evaporation at 100 °C for 1 hour, followed by filling with nitrogen gas. For the shell precursors, 1mL of 1 M diethyl zinc/toluene solution was mixed with 4 mL TOP to make 0.2 M Zn stock solution. In a separate flask, 0.2 M TOPS stock solution was prepared by mixing 32 mg

sulfur powder and 5 mL TOP. To the CdTe QDs solution, the Zn stock solution was injected at 150 °C. After 15 minutes of stirring, the S stock solution was then added to the solution. The amounts of Zn/S precursors were determined by the procedure in Appendix B in order to deposit 0.5 monolayer (ML). The reaction solution was kept at 150 °C for 3 hours. Then, a second addition of 0.5 ML Zn/S precursors were injected in the same manner, and the solution was allowed to stir for 16 hours (overnight) to ensure the complete deposition of total 1.0 ML of ZnS shell. After the deposition of 1.0 ML of a ZnS shell, the reaction temperature could be increased up to 250 °C. Reaction parameters at each shell deposition were summarised in Table 6.2. The final QDs could be isolated by precipitation with acetone and re-dispersion in hexane, resulting in a red solution with bright emission at 660 nm.

Thickness (ML)	Temperature (°C)	Reaction time (hours)
0.5	150	3.0
1.0	150	16 (overnight)
1.5	190	1.5
2.0	190	1.5
3.0	230	1.5
4.0	230	1.5
5.0	250	1.0
6.0	250	1.0

Table 6.2. List of the reaction conditions for CdTe/ZnS QDs. Shell thickness (ML = monolayer), reaction temperature, and reaction time.

6.5.2 Phase Transfer with Hydrophobins

In a typical reaction, 100 µL of as-received H*Protein B (50 mg/mL) was dissolved in 2 mL water, and the mixture was sonicated for one minute to ensure that the hydrophobins were dispersed in the solution. To the hydrophobin solution, 50 µL of CdTe/ZnS QDs/hexane solution (concentration was assumed to be 5 µM using the equation (13)) was added and the solution was sonicated for 5 minutes, resulting in a

cloudy emulsion. After storing the emulsion at 4 °C for 2 hours, the solution was filtered through a filtering paper (particle retention: 11 μm) and centrifuged for 2 minutes at 4,000 rpm, resulting in two phases: a relatively clear solution phase and a turbid foam. The solution layer was taken and charged in a centrifugal concentrator (Vivaspin 4, 100 kDa cut-off). Then the solution was centrifuged for 5 minutes at 4,000 rpm, separating a few mL of the solvent from the solution. The centrifugation process was repeated until the solution volume reduced to 200 μL in the centrifugal concentrator. The concentrated solution was diluted with 3.5 mL water and the concentration process was repeated again, resulting in brown solution with a slight turbidity.

Ultra-centrifugation was conducted using an Optima™ L-100 K BioSafe centrifuge system with type 50.2 Ti rotor, fixed-angle. Typically, 5 mL of the hydrophobin-QDs solution after 11 μm cut-off filtration was put into a 5 ml tube and applied at 300,000 g for 30 minutes, yielding a brown pellet. The work was carried out at the School of Biomedical Sciences, King's College London with the support of Dave Lincoln.

For hydrophobin-CdSe/ZnS QDs, as-received CdSe/ZnS QDs/toluene solution was used instead of CdTe/ZnS QDs, and followed by the same procedure, yielding a clear orange solution. The solution was stored at 4 °C until needed.

6.5.3 Cell Imaging

In the cell viability measurements, macrophages (J774A.1) were incubated with the hydrophobin-CdTe/ZnS QDs at a concentration of 0.015 μM (determined by the calculation described in Appendix A) in cell culture medium for 2 hours, and then the particles were removed and the cells were washed three times. Then, the cells were stained with crystal violet and the dye absorbance was measured in a spectrophotometer at 570 nm. Crystal violet partitions into cell membranes can be used to quantify the number of cells remaining attached to the plate after treatment and washing (i.e. the number of living cells remaining). For the evaluation of cell viability, the average absorbance of the control wells, which received no QD treatment, was regarded as 100 % cell viability, and the percentage of viable macrophages in each well treated with QD was calculated as a % of the control.

For the cell imaging measurements, macrophages were incubated with the 0.015 μM hydrophobin-CdTe/ZnS QDs solution in cell culture medium for 2 hours, and the

particles were removed and the cells washed three times. Cells were then fixed with 4 % paraformaldehyde in phosphate buffered saline and the nuclei stained with 4',6-diamidino-2-phenylindole. Images of the cell layers were acquired with a confocal laser scanning microscope (Leica) at a magnification of 20x. The excitation wavelength was 514 nm, whereas the detection wavelength was 500-550 nm. This work was done at the Institute of Pharmaceutical Sciences, King's College London by Raha Ahmad Khanbeigi (L.A. Dailey group).

Chapter 7

Conclusion

In this thesis, the synthesis of inorganic nanomaterials based on CdTe has been discussed. In order to address the issues arisen in the use of semiconductor QDs, novel methodologies for the QDs synthesis in both aqueous and organic media were developed. Optical and structural characteristics of the prepared nanomaterials were analysed, and biological imaging studies were conducted with water-soluble nanomaterials.

7.1 Summary of Work

The work presented in this thesis was motivated by a need that underlies the field of quantum dots sciences; despite the fact that many scientific papers have reported novel nanomaterials based on semiconductor QDs, a wealth of systematic studies and practical applications are still required. Here, we developed a variety of synthetic methodologies based on CdTe QDs in both aqueous and organic media to overcome the existing difficulties of cadmium-containing QDs for further applications. The technological problems in semiconductor QDs (particularly II-VI QDs) include: an acute toxicity from cadmium, an environmental impact in the synthesis, the little-known surface chemistry of QDs, and the reduced quality of QDs after phase transfer or other further processing.

In the first experimental chapter, we provided the aqueous synthesis of core/shell/shell type QDs. The QDs in this work were synthesised using several synthetic techniques that have been recently developed in the field of colloidal QDs synthesis. The combination of a CdTe core and a CdSe shell could exhibit a staggered band gap, resulting in the emission wavelength which is inaccessible in each of material itself. Also, the inherent toxicity was reduced by depositing another shell consisting of relatively benign material, ZnSe. We adopted the SIPOP method in aqueous solution to

make CdSe/CdSe/ZnSe QDs, and as a result of this, the synthetic complexity could be significantly reduced and the products were applied to tissue imaging without the need of further surface processing.

Characterisations of the synthesised CdTe/CdSe/ZnSe QDs showed that the QDs were 4.0 nm in diameter and had emission in the NIR region, indicating the formation of core/shell/shell structure. PL QY of the final product was 4.8 %, which enabled us to conduct the deep-tissue imaging study. The QDs seemed to move *via* the lymphatic tracts of a rat and showed detectable fluorescence in the tissue. We also investigated the reaction mechanism for CdTe/CdSe/ZnSe QDs, suggesting several unusual growth modes compared to other conventional QDs synthesis: digestive ripening and an absence of the Ostwald ripening.

In the second experimental chapter, the influences of reactive cation species towards colloidal QDs were studied. Post-synthetic chemical transformation, a recently developed technique in nanochemistry, has yielded a variety of nanomaterials with unique structural/optical properties when compared to the standard nanocrystals prepared with conventional synthetic methodologies. We synthesised CdTe QDs *via* an established organometallic route and used them as a starting material in order to overcome the problems such as a limited optical range.

As a "proof of concept" experiment, mercury cations were added to a CdTe QDs solution at room-temperature, causing an immediate solution colour change. Optical studies showed that both emission and absorption spectra shifted towards the NIR region. With elemental analysis, it was suggested that mercury cations reacted with CdTe QDs to form CdHgTe nanoalloys, which was in good agreement with obtained optical spectra. TEM studies showed that separated CdTe particles were fused to form complex anisotropic structures after the mercury cation addition. Given these observations, we suggested the possible mechanism of CdHgTe formation, based on the redox potential of mercury cation.

The room-temperature reaction was then applied to other combinations of metal cations and nanocrystals. Adding metal cations of far-positive redox potential (Au^{3+}, Ag^{+}) to the CdTe QDs solution caused both structural and optical changes, whilst adding metal cations with relatively negative redox potential (Zn^{2+}, Pb^{2+} and Cd^{2+}) did not give any significant effect on the original CdTe QDs. Additionally, mercury cations were reacted with CdSe QDs/nanorods and CdTe tetrapods. Whilst structural changes were not as

obvious as those in CdTe QDs, all the reactions caused spectral red-shifting after the mercury addition. These results reinforced the suggested hypothesis that the redox potential of metal cations has a key role in the surface chemistry of nanomaterials. Although the theoretical understanding of these intriguing phenomena is yet to be fully developed, we believe these observations and suggestions may contribute to the synthesis of more complex nanostructure prepared by post-synthetic chemical transformations.

The third experimental chapter was intended to address the problem of dual-precursor synthesis. By using single-source precursors (SSPs) for CdTe QDs synthesis, large quantities of CdTe QDs were prepared reproducibly. The synthesis of $Cd(TePh)_2$, the SSPs for CdTe QDs, was developed using a combination of several methods, and the use of harmful dimethyl cadmium was successfully avoided in the synthesis.

Pyrolysis of $Cd(TePh)_2$ in oleylamine resulted in the formation of CdTe QDs, showing the size-dependent quantum size effects. The analysis showed that the particles growth mechanism was comparable to thiol-capped counterparts. The PL QY of core CdTe QDs was up to 20 %. On the CdTe core, a ZnS shell was deposited using $ZnDDTC_2$ in order to improve the optical property of the QDs. However, the shell deposition caused a decrease in emission efficiency. Structural characterisations using TEM and XRD showed less-common features when compared to other core/shell QDs synthesised *via* conventional methods. Our results indicated an inefficient shell deposition, as well as a crystal phase transition.

In the final experimental chapter, a new method for the phase transfer of QDs was developed. In order to convert hydrophobic QDs into hydrophilic particles, we have chosen hydrophobins, amphiphilic proteins, as a phase transfer agent. As a standard QD sample, high-quality CdTe/ZnS QDs were synthesised and dispersed in hexane. The hydrophobin-CdTe/ZnS QDs were prepared by sonicating a mixture of the hydrophobin aqueous solution and the QDs/hexane solution, yielding an emulsion with bright photoluminescence. To remove excess hydrophobins in the solution, two types of isolation methods (ultra-centrifugation and a centrifugal concentrator) were examined. TEM and DLS showed that purification with the centrifugal concentrator yielded favourable results, clearly indicating an existence of an individual hydrophobin-CdTe/ZnS QD conjugate. However, emission efficiency was somewhat reduced from this processing and the PL QY of the final purified product was found to be 3.5 % (from

the original PL QY of 15 %). Using the same procedure, commercially available CdSe/ZnS QDs were converted into water-soluble QDs. Whilst the products showed more clustered behaviour than those from CdTe/ZnS QDs, they showed excellent optical properties such as transparency in solution. The prepared hydrophobin-CdTe/ZnS QDs were applied to biological imaging. Whilst incubation with macrophages with hydrophobin-CdTe/ZnS QDs did not show any acute toxicity, cell imaging study showed non-specific binding-like behaviour of the hydrophobin-QDs.

7.2 Future Work

Since early 1980s, a number of papers have been published on the synthesis of novel cadmium-containing nanomaterials which have excellent optical properties and/or advantageous structures. However, it is arguable that many papers focused only on the synthesis and the practical applications using these nanomaterials have not been fully developed. From this viewpoint, our work presented in this thesis is still short of our objective; the CdTe-based nanomaterials synthesised in this thesis should be utilised to satisfy the needs in relevant fields.

Particularly, nanotoxicology has become a growing concern when using semiconductor QDs as a fluorescence marker. As we have shown the phase transfer using hydrophobins and the aqueous synthesis of CdTe/CdSe/ZnSe QDs can be a powerful tool for imaging biological samples, further biological/clinical investigation using these QDs are expected. For example, in addition to acute toxicity, an influence of long-term exposure to the QDs, oxidative stress caused by QDs' photo-excitation and the comparison with other imaging agents (e.g. fluorescent proteins, organic dyes and conjugated polymers) will be the next step.

It is well known that the surface chemistry of the nanomaterials has a significant effect towards the biological activities. Therefore, hydrophobin-encapsulation of nanomaterials is expected to be a standard technique for biological experiment because hydrophobins are regarded as biocompatible and can provide the homogeneous surface environment regardless of nanomaterials. As a future interest, phase transfer reaction developed in our work should be applied to other nanomaterials such as iron oxide nanoparticles or gold nanoparticles.

In the work of room-temperature chemical transformation described in Chapter 3, a major problem was the synthesised CdHgTe nanoalloys were unstable in solution. Therefore, improving the stability of synthesised materials will be necessary. Considering the molecular welding effect, we believe it may contribute to the synthesis of nanostructures where particles are attached to each other in the pursuit of highly organized designer structures with very specific optoelectronic functions.[92] When combined with intelligent synthesis,[294] a wide range of materials may become accessible.

For the CdTe/ZnS QDs *via* a single-source route, it is essential to improve the quality of the QDs for other applications. For example, controlling particles growth mode (e.g. suppressing Ostwald ripening) can be achieved by changing reaction conditions, yielding mono-dispersed QDs. Also, the ZnS shell formation on the CdTe core should be optimised in order to obtain bright QDs which are comparable to other conventional core/shell QDs from dual-precursors routes.

Bibliography

1 Schmid, G., *Nanoparticles: From Theory to Application*. Wiley-VCH: **2005**.

2 Winter, M. *WebElements: The Periodic Table on the Web*. http://www.webelements.com/ **2010**. March.

3 Papadopoulos, S.; Jurgens, K. D.; Gros, G., *Protein Diffusion in Living Skeletal Muscle Fibers: Dependence on Protein Size, Fiber Type, and Contraction*. Biophys. J. **2000,** *79* (4), p. 2084-2094.

4 Persons, E. L., *Studies on Red Blood Cell Diameter - III The Relative Diameter of Immature (reticulocytes) and Adult Red Blood Cells in Health and Anemia, Especially in Pernicious Anemia*. J. Clin. Invest. **1929,** *7* (4), p. 615-629.

5 Berger, M., *Nano-Society: Pushing the Boundaries of Technology*. Royal Society of Chemistry: **2009**; p. 317.

6 Eigler, D. M.; Schweizer, E. K., *Positioning Single Atoms with a Scanning Tunneling Microscope*. Nature **1990,** *344* (6266), p. 524-526.

7 Deshpande, A.; Yildirim, H.; Kara, A.; Acharya, D. P.; Vaughn, J.; Rahman, T. S.; Hla, S. W., *Atom-by-atom Extraction Using the Scanning Tunneling Microscope Tip-cluster Interaction*. Phys. Rev. Lett. **2007,** *98* (2), p. 028304.1-028304.4.

8 Tinazli, A.; Piehler, J.; Beuttler, M.; Guckenberger, R.; Tampe, R., *Native Protein Nanolithography that can Write, Read and Erase*. Nat. Nanotechnol. **2007,** *2* (4), p. 220-225.

9 Iijima, S.; Ichihashi, T., *Single-Shell Carbon Nanotubes of 1-nm Diameter*. Nature **1993,** *363* (6430), p. 603-605.

10 Thomson_Reuters *Web of Knowledge*. http://www.webofknowledge.com/ **2011**. August.

11 Ahn, J. H.; Kim, H. S.; Lee, K. J.; Jeon, S.; Kang, S. J.; Sun, Y. G.; Nuzzo, R. G.; Rogers, J. A., *Heterogeneous Three-dimensional Electronics by Use of Printed Semiconductor Nanomaterials*. Science **2006,** *314* (5806), p. 1754-1757.

12 Saito, N.; Aoki, K.; Usui, Y.; Shimizu, M.; Hara, K.; Narita, N.; Ogihara, N.; Nakamura, K.; Ishigaki, N.; Kato, H.; Haniu, H.; Taruta, S.; Kim, Y. A.; Endo, M., *Application of Carbon Fibers to Biomaterials: A New Era of Nano-level Control of Carbon Fibers after 30-years of Development*. Chem. Soc. Rev. **2011,** *40* (7), p. 3824-3834.

13 Schrlau, M. G.; Bau, H. H., *Carbon Nanopipettes for Cell Surgery*. Jala **2010,** *15* (2), p. 145-151.

14 Yu, Z.; McKnight, T. E.; Ericson, M. N.; Melechko, A. V.; Simpson, M. L.; Morrison, B., *Vertically Aligned Carbon Nanofiber Arrays Record Electrophysiological Signals from Hippocampal Slices*. Nano Lett. **2007,** *7* (8), p. 2188-2195.

15 Liu, D. D.; Yi, C. Q.; Zhang, D. W.; Zhang, J. C.; Yang, M. S., *Inhibition of Proliferation and Differentiation of Mesenchymal Stern Cells by Carboxylated Carbon Nanotubes*. ACS Nano **2010,** *4* (4), p. 2185-2195.

16 Marches, R.; Mikoryak, C.; Wang, R. H.; Pantano, P.; Draper, R. K.; Vitetta, E. S., *The Importance of Cellular Internalization of Antibody-targeted Carbon Nanotubes in the Photothermal Ablation of Breast Cancer Cells*. Nanotechnology **2011,** *22* (9), p. 095101

17 Qu, L.; Dai, L., *Gecko-foot-mimetic Aligned Single-walled Carbon Nanotube Dry Adhesives with Unique Electrical and Thermal Properties*. Adv. Mater. **2007,** *19* (22), p. 3844-3849.

18 Lee, J.; Kotov, N. A., *Thermometer Design at the Nanoscale*. Nano Today **2007,** *2* (1), p. 48-51.

19 Kowalczyk, P.; Holyst, R., *Efficient Adsorption of Super Greenhouse Gas (Tetrafluoromethane) in Carbon Nanotubes*. Environ. Sci. Technol. **2008,** *42* (8), p. 2931-2936.

20 Frank, B.; Rinaldi, A.; Blume, R.; Schlogl, R.; Su, D. S., *Oxidation Stability of Multiwalled Carbon Nanotubes for Catalytic Applications*. Chem. Mater. **2010,** *22* (15), p. 4462-4470.

21 Su, J. Y. S. J. Y.; Guo, H. X., *Control of Unidirectional Transport of Single-File Water Molecules through Carbon Nanotubes in an Electric Field*. ACS Nano **2011,** *5* (1), p. 351-359.

22 Yu, G. H.; Cao, A. Y.; Lieber, C. M., *Large-area Blown Bubble Films of Aligned Nanowires and Carbon Nanotubes*. Nat. Nanotechnol. **2007,** *2* (6), p. 372-377.

23 Dong, L. X.; Tao, X. Y.; Zhang, L.; Zhang, X. B.; Nelson, B. J., *Nanorobotic Spot Welding: Controlled Metal Deposition with Attogram Precision from Copper-filled Carbon Nanotubes*. Nano Lett. **2007,** *7* (1), p. 58-63.

24 Geim, A. K.; Novoselov, K. S., *The Rise of Graphene*. Nat. Mater. **2007,** *6* (3), p. 183-191.

25 Geim, A. K.; Kim, P. *Carbon Wonderland: Graphene, A Newly Isolated Form of Carbon, Provides a Rich Lode of Novel Fundamental Physics and Practical Applications*. http://www.scientificamerican.com/article.cfm?id=carbon-wonderland **2008**. April.

26 Bae, S.; Kim, H.; Lee, Y.; Xu, X. F.; Park, J. S.; Zheng, Y.; Balakrishnan, J.; Lei, T.; Kim, H. R.; Song, Y. I.; Kim, Y. J.; Kim, K. S.; Ozyilmaz, B.; Ahn, J. H.; Hong, B. H.; Iijima, S., *Roll-to-roll Production of 30-inch Graphene Films for Transparent Electrodes*. Nat. Nanotechnol. **2010,** *5* (8), p. 574-578.

27 Xia, Y.; Xiong, Y. J.; Lim, B.; Skrabalak, S. E., *Shape-Controlled Synthesis of Metal Nanocrystals: Simple Chemistry Meets Complex Physics?* Angew. Chem.-Int. Edit. **2009,** *48* (1), p. 60-103.

28 Park, J.; Joo, J.; Kwon, S. G.; Jang, Y.; Hyeon, T., *Synthesis of Monodisperse Spherical Nanocrystals*. Angew. Chem.-Int. Edit. **2007,** *46* (25), p. 4630-4660.

29 Stehr, J.; Hrelescu, C.; Sperling, R. A.; Raschke, G.; Wunderlich, M.; Nichtl, A.; Heindl, D.; Kurzinger, K.; Parak, W. J.; Klar, T. A.; Feldmann, J., *Gold NanoStoves for Microsecond DNA Melting Analysis*. Nano Lett. **2008,** *8* (2), p. 619-623.

30 Miranda, O. R.; Creran, B.; Rotello, V. M., *Array-based Sensing with Nanoparticles: 'Chemical Noses' for Sensing Biomolecules and Cell Surfaces*. Curr. Opin. Chem. Biol. **2010,** *14* (6), p. 728-736.

31 Park, S. Y.; Lytton-Jean, A. K. R.; Lee, B.; Weigand, S.; Schatz, G. C.; Mirkin, C. A., *DNA-programmable Nanoparticle Crystallization*. Nature **2008,** *451* (7178), p. 553-556.

32 Mirkin, C. A.; Letsinger, R. L.; Mucic, R. C.; Storhoff, J. J., *A DNA-based Method for Rationally Assembling Nanoparticles into Macroscopic Materials*. Nature **1996,** *382* (6592), p. 607-609.

33 Auyeung, E.; Cutler, J. I.; Macfarlane, R. J.; Jones, M. R.; Wu, J. S.; Liu, G.; Zhang, K.; Osberg, K. D.; Mirkin, C. A., *Synthetically Programmable Nanoparticle Superlattices Using a Hollow Three-dimensional Spacer Approach*. Nat. Nanotechnol. **2012,** *7* (1), p. 24-28.

34 Zhu, H. Y.; Ke, X. B.; Yang, X. Z.; Sarina, S.; Liu, H. W., *Reduction of Nitroaromatic Compounds on Supported Gold Nanoparticles by Visible and Ultraviolet Light*. Angew. Chem.-Int. Edit. **2010,** *49* (50), p. 9657-9661.

35 Ju, S. Y.; Facchetti, A.; Xuan, Y.; Liu, J.; Ishikawa, F.; Ye, P. D.; Zhou, C. W.; Marks, T. J.; Janes, D. B., *Fabrication of Fully Transparent Nanowire Transistors for Transparent and Flexible Electronics*. Nat. Nanotechnol. **2007,** *2* (6), p. 378-384.

36 Zhu, D. F.; He, Q. G.; Chen, Q.; Fu, Y. Y.; He, C.; Shi, L. Q.; Meng, X.; Deng, C. M.; Cao, H. M.; Cheng, J. G., *Sensitivity Gains in Chemosensing by Optical and Structural Modulation of Ordered Assembly Arrays of ZnO Nanorods*. ACS Nano **2011,** *5* (6), p. 4293-4299.

37 Xu, S.; Qin, Y.; Xu, C.; Wei, Y. G.; Yang, R. S.; Wang, Z. L., *Self-powered Nanowire Devices*. Nat. Nanotechnol. **2010,** *5* (5), p. 366-373.

38 Cha, S. N.; Seo, J. S.; Kim, S. M.; Kim, H. J.; Park, Y. J.; Kim, S. W.; Kim, J. M., *Sound-Driven Piezoelectric Nanowire-Based Nanogenerators*. Adv. Mater. **2010,** *22* (42), p. 4726-4730.

39 Dames, P.; Gleich, B.; Flemmer, A.; Hajek, K.; Seidl, N.; Wiekhorst, F.; Eberbeck, D.; Bittmann, I.; Bergemann, C.; Weyh, T.; Trahms, L.; Rosenecker, J.; Rudolph, C., *Targeted Delivery of Magnetic Aerosol Droplets to the Lung*. Nat. Nanotechnol. **2007,** *2* (8), p. 495-499.

40 Liu, J. F.; Zhao, Z. S.; Jiang, G. B., *Coating Fe_3O_4 Magnetic Nanoparticles with Humic Acid for High Efficient Removal of Heavy Metals in Water*. Environ. Sci. Technol. **2008,** *42* (18), p. 6949-6954.

41 Yin, Y. D.; Rioux, R. M.; Erdonmez, C. K.; Hughes, S.; Somorjai, G. A.; Alivisatos, A. P., *Formation of Hollow Nanocrystals Through the Nanoscale Kirkendall Effect*. Science **2004,** *304* (5671), p. 711-714.

42 Fan, H. J.; Gosele, U.; Zacharias, M., *Formation of Nanotubes and Hollow Nanoparticles Based on Kirkendall and Diffusion Processes: A review*. Small **2007,** *3* (10), p. 1660-1671.

43 Cabot, A.; Ibanez, M.; Guardia, P.; Alivisatos, A. P., *Reaction Regimes on the Synthesis of Hollow Particles by the Kirkendall Effect*. J. Am. Chem. Soc. **2009,** *131* (32), p. 11326-11328.

44 Suzuki, T.; Okazaki, K.; Suzuki, S.; Shibayama, T.; Kuwabata, S.; Torimoto, T., *Nanosize-Controlled Syntheses of Indium Metal Particles and Hollow Indium Oxide Particles via the Sputter Deposition Technique in Ionic Liquids*. Chem. Mater. **2010,** *22* (18), p. 5209-5215.

45 Suk, J. S.; Suh, J.; Choy, K.; Lai, S. K.; Fu, J.; Hanes, J., *Gene Delivery to Differentiated Neurotypic Cells with RGD and HIV Tat Peptide Functionalized Polymeric Nanoparticles*. Biomaterials **2006,** *27* (29), p. 5143-5150.

46 Vohra, V.; Giovanella, U.; Tubino, R.; Murata, H.; Botta, C., *Electroluminescence from Conjugated Polymer Electrospun Nanofibers in Solution Processable Organic Light-Emitting Diodes*. ACS Nano **2011,** *5* (7), p. 5572-5578.

47 Fischlechner, M.; Donath, E., *Viruses as Building Blocks for Materials and Devices*. Angew. Chem.-Int. Edit. **2007,** *46* (18), p. 3184-3193.

48 Stephanopoulos, N.; Liu, M. H.; Tong, G. J.; Li, Z.; Liu, Y.; Yan, H.; Francis, M. B., *Immobilization and One-Dimensional Arrangement of Virus Capsids with Nanoscale Precision Using DNA Origami*. Nano Lett. **2010,** *10* (7), p. 2714-2720.

49 Robertson, K. L.; Soto, C. M.; Archer, M. J.; Odoemene, O.; Liu, J. L., *Engineered T4 Viral Nanoparticles for Cellular Imaging and Flow Cytometry*. Bioconjugate Chem. **2011,** *22* (4), p. 595-604.

50 Fernandes, R.; Roy, V.; Wu, H. C.; Bentley, W. E., *Engineered Biological Nanofactories Trigger Quorum Sensing Response in Targeted Bacteria*. Nat. Nanotechnol. **2010,** *5* (3), p. 213-217.

51 Akin, D.; Sturgis, J.; Ragheb, K.; Sherman, D.; Burkholder, K.; Robinson, J. P.; Bhunia, A. K.; Mohammed, S.; Bashir, R., *Bacteria-mediated Delivery of Nanoparticles and Cargo into Cells*. Nat. Nanotechnol. **2007,** *2* (7), p. 441-449.

52 Moghimi, S. M.; Hunter, A. C.; Murray, J. C., *Nanomedicine: Current Status and Future Prospects*. Faseb J. **2005,** *19* (3), p. 311-330.

53 Wagner, V.; Dullaart, A.; Bock, A. K.; Zweck, A., *The Emerging Nanomedicine Landscape*. Nat. Biotechnol. **2006,** *24* (10), p. 1211-1217.

54 Jennings, L. E.; Long, N. J., *'Two is Better than One'-probes for Dual-modality Molecular Imaging*. Chem. Commun. **2009,** (24), p. 3511-3524.

55 de Rosales, R. T. M.; Tavare, R.; Paul, R. L.; Jauregui-Osoro, M.; Protti, A.; Glaria, A.; Varma, G.; Szanda, I.; Blower, P. J., *Synthesis of $^{64}Cu^{II}$-Bis(dithiocarbamatebisphosphonate) and Its Conjugation with Superparamagnetic Iron Oxide Nanoparticles: In Vivo Evaluation as Dual-Modality PET-MRI Agent*. Angew. Chem.-Int. Edit. **2011,** *50* (24), p. 5509-5513.

56 Howes, P.; Green, M.; Bowers, A.; Parker, D.; Varma, G.; Kallumadil, M.; Hughes, M.; Warley, A.; Brain, A.; Botnar, R., *Magnetic Conjugated Polymer Nanoparticles as Bimodal Imaging Agents*. J. Am. Chem. Soc. **2010,** *132* (28), p. 9833-9842.

57 Kim, B. Y. S.; Rutka, J. T.; Chan, W. C. W., *Current Concepts: Nanomedicine*. N. Engl. J. Med. **2010,** *363* (25), p. 2434-2443.

58 Baroli, B.; Ennas, M. G.; Loffredo, F.; Isola, M.; Pinna, R.; Lopez-Quintela, M. A., *Penetration of Metallic Nanoparticles in Human Full-thickness Skin*. J. Invest. Dermatol. **2007,** *127* (7), p. 1701-1712.

59 Kagan, V. E.; Konduru, N. V.; Feng, W. H.; Allen, B. L.; Conroy, J.; Volkov, Y.; Vlasova, II; Belikova, N. A.; Yanamala, N.; Kapralov, A.; Tyurina, Y. Y.; Shi, J. W.; Kisin, E. R.; Murray, A. R.; Franks, J.; Stolz, D.; Gou, P. P.; Klein-Seetharaman, J.; Fadeel, B.; Star, A.; Shvedova, A. A., *Carbon Nanotubes Degraded by Neutrophil Myeloperoxidase Induce Less Pulmonary Inflammation*. Nat. Nanotechnol. **2010,** *5* (5), p. 354-359.

60 Yoffe, A. D., *Low-dimensional Systems - Quantum-size Effects and Electronic-properties of Semiconductor Microcrystallites (Zero-dimensional Systems) and Some Quasi-2-dimensional Systems*. Adv. Phys. **1993,** *42* (2), p. 173-266.

61 Dabbousi, B. O.; RodriguezViejo, J.; Mikulec, F. V.; Heine, J. R.; Mattoussi, H.; Ober, R.; Jensen, K. F.; Bawendi, M. G., *(CdSe)ZnS Core-shell Quantum Dots: Synthesis and Characterization of a Size Series of Highly Luminescent Nanocrystallites*. J. Phys. Chem. B **1997,** *101* (46), p. 9463-9475.

62 Yin, Y.; Alivisatos, A. P., *Colloidal Nanocrystal Synthesis and the Organic-inorganic Interface*. Nature **2005,** *437* (7059), p. 664-670.

63 Green, M., *The Nature of Quantum Dot Capping Ligands*. J. Mater. Chem. **2010,** *20* (28), p. 5797-5809.

64 Peng, Z. A.; Peng, X. G., *Formation of High-quality CdTe, CdSe, and CdS Nanocrystals Using CdO as Precursor*. J. Am. Chem. Soc. **2001,** *123* (1), p. 183-184.

65 Aldana, J.; Wang, Y. A.; Peng, X. G., *Photochemical Instability of CdSe Nanocrystals Coated by Hydrophilic Thiols*. J. Am. Chem. Soc. **2001,** *123* (36), p. 8844-8850.

66 Becerra, L. R.; Murray, C. B.; Griffin, R. G.; Bawendi, M. G., *Investigation of the Surface Morphology of Capped CdSe Nanocrystallites by ^{31}P Nuclear Magnetic Resonance*. The Journal of Chemical Physics **1994,** *100* (4), p. 3297-3300.

67 Rempel, J. Y.; Trout, B. L.; Bawendi, M. G.; Jensen, K. F., *Density Functional Theory Study of Ligand Binding on CdSe (0001), (000$\bar{1}$), and (11$\bar{2}$0) Single Crystal Relaxed and Reconstructed Surfaces: Implications for Nanocrystalline Growth*. J. Phys. Chem. B **2006,** *110* (36), p. 18007-18016.

68 Manna, L.; Scher, E. C.; Alivisatos, A. P., *Synthesis of Soluble and Processable Rod-, Arrow-, Teardrop-, and Tetrapod-shaped CdSe Nanocrystals*. J. Am. Chem. Soc. **2000,** *122* (51), p. 12700-12706.

69 Morris-Cohen, A. J.; Donakowski, M. D.; Knowles, K. E.; Weiss, E. A., *The Effect of a Common Purification Procedure on the Chemical Composition of the Surfaces of CdSe Quantum Dots Synthesized with Trioctylphosphine Oxide*. J. Phys. Chem. C **2010,** *114* (2), p. 897-906.

70 Liu, I. S.; Lo, H. H.; Chien, C. T.; Lin, Y. Y.; Chen, C. W.; Chen, Y. F.; Su, W. F.; Liou, S. C., *Enhancing Photoluminescence Quenching and Photoelectric Properties of CdSe Quantum Dots with Hole Accepting Ligands*. J. Mater. Chem. **2008,** *18* (6), p. 675-682.

71 Greenham, N. C.; Peng, X. G.; Alivisatos, A. P., *Charge Separation and Transport in Conjugated-polymer/semiconductor-nanocrystal Composites Studied by Photoluminescence Quenching and Photoconductivity*. Phys. Rev. B **1996,** *54* (24), p. 17628-17637.

72 Medintz, I. L.; Uyeda, H. T.; Goldman, E. R.; Mattoussi, H., *Quantum Dot Bioconjugates for Imaging, Labelling and Sensing*. Nat. Mater. **2005,** *4* (6), p. 435-446.

73 Jaeckel, G., *Über einige neuzeitliche Absorptionsgläser*. Zeitschrift für Technische Physik **1926,** *6*, p. 301.

74 Steigerwald, M. L.; Sprinkle, C. R., *Organometallic Synthesis of II-VI Semiconductors .1. Formation and Decomposition of Bis(organotelluro)mercury and bis(organotelluro)cadmium Compounds*. J. Am. Chem. Soc. **1987,** *109* (23), p. 7200-7201.

75 Brennan, J. G.; Siegrist, T.; Carroll, P. J.; Stuczynski, S. M.; Brus, L. E.; Steigerwald, M. L., *The Preparation of Large Semiconductor Clusters via the Pyrolysis of a Molecular Precursor*. J. Am. Chem. Soc. **1989,** *111* (11), p. 4141-4143.

76 Brennan, J. G.; Siegrist, T.; Carroll, P. J.; Stuczynski, S. M.; Reynders, P.; Brus, L. E.; Steigerwald, M. L., *Bulk and Nanostructure Group-II-VI Compounds from Molecular Organometallic Precursors*. Chem. Mater. **1990,** *2* (4), p. 403-409.

77 Murray, C. B.; Norris, D. J.; Bawendi, M. G., *Synthesis and Characterization of Nearly Monodisperse CdE (E = S, Se, Te) Semiconductor Nanocrystallites*. J. Am. Chem. Soc. **1993,** *115* (19), p. 8706-8715.

78 Spanhel, L.; Haase, M.; Weller, H.; Henglein, A., *Photochemistry of Colloidal Semiconductors .20. Surface Modification and Stability of Strong luminescing CdS Particles*. J. Am. Chem. Soc. **1987,** *109* (19), p. 5649-5655.

79 Kortan, A. R.; Hull, R.; Opila, R. L.; Bawendi, M. G.; Steigerwald, M. L.; Carroll, P. J.; Brus, L. E., *Nucleation and Growth of CdSe on ZnS Quantum Crystallite Seeds, and vice versa, in inverse Micelle Media*. J. Am. Chem. Soc. **1990,** *112* (4), p. 1327-1332.

80 Hines, M. A.; Guyot-Sionnest, P., *Synthesis and Characterization of Strongly Luminescing ZnS-Capped CdSe Nanocrystals*. J. Phys. Chem. **1996,** *100* (2), p. 468-471.

81 Peng, X. G.; Manna, L.; Yang, W. D.; Wickham, J.; Scher, E.; Kadavanich, A.; Alivisatos, A. P., *Shape Control of CdSe Nanocrystals*. Nature **2000,** *404* (6773), p. 59-61.

82 Peng, Z. A.; Peng, X., *Mechanisms of the Shape Evolution of CdSe Nanocrystals*. J. Am. Chem. Soc. **2001,** *123* (7), p. 1389-1395.

83 Manna, L.; Milliron, D. J.; Meisel, A.; Scher, E. C.; Alivisatos, A. P., *Controlled Growth of Tetrapod-branched Inorganic Nanocrystals*. Nat. Mater. **2003,** *2* (6), p. 382-385.

84 Bunge, S. D.; Krueger, K. M.; Boyle, T. J.; Rodriguez, M. A.; Headley, T. J.; Colvin, V. L., *Growth and Morphology of Cadmium Chalcogenides: the Synthesis of Nanorods, Tetrapods, and Spheres from CdO and $Cd(O_2CCH_3)_2$*. J. Mater. Chem. **2003,** *13* (7), p. 1705-1709.

85 Cho, J. W.; Kim, H. S.; Kim, Y. J.; Jang, S. Y.; Park, J.; Kim, J. G.; Cha, E. H., *Phase-tuned Tetrapod-shaped CdTe Nanocrystals by Ligand Effect*. Chem. Mater. **2008,** *20* (17), p. 5600-5609.

86 Kim, S.; Fisher, B.; Eisler, H. J.; Bawendi, M., *Type-II Quantum Dots: CdTe/CdSe(core/shell) and CdSe/ZnTe(core/shell) Heterostructures*. J. Am. Chem. Soc. **2003,** *125* (38), p. 11466-11467.

87 Penn, R. L.; Banfield, J. F., *Morphology Development and Crystal Growth in Nanocrystalline Aggregates under Hydrothermal Conditions: Insights from Titania*. Geochim. Cosmochim. Acta **1999,** *63* (10), p. 1549-1557.

88 Tang, Z. Y.; Kotov, N. A.; Giersig, M., *Spontaneous Organization of Single CdTe Nanoparticles into Luminescent Nanowires*. Science **2002,** *297* (5579), p. 237-240.

89 Lu, W. G.; Gao, P. X.; Bin Jian, W.; Wang, Z. L.; Fang, J. Y., *Perfect Orientation Ordered in-situ One-dimensional Self-assembly of Mn-doped PbSe Nanocrystals*. J. Am. Chem. Soc. **2004,** *126* (45), p. 14816-14821.

90 Cho, K. S.; Talapin, D. V.; Gaschler, W.; Murray, C. B., *Designing PbSe Nanowires and Nanorings through Oriented Attachment of Nanoparticles*. J. Am. Chem. Soc. **2005,** *127* (19), p. 7140-7147.

91 Koh, W. K.; Bartnik, A. C.; Wise, F. W.; Murray, C. B., *Synthesis of Monodisperse PbSe Nanorods: A Case for Oriented Attachment*. J. Am. Chem. Soc. **2010,** *132* (11), p. 3909-3913.

92 Milliron, D. J.; Hughes, S. M.; Cui, Y.; Manna, L.; Li, J. B.; Wang, L. W.; Alivisatos, A. P., *Colloidal Nanocrystal Heterostructures with Linear and Branched Topology*. Nature **2004,** *430* (6996), p. 190-195.

93 Mokari, T.; Rothenberg, E.; Popov, I.; Costi, R.; Banin, U., *Selective Growth of Metal Tips onto Semiconductor Quantum Rods and Tetrapods*. Science **2004,** *304* (5678), p. 1787-1790.

94 Talapin, D. V.; Koeppe, R.; Gotzinger, S.; Kornowski, A.; Lupton, J. M.; Rogach, A. L.; Benson, O.; Feldmann, J.; Weller, H., *Highly Emissive Colloidal CdSe/CdS Heterostructures of Mixed Dimensionality*. Nano Lett. **2003,** *3* (12), p. 1677-1681.

95 Zhong, H.; Scholes, G. D., *Shape Tuning of Type II CdTe-CdSe Colloidal Nanocrystal Heterostructures through Seeded Growth*. J. Am. Chem. Soc. **2009,** *131* (26), p. 9170-9171.

96 Kudera, S.; Carbone, L.; Casula, M. F.; Cingolani, R.; Falqui, A.; Snoeck, E.; Parak, W. J.; Manna, L., *Selective Growth of PbSe on One or Both Tips of Colloidal Semiconductor Nanorods*. Nano Lett. **2005,** *5* (3), p. 445-449.

97 Shieh, F.; Saunders, A. E.; Korgel, B. A., *General Shape Control of Colloidal CdS, CdSe, CdTe Quantum Rods and Quantum Rod Heterostructures*. J. Phys. Chem. B **2005,** *109* (18), p. 8538-8542.

98 Bailey, R. E.; Nie, S. M., *Alloyed Semiconductor Quantum Dots: Tuning the Optical Properties without Changing the Particle Size*. J. Am. Chem. Soc. **2003,** *125* (23), p. 7100-7106.

99 Rogach, A. L.; Harrison, M. T.; Kershaw, S. V.; Kornowski, A.; Burt, M. G.; Eychmuller, A.; Weller, H., *Colloidally Prepared CdHgTe and HgTe Quantum Dots with Strong Near-infrared Luminescence*. Phys. Status Solidi B-Basic Res. **2001,** *224* (1), p. 153-158.

100 Zhong, X. H.; Feng, Y. Y.; Knoll, W.; Han, M. Y., *Alloyed $Zn_xCd_{1-x}S$ Nanocrystals with Highly Narrow Luminescence Spectral Width*. J. Am. Chem. Soc. **2003,** *125* (44), p. 13559-13563.

101 Gurusinghe, N. P.; Hewa-Kasakarage, N. N.; Zamkov, M., *Composition-tunable Properties of CdS_xTe_{1-x} Alloy Nanocrystals*. J. Phys. Chem. C **2008,** *112* (33), p. 12795-12800.

102 Pons, T.; Lequeux, N.; Mahler, B.; Sasnouski, S.; Fragola, A.; Dubertret, B., *Synthesis of Near-infrared-emitting, Water-soluble CdTeSe/CdZnS Core/Shell Quantum Dots*. Chem. Mater. **2009,** *21* (8), p. 1418-1424.

103 Norris, D. J.; Efros, A. L.; Erwin, S. C., *Doped Nanocrystals*. Science **2008,** *319* (5871), p. 1776-1779.

104 Raola, O. E.; Strouse, G. F., *Synthesis and Characterization of Eu-doped Cadmium Selenide Nanocrystals*. Nano Lett. **2002,** *2* (12), p. 1443-1447.

105 Meulenberg, R. W.; van Buuren, T.; Hanif, K. M.; Willey, T. M.; Strouse, G. F.; Terminello, L. J., *Structure and Composition of Cu-doped CdSe Nanocrystals Using Soft X-ray Absorption Spectroscopy*. Nano Lett. **2004,** *4* (11), p. 2277-2285.

106 Son, D. H.; Hughes, S. M.; Yin, Y. D.; Alivisatos, A. P., *Cation Exchange Reactions-in Ionic Nanocrystals*. Science **2004,** *306* (5698), p. 1009-1012.

107 Luther, J. M.; Zheng, H. M.; Sadtler, B.; Alivisatos, A. P., *Synthesis of PbS Nanorods and Other Ionic Nanocrystals of Complex Morphology by Sequential Cation Exchange Reactions*. J. Am. Chem. Soc. **2009,** *131* (46), p. 16851-16857.

108 Sadtler, B.; Demchenko, D. O.; Zheng, H.; Hughes, S. M.; Merkle, M. G.; Dahmen, U.; Wang, L. W.; Alivisatos, A. P., *Selective Facet Reactivity during Cation Exchange in Cadmium Sulfide Nanorods*. J. Am. Chem. Soc. **2009,** *131* (14), p. 5285-5293.

109 Pietryga, J. M.; Werder, D. J.; Williams, D. J.; Casson, J. L.; Schaller, R. D.; Klimov, V. I.; Hollingsworth, J. A., *Utilizing the Lability of Lead Selenide to Produce Heterostructured*

Nanocrystals with Bright, Stable Infrared Emission. J. Am. Chem. Soc. **2008,** *130* (14), p. 4879-4885.

110 Zhang, J. T.; Tang, Y.; Lee, K.; Min, O. Y., *Nonepitaxial Growth of Hybrid Core-Shell Nanostructures with Large Lattice Mismatches*. Science **2010,** *327* (5973), p. 1634-1638.

111 Green, M.; Rahman, P.; Smyth-Boyle, D., *Ionic Liquid Passivated CdSe Nanocrystals*. Chem. Commun. **2007,** (6), p. 574-576.

112 Bullen, C.; van Embden, J.; Jasieniak, J.; Cosgriff, J. E.; Mulder, R. J.; Rizzardo, E.; Gu, M.; Raston, C. L., *High Activity Phosphine-Free Selenium Precursor Solution for Semiconductor Nanocrystal Growth*. Chem. Mater. **2010,** *22* (14), p. 4135-4143.

113 Schumacher, W.; Nagy, A.; Waldman, W. J.; Dutta, P. K., *Direct Synthesis of Aqueous CdSe/ZnS-based Quantum Dots Using Microwave Irradiation*. J. Phys. Chem. C **2009,** *113* (28), p. 12132-12139.

114 Zanella, M.; Abbasi, A. Z.; Schaper, A. K.; Parak, W. J., *Discontinuous Growth of II-VI Semiconductor Nanocrystals from Different Materials*. J. Phys. Chem. C **2010,** *114* (14), p. 6205-6215.

115 Piepenbrock, M. O. M.; Stirner, T.; O'Neill, M.; Kelly, S. M., *Growth Dynamics of CdTe Nanoparticles in Liquid and Crystalline Phases*. J. Am. Chem. Soc. **2007,** *129* (24), p. 7674-7679.

116 Nirmal, M.; Norris, D. J.; Kuno, M.; Bawendi, M. G.; Efros, A. L.; Rosen, M., *Observation of the Dark Exciton in CdSe Quantum Dots*. Phys. Rev. Lett. **1995,** *75* (20), p. 3728-3731.

117 Jones, M.; Lo, S. S.; Scholes, G. D., *Quantitative Modeling of the Role of Surface Traps in CdSe/CdS/ZnS Nanocrystal Photoluminescence Decay Dynamics*. Proc. Natl. Acad. Sci. **2009,** *106* (9), p. 3011-3016.

118 Bruchez, M.; Moronne, M.; Gin, P.; Weiss, S.; Alivisatos, A. P., *Semiconductor Nanocrystals as Fluorescent Biological Labels*. Science **1998,** *281* (5385), p. 2013-2016.

119 Chan, W. C. W.; Nie, S. M., *Quantum Dot Bioconjugates for Ultrasensitive Nonisotopic Detection*. Science **1998,** *281* (5385), p. 2016-2018.

120 Green, M.; Harwood, H.; Barrowman, C.; Rahman, P.; Eggeman, A.; Festry, F.; Dobson, P.; Ng, T., *A Facile Route to CdTe Nanoparticles and Their Use in Bio-labelling*. J. Mater. Chem. **2007,** *17* (19), p. 1989-1994.

121 Green, M.; Williamson, P.; Samalova, M.; Davis, J.; Brovelli, S.; Dobson, P.; Cacialli, F., *Synthesis of Type II/type I CdTe/CdS/ZnS Quantum Dots and Their Use in Cellular Imaging*. J. Mater. Chem. **2009,** *19* (44), p. 8341-8346.

122 Zhang, Y.; Li, Y.; Yan, X. P., *Aqueous Layer-by-layer Epitaxy of Type-Il CdTe/CdSe Quantum Dots with Near-infrared Fluorescence for Bioimaging Applications*. Small **2009,** *5* (2), p. 185-189.

123 Li, L.; Reiss, P., *One-pot Synthesis of Highly Luminescent InP/ZnS Nanocrystals without Precursor Injection*. J. Am. Chem. Soc. **2008,** *130* (35), p. 11588-11589.

124 Xu, S.; Ziegler, J.; Nann, T., *Rapid Synthesis of Highly Luminescent InP and InP/ZnS Nanocrystals*. J. Mater. Chem. **2008,** *18* (23), p. 2653-2656.

125 Narayanaswamy, A.; Feiner, L. F.; van der Zaag, P. J., *Temperature Dependence of the Photoluminescence of InP/ZnS Quantum Dots*. J. Phys. Chem. C **2008,** *112* (17), p. 6775-6780.

126 Ryu, E.; Kim, S.; Jang, E.; Jun, S.; Jang, H.; Kim, B.; Kim, S. W., *Step-Wise Synthesis of InP/ZnS Core-Shell Quantum Dots and the Role of Zinc Acetate*. Chem. Mater. **2009,** *21* (4), p. 573-575.

127 Giepmans, B. N. G.; Adams, S. R.; Ellisman, M. H.; Tsien, R. Y., *Review - The Fluorescent Toolbox for Assessing Protein Location and Function*. Science **2006,** *312* (5771), p. 217-224.

128 Hell, S. W., *Far-field Optical Nanoscopy*. Science **2007,** *316* (5828), p. 1153-1158.

129 Smith, A. M.; Nie, S., *Next-generation Quantum Dots*. Nat. Biotechnol. **2009,** *27* (8), p. 732-733.

130 Wang, X. Y.; Ren, X. F.; Kahen, K.; Hahn, M. A.; Rajeswaran, M.; Maccagnano-Zacher, S.; Silcox, J.; Cragg, G. E.; Efros, A. L.; Krauss, T. D., *Non-blinking Semiconductor Nanocrystals*. Nature **2009,** *459* (7247), p. 686-689.

131 Breus, V. V.; Heyes, C. D.; Nienhaus, G. U., *Quenching of CdSe-ZnS Core-Shell Quantum Dot Luminescence by Water-soluble Thiolated Ligands*. J. Phys. Chem. C **2007,** *111* (50), p. 18589-18594.

132 Wuister, S. F.; De Mello Donegá, C.; Meijerink, A., *Influence of Thiol Capping on the Exciton Luminescence and Decay Kinetics of CdTe and CdSe Quantum Dots*. J. Phys. Chem. B **2004,** *108* (45), p. 17393-17397.

133 Wuister, S. F.; De Mello Donegá, C.; Meijerink, A., *Luminescence Temperature Antiquenching of Water-soluble CdTe Quantum Dots: Role of the Solvent*. J. Am. Chem. Soc. **2004,** *126* (33), p. 10397-10402.

134 Medintz, I. L.; Pons, T.; Trammell, S. A.; Grimes, A. F.; English, D. S.; Blanco-Canosa, J. B.; Dawson, P. E.; Mattoussi, H., *Interactions between Redox Complexes and Semiconductor Quantum Dots Coupled via a Peptide Bridge*. J. Am. Chem. Soc. **2008,** *130* (49), p. 16745-16756.

135 Uematsu, T.; Taniguchi, S.; Torimoto, T.; Kuwabata, S., *Emission Quench of Water-soluble ZnS-AgInS$_2$ Solid Solution Nanocrystals and Its Application to Chemosensors*. Chem. Commun. **2009,** (48), p. 7485-7487.

136 Gur, I.; Fromer, N. A.; Geier, M. L.; Alivisatos, A. P., *Air-stable All-inorganic Nanocrystal Solar Cells Processed from Solution*. Science **2005,** *310* (5747), p. 462-465.

137 Kongkanand, A.; Tvrdy, K.; Takechi, K.; Kuno, M.; Kamat, P. V., *Quantum Dot Solar Cells. Tuning Photoresponse through Size and Shape Control of CdSe-TiO$_2$ Architecture*. J. Am. Chem. Soc. **2008,** *130* (12), p. 4007-4015.

138 Xi, L. F.; Boothroyd, C.; Lam, Y. M., *Controlled Synthesis of CdTe and CdSe Multiblock Heteronanostructures*. Chem. Mater. **2009,** *21* (8), p. 1465-1470.

139 Smith, A. M.; Nie, S. M., *Semiconductor Nanocrystals: Structure, Properties, and Band Gap Engineering*. Accounts Chem. Res. **2010,** *43* (2), p. 190-200.

140 Wang, X. H.; Koleilat, G. I.; Tang, J.; Liu, H.; Kramer, I. J.; Debnath, R.; Brzozowski, L.; Barkhouse, D. A. R.; Levina, L.; Hoogland, S.; Sargent, E. H., *Tandem Colloidal Quantum Dot Solar Cells Employing a Graded Recombination Layer*. Nat. Photonics **2011,** *5* (8), p. 480-484.

141 Nozik, A. J., *Quantum Dot Solar Cells*. Physica E **2002,** *14* (1-2), p. 115-120.

142 Schaller, R. D.; Klimov, V. I., *High Efficiency Carrier Multiplication in PbSe Nanocrystals: Implications for Solar Energy Conversion*. Phys. Rev. Lett. **2004,** *92* (18), p. 186601.1-186601.4.

143 Binks, D. J., *Multiple Exciton Generation in Nanocrystal Quantum Dots - Controversy, Current Status and Future Prospects*. Physical Chemistry Chemical Physics **2011,** *13* (28), p. 12693-12704.

144 Klimov, V. I.; Mikhailovsky, A. A.; Xu, S.; Malko, A.; Hollingsworth, J. A.; Leatherdale, C. A.; Eisler, H. J.; Bawendi, M. G., *Optical Gain and Stimulated Emission in Nanocrystal Quantum Dots*. Science **2000,** *290* (5490), p. 314-317.

145 Ivanov, S. A.; Piryatinski, A.; Nanda, J.; Tretiak, S.; Zavadil, K. R.; Wallace, W. O.; Werder, D.; Klimov, V. I., *Type-II Core/shell CdS/ZnSe Nanocrystals: Synthesis, Electronic Structures, and Spectroscopic Properties*. J. Am. Chem. Soc. **2007,** *129* (38), p. 11708-11719.

146 Keuleyan, S.; Lhuillier, E.; Brajuskovic, V.; Guyot-Sionnest, P., *Mid-infrared HgTe Colloidal Quantum Dot Photodetectors*. Nat. Photonics **2011,** *5* (8), p. 489-493.

147 Tsay, J. M.; Trzoss, M.; Shi, L. X.; Kong, X. X.; Selke, M.; Jung, M. E.; Weiss, S., *Singlet Oxygen Production by Peptide-coated Quantum Dot-photosensitizer Conjugates*. J. Am. Chem. Soc. **2007,** *129* (21), p. 6865-6871.

148 Yu, W. W.; Qu, L. H.; Guo, W. Z.; Peng, X. G., *Experimental Determination of the Extinction Coefficient of CdTe, CdSe, and CdS Nanocrystals*. Chem. Mater. **2003,** *15* (14), p. 2854-2860.

149 Yu, W. W.; Wang, Y. A.; Peng, X. G., *Formation and Stability of Size-, Shape-, and Structure-controlled CdTe Nanocrystals: Ligand Effects on Monomers and Nanocrystals*. Chem. Mater. **2003,** *15* (22), p. 4300-4308.

150 Mohr, P. J.; Taylor, B. N.; Newell, D. B. *The 2010 CODATA Recommended Values of the Fundamental Physical Constants*. http://physics.nist.gov/constants **2012**. February.

151 Trindade, T.; O'Brien, P.; Pickett, N. L., *Nanocrystalline Semiconductors: Synthesis, Properties, and Perspectives*. Chem. Mater. **2001,** *13* (11), p. 3843-3858.

152 Talapin, D. V.; Haubold, S.; Rogach, A. L.; Kornowski, A.; Haase, M.; Weller, H., *A Novel Organometallic Synthesis of Highly Luminescent CdTe Nanocrystals*. J. Phys. Chem. B **2001,** *105* (12), p. 2260-2263.

153 Smith, A. M.; Mohs, A. M.; Nie, S., *Tuning the Optical and Electronic Properties of Colloidal Nanocrystals by Lattice Strain*. Nat. Nanotechnol. **2009,** *4* (1), p. 56-63.

154 Rajh, T.; Micic, O. I.; Nozik, A. J., *Synthesis and Characterization of Surface-Modified Colloidal CdTe Quantum Dots*. J. Phys. Chem. **1993,** *97* (46), p. 11999-12003.

155 Rogach, A. L.; Katsikas, L.; Kornowski, A.; Su, D. S.; Eychmuller, A.; Weller, H., *Synthesis and Characterization of Thiol-stabilized CdTe Nanocrystals*. Ber. Bunsen-Ges. Phys. Chem. Chem. Phys. **1996,** *100* (11), p. 1772-1778.

156 Rogach, A. L.; Franzl, T.; Klar, T. A.; Feldmann, J.; Gaponik, N.; Lesnyak, V.; Shavel, A.; Eychmüller, A.; Rakovich, Y. P.; Donegan, J. F., *Aqueous Synthesis of Thiol-capped CdTe Nanocrystals: State-of-the-art*. J. Phys. Chem. C **2007,** *111* (40), p. 14628-14637.

157 Zheng, Y. G.; Gao, S. J.; Ying, J. Y., *Synthesis and Cell-imaging Applications of Glutathione-capped CdTe Quantum Dots*. Adv. Mater. **2007,** *19* (3), p. 376-380.

158 Lovric, J.; Bazzi, H. S.; Cuie, Y.; Fortin, G. R. A.; Winnik, F. M.; Maysinger, D., *Differences in Subcellular Distribution and Toxicity of Green and Red Emitting CdTe Quantum Dots*. J. Mol. Med. **2005,** *83* (5), p. 377-385.

159 Jia, N. Q.; Lian, Q.; Shen, H. B.; Wang, C.; Li, X. Y.; Yang, Z. N., *Intracellular Delivery of Quantum Dots Tagged Antisense Oligodeoxynucleotides by Functionalized Multiwalled Carbon Nanotubes*. Nano Lett. **2007,** *7* (10), p. 2976-2980.

160 Li, Y. L.; Jing, L. H.; Qiao, R. R.; Gao, M. Y., *Aqueous Synthesis of CdTe Nanocrystals: Progresses and Perspectives*. Chem. Commun. **2011,** *47* (33), p. 9293-9311.

161 Byrne, S. J.; Corr, S. A.; Rakovich, T. Y.; Gun'ko, Y. K.; Rakovich, Y. P.; Donegan, J. F.; Mitchell, S.; Volkov, Y., *Optimisation of the Synthesis and Modification of CdTe Quantum Dots for Enhanced Live Cell Imaging*. J. Mater. Chem. **2006,** *16* (28), p. 2896-2902.

162 Rikans, L. E.; Yamano, T., *Mechanisms of Cadmium-mediated Acute Hepatotoxicity*. J. Biochem. Mol. Toxicol. **2000,** *14* (2), p. 110-117.

163 Bottrill, M.; Green, M., *Some Aspects of Quantum Dot Toxicity*. Chem. Commun. **2011,** *47* (25), p. 7039-7050.

164 Green, M.; Howman, E., *Semiconductor Quantum Dots and Free Radical Induced DNA Nicking*. Chem. Commun. **2005,** (1), p. 121-123.

165 Ipe, B. I.; Lehnig, M.; Niemeyer, C. M., *On the Generation of Free Radical Species from Quantum Dots*. Small **2005,** *1* (7), p. 706-709.

166 Cho, S. J.; Maysinger, D.; Jain, M.; Roder, B.; Hackbarth, S.; Winnik, F. M., *Long-term Exposure to CdTe Quantum Dots Causes Functional Impairments in Live Cells*. Langmuir **2007,** *23* (4), p. 1974-1980.

167 Zhang, Y.; Li, Y.; Yan, X. P., *Photoactivated CdTe/CdSe Quantum Dots as a Near Infrared Fluorescent Probe for Detecting Biothiols in Biological Fluids*. Anal. Chem. **2009,** *81* (12), p. 5001-5007.

168 Priyam, A.; Bhattacharya, S. C.; Saha, A., *Volatile Interface of Biological Oxidant and Luminescent CdTe Quantum Dots: Implications in Nanodiagnostics*. Physical Chemistry Chemical Physics **2009,** *11* (3), p. 520-527.

169 Wang, S. P.; Mamedova, N.; Kotov, N. A.; Chen, W.; Studer, J., *Antigen/antibody Immunocomplex from CdTe Nanoparticle Bioconjugates*. Nano Lett. **2002,** *2* (8), p. 817-822.

170 Gaponik, N.; Wolf, A.; Marx, R.; Lesnyak, V.; Schilling, K.; Eychmuller, A., *Three-Dimensional Self-Assembly of Thiol-Capped CdTe Nanocrystals: Gels and Aerogels as Building Blocks for Nanotechnology*. Adv. Mater. **2008,** *20* (22), p. 4257-4262.

171 Chen, H. J.; Lesnyak, V.; Bigall, N. C.; Gaponik, N.; Eychmuller, A., *Self-Assembly of TGA-Capped CdTe Nanocrystals into Three-Dimensional Luminescent Nanostructures*. Chem. Mater. **2010,** *22* (7), p. 2309-2314.

172 Yang, J.; Zhou, Y. L.; Zheng, S. L.; Liu, X. F.; Qiu, X. H.; Tang, Z. Y.; Song, R.; He, Y. J.; Ahn, C. W.; Kim, J. W., *Self-Reorganization of CdTe Nanoparticles into Near-Infrared $Hg_{1-x}Cd_xTe$ Nanowire Networks*. Chem. Mater. **2009,** *21* (14), p. 3177-3182.

173 Tsay, J. M.; Pflughoefft, M.; Bentolila, L. A.; Weiss, S., *Hybrid Approach to the Synthesis of Highly Luminescent CdTe/ZnS and CdHgTe/ZnS Nanocrystals*. J. Am. Chem. Soc. **2004,** *126* (7), p. 1926-1927.

174 Kim, S.; Lim, Y. T.; Soltesz, E. G.; De Grand, A. M.; Lee, J.; Nakayama, A.; Parker, J. A.; Mihaljevic, T.; Laurence, R. G.; Dor, D. M.; Cohn, L. H.; Bawendi, M. G.; Frangioni, J. V.,

Near-infrared Fluorescent Type II Quantum Dots for Sentinel Lymph Node Mapping. Nat Biotech **2004,** *22* (1), p. 93-97.

175 Chen, C. Y.; Cheng, C. T.; Lai, C. W.; Hu, Y. H.; Chou, P. T.; Chou, Y. H.; Chiu, H. T., *Type-II CdSe/CdTe/ZnTe (Core-shell-shell) Quantum Dots with Cascade Band Edges: The Separation of Electron (at CdSe) and Hole (at ZnTe) by the CdTe Layer*. Small **2005,** *1* (12), p. 1215-1220.

176 Blackman, B.; Battaglia, D.; Peng, X., *Bright and Water-soluble Near IR-emitting CdSe/CdTe/ZnSe Type-II/type-I Nanocrystals, Tuning the Efficiency and Stability by Growth*. Chem. Mater. **2008,** *20* (15), p. 4847-4853.

177 Zhang, W.; Chen, G.; Wang, J.; Ye, B.-C.; Zhong, X., *Design and Synthesis of Highly Luminescent Near-Infrared-Emitting Water-Soluble CdTe/CdSe/ZnS Core/Shell/Shell Quantum Dots*. Inorg. Chem. **2009,** *48* (20), p. 9723-9731.

178 Chen, C. Y.; Cheng, C. T.; Yu, J. K.; Pu, S. C.; Cheng, Y. M.; Chou, P. T.; Chou, Y. H.; Chiu, H. T., *Spectroscopy and Femtosecond Dynamics of Type-II CdSe/ZnTe Core-shell Semiconductor Synthesized via the CdO Precursor*. J. Phys. Chem. B **2004,** *108* (30), p. 10687-10691.

179 Cheng, C. T.; Chen, C. Y.; Lai, C. W.; Liu, W. H.; Pu, S. C.; Chou, P. T.; Chou, Y. H.; Chiu, H. T., *Syntheses and Photophysical Properties of Type-II CdSe/ZnTe/ZnS (Core/Shell/Shell) Quantum Dots*. J. Mater. Chem. **2005,** *15* (33), p. 3409-3414.

180 Kim, S. W.; Zimmer, J. P.; Ohnishi, S.; Tracy, J. B.; Frangioni, J. V.; Bawendi, M. G., *Engineering $InAs_xP_{1-x}$/InP/ZnSe III-V Alloyed Core/shell Quantum Dots for the Near-infrared*. J. Am. Chem. Soc. **2005,** *127* (30), p. 10526-10532.

181 Zimmer, J. P.; Kim, S. W.; Ohnishi, S.; Tanaka, E.; Frangioni, J. V.; Bawendi, M. G., *Size Series of Small Indium Arsenide-zinc Selenide Core-shell Nanocrystals and Their Application to in vivo Imaging*. J. Am. Chem. Soc. **2006,** *128* (8), p. 2526-2527.

182 Rogach, A.; Kershaw, S.; Burt, M.; Harrison, M.; Kornowski, A.; Eychmuller, A.; Weller, H., *Colloidally Prepared HgTe Nanocrystals with Strong Room-temperature Infrared Luminescence*. Adv. Mater. **1999,** *11* (7), p. 552-555.

183 Qian, H.; Dong, C.; Peng, J.; Qiu, X.; Xu, Y.; Ren, J., *High-quality and Water-soluble Near-infrared Photolumineseent CdHgTe/CdS Quantum Dots Prepared by Adjusting Size and Composition*. J. Phys. Chem. C **2007,** *111* (45), p. 16852-16857.

184 Lesnyak, V.; Lutich, A.; Gaponik, N.; Grabolle, M.; Plotnikov, A.; Resch-Genger, U.; Eychmuller, A., *One-pot Aqueous Synthesis of High Quality Near Infrared Emitting $Cd_{1-x}Hg_xTe$ Nanocrystals*. J. Mater. Chem. **2009,** *19* (48), p. 9147-9152.

185 Zeng, R.; Zhang, T.; Liu, J.; Hu, S.; Wan, Q.; Liu, X.; Peng, Z.; Zou, B., *Aqueous Synthesis of Type-II CdTe/CdSe Core-shell Quantum Dots for Fluorescent Probe Labeling Tumor Cells*. Nanotechnology **2009,** *20* (9), p. 095102

186 Tian, J. N.; Liu, R. J.; Zhao, Y. C.; Peng, Y.; Hong, X.; Xu, Q.; Zhao, S. L., *Synthesis of CdTe/CdS/ZnS Quantum Dots and Their Application in Imaging of Hepatocellular Carcinoma Cells and Immunoassay for Alpha Fetoprotein*. Nanotechnology **2010,** *21* (30), p. 305101

187 He, Y.; Zhong, Y. L.; Su, Y. Y.; Lu, Y. M.; Jiang, Z. Y.; Peng, F.; Xu, T. T.; Su, S.; Huang, Q.; Fan, C. H.; Lee, S. T., *Water-Dispersed Near-Infrared-Emitting Quantum Dots of Ultrasmall Sizes for In Vitro and In Vivo Imaging*. Angew. Chem.-Int. Edit. **2011,** *50* (25), p. 5694-5697.

188 Deng, Z. T.; Schulz, O.; Lin, S.; Ding, B. Q.; Liu, X. W.; Wei, X. X.; Ros, R.; Yan, H.; Liu, Y., *Aqueous Synthesis of Zinc Blende CdTe/CdS Magic-Core/Thick-Shell Tetrahedral-Shaped Nanocrystals with Emission Tunable to Near-Infrared*. J. Am. Chem. Soc. **2010,** *132* (16), p. 5592-5593.

189 Kim, J. I.; Lee, J.-K., *Sub-kilogram-Scale One-Pot Synthesis of Highly Luminescent and Monodisperse Core/Shell Quantum Dots by the Successive Injection of Precursors*. Adv. Funct. Mater. **2006,** *16* (16), p. 2077-2082.

190 Capasso, F. M., G., *Heterojunction Band Discontinuities: Physics and Device Applications*. **1987**.

191 Bergkvist, M.; Mark, S. S.; Yang, X.; Angert, E. R.; Batt, C. A., *Bionanofabrication of Ordered Nanoparticle Arrays: Effect of Particle Properties and Adsorption Conditions*. J. Phys. Chem. B **2004,** *108* (24), p. 8241-8248.

192 Mikulec, F. V. *PhD Thesis*. MIT, **1999**.

193 Rogach, A. L., *Nanocrystalline CdTe and CdTe(S) Particles: Wet Chemical Preparation, Size-dependent Optical Properties and Perspectives of Optoelectronic Applications*. Mater. Sci. Eng. B-Solid State Mater. Adv. Technol. **2000,** *69*, p. 435-440.

194 Uematsu, T.; Kitajima, H.; Kohma, T.; Torimoto, T.; Tachibana, Y.; Kuwabata, S., *Tuning of the Fluorescence Wavelength of CdTe Quantum Dots with 2nm Resolution by Size-selective Photoetching*. Nanotechnology **2009,** *20* (21), p. 215302

195 Hankare, P. P.; Bhuse, V. M.; Garadkar, K. M.; Jadhav, A. D., *A Novel Method to Grow Polycrystalline HgSe Thin Film*. Mater. Chem. Phys. **2001,** *71* (1), p. 53-57.

196 Fang, Z.; Li, Y.; Zhang, H.; Zhong, X.; Zhu, L., *Facile Synthesis of Highly Luminescent UV-blue-emitting ZnSe/ZnS Core/Shell Nanocrystals in Aqueous Media*. J. Phys. Chem. C **2009,** *113* (32), p. 14145-14150.

197 Howes, P.; Green, M.; Johnston, C.; Crossley, A., *Synthesis and Shape Control of Mercury Selenide (HgSe) Quantum Dots*. J. Mater. Chem. **2008,** *18* (29), p. 3474-3480.

198 Parr, R. G.; Pearson, R. G., *Absolute Hardness - Companion Parameter to Absolute Electronegativity*. J. Am. Chem. Soc. **1983,** *105* (26), p. 7512-7516.

199 Grabolle, M.; Spieles, M.; Lesnyak, V.; Gaponik, N.; Eychmuller, A.; Resch-Genger, U., *Determination of the Fluorescence Quantum Yield of Quantum Dots: Suitable Procedures and Achievable Uncertainties*. Anal. Chem. **2009,** *81* (15), p. 6285-6294.

200 Niu, H. J.; Gao, M. Y., *Diameter-tunable CdTe Nanotubes Templated by 1D Nanowires of Cadmium Thiolate Polymer*. Angew. Chem.-Int. Edit. **2006,** *45* (39), p. 6462-6466.

201 Zhang, H.; Wang, D. Y.; Mohwald, H., *Ligand-selective Aqueous Synthesis of One-dimensional CdTe Nanostructures*. Angew. Chem.-Int. Edit. **2006,** *45* (5), p. 748-751.

202 Dance, I. G.; Scudder, M. L.; Secomb, R., *Cadmium Thiolates - Tetrahedral CdS_4 and Dodecahedral CdS_4O_4 Coordination in Catena-Bis(carbethoxymethanethiolato)cadmium(II)*. Inorg. Chem. **1983,** *22* (12), p. 1794-1797.

203 Prasad, B. L. V.; Stoeva, S. I.; Sorensen, C. M.; Klabunde, K. J., *Digestive Ripening of Thiolated Gold Nanoparticles: The Effect of Alkyl Chain Length*. Langmuir **2002,** *18* (20), p. 7515-7520.

204 Samia, A. C. S.; Hyzer, K.; Schlueter, J. A.; Qin, C. J.; Jiang, J. S.; Bader, S. D.; Lin, X. M., *Ligand Effect on the Growth and the Digestion of Co Nanocrystals*. J. Am. Chem. Soc. **2005,** *127* (12), p. 4126-4127.

205 Hines, M. A.; Scholes, G. D., *Colloidal PbS Nanocrystals with Size-tunable Near-infrared Emission: Observation of Post-synthesis Self-narrowing of the Particle Size Distribution*. Adv. Mater. **2003,** *15* (21), p. 1844-1849.

206 Talapin, D. V.; Yin, Y. D., *Themed Issue: Chemical Transformations of Nanoparticles*. J. Mater. Chem. **2011,** *21* (31), p. 11454-11456.

207 Vasquez, Y.; Henkes, A. E.; Bauer, J. C.; Schaak, R. E., *Nanocrystal Conversion Chemistry: A Unified and Materials-general Strategy for the Template-based Synthesis of Nanocrystalline Solids*. J. Solid State Chem. **2008,** *181* (7), p. 1509-1523.

208 Dloczik, L.; Konenkamp, R., *Nanostructure Transfer in Semiconductors by Ion Exchange*. Nano Lett. **2003,** *3* (5), p. 651-653.

209 Deka, S.; Falqui, A.; Bertoni, G.; Sangregorio, C.; Poneti, G.; Morello, G.; De Giorgi, M.; Giannini, C.; Cingolani, R.; Manna, L.; Cozzoli, P. D., *Fluorescent Asymmetrically Cobalt-Tipped CdSe@CdS Core@Shell Nanorod Heterostructures Exhibiting Room-Temperature Ferromagnetic Behavior*. J. Am. Chem. Soc. **2009,** *131* (35), p. 12817-12828.

210 Kraus, R. M.; Lagoudakis, P. G.; Rogach, A. L.; Talapin, D. V.; Weller, H.; Lupton, J. M.; Feldmann, J., *Room-temperature Exciton Storage in Elongated Semiconductor Nanocrystals*. Phys. Rev. Lett. **2007,** *98* (1), p. 017401.

211 Choi, C. L.; Koski, K. J.; Sivasankar, S.; Alivisatos, A. P., *Strain-Dependent Photoluminescence Behavior of CdSe/CdS Nanocrystals with Spherical, Linear, and Branched Topologies*. Nano Lett. **2009,** *9* (10), p. 3544-3549.

212 Green, M.; Wakefield, G.; Dobson, P. J., *A Simple Metalorganic Route to Organically Passivated Mercury Telluride Nanocrystals*. J. Mater. Chem. **2003,** *13* (5), p. 1076-1078.

213 Wichiansee, W.; Nordin, M. N.; Green, M.; Curry, R. J., *Synthesis and Optical Characterization of Infra-red Emitting Mercury Sulfide (HgS) Quantum Dots*. J. Mater. Chem. **2011,** *21* (20), p. 7331-7336.

214 Jain, P. K.; Amirav, L.; Aloni, S.; Alivisatos, A. P., *Nanoheterostructure Cation Exchange: Anionic Framework Conservation*. J. Am. Chem. Soc. **2010,** *132* (29), p. 9997-9999.

215 Tari, D.; De Giorgi, M.; Della Sala, F.; Carbone, L.; Krahne, R.; Manna, L.; Cingolani, R.; Kudera, S.; Parak, W. J., *Optical Properties of Tetrapod-shaped CdTe Nanocrystals*. Appl. Phys. Lett. **2005,** *87* (22), p. 224101

216 Kumar, S.; Nann, T., *Shape Control of II-VI Semiconductor Nanomateriats*. Small **2006,** *2* (3), p. 316-329.

217 Vergard, L.; Schjelderup, H., *Constitution of Mixed Crystals*. Phys. Z. **1917,** *18*, p. 93-96.

218 Piepenbrock, M. O. M.; Stirner, T.; Kelly, S. M.; O'Neill, M., *A Low-temperature Synthesis for Organically Soluble HgTe Nanocrystals Exhibiting Near-infrared Photoluminescence and Quantum Confinement*. J. Am. Chem. Soc. **2006,** *128* (21), p. 7087-7090.

219 Steckel, J. S.; Yen, B. K. H.; Oertel, D. C.; Bawendi, M. G., *On the Mechanism of Lead Chalcogenide Nanocrystal Formation*. J. Am. Chem. Soc. **2006,** *128* (40), p. 13032-13033.

220 Liu, H. T.; Owen, J. S.; Alivisatos, A. P., *Mechanistic Study of Precursor Evolution in Colloidal Group II-VI Semiconductor Nanocrystal Synthesis*. J. Am. Chem. Soc. **2007,** *129* (2), p. 305-312.

221 Kumar, S.; Ade, M.; Nann, T., *Synthesis and Structural Metastability of CdTe Nanowires*. Chem.-Eur. J. **2005,** *11* (7), p. 2220-2224.

222 Smith, A. M.; Nie, S., *Bright and Compact Alloyed Quantum Dots with Broadly Tunable Near-Infrared Absorption and Fluorescence Spectra through Mercury Cation Exchange*. J. Am. Chem. Soc. **2010,** *133* (1), p. 24-26.

223 Kapitonov, A. M.; Stupak, A. P.; Gaponenko, S. V.; Petrov, E. P.; Rogach, A. L.; Eychmuller, A., *Luminescence Properties of Thiol-stabilized CdTe Nanocrystals*. J. Phys. Chem. B **1999,** *103* (46), p. 10109-10113.

224 Tang, Z. Y.; Podsiadlo, P.; Shim, B. S.; Lee, J.; Kotov, N. A., *The Effect of Stabilizer Density on Transformation of CdTe Nanoparticles Induced by Ag Cations*. Adv. Funct. Mater. **2008,** *18* (23), p. 3801-3808.

225 Green, M.; Smyth-Boyle, D., *Directed Growth of Gold Nanostructures Using a Nucleoside/nucleotide*. J. Mater. Chem. **2007,** *17* (34), p. 3588-3590.

226 Hankare, P. P.; Bhuse, V. M.; Garadkar, K. M.; Delekar, S. D.; Bhagat, P. R., *CdHgSe Thin Films: Preparation, Characterization and Optoelectronic Studies*. Semicond. Sci. Technol. **2004,** *19* (2), p. 277-284.

227 Cumberland, S. L.; Hanif, K. M.; Javier, A.; Khitrov, G. A.; Strouse, G. F.; Woessner, S. M.; Yun, C. S., *Inorganic Clusters as Single-source Precursors for Preparation of CdSe, ZnSe, and CdSe/ZnS Nanomaterials*. Chem. Mater. **2002,** *14* (4), p. 1576-1584.

228 Malik, M. A.; Afzaal, M.; O'Brien, P., *Precursor Chemistry for Main Group Elements in Semiconducting Materials*. Chem. Rev. **2010,** *110* (7), p. 4417-4446.

229 Yang, Y. A.; Wu, H. M.; Williams, K. R.; Cao, Y. C., *Synthesis of CdSe and CdTe Nanocrystals Without Precursor Injection*. Angew. Chem.-Int. Edit. **2005,** *44* (41), p. 6712-6715.

230 Green, M.; O'Brien, P., *A Novel Synthesis of Cadmium Phosphide Nanoparticles Using the Single-source Precursor* $(MeCdP^tBu_2)_3$. Adv. Mater. **1998,** *10* (7), p. 527-528.

231 Garje, S. S.; Ritch, J. S.; Eisler, D. J.; Afzaal, M.; O'Brien, P.; Chivers, T., *Chemical Vapour Deposition of II-VI Semiconductor Thin Films using* $M((TeP^iPr_2)_2N)_2$ *(M = Cd, Hg) as Single-source Precursors*. J. Mater. Chem. **2006,** *16* (10), p. 966-969.

232 Green, M.; Prince, P.; Gardener, M.; Steed, J., *Mercury(II) N,N '-methyl-phenylethyl-dithiocarbamate and Its Use as a Precursor for the Room-temperature Solution Deposition of Beta-HgS Thin Films*. Adv. Mater. **2004,** *16* (12), p. 994-996.

233 Osakada, K.; Yamamoto, T., *Formation of ZnS and CdS by Thermolysis of Homoleptic Thiolato Compounds* $[M(SMe)_2]_n$ *(M = Zn, Cd)*. J. Chem. Soc.-Chem. Commun. **1987,** (14), p. 1117-1118.

234 Stuczynski, S. M.; Brennan, J. G.; Steigerwald, M. L., *Formation of Metal Chalcogen Bonds by the Reaction of Metal Alkyls with Silyl Chalcogenides*. Inorg. Chem. **1989,** *28* (25), p. 4431-4432.

235 Dance, I. G.; Garbutt, R. G.; Craig, D. C.; Scudder, M. L., *The Different Nonmolecular Polyadamantanoid Crystal-Structures of* $Cd(SPh)_2$ *and* $Cd(SC_6H_4Me\text{-}4)_2$ *- Analogies with Microporous Aluminosilicate Frameworks*. Inorg. Chem. **1987,** *26* (24), p. 4057-4064.

236 Trindade, T.; Obrien, P., *A Single Source Approach to the Synthesis of CdSe Nanocrystallites*. Adv. Mater. **1996,** *8* (2), p. 161-163.

237 Trindade, T.; Obrien, P., *Synthesis of CdS and CdSe Nanoparticles by Thermolysis of Diethyldithio- or Diethyldiseleno-carbamates of Cadmium*. J. Mater. Chem. **1996,** *6* (3), p. 343-347.

238 Revaprasadu, N.; Malik, M. A.; O'Brien, P.; Zulu, M. M.; Wakefield, G., *Single-source Molecular Precursors for the Deposition of Zinc Selenide Quantum Dots*. J. Mater. Chem. **1998,** *8* (8), p. 1885-1888.

239 Lazell, M.; O'Brien, P., *A Novel Single Source Precursor Route to Self Capping CdS Quantum Dots*. Chem. Commun. **1999,** (20), p. 2041-2042.

240 Lazell, M.; Norager, S. J.; O'Brien, P.; Revaprasadu, N., *The Use of Dithio- and Diselenocarbamates as Precursors to Nanoscale Materials*. Mater. Sci. Eng. C-Biomimetic Supramol. Syst. **2001,** *16* (1-2), p. 129-133.

241 Crouch, D. J.; O'Brien, P.; Malik, M. A.; Skabara, P. J.; Wright, S. P., *A One-step Synthesis of Cadmium Selenide Quantum Dots from a Novel Single Source Precursor*. Chem. Commun. **2003,** (12), p. 1454-1455.

242 Thoma, S. G.; Sanchez, A.; Provencio, P. P.; Abrams, B. L.; Wilcoxon, J. P., *Synthesis, Optical Properties, and Growth Mechanism of Blue-emitting CdSe Nanorods*. J. Am. Chem. Soc. **2005,** *127* (20), p. 7611-7614.

243 Jun, Y. W.; Choi, C. S.; Cheon, J., *Size and Shape Controlled ZnTe Nanocrystals with Quantum Confinement Effect*. Chem. Commun. **2001,** (01), p. 101-102.

244 Bochmann, M.; Bwembya, G.; Webb, K. J.; Malik, M. A.; Walsh, J. R.; O'Brien, P., Arene Chalcogenolato Complexes of Zinc and Cadmium. In *Inorganic Syntheses*, John Wiley & Sons, Inc.: **2007**; p. 19-24.

245 Ohira, N.; Aso, Y.; Otsubo, T.; Ogura, F., *Organotelluriums .4. Reduction of Aromatic Nitro-compounds to Amines by Benzenetellurol*. Chem. Lett. **1984,** (6), p. 853-854.

246 Gaponik, N.; Talapin, D. V.; Rogach, A. L.; Hoppe, K.; Shevchenko, E. V.; Kornowski, A.; Eychmüller, A.; Weller, H., *Thiol-capping of CdTe Nanocrystals: An Alternative to Organometallic Synthetic Routes*. J. Phys. Chem. B **2002,** *106* (29), p. 7177-7185.

247 Piven, N.; Susha, A. S.; Doeblinger, M.; Rogach, A. L., *Aqueous Synthesis of Alloyed $CdSe_xTe_{1-x}$ Nanocrystals*. J. Phys. Chem. C **2008,** *112* (39), p. 15253-15259.

248 Tang, Z. Y.; Wang, Y.; Shanbhag, S.; Kotov, N. A., *Spontaneous CdTe -> alloy -> CdS Transition of Stabilizer-depleted CdTe Nanoparticles Induced by EDTA*. J. Am. Chem. Soc. **2006,** *128* (21), p. 7036-7042.

249 Dethlefsen, J. R.; Dossing, A., *Preparation of a ZnS Shell on CdSe Quantum Dots Using a Single-Molecular ZnS Precursor*. Nano Lett. **2011,** *11* (5), p. 1964-1969.

250 Chen, D. A.; Zhao, F.; Qi, H.; Rutherford, M.; Peng, X. G., *Bright and Stable Purple/Blue Emitting CdS/ZnS Core/Shell Nanocrystals Grown by Thermal Cycling Using a Single-Source Precursor*. Chem. Mater. **2010,** *22* (4), p. 1437-1444.

251 Jung, Y. K.; Kim, J. I.; Lee, J. K., *Thermal Decomposition Mechanism of Single-Molecule Precursors Forming Metal Sulfide Nanoparticles*. J. Am. Chem. Soc. **2010,** *132* (1), p. 178-184.

252 Green, M.; Allsop, N.; Wakefield, G.; Dobson, P. J.; Hutchison, J. L., *Trialkylphosphine Oxide/amine Stabilised Silver Nanocrystals - The Importance of Steric Factors and Lewis Basicity in Capping Agents*. J. Mater. Chem. **2002,** *12* (9), p. 2671-2674.

253 Haubold, S.; Haase, M.; Kornowski, A.; Weller, H., *Strongly Luminescent InP/ZnS Core-shell Nanoparticles*. ChemPhysChem **2001,** *2* (5), p. 331-334.

254 Protiere, M.; Reiss, P., *Facile Synthesis of Monodisperse ZnS Capped CdS Nanocrystals Exhibiting Efficient Blue Emission*. Nanoscale Res. Lett. **2006,** *1* (1), p. 62-67.

255 Michalet, X.; Pinaud, F. F.; Bentolila, L. A.; Tsay, J. M.; Doose, S.; Li, J. J.; Sundaresan, G.; Wu, A. M.; Gambhir, S. S.; Weiss, S., *Quantum Dots for Live Cells, in vivo Imaging, and Diagnostics*. Science **2005,** *307* (5709), p. 538-544.

256 Smith, A. M.; Duan, H. W.; Mohs, A. M.; Nie, S. M., *Bioconjugated Quantum Dots for in vivo Molecular and Cellular Imaging*. Adv. Drug Deliv. Rev. **2008,** *60* (11), p. 1226-1240.

257 Delehanty, J. B.; Mattoussi, H.; Medintz, I. L., *Delivering Quantum Dots into Cells: Strategies, Progress and Remaining issues*. Anal. Bioanal. Chem. **2009,** *393* (4), p. 1091-1105.

258 Dubertret, B.; Skourides, P.; Norris, D. J.; Noireaux, V.; Brivanlou, A. H.; Libchaber, A., *In vivo Imaging of Quantum Dots Encapsulated in Phospholipid Micelles*. Science **2002,** *298* (5599), p. 1759-1762.

259 Kairdolf, B. A.; Smith, A. M.; Nie, S., *One-Pot Synthesis, Encapsulation, and Solubilization of Size-Tuned Quantum Dots with Amphiphilic Multidentate Ligands*. J. Am. Chem. Soc. **2008,** *130* (39), p. 12866-12867.

260 Mattoussi, H.; Mauro, J. M.; Goldman, E. R.; Anderson, G. P.; Sundar, V. C.; Mikulec, F. V.; Bawendi, M. G., *Self-assembly of CdSe-ZnS Quantum Dot Bioconjugates Using an Engineered Recombinant Protein*. J. Am. Chem. Soc. **2000,** *122* (49), p. 12142-12150.

261 Duan, H. W.; Nie, S. M., *Cell-penetrating Quantum Dots Based on Multivalent and Endosome-disrupting Surface Coatings*. J. Am. Chem. Soc. **2007,** *129* (11), p. 3333-3338.

262 Kovalenko, M. V.; Scheele, M.; Talapin, D. V., *Colloidal Nanocrystals with Molecular Metal Chalcogenide Surface Ligands*. Science **2009,** *324* (5933), p. 1417-1420.

263 Pinaud, F.; King, D.; Moore, H. P.; Weiss, S., *Bioactivation and Cell Targeting of Semiconductor CdSe/ZnS Nanocrystals with Phytochelatin-related Peptides*. J. Am. Chem. Soc. **2004,** *126* (19), p. 6115-6123.

264 Ji, M. L.; Yang, W. L.; Ren, Q. G.; Lu, D. R., *Facile Phase Transfer of Hydrophobic Nanoparticles with Poly(ethylene glycol) Grafted Hyperbranched Poly(amido amine)*. Nanotechnology **2009,** *20* (7), p. 075101

265 Owen, J. S.; Park, J.; Trudeau, P. E.; Alivisatos, A. P., *Reaction Chemistry and Ligand Exchange at Cadmium-selenide Nanocrystal Surfaces*. J. Am. Chem. Soc. **2008,** *130* (37), p. 12279-12281.

266 Dong, A. G.; Ye, X. C.; Chen, J.; Kang, Y. J.; Gordon, T.; Kikkawa, J. M.; Murray, C. B., *A Generalized Ligand-Exchange Strategy Enabling Sequential Surface Functionalization of Colloidal Nanocrystals*. J. Am. Chem. Soc. **2011,** *133* (4), p. 998-1006.

267 Nag, A.; Kovalenko, M. V.; Lee, J.-S.; Liu, W.; Spokoyny, B.; Talapin, D. V., *Metal-free Inorganic Ligands for Colloidal Nanocrystals: S^{2-}, HS^{-}, Se^{2-}, HSe^{-}, Te^{2-}, HTe^{-}, TeS_3^{2-}, OH^{-}, and NH^{2-} as Surface Ligands*. J. Am. Chem. Soc. **2011,** *133* (27), p. 10612-10620.

268 Schroeder, J. E.; Shweky, I.; Shmeeda, H.; Banin, U.; Gabizon, A., *Folate-mediated Tumor Cell Uptake of Quantum Dots Entrapped in Lipid Nanoparticles*. J. Control. Release **2007,** *124* (1-2), p. 28-34.

269 Lees, E. E.; Nguyen, T. L.; Clayton, A. H. A.; Mulvaney, P.; Muir, B. W., *The Preparation of Colloidally Stable, Water-Soluble, Biocompatible, Semiconductor Nanocrystals With a Small Hydrodynamic Diameter*. ACS Nano **2009,** *3* (5), p. 1121-1128.

270 Yu, W. W.; Chang, E.; Falkner, J. C.; Zhang, J. Y.; Al-Somali, A. M.; Sayes, C. M.; Johns, J.; Drezek, R.; Colvin, V. L., *Forming Biocompatible and Nonaggregated Nanocrystals in Water Using Amphiphilic Polymers*. J. Am. Chem. Soc. **2007,** *129* (10), p. 2871-2879.

271 Ning, Y.; Zhang, H.; Han, J. S.; Yang, C. H.; Liu, Y.; Zhou, D.; Yang, B., *Versatile Fabrication of Water-dispersible Nanoparticle-amphiphilic Copolymer Composite Microspheres with Specific Functionalities*. J. Mater. Chem. **2011,** *21* (19), p. 6837-6843.

272 Goldman, E. R.; Balighian, E. D.; Mattoussi, H.; Kuno, M. K.; Mauro, J. M.; Tran, P. T.; Anderson, G. P., *Avidin: A Natural Bridge for Quantum Dot-antibody Conjugates*. J. Am. Chem. Soc. **2002,** *124* (22), p. 6378-6382.

273 Wohlleben, W.; Subkowski, T.; Bollschweiler, C.; von Vacano, B.; Liu, Y. Q.; Schrepp, W.; Baus, U., *Recombinantly Produced Hydrophobins from Fungal Analogues as Highly Surface-active Performance Proteins*. Eur. Biophys. J. Biophys. Lett. **2010,** *39* (3), p. 457-468.

274 Valo, H. K.; Laaksonen, P. H.; Peltonen, L. J.; Linder, M. B.; Hirvonen, J. T.; Laaksonen, T. J., *Multifunctional Hydrophobin: Toward Functional Coatings for Drug Nartoplarticles*. ACS Nano **2010,** *4* (3), p. 1750-1758.

275 Linder, M. B., *Hydrophobins: Proteins that Self Assemble at Interfaces*. Curr. Opin. Colloid Interface Sci. **2009,** *14* (5), p. 356-363.

276 Wessels, J. G. H., *Developmental Regulation of Fungal Cell-wall Formation*. Annu. Rev. Phytopathol. **1994,** *32*, p. 413-437.

277 Kyte, J.; Doolittle, R. F., *A Simple Method for Displaying the Hydropathic Character of a Protein*. J. Mol. Biol. **1982,** *157* (1), p. 105-132.

278 Yu, L.; Zhang, B. H.; Szilvay, G. R.; Sun, R.; Janis, J.; Wang, Z. F.; Feng, S. R.; Xu, H. J.; Linder, M. B.; Qiao, M. Q., *Protein HGFI from the Edible Mushroom Grifola Frondosa is a Novel 8 kDa Class I Hydrophobin That Forms Rodlets in Compressed Monolayers*. Microbiology-(UK) **2008,** *154*, p. 1677-1685.

279 Schulz, A.; Liebeck, B. M.; John, D.; Heiss, A.; Subkowski, T.; Boker, A., *Protein-mineral Hybrid Capsules from Emulsions Stabilized with an Amphiphilic Protein*. J. Mater. Chem. **2011,** *21* (26), p. 9731-9736.

280 Wang, Z. F.; Wang, Y. Y.; Huang, Y. J.; Li, S.; Feng, S. R.; Xu, H. J.; Qiao, M. Q., *Characterization and Application of Hydrophobin-dispersed Multi-walled Carbon Nanotubes*. Carbon **2010,** *48* (10), p. 2890-2898.

281 Laaksonen, P.; Kivioja, J.; Paananen, A.; Kainlauri, M.; Kontturi, K.; Ahopelto, J.; Linder, M. B., *Selective Nanopatterning Using Citrate-Stabilized Au Nanoparticles and Cystein-Modified Amphiphilic Protein*. Langmuir **2009,** *25* (9), p. 5185-5192.

282 Zhang, X. L.; Penfold, J.; Thomas, R. K.; Tucker, I. M.; Petkov, J. T.; Bent, J.; Cox, A.; Grillo, I., *Self-Assembly of Hydrophobin and Hydrophobin/Surfactant Mixtures in Aqueous Solution*. Langmuir **2011,** *27* (17), p. 10514-10522.

283 von Vacano, B.; Xu, R.; Hirth, S.; Herzenstiel, I.; Ruckel, M.; Subkowski, T.; Baus, U., *Hydrophobin can Prevent Secondary Protein Adsorption on Hydrophobic Substrates without Exchange*. Anal. Bioanal. Chem. **2011,** *400* (7), p. 2031-2040.

284 Kurppa, K.; Jiang, H.; Szilvay, G. R.; Nasibulin, A. G.; Kauppinen, E. L.; Linder, M. B., *Controlled Hybrid Nanostructures Through Protein-mediated Noncovalent Functionalization of Carbon Nanotube*. Angew. Chem.-Int. Edit. **2007,** *46* (34), p. 6446-6449.

285 Laaksonen, P.; Kainlauri, M.; Laaksonen, T.; Shchepetov, A.; Jiang, H.; Ahopelto, J.; Linder, M. B., *Interfacial Engineering by Proteins: Exfoliation and Functionalization of Graphene by Hydrophobins*. Angew. Chem.-Int. Edit. **2010,** *49* (29), p. 4946-4949.

286 Beckman Coulter, I. *Delsa Nano Submicron Particle Size and Zeta Potential, User's Manual*; **2008**; p. xxiii - xxviii.

287 Howes, P. *PhD Thesis*. King's College London, **2010**.

288 Zhang, M. Y.; Li, J.; Xing, G. M.; He, R.; Li, W.; Song, Y.; Guo, H. L., *Variation in the Internalization of Differently Sized Nanoparticles Induces Different DNA-damaging Effects on a Macrophage Cell Line*. Arch. Toxicol. **2011,** *85* (12), p. 1575-1588.

289 Sigma-Aldrich *Lumidot™ 590, CdSe/ZnS (694622), core-shell type quantum dots, 5 mg/mL in toluene*. http://www.sigmaaldrich.com/ **2012**. February.

290 BASF *H* Protein B (5012627): Capabilities of H star Protein B*. http://www.hydrophobin.basf.com/portal/basf2/en/dt.jsp?setCursor=1_472681 **2011**. July.

291 National_Institutes_of_Health *ImageJ: Image Processing and Analysis in Java*. http://rsbweb.nih.gov/ij/ **2009**. November.

292 Rurack, K.; Spieles, M., *Fluorescence Quantum Yields of a Series of Red and Near-Infrared Dyes Emitting at 600-1000 nm*. Anal. Chem. **2011,** *83* (4), p. 1232-1242.

293 Boudjouk, P.; Remington, M. P.; Grier, D. G.; Triebold, W.; Jarabek, B. R., *2,2,4,4,6,6-Hexabenzylcyclotristannatellurane ($Bn_2SnTe)_3$. Synthesis and Structural Characterization of an Organometallic Single-source Precursor to Phase-pure, Polycrystalline SnTe*. Organometallics **1999,** *18* (22), p. 4534-4537.

294 Krishnadasan, S.; Brown, R. J. C.; Demello, A. J.; Demello, J. C., *Intelligent Routes to the Controlled Synthesis of Nanoparticles*. Lab Chip **2007,** *7* (11), p. 1434-1441.

Appendix A

Concentration of QDs

Concentrations of prepared QDs samples were calculated using the method presented by Yu *et al*.[A1] The formulae are based on the experimental observation that the extinction coefficient per mole of high quality CdE (E = S, Se, Te) QDs was found to be dependent on nanocrystals size; the theory can be further extended to determine the concentration of the nanocrystals sample by a combination of the Lambert–Beer law and absorption profiles.

Systematic characterisation of mono-dispersed CdE QDs using both mass spectrometry and optical spectroscopy suggested the relationship between an excitonic peak (λ) and a diameter (D) as:

$$\mathrm{D} = (9.8127 \times 10^{-7})\lambda^3 - (1.7147 \times 10^{-3})\lambda^2 + (1.0064)\lambda - 194.84 \quad (11)$$

The equation is only applicable to CdTe QDs. For other QDs, see the literature.[A1] Extinction coefficient, ϵ, of the CdTe QDs can be obtained from an empirical function of the nanocrystals size as follows.

$$\epsilon = 10043(\mathrm{D})^{2.12} \quad (12)$$

From the Lambert-Beer law, the concentration of the CdTe QDs (C) is acquired.

$$\mathrm{C} = \mathrm{A}_{cal}/\epsilon \cdot L \quad (13)$$

L is the path length of the cuvette, and A_{cal} is a calibrated absorbance (where mono-dispersity of the sample was taken in to account). The A_{cal} can be calculated by the equation below.

$$A_{cal} = A_m \cdot (\mathrm{hwhm})/K \quad (14)$$

A_m is the measured absorbance at the first excitonic peak and *K* is an average hwhm (half width at half maximum) on the long wavelength side. In the case of CdTe QDs, *K* = 18 nm. Figure A-1 explains an example of the concentration determination process.

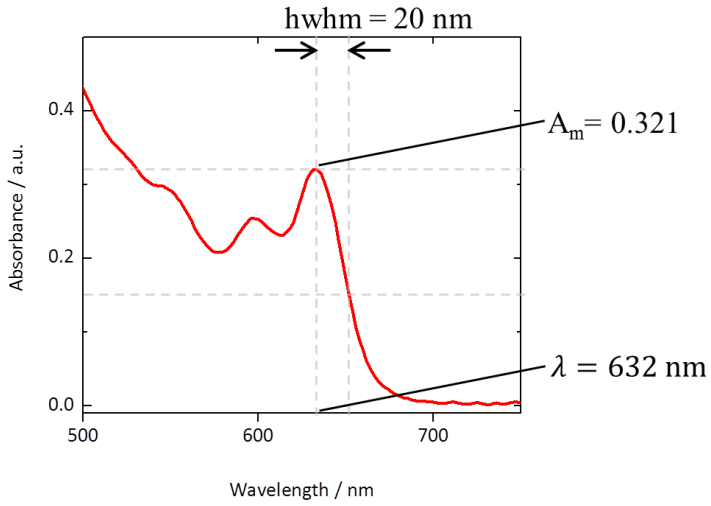

$$\lambda = 632\ \text{nm} \Leftrightarrow \text{D} = (9.8127 \times 10^{-7})\lambda^3 - (1.7147 \times 10^{-3})\lambda^2 + (1.0064)\lambda - 194.84 = 4.02\ (\text{nm})$$

$$\epsilon = 10043(\text{D})^{2.12} = 10043(3.01)^{2.12} = 1.92 \cdot 10^5\ (\text{cm}^{-1}\text{M}^{-1})$$

$$A_{cal} = A_m \cdot (\text{hwhm})/K = 0.321 \cdot 20\,/18 = 0.357$$

$$\text{C} = \text{A}_{cal}/\epsilon \cdot L = 0.357\,/\,1.04 \cdot 10^5 \cdot 1 = 1.84\ (\mu\text{M})$$

Figure A-1. Typical absorption spectrum of CdTe QDs (4.02 nm diameter) and the calculation process for particles concentration based on spectral data.

References

A1 Yu, W. W.; Qu, L. H.; Guo, W. Z.; Peng, X. G., *Experimental Determination of the Extinction Coefficient of CdTe, CdSe, and CdS Nanocrystals*. Chem. Mater. **2003,** *15* (14), p. 2854-2860.

Appendix B

Calculation of the Amount of Shell Sources for One Monolayer

In the synthesis of core/shell QDs using the successive ionic layer adsorption and reaction method, it is essential that the shell source added does not exceed the amount required to form just one layer; if excess shell precursors was present in solution, undesired nucleation occurred, which decreased the quality of the resulting core/shell QDs. Crystallographic parameters, as well as some basic physical properties, were taken into account in order to determine the amount of shell precursors to be added. First step was to calculate the shell thickness for one layer of shell material. In the case of ZnS, where two possible crystal structures are expected, we took an average thickness from two structures for further processing.[B1] Figure B-1 shows crystal structures of wurtzite (hexagonal) and zinc blende (cubic) ZnS. From the wurtzite structure, the monolayer thickness (*d*) was assumed to be half of the c-lattice parameter (*c*):

$$d = \mathrm{c}/2 = 0.626/2 = 0.313 \text{ (nm)} \quad (15)$$

Also, the shell thickness is thought to be equivalent to the height of a tetrahedron highlighted in Figure B-1. In the zinc blende structure, shell thickness (d') was obtained based on the height of a tetrahedron:

$$d' = \mathrm{a}/\sqrt{3} = 0.542/\sqrt{3} = 0.313 \text{ (nm)} \quad (16)$$

Where *a* is the lattice parameter of zinc blende ZnS. Therefore, the average shell thickness of one monolayer was 0.313 nm.

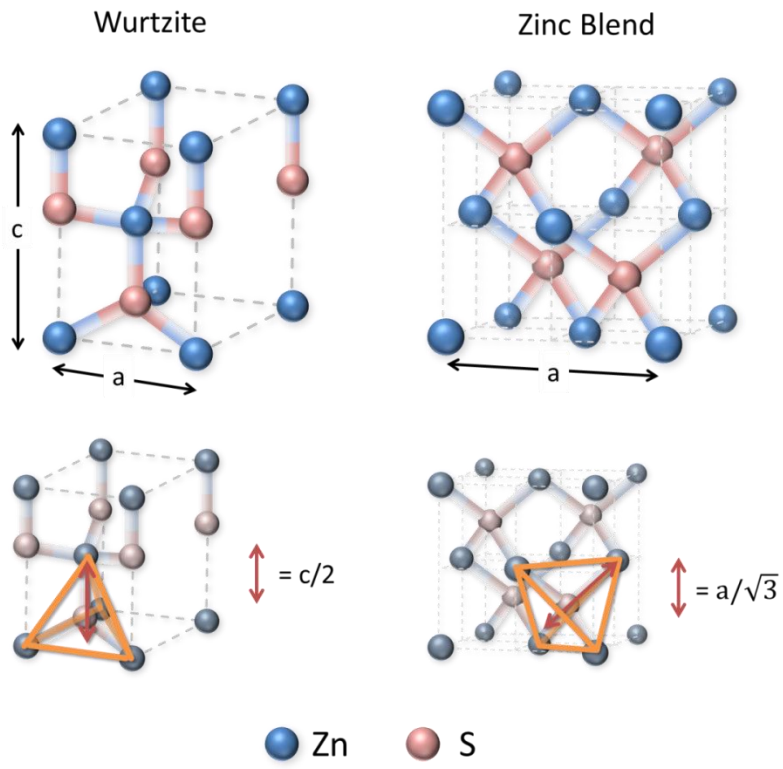

Figure B-1. Schematics of wurtzite and zinc blende ZnS crystals. The tetrahedron units consisting of four zinc atoms are highlighted in orange lines.

Figure B-2 shows the schematics of CdTe/ZnS QDs. For the simplicity, it is hypothesised that a particle is completely spherical and a shell forms concentrically.

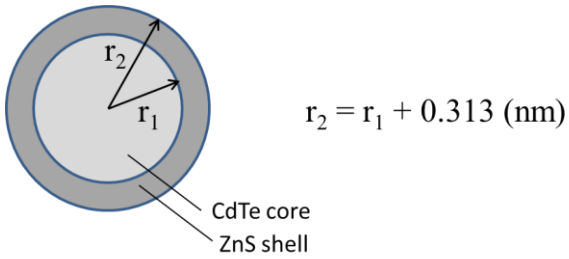

Figure B-2. Simplified structure of a CdTe particle with a monolayer of ZnS shell.

When a core diameter is 4.0 nm (r_1 = 2.0 nm), the volume of a layer of ZnS shell can be calculated as follows.

(Volume of CdTe, V_1)

$$V_1 = \frac{4}{3}\pi \cdot {r_1}^3 = \frac{4}{3}\pi \cdot (2.0 \times 10^{-9})^3 = 33.49 \times 10^{-27}(m^3) \quad (17)$$

(Volume of CdTe+ZnS, V_2)

$$V_2 = \frac{4}{3}\pi \cdot {r_2}^3 = \frac{4}{3}\pi \cdot \left((2.0 + 0.313) \times 10^{-9}\right)^3 = 51.81 \times 10^{-27}\ (m^3) \quad (18)$$

Therefore, the volume of ZnS shell is $V_{ZnS} = V_2 - V_1 = 18.32 \times 10^{-27}$ m^3. The molar amount of ZnS precursor (*X*) per CdTe core particle is described as follows:

$$X = {V_{ZnS} \cdot D}/{M_W} = 18.32 \times 10^{-27} \cdot 4.10 \times 10^{-6}/97.474$$

$$= 7.71 \times 10^{-22}\ (\text{mol per a particle}) \quad (19)$$

where *D* is the density of ZnS (4.10×10^{-6} g/m^3), and M_w is the molecular weight on ZnS (97.474 g/mol).[B2] Finally, the overall amount of ZnS precursors for the CdTe solution can be calculated by the obtained *X* value.

$$[ZnS] = X \cdot C_{CdTe} \cdot V_{solution} \cdot N_A \quad (20)$$

C_{CdTe} is the concentration of CdTe QDs solution calculated from equation (12), $V_{solution}$ is the volume of the CdTe solution, and N_A is the Avogadro constant (6.02×10^{23}).[B3] When we use 10 mL of the solution having the absorption spectrum as shown in Figure A-1, the equation (20) is substituted as follows.

$$[ZnS] = 7.71 \times 10^{-22} \cdot 1.84 \times 10^{-6} \cdot \frac{10}{1000} \cdot 6.02 \times 10^{23}$$

$$= 8.5 \times 10^{-6}\ (\text{mol})$$

For the second shell deposition, the volume of the second layer of ZnS shell can be obtained by a re-calculation of equation (17) and (18) with new radii. Then, the new values of *X* and [ZnS] can be calculated in the same manner using equation (19) and (20).

References

B1 Chen, D. A.; Zhao, F.; Qi, H.; Rutherford, M.; Peng, X. G., *Bright and Stable Purple/Blue Emitting CdS/ZnS Core/Shell Nanocrystals Grown by Thermal Cycling Using a Single-Source Precursor*. Chem. Mater. **2010,** *22* (4), p. 1437-1444.

B2 National_Center_for_Biotechnology_Information *Pubchem*. http://pubchem.ncbi.nlm.nih.gov/ **2012**. February.

B3 National_Institute_of_Standards_and_Technology *Fundamental Physical Constants*. http://physics.nist.gov/cgi-bin/cuu/Value?na **2012**. February.